Coupling shell growth and geochemistry in giant clams to explore biomineralization pathways

Kimberley Marshall-Mills

School of Earth and Environmental Sciences

Cardiff University

Thesis submitted for the Degree of Doctor of Philosophy

March 2024

Summary

Coral reefs are highly vulnerable to a multitude of global to local stressors associated with human activity and are declining at an alarming rate. In recent years, nearshore turbid coral reefs (light-limited habitats with high sediment input) have emerged as important conservation hotspots due to their potential resilience. They show quick recovery after disturbance and thermal stress and are forecast to play a critical role in the future of marine biodiversity. However, they are understudied compared to their clear water counterparts, with more information needed on how reef-building animals grow calcium carbonate ($CaCO_3$) skeletons in turbid reefs.

This thesis explores the intricate biomineralization processes of giant clams (Cardiidae: Tridacninae) across a turbidity gradient in the Coral Triangle region of Sabah, Malaysia. Giant clams are important reef builders facing numerous threats including bleaching and habitat degradation. They also serve as desirable bioarchives, offering insight into past environmental and climactic conditions at high temporal resolution because they grow fast (5–60 µm per day) and live long (>100 years). Herein, I employ and optimize high-resolution imaging and geochemical analysis to disentangle how environmental (e.g. temperature, light availability) and physiological factors interact with shell growth dynamics on turbid reefs.

For the first time, the findings herein highlight the significant influence of turbid reefs on shell composition, revealing variation in intra-annual growth, microstructure, crystallographic organization, and element-to-calcium ratios of biominerals. These differences suggest giant clams from turbid reefs are biomechanically superior to low turbid reefs, with implications for their material properties. I hypothesize these changes may be driven by modifications to metabolism, governed by variation in mixotrophic feeding under different turbidity regimes. Overall, this work emphasizes that turbid reefs are key conservation hotspots, potentially shielding giant clams from widespread disturbances. Such insights are crucial for the conservation of reef calcifying organisms amidst anthropogenic change.

Publications

Peer-reviewed articles associated with this thesis.

Chapter 3 has been modified and published as:

Mills, K. John, E.H. Muir, D.D. *et al.* (2023). Growth responses of mixotrophic giant clams on nearshore turbid coral reefs. *Coral Reefs* 42, 593–608. https://doi.org/10.1007/s00338-023-02366-8

Chapter 4 has been modified and published as:

Mills, K. Muir, D.D. Oldroyd, A. *et al.* (2024). Microstructure and crystallographic texture data in modern giant clam shells (*Tridacna squamosa* and *Hippopus hippopus*). *Data in Brief* 52, 109947. https://doi.org/10.1016/j.dib.2023.109947

Mills, K. (2022). Understanding shell growth in giant clams with EBSD. *Nature Reviews Earth and Environment* 3, 424. https://doi.org/10.1038/s43017-022-00311-x

Chapter 5 has been submitted to *Scientific Reports* and is under review as:

Mills, K. Sosdian, S. Muir, D. *et al.* Giant clams modify crystallographic and geochemical pathways of shell formation in response to turbidity.

Chapter 6 is in preparation for submission to *Palaeogeography, Palaeoclimatology, Palaeoecology* as:

Mills, K. John, E.H. Sosdian, S. *et al.* Diagenesis in fossil giant clam shells: using crystallographic texture to detect alteration from pristine to secondary aragonite.

Peer-reviewed articles relevant to, but not associated with this thesis.

The following article is in preparation for submission to *Nanoscale* as:

Davies-Jones, J. Graf, A., Davies. P.R., John, E.H., **Mills, K**. *et al.* Characterization of the Nanostructure and Composition of Mollusc Shells using Advanced Spectroscopic and Imaging Techniques.

Acknowledgements

I am deeply grateful to my supervisory team for their unwavering support and invaluable guidance throughout this journey. Foremost, my supervisors at Cardiff, who I owe so much gratitude for where I am today—thank you for always being there! Firstly, Sindia Sosdian for taking a chance on me with this PhD and encouraging me to pursue my own directions, providing support every step of the way and the countless discussions that shaped this thesis. I must also extend my gratitude to Eleanor John, for many discussions, insights, expertise, and assistance with giant clam specimens. Also, to Duncan Muir for his wealth of knowledge on microscopy and imaging and for the hours (if not days) of discussion on crystallographic properties. Also, I further extend my thanks to my supervisors at the Natural History Museum, Nadia Santodomingo and Ken Johnson. Nadia's extensive knowledge, along with her overall enthusiasm and guidance on the coral reefs in Darvel Bay were instrumental to this thesis, as well as Ken's helpful insights. You've been key in shaping me into the scientist I've become and continue to strive to be.

This thesis would not have been possible without help from the Borneo Marine Research Institute (Universiti Malaysia Sabah) in Sabah. Especially, thanks to Allia Rosedy and Zarinah Waheed for help with sample collection, permits applications, and other key research and logistic aspects of the project. Fieldwork was possible thanks to Dominic Monteroso (Darvel Bay Diving Centre). Without your hard work, I would not hold the amazing sample set I have used! Thanks also to the Natural History Museum London, for use of fossil specimens for analysis in this PhD.

Throughout my PhD journey, I've received exceptional technical and laboratory support. In particular, Anthony Oldroyd's patience and generosity in teaching and assisting me with thin section sample preparation, XRD and LOI—you are greatly appreciated within the school! Duncan Muir's mentorship in SEM and EBSD techniques and his perseverance with the project allowed many new avenues of exploration that would otherwise not have been possible. In addition, I am grateful to Greg Shaw at Cardiff School of Chemistry for taking time out of his schedule and

assisting me with Raman spectroscopy. I would also like to thank Ben Buse at Bristol University for assisting a complete novice with the collection of EPMA data.

I extend my gratitude to the enthusiastic members of the MÔR research group for always providing mounds of enthusiasm, advice, and camaraderie. The support they have provided over the years has been instrumental to the completion of this thesis. I also extend this appreciation to the entire community of the School of Earth and Environmental Sciences at Cardiff, particularly my fellow PhD students for sharing this journey. Also, I can't forget the talented undergraduates who contributed to this work through various projects, including Natalie and Mia for help with counting specimens and providing new perspectives and insights.

I am grateful to the GW4+ DTP community for sharing experiences, friendship and supporting each other throughout our time together. Especially, the 'palaeo-pals', Amy, Madleen and Emma, for all the chats, adventures and fun along the way.

I further extend thanks to Amgueddfa Cymru—National Museum Wales for lending additional giant clam specimens for this project. In addition, the years I spent at the museum before starting this PhD have undoubtably been a key part in my success and I especially thank Kate, Teresa, Harry and Anna for nurturing my growth as a scientist for the last seven or more years!

Lastly, I am forever grateful to my family, especially my husband Joe, for his unwavering support and belief in me. And I cannot forget my cherished greyhound, Frodo, for his companionship and reminders to take breaks, go for walkies and just enjoy life. He may be the only dog in the world that's well versed in the research of giant clams!

Thank you all for being an integral part of this remarkable journey.

Commonly used abbreviations

OW Ocean warming

OA Ocean acidification CO_2 Carbon dioxide

H_2CO_3 Carbonic acid

HCO_3^- Bicarbonate ion

H^+ Hydrogen ion

CO_3^{2-} Carbonate ion

Ω Calcium carbonate saturation state

Ca^{2+} Calcium ion

NPP Net primary production

OM Organic matrix

CL Crossed-lamellar microstructure

CCL Complex crossed-lamellar microstructure

CCL-I Irregular complex crossed-lamellar microstructure

CCL-P Complex crossed-lamellar with prisms microstructure

IL Inner shell layer

OL Outer shell layer

PL Pallial line (or pallial myostracum)

AM Adductor myostracum

N Nitrogen

P Phosphorous

El/Ca Element-to-calcium ratio

Mg/Ca Magnesium-to-calcium ratio

Sr/Ca Strontium-to-calcium ratio

K_d(490) Diffuse attenuation coefficient of spectral irradiance at 490 nm wavelength

SST Sea surface temperature

SSS Sea surface salinity

TSS Total suspended solids

CF Calcifying fluid

HCl Hydrochloric acid

SEM Scanning electron microscopy

SE Secondary electron image

EBSD Electron backscatter diffraction

BKP Backscatter Kikuchi pattern

MUD Multiple of uniform density statistic

EPMA Electron microprobe microanalysis

XRD X-Ray Diffraction

LOI Loss on ignition

NHM Natural History Museum

NMW Amgueddfa Cymru—National Museum Wales

3D Three-dimensional

DGR Daily growth rate

POM Particulate organic matter

SGI Standardized growth index

GL Growth band (or growth increment, growth line)

GD Growth direction (or DOG, direction of growth)

EBSP Electron backscatter pattern

MAD Mean angular deviation

BC Band contrast image

CPO Crystallographic preferred orientation

IPF Inverse pole figure map

Table of Contents

1. Background and introduction 1
1.1 Background 1
1.1.1 Coral reefs in a changing ocean 1
1.1.1.1 Ocean warming 1
1.1.1.2 Ocean acidification 2
1.1.1.3 Local stressors 3
1.1.2 Marginal coral reefs as refugia 4
1.1.2.1 Deep clear water reefs 4
1.1.2.2 Shallow turbid water reefs 5
1.2 Introduction 6
1.2.1 Giant clams 6
1.2.1.1 Taxonomy 7
1.2.1.2 Distribution 8
1.2.1.3 Feeding 8
1.2.1.4 Morphology 9
1.2.1.5 Ecology 12
1.2.1.6 Threats 12
1.2.1.6.1 Bleaching 13
1.2.1.6.2 Exploitation 13
1.2.1.6.3 Sediment stress and elevated nutrient levels 13
1.2.1.6.4 Conservation status 14
1.2.2 Giant clams as bioarchives 15
1.2.2.1 Growth banding 17
1.2.2.2 Microstructure 18
1.2.2.3 Crystallographic texture 21
1.2.2.4 Trace element profiles 23
1.2.2.4.1 Mg/Ca 23
1.2.2.4.2 Sr/Ca 24
1.2.2.4.3 Ba/Ca 25
1.2.3 Complications of using giant clams as bioarchives 25
1.2.3.1 Diagenetic alteration 25
1.2.3.2 Vital effects 26
1.2.4 Thesis outline: Coupling shell growth and geochemistry in giant clams to explore biomineralization pathways 28

1.2.4.1 Aims 28
1.2.4.2 Layout 29
2. Study sites and methodology 32
2.1 Borneo 32
2.1.1 Temperature 33
2.1.2 Rainfall 33
2.1.3 Topography 34
2.1.4 Land use 34
2.2. Sabah 34
2.2.1 Temperature 36
2.2.2 Rainfall 36
2.2.3 Tropical cyclones 37
2.2.4 Land use 37
2.3 Study localities 38
2.3.1 Darvel Bay 38
2.3.1.1 Triangle 43
2.3.1.2 Baik 44
2.3.1.3 THalu 46
2.3.1.4 Sakar 47
2.3.1.5 Misan 48
2.3.1.6 Blue Lagoon 49
2.3.2 Semporna Region 51
2.3.3 Stratigraphic formations 51
2.4 Study samples 53
2.4.1 Modern shells 53
2.4.2 Fossil shells 56
2.4.3 Sample preparation procedure 58
2.5 Imaging analysis 60
2.5.1 Light microscopy 60
2.5.2 Scanning electron microscopy (SEM) 63
2.5.3 Electron backscatter diffraction (EBSD) 64
2.6 Electron probe microanalysis (EPMA) 67
2.7 X-ray diffraction (XRD) 68
2.8 Raman spectroscopy 69
2.9 Loss on ignition (LOI) 71
2.10 Environmental data 72

2.10.1 *In situ* 72
2.10.2 Remote sensed data 72
2.10.2.1 Remote sensed validation 74
2.10.3 Characterization of environment 75
2.10.3.1 Turbidity 75
2.10.3.2 Monthly analysis of environmental parameters at Baik and Triangle 76
2.10.3.3 High resolution analysis of sea surface temperature and lux at Baik and Triangle 78
2.10.3.4 Tidal data at Lahad Datu 80
2.10.3.5. Total solids content 80
2.11 Data analysis 83
3. Growth responses of giant clam shells to turbid reefs 84
3.1 Abstract 84
3.2 Introduction 85
3.3 Methods Summary 87
3.3.1 Diagenetic screening 87
3.3.1.1 SEM 87
3.3.1.2 Raman spectroscopy 87
3.3.2 Environmental data 88
3.3.3 Construction of mean shell growth chronologies 88
3.3.4 Data analysis 89
3.4 Results 93
3.4.1 Diagenetic screening 93
3.4.2 Environmental data 94
3.4.3 Growth band microstructure 95
3.4.4 Annual shell growth 100
3.4.5 Seasonal shell growth and environmental relationships 103
3.4.6 Daily shell growth using spectral analysis 109
3.5 Discussion 111
3.5.1 Multi-method approach to sclerochronology in giant clams 111
3.5.2 Shell growth mediated by ontogeny 113
3.5.3 Environmental influences on shell growth 114
3.5.3.1 Influences on annual shell growth 115
3.5.3.2 Influences on monthly shell growth 116
3.5.3.3 Influences on daily shell growth 118

3.5.4 Conclusion 118
4. Improving electron backscatter diffraction (EBSD) data in giant clams by post-acquisition refinement 120
4.1 Abstract 120
4.2 Introduction 121
4.3 Methods 123
4.3.1 SEM 124
4.3.2 EBSD 124
4.3.2.1 Sample preparation 124
4.3.2.2 Data acquisition 125
4.3.2.3 Post-acquisition refinement 126
4.3.2.4 Data analysis 127
4.4 Results 128
4.4.1 Microstructure 128
4.4.2 EBSD post-acquisition refinement 129
4.4.3 EBSD crystallographic texture in *H. hippopus* and *T. squamosa* 132
4.5 Discussion 137
4.5.1 Conclusion 139
5. Biomineralization plasticity in giant clam shells from turbid reefs: integrating physical and geochemical pathways 140
5.1 Abstract 140
5.2 Introduction 141
5.3 Methods Summary 143
5.3.1 SEM 144
5.3.2 EBSD 145
5.3.3 EPMA 145
5.3.4 Data analysis 146
5.4 Results 146
5.4.1 Microstructural features 146
5.4.2 Crystallographic features 149
5.4.3 Geochemical features 152
5.5 Discussion 157
5.5.1 Shell architecture 157
5.5.2 Shell geochemistry 158
5.5.3 Implications for biomechanical properties 163
5.5.4 Conclusion 164

6. Diagenesis in fossil giant clam shells: using crystallographic texture to detect alteration from pristine to secondary aragonite 165
6.1 Abstract 165
6.2 Introduction 166
6.3 Methods Summary 169
6.3.1 XRD 169
6.3.2 Raman spectroscopy 170
6.3.3 SEM 171
6.3.4 EBSD 171
6.3.5 LOI 172
6.4 Results 172
6.4.1 Nano- to microscale microstructural and crystallographic features 172
6.4.1.1 Characteristics of modern giant clam shells 172
6.4.1.2 Preservation of fossil giant clam shells 180
6.4.2 Grouping of shell features 189
6.5 Discussion 193
6.5.1 Conclusion 196
7. Conclusions and future directions 198
7.1 Thesis summary and synthesis 198
7.2 Contribution to knowledge 199
7.4 Limitations and future work 203
7.4.1 Age of specimens 203
7.4.2 Mixotrophy 204
7.4.3 EPMA sample size 204
7.4.4 Biomechanical properties 205
7.4.5 Geochemical alterations in diagenesis 205
7.4 Concluding remarks 206
8. References 208
Appendix A 253
Appendix B 253
Appendix C 253
Appendix D 253

List of Figures

Figure 1.1. Tridacna squamosa photographed in 2019. 7

Figure 1.2. The distribution of giant clam species within the Indo-Pacific region.. 8

Figure 1.3. Dorsal view of live *Tridacna squamosa* collected by the Reefugia Team in 2019. 10

Figure 1.4. Morphological features of the outer shell surface of *Tridacna squamosa*. 11

Figure 1.5. Morphological features of the inner shell of *Tridacna squamosa*. 11

Figure 1.6. Schematic sketch of the hierarchical crossed-lamellar microstructure..... 20

Figure 1.7. Shell microstructure and crystallographic orientation of *Tridacna gigas*.. 23

Figure 2.1. Map of Borneo 32

Figure 2.2. Map of northern Borneo 35

Figure 2.3. Annual mean rainfall map of Sabah 37

Figure 2.4. Reef extent in northeastern Sabah 40

Figure 2.5. Location of six sampling sites in Darvel Bay 41

Figure 2.6. Bathymetry of Darvel Bay …….. 42

Figure 2.7. Location of ‘high turbid’ Triangle Reef 43

Figure 2.8. Images taken in 2019 from Reefugia expedition to Triangle Reef 44

Figure 2.9. Location of ‘low turbid’ Baik Reef. 45

Figure 2.10. Images taken in 2019 from Reefugia expedition to Baik Reef. 46

Figure 2.11. Location of Tamanong Halu (THalu) sampling site 47

Figure 2.12. Images taken in 2019 from Reefugia expedition to THalu Reef..... 47

Figure 2.13. Location of Sakar North (Sakar) sampling site 48

Figure 2.14. Images taken in 2019 from Reefugia expedition to Sakar Reef 48

Figure 2.15. Location of Sakar South Misan (Misan) sampling site 49

Figure 2.16. Images taken in 2019 from Reefugia expedition to Misan Reef 49

Figure 2.17. Location of Blue Lagoon offshore clear water sampling site. 50

Figure 2.18. Images taken in 2019 from Reefugia expedition to Blue Lagoon Reef. 50

Figure 2.19. Location of fossil giant clam sample sites in eastern and northeastern Borneo. 52

Figure 2.20. Dead collected giant clam shells from Darvel Bay 54

Figure 2.21. Two giant clam *Tridacna squamosa* shells from the Semporna region. 55

Figure 2.22. Two giant clam *Tridacna* spp. fossil shells from outcrops in eastern East Kalimantan and eastern Sabah. 56

Figure 2.23. Sample preparation procedure for giant clam shells 59

Figure 2.24. Tridacna squamosa shell valve on platform of diamond saw apparatus. 60

Figure 2.25. Examples from a set of transmitted images of *Tridacna squamosa* 61

Figure 2.26. The inner shell layer edge and pallial line of *Tridacna squamosa* 62

Figure 2.27. Author operating Zeiss Sigma HD field emission gun SEM 64

Figure 2.28. Sample chamber inside the SEM, showing EBSD sample holder 65

Figure 2.29. Simplified schematic of experimental set-up for electron backscatter diffraction data collection……. 66

Figure 2.30. Relative intensity versus Raman shift of typical Raman spectra of calcium carbonate minerals. 71

Figure 2.31. Sea surface temperature from *in situ* HOBO loggers and MODIS remote sensed data from key reef sites Triangle and Baik 74

Figure 2.32. Monthly average environmental data from Baik and Triangle reefs in Darvel bay for 2018–2020, relating to last year of growth for samples collected live in April 2019 and February 2020 77

Figure 2.33. Monthly variation of sea surface salinity in Darvel Bay for 2018–2020. Data are for period of last year of growth for 2019 and 2020 live collected shells. ... 78

Figure 2.34. 10 minute sea surface temperature and light HOBO data from Baik and Triangle key reef sites in Darvel Bay for November 2019, representative of the early wet season 79

Figure 2.35. 10 minute sea surface temperature and light HOBO data from Baik and Triangle key reef sites in Darvel Bay for May 2019, representative of the early dry season. 79

Figure 2.36. Tidal data for Lahad Datu between 2020 and 2021. 80

Figure 3.1. Scanning electron microscopy images of *Tridacna squamosa* thin sections, showing evidence of original aragonite microstructures 93

Figure 3.2. Raman spectra of nine *Tridacna squamosa* shell samples collected dead from Darvel Bay and unknown collection status from Semporna reefs 94

Figure 3.3. Principal component analysis (PCA) for environmental data from Baik and Triangle reefs in Darvel Bay 95

Figure 3.4. SEM images of the microstructure in *Tridacna squamosa* from Triangle and Baik reefs 97

Figure 3.5. Relationship between days alive and daily growth rate for individual counts incorporated into final mean shell growth chronologies from live collected *Tridacna squamosa* shells 98

Figure 3.6. Relationship between days alive and daily growth rate for individual counts incorporated into final mean shell growth chronologies from dead collected *Tridacna squamosa* shells 99

Figure 3.7. All mean shell growth chronologies derived from daily growth increment widths of live and dead collected *Tridacna squamosa* for comparison of shell growth over lifespan. 102

Figure 3.8. Dated mean shell growth chronologies derived from daily growth increment widths for *Tridacna squamosa* collected from Triangle and Baik 104

Figure 3.9. Standardized growth chronologies for last year of growth for *Tridacna squamosa* shells collected alive and dead. 105

Figure 3.10. Floating standardized growth chronologies for dead collected *Tridacna squamosa* shells from Darvel Bay. 106

Figure 3.11. Added-variable plots of individual explanatory variables versus dependent shell standardized growth chronologies for period corresponding to last year of growth for sample SS_BAIK..... 107

Figure 3.12. Added-variable plots of individual explanatory variables versus dependent shell standardized growth chronologies for period corresponding to last year of growth for sample NS207..... 107

Figure 3.13. Added-variable plots of individual explanatory variables versus dependent shell standardized growth chronologies for period corresponding to last year of growth for sample SS_CT 108

Figure 3.14. Added-variable plots of individual explanatory variables versus dependent shell SGI for period corresponding to last year of growth for sample ZW156. 108

Figure 3.15. Comparison of monthly growth pattern for last year of growth in shells collected alive from the Baik and Triangle reefs 109

Figure 3.16. Multitaper method power spectra of daily maximum tide and daily standardized growth index growth chronology of Triangle reef shell ZW156 in frequency space 110

Figure 3.17. Multitaper method power spectra of daily standardized growth index chronologies for daily maximum tide and shells SS_CT, SS_BAIK, NS207 in frequency space. 110

Figure 3.18. Secondary electron image of the outer- and inner shell layer of *Tridacna squamosa*. 113

Figure 3.19. Mean daily growth rate of the inner shell layer for Darvel Bay and Semporna Tridacnidae from the current study, compared to published growth values. 115

Figure 4.1. Schematic showing section location of a giant clam shell along the maximum growth axis 123

Figure 4.2. Thin section showing rectangles of copper tape to help eliminate charging and to assist with targeting specific areas of the sample for EBSD mapping 125

Figure 4.3. In-lens secondary electron images showing the microstructure of the giant clam shells SS02B_CT and SS01B_SN 128

Figure 4.4. Relationship between fraction of indexed patterns for aragonite and manual selection of number of reflectors for aragonite within the OINA and HKL databases in AZtec 6.0 software (Oxford Instruments) 130

Figure 4.5. Fraction of indexed pattern for aragonite using standard Hough based detection by manually selecting the number of reflectors for orthorhombic aragonite with the HKL database in AZtec 6.0 software (Oxford Instruments) 131

Figure 4.6. EBSD band contrast (pattern quality) images of the inner shell layer in giant clam shells 133

Figure 4.7. EBSD inverse pole figure (IPF-Y) map showing the microstructure and texture of paired daily growth lines within the inner layer of a *Hippopus hippopus* shell (SS01B_SN). 135

Figure 4.8. EBSD inverse pole figure (IPF-Y) map showing the complex crossed lamellar microstructure and texture of the inner layer of a *Tridacna squamosa* shell (SS02B_CT) 136

Figure 5.1. Microstructure of high turbid and low turbid giant clam shells 148

Figure 5.2. Representation of nanograins on the surface of shell crystals 149

Figure 5.3. Crystallographic texture of high turbid and low turbid giant clam shells. 151

Figure 5.4. Geochemical profiles of element-to-calcium ratios for high turbid and low turbid giant clam shells 153

Figure 5.5. Example of a microboring hole present in the outer shell layer of *Tridacna squamosa* (SS_CT) from high turbid reef Triangle 154

Figure 5.6. Sub-daily resolved EPMA maps for Sr/Ca and Mg/Ca in a region of the outer shell layer in the low turbid giant clam (SS_BAIK) shell 154

Figure 5.7. Simplified conceptual representation of the biomineralization mechanism in tridacnid giant clams. 161

Figure 6.1. Valve of *Tridacna squamosa*, showing where slice for analysis was acquired and three numbered black rectangular regions used for preservation screening 170

Figure 6.2. XRD diffractograms of shells of modern *Tridacna squamosa* and fossil *Tridacna* 174

Figure 6.3. Scanning electron microscopy images showing the complex crossed lamellar microstructure of the inner shell layer of modern *Tridacna squamosa* shells…..... 175

Figure 6.4. Electron backscatter diffraction maps for modern *Tridacna squamosa*. 178

Figure 6.5. Relative frequency versus distribution of grain area for representative 100 x 100 μm electron backscatter diffraction map regions 179

Figure 6.6. Raman spectra of fossil giant clam shell samples collected from eastern Borneo. 181

Figure 6.7. Scanning electron microscopy images showing the microstructure of the inner shell layer for Pliocene and Miocene fossil giant clam shells 182

Figure 6.8. Electron backscatter diffraction maps for fossil giant clam shells 184

Figure 6.9. Electron backscatter diffraction maps for the Miocene fossil giant clam, showing different regions of the shell that moderately vary from modern samples. 186

Figure 6.10. Electron backscatter diffraction phase map for area Miocene3 within sample TF108, showing small patches of calcite and potentially dolomite between aragonite grains 187

Figure 6.11. Electron backscatter diffraction map for the Pliocene fossil giant clam, showing a region of the inner layer shell edge/periphery, where variation in crystal size is observed 188

Figure 6.12. Overview of crystallographic texture from electron backscatter diffraction data of modern and fossil giant clam shells 191

List of Tables

Table 2.1. Summary of nearby coastal environment and human activities of modern coral reef and fossil sampling sites in eastern and northeastern Borneo 51

Table 2.2. Giant clam specimens used in this thesis 57

Table 2.3. In situ and remote sensed derived products used in this thesis 73

Table 2.4. Coral reef sampling sites surveyed in Darvel Bay (East Sabah, Malaysia) and mean annual K_d(490) (2019–2020) 76

Table 2.5. Total solids content in milligrams per litre for key reef sites Baik and Triangle 82

Table 3.1. Raw count data of each shell growth chronology for thirteen *Tridacna squamosa* shells 91

Table 3.2. Each growth chronology incorporated into combined final growth chronologies for *Tridacna squamosa* shells 101

Table 3.3. Post hoc Tukey HSD test for differences in standardized growth index growth rate 103

Table 4.1. Hough resolution and indexed fraction of aragonite for *T. squamosa* using the HKL database 131

Table 4.2. Area of interest parameters and indexed fraction of aragonite for *T. squamosa* using the HKL database 132

Table 5.1. List of four studied samples of *Tridacna squamosa* from Baik (low turbid) and Triangle (high turbid) reefs in Darvel Bay. 144

Table 5.2. Post hoc Tukey HSD test results for Sr/Ca between shells from the Triangle (SS_CT) and Baik (SS_BAIK) reefs in the wet season and dry season 155

Table 5.3. Pairwise comparison of Mg/Ca between shells from the Triangle (SS_CT) and Baik (SS_BAIK) reefs in the wet season and dry season 156

Table 6.1. Bulk loss on ignition measurements for the inner shell layer of tested giant clam samples 176

1. Background and introduction

1.1 Background

1.1.1 Coral reefs in a changing ocean

Tropical coral reefs are one of the most biodiverse ecosystems on the planet (Knowlton et al. 2010), hosting an estimated 830,000 species worldwide (Fisher et al. 2015). Despite their remarkable diversity, they are alarmingly fragile, undergoing significant transformations attributable to the unprecedented pace of human intervention characterizing the Anthropocene (Hoegh-Guldberg 1999; Steffen et al. 2011). Global climate change from the release of man-made greenhouse gas emissions (manifesting as ocean warming and acidification) and localized human activities (e.g. intensive overfishing, pollution, physical habitat deterioration) are key drivers of change to how calcifying organisms, those that deposit calcium carbonate ($CaCO_3$) biominerals, make their hard shells and skeletons. These alterations lead to wide-ranging effects, from shifts in ecosystem function, reef structural integrity and community composition to individual organismal responses, such physiological response (Hughes et al. 2003; Hoegh-Guldberg et al. 2007; Bongaerts et al. 2010; Wear and Thurber 2015; Cinner et al. 2016; Sully and van Woesik 2020). Approximately 275 million people live within 30 km of coral reefs, many of which situated in countries with high socio-economic reliance on the goods and services they provide (Burke et al. 2011). In many of these regions, reef fisheries yield, reef associated employment, and reef tourism are being, and projected to be, considerably impacted (Hoegh-Guldberg et al. 2007; Burke et al. 2011; McClanahan 2022).

1.1.1.1 Ocean warming

The ocean plays a profound role in moderating atmospheric climate change. In recent decades, it has absorbed 90% of excess heat emitted from the burning of greenhouse gases (Rhein et al. 2013). Consequently, average ocean temperature has risen (ocean warming, OW) by 0.9°C, with further warming of 2.9°C predicted by 2100 (emission scenario SSP5-8.5) (Fox-Kemper et al. 2021). As OW intensifies, occurrences of large-scale coral bleaching have become more frequent and severe in recent years (e.g.

Hughes et al. 2017). Bleaching (or whitening) is caused by a loss of symbiotic dinoflagellates from host tissue, leading to a reduction or exclusion in the transfer of nutrients from symbiont to host, which can starve and kill the host organism (e.g. Leggat et al. 2003). It is projected that an overwhelming majority of tropical coral reefs will experience severe annual bleaching by the mid 21st century under fossil fuel aggressive emissions scenarios (van Hooidonk et al. 2014). Bleaching is not restricted to corals alone but can impact any animal in symbiotic association with dinoflagellate algae in the genus *Symbiodinium* (e.g. Douglas 2003), including sponges (e.g. McMurray et al. 2011), anemones (e.g. Saenz-Agudelo et al. 2011) and clams (Junchompoo et al. 2013). However, the response to bleaching from other taxon aside from corals is understudied and the impacts of thermal stress are largely unknown.

1.1.1.2 Ocean acidification

Carbon dioxide (CO_2) emissions absorbed by the world's oceans are another global concern for coral reef declination. When CO_2 enters seawater, it dissolves and forms carbonic acid (H_2CO_3), which dissociates into bicarbonate (HCO_3^-) and hydrogen ions (H^+) (Doney et al. 2009). Due to a rise in the concentration of H^+, seawater becomes more acidic (ocean acidification, OA), decreasing both the availability of free carbonate ions (CO_3^{2-}) and the calcium carbonate saturation state (Ω) (e.g. van Hooidonk et al. 2013). Biotic calcification relies on available calcium (Ca^{2+}) and CO_3^{2-} ions, hence acidic conditions make it difficult for reef-builders to grow and deposit their shells (Feely et al. 2009), compromising the important role coral reefs play in the carbon cycle and the carbonate system.

Average ocean pH has already reduced by 0.1 units due to OA and a further reduction of 0.4 pH units is projected by 2100 (emission scenario SSP5-8.5) (Canadell et al. 2021). OA is known to negatively impact skeletal density and increase susceptibility to erosion in many coral species through dissolution of their $CaCO_3$ skeletons (Hoegh-Guldberg et al. 2007). Since reef persistence depends on an accretion-erosion balance (e.g. Silbiger et al. 2014), changes that favour erosion over accretion will deteriorate reefs. However, there is considerable variability in not only species- (e.g. Pandolfi et al. 2011) and site-specific responses (e.g. Yee and Barron 2010) to OA, but

also in local population adaption and adaptive phenotypic plasticity (Vargas et al. 2017), meaning that global-scale impacts of OA are highly variable and non-uniform.

1.1.1.3 Local stressors

Local stressors also pose significant threats to coral reefs, encompassing a broad spectrum of factors, including overfishing (Roberts 1995), predation (e.g. Kayal et al. 2012), extreme weather disturbances (e.g. De'ath et al 2012), coral disease (Moriarty et al. 2020), pollution (Pastorok and Bilyard 1985), and sedimentation from unprecedented coastal development (Rogers 1990). The synergistic impact of local stressors has been demonstrated to be responsible for substantial declines observed in the cover of hard coral species (e.g. De'ath et al. 2012). Local stressors also interplay with global stressors, showing detrimental effects on both an individual organismal level to overall reef ecosystem health (Ban et al. 2014). For example, diminished water quality can significantly reduce coral resilience to bleaching events, drastically exacerbating time of recovery (Carilli et al. 2009). Similarly, coral mass bleaching is known to increase subsequent susceptibility to outbreak of disease, which may peak several months after the onset of bleaching (Miller et al. 2009). It is recognised that there is an urgent need to enhance the evaluation and implementation of site-specific local management practices to improve coral reef resilience to both local and global stressors (Shaver et al. 2018).

Traditionally, conservation and management efforts have concentrated on isolated reef habitats far removed from human disturbances (e.g. Gilmour et al. 2013). Established ideas of coral reef optimization have been concerned with stenotolerant habitats (i.e. those that have limited ability to adapt to changing environmental conditions) (Kleypas et al. 1999), limited to shallow, sunlit and clear waters (e.g. Perry and Larcombe 2003; Sully and van Woesik 2020). However, this necessitates a shift in perspective towards understanding and addressing the broader ecological dynamics that play a role in reef resilience (Hoegh-Guldberg et al. 2007). Not only do numerous stressors and stressor interactions remain poorly understood, but there is also a lack of knowledge in relation to the responses of other reef calcifers aside from corals.

1.1.2 Marginal coral reefs as refugia

In the last decades, reef scientists have increasingly highlighted marginal reefs, those existing close to their environmental limits (Kleypas et al. 1999), as more resilient to external stressors than 'traditional' coral reefs. These atypical reefs, traditionally perceived as 'sub-optimal,' may be suitable as alternatives for coral reef development (Perry and Larcombe 2003), shielding coral communities from large scale disturbance and acting as refugia. By concentrating on non-traditional reefs that strongly defy expectations and challenge conventional views, we may understand how reef organisms adapt to a changing ocean and confront long-term climate change (Cinner et al. 2016).

Marginal reefs can be divided into two key types: deep clear water reefs (e.g. Cinner et al. 2016) and nearshore shallow water reefs with high turbidity and sediment input (Perry and Larcombe 2003; Cacciapaglia and van Woesik 2016; Browne et al. 2019; Sully and van Woesik 2020). Although these environments are light-limited compared to 'traditional' shallow clear water reefs, the ability for corals to survive and thrive on marginal reefs has been demonstrated (e.g Waheed and Hoeksema 2013), despite lower levels of photosynthetically active radiation (PAR) required for calcification and photosynthesis (Loiola et al. 2019). Given that low-light reef environments are capable of alleviating bleaching stress induced by elevated temperatures (e.g. Cacciapaglia and van Woesik 2016; Sully and van Woesik 2020), marginal reefs may buffer against thermal stress by shading corals. This is because photoinhibition is enhanced as rates of light energy absorption exceed consumption, reducing the photosynthetic fixation of carbon dioxide (CO_2) in high light environments (Takahashi and Murata 2008).

1.1.2.1 Deep clear water reefs

Deep clear water reefs are situated in the upper mesophotic zone, with depths between 30 to 60 m (Bongaerts et al. 2010; Kahng et al. 2010). Although they may escape from heat stress at these depths, they host less coral biodiversity than shallower reefs, being restrictive in which species are able to inhabit them (Bongaerts et al. 2010; Kahng et al. 2010). Hence, their potential for acting as refuge for "traditional reefs" is limited. Community structure is also largely different from shallow water

habitats, and structural complexity reduced (Kahng et al. 2010). Further, connectivity to shallow reefs is a highlighted problem when envisaging them as a refuge for "traditional" reefs (e.g. Bongaerts et al. 2010; Morais and Santos 2018).

1.1.2.2 Shallow turbid water reefs

Nearshore shallow water turbid reefs are characterized by regimes of significant seasonal or continuous sedimentation and small suspended particles (Perry and Larcombe 2003; Senior 2020). Recently, it has been shown that they can mitigate bleaching and recover quickly after thermal stress events, hosting high live coral cover and diversity (Perry and Larcombe 2003; Waheed and Hoeksema 2013; Cacciapaglia and van Woesik 2016; Morgan et al. 2017; Browne et al. 2019; Sully and van Woesik 2020; Rosedy et al. 2023), even in artificial communities where engineering works provide manmade substrate (Lane and Lim 2013). Although the species composition of reef benthic communities does change with sediment parameters (Waheed et al. 2015; Browne et al. 2019; Senior 2020), a shallow-deep continuum is not necessary with turbid reefs, opposed to deeper refugia. Moreover, early diversification of ancient coral communities in the Coral Triangle occurred in shallow turbid habitats containing significantly high coral species and genera diversity, with the persistence of these taxa lasting over geologic timescales (Santodomingo et al. 2016).

Due to their proximity to the coastline, many turbid reefs are situated close to human settlements and are highly susceptible to local pressures, such as land-use change (Browne et al. 2019) and pollution (Sully and van Woesik 2020). The 'marginal reef paradox' hypothesis postulated by Soares (2020) conceptualizes this difficulty, which states that marginal reefs are more resistant to global change, but less resistant than 'traditional' reefs to local change and need much more management and conservation action. Since the facilitation of shading is thought to be limited to mostly naturally turbid waters (Cacciapaglia and van Woesik 2016), it is of importance to identify suitable localities for potential turbid reef refugia and candidates have been recommended in areas with low anthropogenic activity (e.g. Santodomingo et al. 2016; Browne et al. 2019). Increasing our currently limited understanding of abiotic-biotic dynamics on turbid reefs will further shed light on the viability of these favourable contenders for long-term climate change refugia.

1.2 Introduction

1.2.1 Giant clams

Giant clams are the largest (Rosewater 1965; Ma et al. 2020) and among the longest lived of mollusc bivalves, occurring in the fossil record from the Eocene (Rosewater 1965). They are widespread and conspicuous inhabitants of tropical coral reef communities, revealing colourful and bright outer mantle tissues that are a charismatic component of reef habitats (Rosewater 1969; Neo 2020) (Figure 1.1). They carry out critical roles in the reef community due to their contributions to the structure, complexity, and ecology of reefs (Neo et al. 2015). Like many reef species, they are under threat from a multitude of local to global stressors (Neo et al. 2015). However, their responses to different stressors are understudied compared to other calcifying reef organisms. It is not understood how their calcification and growth changes between diverse reef environments and the external and internal mechanisms controlling these processes. Increasing understanding of how they respond to local stressors and climate change is required for conservation and management strategies in the context of a rapidly changing ocean (Watson and Neo 2021).

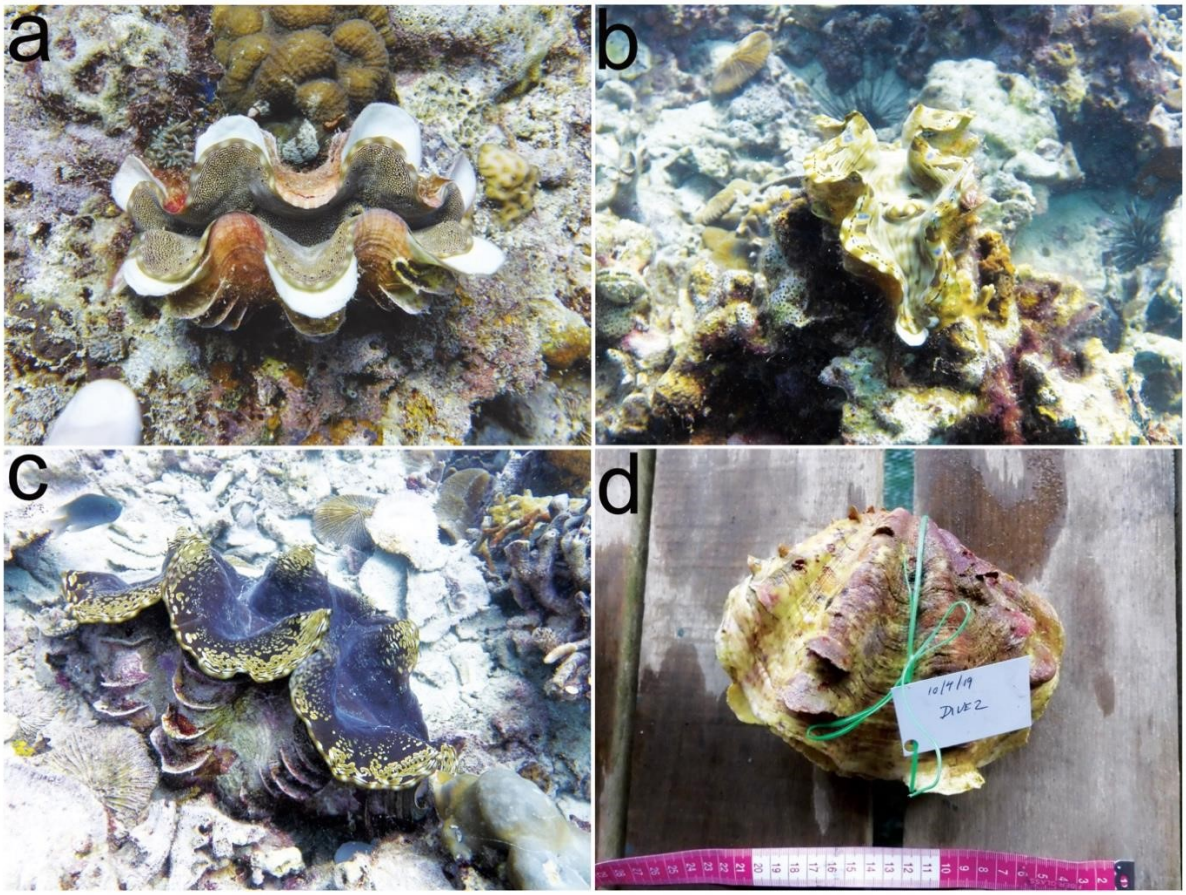

Figure 1.1. **Tridacna squamosa photographed in 2019 by the Reefugia team (a–c), demonstrating the intricate and colourful outer mantle patterns between shell valves. (d)** ***T. squamosa*** **shell valves recently collected from the seafloor.**

1.2.1.1 Taxonomy

Taxonomically, giant clams are classified in the order Cardiida, family Cardiidae and subfamily Tridacninae. The following 12 species exist within the genera *Hippopus* Lamarck, 1779 and *Tridacna* Bruguière, 1797: *Hippopus hippopus* (Linnaeus, 1758); *Hippopus porcellanus* Rosewater, 1982; *Tridacna crocea* Lamarck, 1819; *Tridacna derasa* (Röding, 1798); *Tridacna elongatissima* Bianconi, 1856; *Tridacna maxima* (Röding, 1798); *Tridacna mbalavuana* Ladd, 1934; *Tridacna noae* (Röding, 1798); *Tridacna rosewateri* Sirenko and Scarlato, 1991; *Tridacna squamosa* Lamark, 1819; *Tridacna squamosina* Sturany, 1899; *Tridacna gigas* (Linnaeus, 1758). The latter is the largest species, with maximum shell sizes reaching 1 m or over (e.g. Rosewater 1965; Watanabe et al. 2004; Ma et al. 2020), whilst *T. crocea* (boring clam) is the smallest, reaching 15 cm (Rosewater 1965).

1.2.1.2 Distribution

Tridacnids are primarily distributed along shallow coasts throughout the Indo-Pacific (e.g. Rosewater 1965; Richter et al. 2008; Smith 2011; Borsa et al. 2015; Neo 2020) (Figure 1.2), from South Africa to beyond French Polynesia and Japan to Australia (bin Othman et al. 2010). Three species are known from the Red Sea: *T. maxima* (small giant clam), *T. squamosa* (fluted giant clam) and *T. squamosina*, the latter thought to be endemic to the region and rare (Richter et al. 2008). *Tridacna maxima* (small giant clam) and *T. squamosa* have the broadest geographical distributions, whilst *H. hippopus, T. gigas, T. derasa, T. noae and T. crocea* are intermediate range species (Neo 2020), and *T.* rosewateri, *H. porcellanus* (bin Othman et al. 2010; Neo 2020), *T. mbalavuana* and *T. squamosina* are the most restricted and rarest species (Neo 2020; Tan et al. 2021).

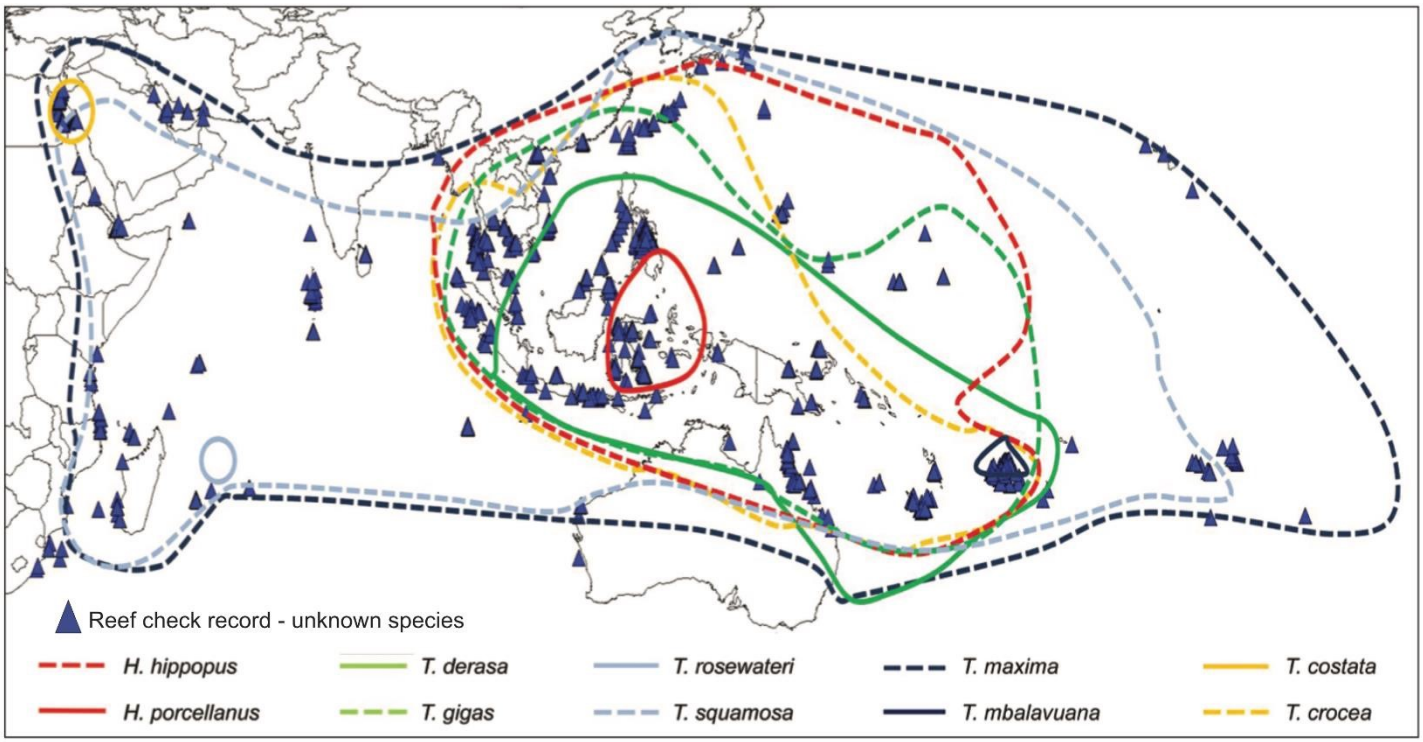

Figure 1.2. **The distribution of giant clam species within the Indo-Pacific region. Modified from: bin Othman et al. (2010).**

1.2.1.3 Feeding

Giant clams generally occupy reefs at shallow depths between 0–30 m (e.g. Rosewater 1965; Klumpp and Lucas 1994; bin Othman et al. 2010; Ma et al. 2020),

where sunlight can easily reach siphonal, or outer, mantle tissue housing photosynthetic zooxanthellae (algal dinoflagellates, family Symbiodiniaceae) (e.g. Pätzold et al. 1991; Lucas 1994). The tridacnid host provides inorganic nutrients to the zooxanthellae and in exchange, clams receive nutrition from translocated photosynthates produced from zooxanthellae (Klumpp et al. 1992). In contrast to corals, which host intracellular symbionts, zooxanthellae in giant clams are situated in an extracellular tubular system (Norton et al. 1992). This 'z-tubule' system extends through the body and connects digestive diverticular ducts of the gut to the outer mantle tissue, where it branches into additional tubes (e.g. secondary and tertiary zooxanthellal tubes) (Norton et al. 1992). An extracellular system with branching tubules may allow for the sub-specialization of symbionts, permitting their heterogeneity in a single clam (Carlos et al. 2000).

Aside from autotrophy, giant clams rely on exogenous food sources (e.g. Rosewater 1965; Klumpp and Lucas 1994; Soo and Todd 2014), filtering particulate organic matter with their incurrent siphon and mostly retaining particles sized between 2 to 50 μm (Soo and Todd 2014). However, the importance of heterotrophic feeding relates to many factors such as species, age, inter- and intraspecific differences in size (Klumpp and Griffiths 1994) and vertical distribution (Jantzen et al. 2008). For example, Klumpp and Griffiths (1994) reported that small individuals of *H. hippopus* obtained most nutrition from particulate food, whilst larger *T. gigas*, *T. crocea* and *T. squamosa* gained all carbon requirements from autotrophy alone. Another study (Jantzen et al. 2008) found that shallow-dwelling species (*T. maxima*) are functionally autotrophic, in contrast to species whose range extends deeper (*T. squamosa*). Deeper species may additionally increase rates of filter-feeding in low light environments (Tedengren et al. 2000), indicating that heterotrophy becomes more important with restricted light in species with a larger vertical distribution. For this reason, mixotrophic species such as *T. squamosa* could tolerate turbid, low light habitats more than species that are known obligate photoautotrophs.

1.2.1.4 Morphology

The valves of tridacnids are orientated somewhat differently from other bivalves, related to their photosynthetic endosymbionts (Rosewater 1965; Klumpp and Lucas

1994). The unusually wide gape between the two valves (Klumpp and Lucas 1994) and exposure of the hypertrophied thickened mantle edge, occupying the most dorsal position of the shell, allows for maximum light exposure (Rosewater 1965) (Figure 1.3). Because the mantle secretes shell material, any modification to the mantle will be reflected in the shell (Rosewater 1965). As such, the umbo, hinge and ligament in giant clams are pushed to an antero-ventral positioning (Rosewater 1965). Despite this enlargement of mantle tissues, much of the additional soft tissues are similar to that of other bivalves (Rosewater 1965).

Species of giant clam may most readily be identified by the morphology of their shell, especially as few clams are collected alive. There are several distinguishing features on the outer shell surface that can aid identification, such as overall shell shape and symmetry, scutes, ribs or folds, fold interstices, the byssal orifice and shell margins (Figure 1.4). The inner shell surface discloses information about the hinge teeth, plicae of the byssal orifice and the ligament (Rosewater 1965) (Figure 1.5). The pallial line, observable to the naked eye in well preserved specimens, demarcates the inner (lateral) and outer (siphonal) mantle (Ip et al. 2017) (Figure 1.5).

Figure 1.3. **Dorsal view of live *Tridacna squamosa* collected by the Reefugia Team in 2019, showing the wide gape between valves and exposed hypertrophied mantle.**

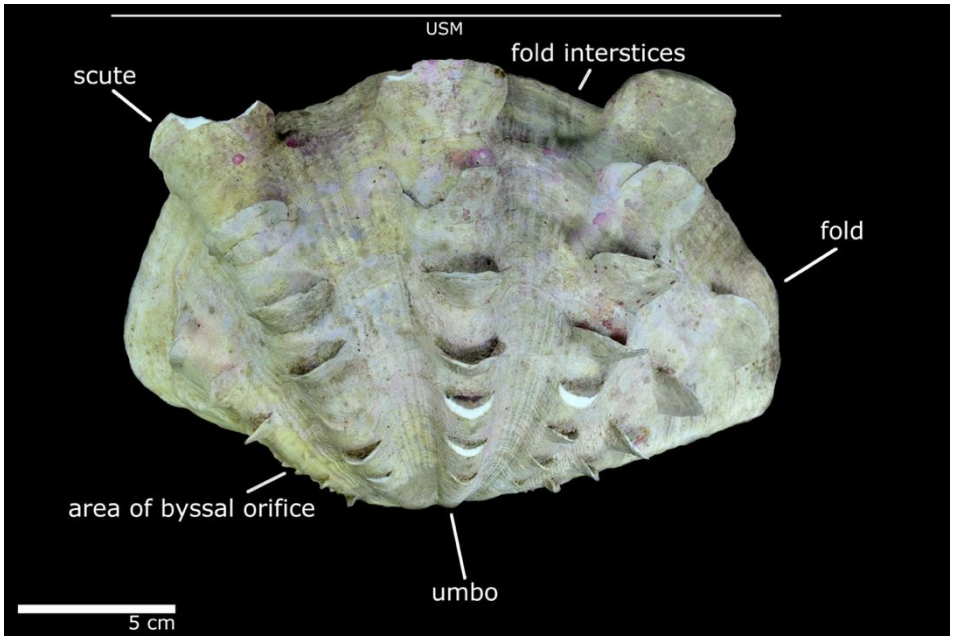

Figure 1.4. **Morphological features of the outer shell surface of *Tridacna squamosa* (SS03B_CT), highlighting the umbo, area of byssal orifice, folds, scutes and fold interstices. The general area of the upper shell margins (USM) is also depicted with fold interstices.**

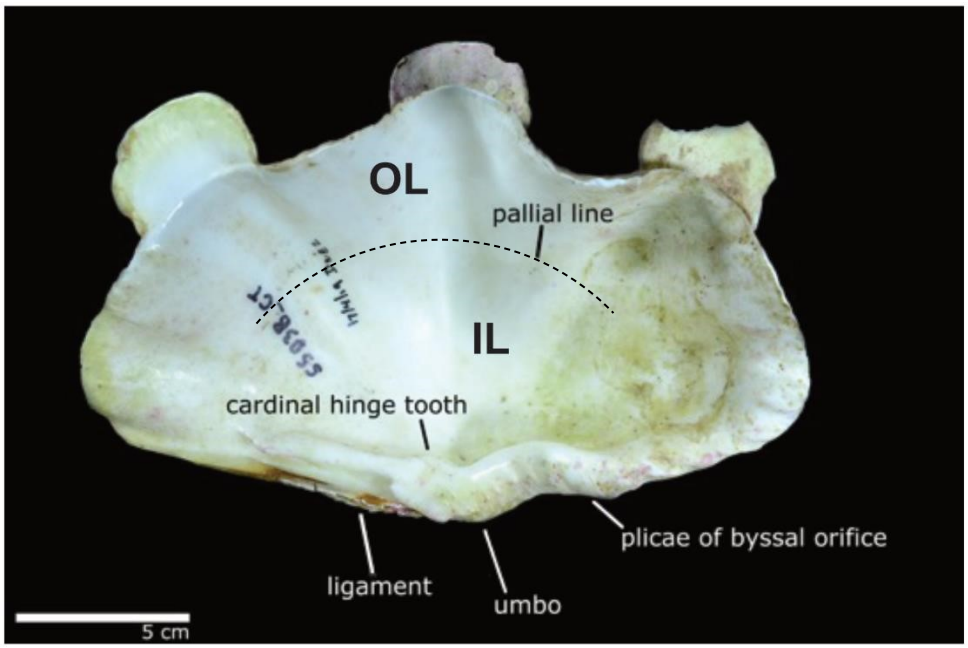

Figure 1.5. **Morphological features of the inner shell of *Tridacna squamosa* (SS03B_CT), highlighting the umbo, plicae of the of byssal orifice, remainder of the ligament, cardinal hinge tooth and pallial line, demarcating the inner shell layer (IL) and outer shell layer (OL), which corresponds to the inner lateral and outer siphonal mantle tissue. Dashed curved line indicates pallial line.**

1.2.1.5 Ecology

Giant clams provide key ecological functions to reef communities. On a reef-wide scale, they counteract eutrophication and the accumulation of algal biomass through filtering large volumes of seawater, discouraging flourishing macroalgae, even in sparser populations (Neo et al. 2015). Although little acknowledged, their exceptionally large $CaCO_3$ shells also significantly contribute to the reef carbonate framework and annual contributions may reach 1,000's kg ha^{-1} in dense populations (Neo et al. 2015). Further, large contributions are made to the net primary production (NPP) of a reef by their photosynthetic zooxanthellae; for example, a comparison of reef flora and fauna by Neo et al. (2015) found that the relative NPP in two *Tridacna* species was higher than that of crustose coralline algae and hard corals. They provide nutrition to a wide variety of organisms and are exploited as a food source by at least 75 predator species (Neo et al. 2015). Their shells give refuge not only to fish, but an abundance of epibionts and ectoparasites, such as macroalgae, sponges, ascidians, nudibranchs, bryozoans, polychaetes and corals, some of which are only found with their tridacnid hosts (e.g. the pontoniinid shrimp) (Neo et al. 2015). If densely aggregated, particular reef patches may also be subject to bioerosion; for instance, *T. crocea* (the boring clam) considerably contributes to sediment production by boring into coral rock and may flatten and break away dead coral heads (Hamner and Jones 1976). Due to their roles as ecosystem engineers and indicators of long-term reef health, giant clams have become the focus of recent conservation strategy in many regions (Neo 2020).

1.2.1.6 Threats

Dramatic declines in giant clam populations resultant of anthropogenic impacts threaten the ecological benefits that healthy, self-sustained populations offer coral reefs (Neo et al. 2015). Climate change, overexploitation, pollution, and habitat degradation may have negative consequences, such as changes in rates of carbonate and biomass production (e.g. bin Othman et al. 2010; Soo and Todd 2014; Neo 2020). Other consequences may be less obvious and require population thresholds to be breached before they are seen; for example, a certain density of clams may be needed to act as shelter for young fish (Neo et al. 2015).

1.2.1.6.1 Bleaching

Due to their endosymbiotic relationship with zooxanthellae, giant clams bleach with an increase in water temperature in similarity with corals (Gomez and MingoaLicuanan, 1998; Junchompoo et al. 2013; Apte et al. 2019). Populations of *T. squamosa* and *T. crocea* subject to sustained temperatures of over 30°C have been recorded to show paling, followed by severe bleaching and ultimately high rates of mortality of 40% (Junchompoo et al. 2013). Some individuals are capable of recolouring from thermal stress (Junchompoo et al. 2013), although reproductive processes related to the production and development of eggs is severely impacted in bleached clams, hindering recruitment success and recovery (Apte et al. 2019; Sayco et al. 2023, 2024). Hence, there is growing impetus to understand which environments offer resilience to bleaching for giant clam populations.

1.2.1.6.2 Exploitation

Although giant clams are subject to multiple pressures, exploitation of wild populations is highlighted as among the greatest of threats (Neo et al. 2017). They have long been of importance to fisheries in the Indo-Pacific and due to shallow distributions, a lack of mobility and a striking appearance, are easily recognised and harvested with basic equipment (Neo 2020; Tan et al. 2021). While commercial harvesting of wild *Tridacna* species is now widely banned, unregulated subsistence fishing is still a pervasive threat (Neo 2020). They also have a long history of being collected for materials and ornamentation (Neo et al. 2020), but due to current low densities in many areas, substantial levels of trade may be restricted to areas where high numbers remain (van Wynsberge et al. 2017). Due to overharvesting, many populations may be functionally extinct, or in some cases locally extinct (bin Othman et al. 2010).

1.2.1.6.3 Sediment stress and elevated nutrient levels

Suspended sediment within the water column reduces light penetration, which is essential for many reef species living in association with endosymbiotic zooxanthellae. In corals, sediment stress can result in slower growth (Risk and Sammarco 1991) or loss of photosynthetic endosymbionts (Dallmeyer et al. 1982). On the other hand, high

sediment levels may reduce mortality under high temperatures due to increased light attenuation, and mixotrophic corals may utilize alternative food sources (Anthony et al. 2007). However, little is known about how giant clams feed and calcify in response to sediment stress. In studies investigating the restoration and health of giant clams in heavily impacted reefs with high sedimentation off Singapore (Guest et al. 2008; Yong et al. 2022), it was found that the survival of *T. squamosa* is comparable to clear water reefs and giant clams grow well. However, excessive sedimentation can physically bury some coral species (Duckworth et al. 2017), smothering them and inhibiting their ability to access light and filter feed (e.g. Jones et al. 2019), leading to starvation. Giant clams exhibit a 'self-cleaning' mechanism in response to sediment that aggregates on their surface, contracting their mantle and exhaling sediment particles through their siphon (Elfwing et al. 2001). However, the threshold of effectiveness for giant clams to remove sediment from their mantle remains unclear, which raises concerns about smothering.

In addition to increased sediment input, increased nutrient concentration of seawater can also significantly impact the growth and fitness of giant clams. Giant clams use nitrogen (N) and phosphorus (P) to support photosynthesis, which are crucial components in various metabolic processes and carbon fixation (Belda et al. 1993a). However excess N or both N and P significantly impact biomineral organization and design, revealing misshapen and porous biominerals (Belda et al. 1993b; Belda-Baillie et al. 1998). Thus, while N and P are essential nutrients for giant clams, their excessive accumulation in seawater can have adverse consequences on giant clam health and resilience.

1.2.1.6.4 Conservation status

Giant clams are of particular importance to reef conservation as they may act as 'flagship taxa' and bring attention to ongoing issues that threaten reefs (Soo and Todd 2014), due to their 'charismatic' and eye-catching large appearance. Under international legislation, they are protected by the convention of International Trade in Endangered Species of Wild Fauna and Flora (CITES). Although CITES does not take the place of national law, it is of global agreement from governments to regulate or ban trade of certain threatened species. Since 1983, giant clams have been included in

CITES Appendix II, which includes “species that may not be threatened with extinction, but in which trade must be controlled in order to avoid utilization incompatible with their survival”. However, this excludes domestic trade, and local sales of shells still take place (Neo 2020). Further, their inclusion on the International Union for Conservation of Nature’s (IUCN) Red List of Threatened Species is outdated and last accessed in 1996, listing only nine of the twelve currently known species and not considering current issues (Neo 2020).

Giant clams are suitable for mariculture, providing opportunities for restocking of depleted populations (bin Othman et al. 2010). Several studies have focused on such restocking programmes, having successfully bred and restocked juvenile clams (e.g. Gomez and Mingoa-Licuanan 2006; Cabaitan et al. 2008), with some programmes even replenishing locally extinction populations (e.g. Cabaitan and Conaco 2017). Yet, even if restocking is successful, current threats related to local and global change remain.

1.2.2 Giant clams as bioarchives

Marine biogenic carbonates are considered valuable tools for (paleo)environmental reconstruction because they can record environmental parameters in the form of geochemical and physical signatures. Due to interactions with the surrounding environment, information on ecology, climate and life history traits can be extracted from their carbonate skeletons (e.g. Peharda et al. 2021). Precisely dated records including sea surface temperature (SST), salinity, precipitation, and water quality may be unlocked from these signatures and used to understand what drives favourable growing conditions or times of stress. Fossilized calcareous remains from taxa including corals, foraminifera and bivalves provide a plethora of environmental information where modern instrumental data may have temporal and/or spatial limitations, particularly in tropical and subtropical regions (e.g. Sano et al. 2012).

Bivalve shells are widely favoured for use as bioarchives for several reasons. Firstly, due to a broad geographical distribution, they occur in most aquatic ecosystems across the planet (Schöne and Surge 2012). They are extremely common organisms, and although there are large fluctuations even in rough estimations of the number of

extant species, approximations are thought to number well into the thousands, or tens of thousands (Bieler and Mikkelsen 2006). Specimens are thus generally easily accessible and environmental data can be extracted from diverse settings. Secondly, some bivalve species have extremely long-life spans, capable of recording long-term environmental change. For example, *Artica islandica*, the ocean quahog, and *Margaritifera margaritifera*, the freshwater pearl mussel may live to around 500 and 200 years respectively (Ziuganov et al. 2000; Butler et al. 2013). Moreover, extending records beyond the lifetime of a single individual permits the reconstruction of multicentennial master chronologies in long-lived species, using techniques derived from dendrochronology (Butler et al. 2009). Thirdly, many bivalves deposit shells with incremental episodic growth patterns, enabling precise temporal alignment of the shell's growth (Schöne and Surge 2012). Accretion of discrete growth layers may represent periodicity on daily, fortnightly, tidal, seasonal, and intra-and inter-annual temporal scales (Schöne and Surge 2012). Finally, bivalves first appeared in the early Cambrian over 500 million years ago and their shells are abundant constituents of the fossil record due to their high fossilization potential (e.g. Schöne and Surge 2012; Bayne 2017). Despite almost a quarter of extant bivalve taxa missing from the record (Valentine et al. 2006), they still have a rich and long presence within it. Hence, bivalves can archive a huge amount of environmental information over geologic timescales in nearly any aquatic habitat.

Giant clams are unique among bivalves because they are capable of documenting ultra-high-resolution environmental variability over long timespans of at least several decades (e.g. Watanabe et al. 2004; Elliot et al. 2009). They have hard, dense aragonite shell structures which often preserve well (e.g. Batenburg et al. 2011; Komagoe et al. 2018) and have large shell sizes and notably fast growth rates (e.g. Pätzold et al. 1991). They are also sessile in adulthood, permitting the recording of environmental change at one location (Yan et al. 2021).

Due to the ability to collect data from giant clams at high temporal resolution, research effort has moved towards using their shells for the reconstruction of daily and aperiodic events, such as light cycles (Sano et al. 2012; Hori et al. 2015), tropical cyclones (Yan et al. 2020) and typhoon events (Komagoe et al. 2018). In some cases, ultra-highresolutions on a sub-daily scale may be necessary to confidently detect

fluctuations and resolve some events individually (Warter et al. 2018). For instance, daily fluctuations in light related to the diurnal cycle has been shown to concur with highly time resolved geochemical measurements of giant clam shells in a study by Sano et al. (2012). Yan et al. (2020) also showed that daily to hourly proxy measurements for tridacnids concurred with instrumental tropical cyclone data from the western Pacific Ocean. In another study (Komagoe et al. 2018), a sampling resolution temporally equating to 2 to 6 days was sufficient to detect previous short term typhoon events at Okinotori Island, Japan (Komagoe et al. 2018). Giant clams have much untapped potential to be used as recorders of (paleo)weather and climate events when analysing their shells at appropriate resolutions and sampling techniques, although a robust understanding of the acquired proxy data is needed to understand its link to the environment.

1.2.2.1 Growth banding

Giant clams have seasonal and annual growth banding patterns that have been long studied and can easily be observed with basic equipment such as a light microscope, or even by the unaided eye (e.g. Bonham 1965). On seasonal scales, variation in light attenuation and water temperature are thought to concur with shell transparency — opaque (transparent) bands coincide with high (low) light levels and high (low) water temperatures under transmitted light (Pätzold et al. 1991). Annually, each macroscopic dark/light couplet represents a single year, which means estimation of age in years is usually straightforward to obtain (e.g. Bonham 1965; Elliot et al. 2009; Batenburg et al. 2011; Warter et al. 2015). However, the temporal resolution of these macroscopic banding patterns is too low to reconstruct changes related to monthly timescales or below.

Giant clams continually grow and deposit between 5 to 60 µm of carbonate daily (Ma et al. 2020). This also enables the identification of daily microgrowth bands both in modern (Watanabe and Oba 1999; Watanabe et al. 2004; Elliot et al. 2009; Aubert et al. 2009; Sano et al. 2012; Hori et al. 2015; Warter at al. 2015; Duprey et al. 2015; Warter and Müller 2017; Gannon et al. 2017; Warter et al. 2018; Komagoe et al. 2018; Ma et al. 2020; Killam et al. 2021; Yan et al. 2021; Zhao et al. 2021; Liu et al. 2022) and fossil giant clam specimens (Warter et al. 2015; Ayling et al. 2015; Warter and

Müller 2017), permitting the correspondence of growth bands to number of solar days elapsed (Watanabe and Oba 1999). This provides exact daily deposition dates (Komagoe et al. 2018), serving as a daily scale temporally aligned chronology of shell growth.

Giant clams have a two layered shell that consists of an inner shell layer (IL) and outer shell layer (OL), separated by a discernible boundary defined as the pallial line (Figure 1.5). Although both the IL and OL may have daily growth bands, the visibility of bands is highly species- and even specimen specific (e.g. Zhao et al. 2021). The use of daily growth banding to reconstruct past environmental settings is still in its infancy and has previously been used predominately to temporally constrain geochemical proxy analysis of giant clams (e.g. Zhao et al. 2023) and vice versa (Arndt et al. 2023). However, recent work suggests that simple daily growth banding measurements on their own can be used to infer environmental change, including changes in SST and light, with more light and warmer temperatures resulting in larger growth band widths (e.g. Zhao et al. 2021). The process of measuring bands is cheap and widely accessible compared to other techniques that require advanced equipment (e.g. geochemical and microstructural analysis). It is yet to be assessed whether the use of daily growth banding as a proxy can be applied to different giant clam species from diverse environments and more work is needed.

1.2.2.2 Microstructure

The building block of bivalve shells is calcium carbonate ($CaCO_3$), the most abundant biogenic compound on earth. Its anhydrous polymorphs (calcite, aragonite and in rare cases vaterite) make up the inorganic component of most mollusc shells, which are intricately interwoven with small amounts of organic biopolymers at multiple hierarchical levels (e.g. Marin et al. 2012). The inorganic shell portion shows tremendous diversity of crystalline architectures (Taylor et al. 1969), each with diverse and unique biomechanical and geochemical properties (e.g. Marin et al. 2012). The organic component, referred to often as the organic matrix (OM), constitutes approximately <1 to 7 wt% (Osuna-Mascaró et al. 2015) and is composed of lipids, proteins, polysaccharides, and chitin (e.g. Weiner and Traub 1984; Marin and Luquet

2004). Generally, shell microstructure comprises one organic layer and two to five superimposed ordered calcified layers (Almagro et al. 2016), which may be categorised into three dimensional (3D) structural orders of hierarchy (e.g. Agbaje et al. 2017). This organic/inorganic system produces shell microstructures that are biomechanically exceptional, far exceeding the material performance (e.g. strength, hardness) of their non-biogenic counterparts (e.g. Currey 1977).

Characteristic shell microstructure morphologies are divided into groups and include columnar prismatic, fibrous prismatic, lamellar, nacre and crossed lamellar for aragonite, and spherulitic, laminar, crossed, helical, homogenous or isolated for calcite (Taylor et al. 1969; Checa 2018). Amongst the most studied types is nacre (mother of pearl) (Marin et al. 2012), composed of tightly packed tablets, forming the inner layer in some molluscs. It is favoured in materials studies due to its high resistance to fracture yet exhibits limited flexibility. In contrast, prismatic microstructures that show moderate resistance to fracture are more flexible, defined by elongated crystals, with parallel sides, which may be straight or slanted and have polygon bases. The most common yet lesser studied type of microstructure typical of bivalve aragonite is crossed lamellar (CL), prevalent in more than 90% of species within the phylum Mollusca (Almagro et al. 2016). CL has an organization that resembles plywood and is characterised by fibre-type blocks of crystals with a distinct crystallization axis crossing at an angle (Faylona et al. 2011). Its hierarchical design consists of three 3D structural orders: 1st order lamellar perpendicular to each other and the shell surface, which resemble sheet-like undulating bands, made up of stacked rows of 2nd order lamellar, composed of 3rd order nanometer scale biomineral units, or crystals (Agbaje et al. 2017; Agbaje et al. 2019; Hou et al. 2020; Höche et al. 2020) (Figure 1.6). Nanograins on the surface of biominerals have additionally been presumed to constitute an additional fourth order (Hou et al. 2020). Whilst CL structures have less resistance to fracture than nacre and other microstructures, they have lower organic contents and are thus thought to be metabolically ‘cheaper’ to construct (e.g. Li et al. 2017).

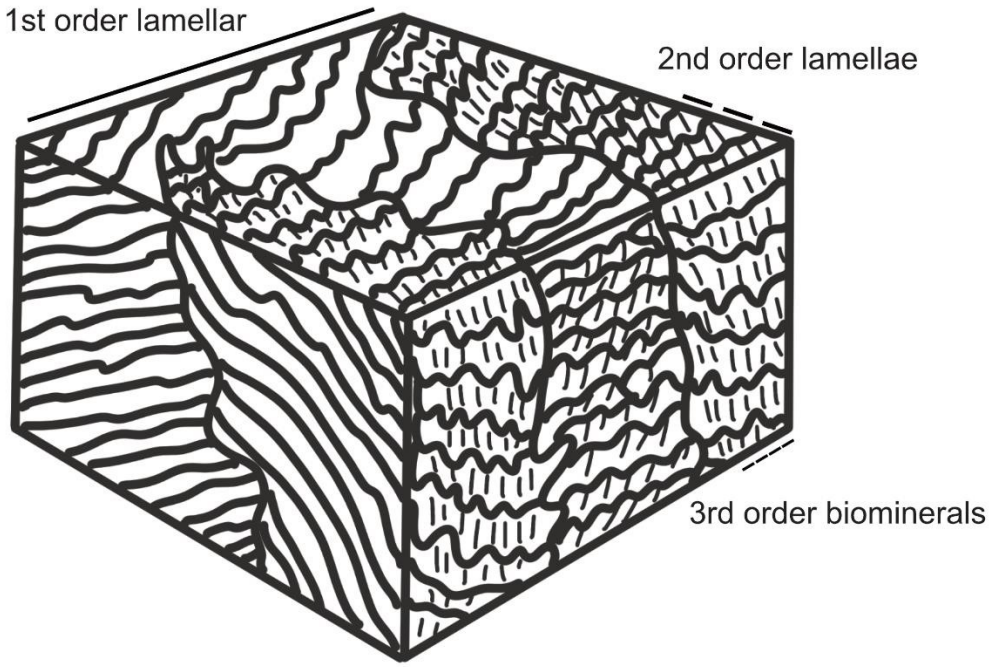

Figure 1.6. **Schematic sketch of the hierarchical crossed-lamellar microstructure, highlighting 1st order lamellae, composed of 2nd order lamellae, which are made up of 3rd order biomineral units. Based on: Taylor et al. (1969).**

In giant clams, the IL has been most widely described as CL (Vogel et al. 2000; Warter et al. 2015; Agbaje et al. 2017, 2019), but also prismatic (Pätzold et al. 1991; Faylona et al. 2011) or complex prismatic (Gannon et al. 2017), divided into sub-daily couplets — a thicker prismatic layer deposited in the day and an additional thinner layer, composed of smaller, oblique crystallites at night (Gannon et al. 2017). An early study by Bonham (1965) additionally reported that the 'extrapallial portion' of the 'inner surface' was prismatic, whilst the 'central basal part' was nacreous. The OL is also predominately reported as CL (Pätzold et al. 1991; Faylona et al. 2011; Brahmi et al. 2019), although Gannon et al. (2017) described it as dendritic. However, most studies characterize tridacnid microstructure based only on a small region within one shell layer in a singular specimen. Hence, there has been little work distinguishing variation between different parts of the shell, different environments, and species. Moreover, CL is known to be sub-categorized into multiple types based on unique crystallographic properties (Almagro et al. 2016) and it is not known how the features of CL microstructures in giant clams vary.

The microstructure of a shell is important in (paleo)environmental studies because it provides valuable information on the setting that an individual lived in (Gannon et al. 2017). The microstructure not only facilitates the interpretation of geochemical proxies but acts as a proxy in itself (Peharda et al. 2021). For example, the size and shape of biomineral units secreted may be controlled by temperature (Höche et al. 2020). Yet, there is little in the current literature on how giant clam microstructure reflects changes in the environment. It has been put forward that light attenuation likely changes biomineral design (Pätzold et al. 1991), but no further indication has been provided on the impact of light on crystallites. One study (Brahmi et al. 2019) investigated the effects of future warming and ocean acidification predictions on giant clam microstructure and recorded modifications in the cohesive properties of lamellae, indicating that both act as forcing variables. Another study (Belda et al. 1993b) found elevated nitrogen and phosphorus change shell density, biomineral shape and overall microstructure, revealing misshapen aragonite crystals, irregular microstructure and porous biominerals. The most comprehensive study of giant clam microstructure with variation in environment to date is by Gannon et al. (2017). By comparing the biomineralization and microstructural patterns of shells from two diverse reef and geographic locations, the authors reported a less defined microstructure at a site more influenced by rainfall and terrestrial nutrient supply.

1.2.2.3 Crystallographic texture

Crystallographic texture encompasses the crystallographic orientation of biominerals that make up different microstructural arrangements. The orientation of biominerals, or crystals, is crucial for skeletal organization and substantially influences the biomechanical properties of the shell, impacting strength, hardness, and resistance to fracture (e.g. Moynihan et al. 2022). In recent years, research has increasingly focused on unravelling the intricacy of crystallographic arrangements of aragonite crystals in bivalve shells and corals and their implications for shell formation and biomineralization (e.g. Checa et al. 2006; Saruwatari et al. 2009; Zhou et al. 2009; Nudelman 2015; Otter et al. 2019; Farfan et al. 2022). However, their potential use as (paleo)environmental proxies is largely untapped. Considering crystallographic orientation is a fundamental level of shell construction and is key to understanding realistic biomineralization scenarios (e.g. Mastropietro et al. 2017), there is potential for it be used as an

extremely high-temporal-resolution proxy (e.g. Coronado et al. 2019). Variation in fine-scale crystallographic organization in response to variable natural and experimental conditions, such as temperature and ocean acidification has been recorded in many molluscs and corals (Fitzer et al. 2014; Hennige et al. 2015; Fitzer et al. 2016; Coronado et al. 2019; Knights et al. 2020). These modifications may give indication of complex and diverse physiological adjustments that reflect changes in the environment, coined as the 'crystallographic vital effect' (CVE) by Coronado et al. (2019). Such studies hint that modifications to physiological activity (e.g. ion transport pathways) produce variable crystallographic characteristics that may be utilized as indirect sensitive proxies of the surrounding ambient environment.

In giant clams, few studies have given insight into the crystallographic properties of their shells. Crystallographic orientation is only known from research of two giant clam shells (Agbaje et al. 2017; Gannon et al. 2017) and shows a strong preferred crystallographic orientation of the [001] axis (Figure 1.7). To date, however, it has not been investigated how shell microstructure together with corresponding crystallographic orientation change between species, with the environment, or even throughout one shell. Understanding crystallographic texture in giant clam shells is crucial not only for comprehending their structural integrity and adaptation to diverse marine environments, but also to understand their place alongside microstructure for proxy use.

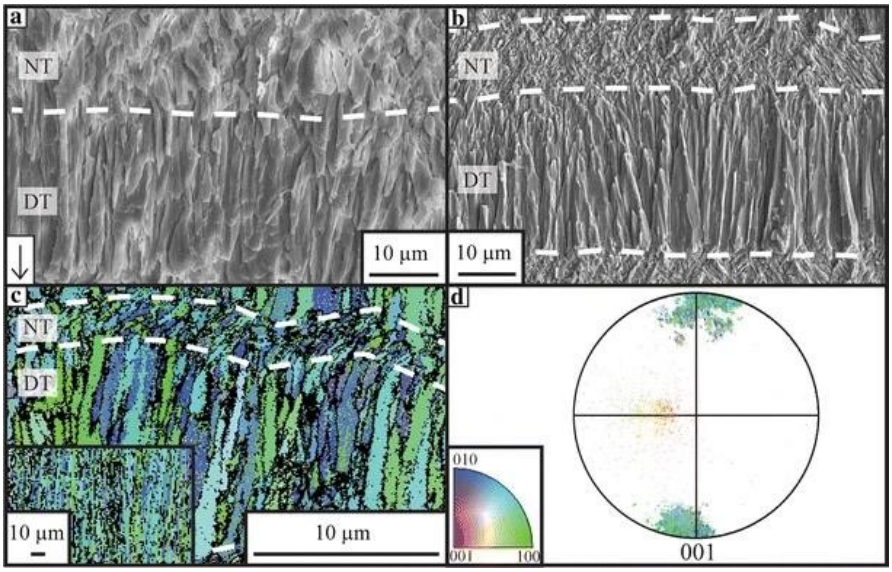

Figure 1.7. **Shell microstructure (a, b) and crystallographic orientation (c, d) of *Tridacna gigas* from Gannon et al. (2017). Pole figure (d) demonstrates strong preferred crystallographic orientation of the [001] axis. NT = nighttime deposition; DT = daytime deposition.**

1.2.2.4 Trace element profiles

In the last two decades, the geochemical fingerprint of marine biogenic carbonates has increasingly been used to gain ultra-high-resolution proxy information of past climatic and environmental variability. The most and longest studied proxies are stable isotopes, primarily shell oxygen ($\delta^{18}O$) and carbon ($\delta^{13}C$) isotopes, which are interpreted as indicators of sea surface temperature (Watanabe and Oba 1999; Aubert et al. 2009; Welsh et al. 2011; Driscoll et al. 2014; Duprey et al. 2015; Ma et al. 2020) and debatably carbon sources from the environment (Killam et al. 2020) or ontogenetic/metabolic shifts (Jones et al. 1986), respectively. However, trace and minor element geochemistry is a fast-emerging field due to its high sensitivity, allowing for precise measurements of trace concentrations in small samples at high spatial resolution, providing information on the distribution of trace elements across individual growth bands or layers. However, the controls on trace element incorporation into bivalve shells is still highly confounding and mechanisms of elemental pathways warrant further investigation.

1.2.2.4.1 Mg/Ca

In many taxa, such as foraminifera, the ratio of magnesium-to-calcium (Mg/Ca) is widely used as a robust proxy to reconstruct past ocean temperature (e.g. John et al.

2023). It is useful in addition to $\delta^{18}O$ due to (1) its insensitivity to changes in sea surface salinity (SSS), enabling SST and SSS to be disentangled (Klein et al. 1996) and (2) its ability to detect much more sensitive changes in SST to shed light on highly time resolved events. However, the use of Mg/Ca in giant clams, like all bivalve species (e.g. Marali et al. 2017), is complicated by biophysiological effects, meaning that the Mg/Ca shell signature will deviate from surrounding ambient seawater and not faithfully record environmental changes. Although profiles of Mg/Ca have shown some seasonal correlation with SST in giant clams (Elliot et al. 2009; Arias-Ruiz et al. 2017), it is likely biological factors and ontogenetic trends across lifespan exhibit predominant control due to a lack of correlation with environmental variables (Elliot et al. 2009; Warter et al. 2015, 2018; de Winter et al. 2023).

It is noteworthy that mineralogical phase influences the substitution of Mg for Ca. The orthorhombic structure of aragonite (9-fold coordination) compared to the rhombohedral structure of calcite (6-fold coordination) (Finch and Allison 2007) suggests that the small cationic radius of Mg favours substitution in calcite over aragonite (e.g. Lippmann 1973). However, Mg is detected in many biogenic aragonite skeletons and is likely hosted in organics rather than substitution within the crystal lattice (Yao et al. 2019).

1.2.2.4.2 Sr/Ca

Similar to Mg/Ca, the strontium-to-calcium (Sr/Ca) ratio of giant clam shells is complicated, yet important to understand due to its potential correlation with the daily light cycle. In comparison to temperate regions, instrumental data for daily light cycles in tropical and subtropical regions is lacking (Sano et al. 2012). Considering insolation largely drives SST and dictates variation in both weather and climate (Sano et al. 2012), it is important to develop (paleo)proxies that measure light. Due to their endosymbiotic relationship with zooxanthellae, tridacnids are thought to be useful for light cycle measurements. In previous studies, Sr/Ca has been interpreted as an ultrahigh-resolution proxy for determining light cycles on sub-daily scales, enabling diurnal variability and climatic parameters to be linked to Sr/Ca insolation (Sano et al. 2012; Hori et al. 2015; Warter et al. 2018; Yan et al. 2020). However, experiments where giant clams are kept under sunshades (de Winter et al. 2023) or continuous

illumination (Warter et al. 2018) show that diurnal Sr/Ca cycles are still present, indicating incorporation is at least partially biologically controlled.

1.2.2.4.3 Ba/Ca

While the interpretation of shell barium-to-calcium (Ba/Ca) ratios for marine bivalves is still a matter of debate, numerous studies (e.g. Lazareth et al. 2003) have associated Ba/Ca with riverine runoff and primary productivity. Certainly, it has been intimated that giant clam shell Ba/Ca relates to changes in seawater productivity concentrations. For instance, Arias-Ruiz et al. (2017) recorded high Ba/Ca in the dry season, when primary productivity was at maximum and Komagoe et al. (2018) noted Ba/Ca peaks resultant from upwellings caused by typhoons. Although other studies (Elliot et al. 2009; Batenburg et al. 2011) have similarly reported that the amplitude and timing of shell Ba/Ca peaks reflect primary productivity, Ba/Ca profiles are not well correlated with Mg/Ca or Sr/Ca, which may be attributed to their biological effects or a lag phase between the annual primary productivity cycle from SST (Batenburg et al. 2011).

1.2.3 Complications of using giant clams as bioarchives

1.2.3.1 Diagenetic alteration

A major obstacle faced when using the skeletons of biogenic carbonates to study past climates and environments is that they experience diagenetic alteration. It is well documented that metastable aragonitic skeletons may undergo extensive alteration through dissolution, reprecipitation of secondary material, and recrystallization to calcite, the thermodynamically most stable polymorph of $CaCO_3$ near the earth's surface (e.g. Brand 1989; Sandberg and Hudson 1990; Hendry et al. 1995). Alteration can occur as early as within the lifetime of the animal, potentially proceeding throughout the geologic record long after its death (e.g. Moore 1989).

Variation in the diagenetic response of carbonate skeletons confuses interpretation between biotic pristine signatures deposited by the organism in its lifetime compared to those that are post-depositional and diagenetically altered. Modifications to pristine

aragonite can alter aspects of not only skeletal structure and mineralogy, but also the original geochemical signature. Many factors lead to differences in the thermodynamic stability of different carbonate minerals and hence any subsequent diagenetic changes to the carbonate skeleton; for example, variations in physico-chemical conditions (e.g. Pederson et al. 2020). The design of the originally formed carbonate skeleton will also hold large influence over susceptibility to diagenetic processes. Differences in microstructural characteristics and the organic matrix at formation/deposition will change permeability and porosity, which affects exchange rates with internal (e.g. pore fluids, organic-bound fluids) and/or external diagenetic fluids (e.g. seawater, meteoric water) (e.g. Gaffey et al. 1991). The distribution of foreign ions, or impurities, within the crystal lattice, such as Mg, will further have influence over the rate of dissolution (e.g. de Boer 1977). Hence, to obtain reliable proxy records of pristine aragonite, a multitude of diagenetic processes and screening techniques must be considered.

Giant clams are generally more resistant to diagenesis than corals, and preserve better due to their dense, non-porous shells (Elliot et al. 2009; Welsh et al. 2011; Komagoe et al. 2018). The availability of unaltered corals may be lacking in many lowlatitude regions and giant clam shells can often be utilised as robust and comprehensive alternatives for the reconstruction of tropical environments. However, diagenesis is still a caveat that can complicate the correct interpretation of records, particularly when using fossil giant clams for high-resolution reconstruction of past environmental and climatic changes. A commonly utilized screening technique for the detection of diagenesis in proxy studies of giant clams is bulk mineralogical analysis (Welsh et al. 2011; Arias-Ruiz et al. 2017; Hu et al. 2020). However, studies at coarser resolutions may overlook changes that occur on fine-scales (i.e. nano- to microscale). Since giant clam shells are extensively utilized for temporal analysis with powerful techniques down to daily or even sub-daily timescales, it is important to understand how highly localized diagenesis affects their use for reliable proxy reconstruction.

1.2.3.2 Vital effects

Shell geochemistry is known to show a strong physiological component in many marine calcifiers because element-to-calcium (El/Ca) ratios deviate from concentrations of surrounding ambient seawater (i.e. non-equilibrium fractionation)

(e.g. Weiner and Dove 2003) and may be orders of magnitude below what is expected (e.g. Schöne et al. 2013; de Winter et al. 2023). This is because the organism tightly controls conditions in its calcifying fluid (CF). The CF is a chemically complex aqueous solution from where biominerals grow and favors biomineralization by increasing saturation state (Ω), pH and dissolved inorganic carbon (DIC) for precipitation of $CaCO_3$ (e.g. Gilbert et al. 2022). Consequently, deposition of the $CaCO_3$ skeleton will exhibit a degree of physiological overprint (e.g. respiration, metabolism, biomineralization, photosymbiotic activity) deviating from thermodynamic equilibrium, coined as the 'vital effect' (Urey et al. 1951). It is critical to understand how these biological components affect skeletal growth and composition not only in the face of a rapidly changing ocean, but also as to whether these physiologically associated features can be distinguished from environmental signals for proxy use.

As with other bivalves (e.g. Poulain et al. 2015), giant clams show heterogenous composition of trace and minor elements between and within their aragonite shell layers (Elliot et al. 2009; Warter et al. 2018; de Winter et al. 2023). Even on sub-daily temporal scales, there are large variations in El/Ca ratios that are likely strongly related to diurnal cyclicity and inherent biological rhythm (de Winter et al. 2023). Mg/Ca and Sr/Ca are particularly difficult to interpret because they may be under strong biological control, which may be related to periodic activity of photosymbiotic algae and other metabolic and biomineralization mechanisms (Elliot et al. 2009; Sano et al. 2012; Hori et al. 2015; Warter et al. 2015; Arias-Ruiz et al. 2017; Warter et al. 2018; de Winter et al. 2023). It is likely that Mg/Ca and Sr/Ca are controlled by a multitude of biological and environmental controls in giant clams, and these effects must be disentangled before these proxies may be routinely applied to environmental reconstruction (Elliot et al. 2009). Moreover, fluctuations in El/Ca are linked to the dictation of mineral formation (e.g. Brosset et al. 2022) and integral to understand biomineralization pathways, but few studies have so far coupled chemical analysis with investigation of microstructure for a holistic view of tridacnid biomineralization pathways.

1.2.4 Thesis outline: Coupling shell growth and geochemistry in giant clams to explore biomineralization pathways

1.2.4.1 Aims

This PhD is part of the project “Reefugia: Reef refugia out of the shadows: dynamics of marginal coral reef ecosystems over the past 30 million years in the Coral Triangle”, funded by the Natural Environment Research Council (NERC: NE/R011044/1). Reefugia addresses the following objectives to understand the dynamics of long-term coral reef refugia in the Coral Triangle region of Southeast Asia: (1) document the changing diversity of corals in marginal reefs over the past 30 million years; (2) characterise and understand environmental conditions on marginal reef habitats using proxies for temperature, salinity, light and primary productivity; (3) access rates of niche shifts of coral species from marginal to clear-water habitats through time.

The current thesis addresses the second of Reefugia’s objectives and investigates how giant clams respond to environmental conditions on turbid coral reefs, important refugia with quick recovery times, high coral cover and biodiversity (section 1.1.2 for more information). Aside from corals, little is known about how calcifiers respond to turbid coral reefs and prior to this work, it is not known if giant clams show variation in biomineralization response in these reef environments. It is important to incorporate other key reef builders into the study of turbid corals reefs to better understand the capabilities of these potential refugia.

Giant clams grow large aragonite shells and are valuable (paleo)environmental tools as they deposit calcium bearing minerals throughout lifespan, showing periodic daily, seasonal and annual growth bands (section 1.2.2 for more information). Due to interactions with the surrounding environment, information on habitat lived in at the time of deposition may be extracted from the physical and geochemical signatures stored in their carbonate skeletons. The primary aim of this thesis is to decipher how external environmental and internal physiological processes impact the biomineralization pathways of modern giant clam shells (*Tridacna squamosa* and *Hippopus hippopus*) from Bornean coral reefs in clear to turbid waters. A secondary

aim is to provide an assessment of fossil giant clams collected from stratigraphic formations in Malaysia and Indonesia to understand how diagenetic overprint impacts structural characteristics of shells and proxy interpretation.

To achieve these aims, three research questions are addressed:

1. **Are biomineralization pathways of giant clams (structural and geochemical properties of shells) different in clear versus turbid reefs?**

2. **What are the physiological and environmental controls on biomineralization pathways in giant clam shells in clear and turbid reefs?**

3. **How does diagenetic alteration impact the structure of fossil giant clam shells?**

1.2.4.2 Layout

Chapter 2 Methods

Chapter 2 gives a detailed description of the methods used throughout this work. This includes environmental and climate information from Borneo and study localities within Darvel Bay in the state of Sabah, using both remote sensed and *in situ* data. Sample collection, preparation, and the techniques for light microscopy, scanning electron microscopy (SEM), electron backscatter diffraction (EBSD), electron microprobe microanalysis (EPMA), X-Ray Diffraction (XRD), Raman Spectroscopy and loss on ignition (LOI) are also described. Due to the large part EBSD plays throughout this thesis, particularly in chapters 5 and 6, and because data acquisition for giant clams can be a challenge with EBSD, an in-depth analysis of data processing for EBSD is provided as an additional chapter (chapter 4).

Chapter 3 Growth responses of giant clam shells to turbid reefs

Chapter 3 investigates the shell growth of modern *T. squamosa* shells from turbid and clear reef environments using daily growth bands. It explores the impact that

environmental parameters have on band width and microstructure and their potential in recording site-specific and regional environmental changes on daily, seasonal and annual time scales. Age models of growth bands are obtained using light microscopy and SEM imaging, and investigated with *in situ* and remote sensed environmental data. Raman spectroscopy and SEM imaging are used to test the preservation of modern samples collected dead from the seafloor. A modified version of this chapter is published in the journal Coral Reefs as Mills et al. (2023).

Chapter 4 Improving electron backscatter diffraction (EBSD) data in giant clams by post-acquisition refinement

Chapter 4 outlines a methodological approach for data acquisition and post-acquisition refinement techniques to optimize EBSD data quality from giant clam shells. It focuses on the inner shell layer (IL) because diagenesis is harder to observe in the IL compared to the outer shell layer (OL) and may often be overlooked. It lays out steps to ensure repeatability of refinement techniques and to allow extraction of further crystallographic properties for future researchers. A modified version of this chapter is published in the journals Data in Brief as Mills et al. (2024) and Nature Earth and Environment Reviews as Mills (2022).

Chapter 5 Biomineralization plasticity in giant clam shells from turbid reefs: integrating physical and geochemical pathways

Chapter 5 explores the impact environmental and potential physiological parameters have on the microstructure, crystallographic orientation, and element-to-calcium ratio (Mg/Ca; Sr/Ca) of giant clam shells. It investigates the link between physical and geochemical features of biominerals, hypothesizing how biomineralization is influenced by El/Ca versus microstructure. SEM, EBSD and EPMA are used to map nano- to microscale characteristics of shell biominerals from turbid and clear reefs to understand how biomineralization pathways are modified with turbidity. A modified version of this chapter is under review in the journal Scientific Reports.

Chapter 6 Diagenesis in fossil giant clam shells: using crystallographic texture to detect alteration from pristine to secondary aragonite

Chapter 6 provides an in-depth comparison of the microstructure and crystallographic texture in fossil giant clam shells (Miocene and Pliocene) from Malaysia and Indonesia, retrieved from stratigraphic formations outcropping on land. The main focus of this chapter is to investigate early alteration within the aragonite phase, which is often overlooked, compared to aragonite to calcite phase transformation. Preservation on a nano- to microscale is investigated using a multi-methodological approach with XRD, Raman Spectroscopy, SEM, EBSD and LOI. Findings are compared to modern shells from a nearby region to obtain an unaltered reference that can be used to detect alteration in fossil analogues. A modified version of this chapter is in preparation for publication in the journal Palaeogeography, Palaeoclimatology, Palaeoecology.

Chapter 7 Conclusions and future directions

Chapter 7 gives a summary of findings from research chapters 3, 4, 5 and 6, synthesizing key conclusions and suggesting future directions to build upon current work.

2. Study sites and methodology

2.1 Borneo

Borneo is the largest island in Asia, occupying a landmass of 73.7 million hectares (Gaveau et al. 2016). It is the only island in the world governed by three countries: Brunei, Indonesia and Malaysia (Figure 2.1). Indonesia occupies most of the land area, divided into the provinces of North, East, South and West Kalimantan, followed by Malaysia, comprised of the two states Sabah and Sarawak, whilst Brunei, an independent sultanate, occupies less than 1% landmass.

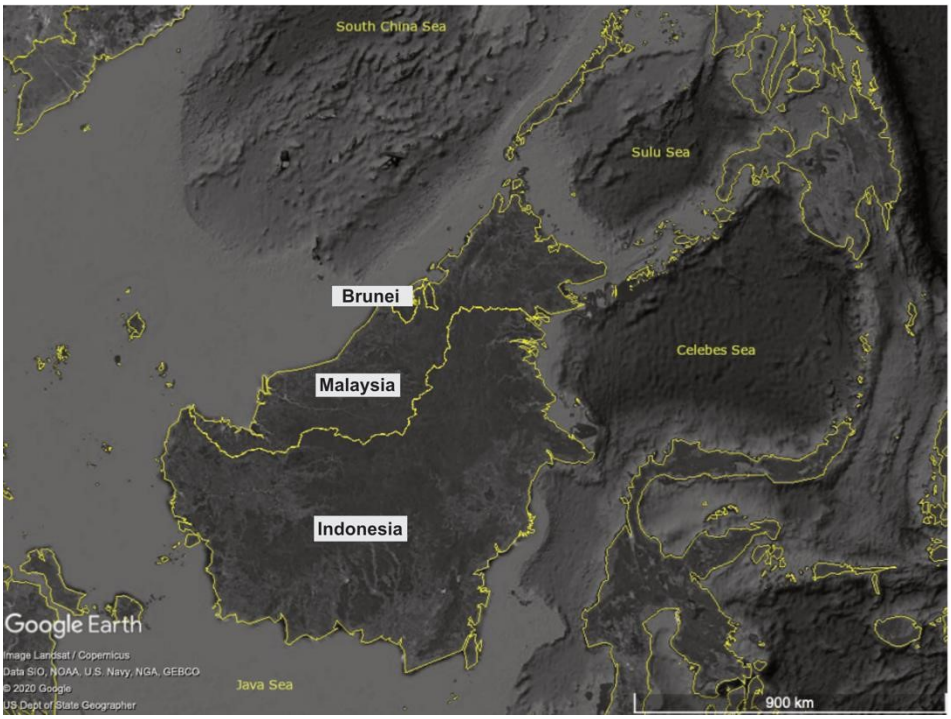

Figure 2.1. **Map of Borneo, showing the three countries (Brunei, Malaysia and Indonesia) on the island and the surrounding Sulu, Celebes, Java and South China Seas. Modified from: Google Earth Pro.**

2.1.1 Temperature

Bisecting the equator, Borneo has a hot and humid tropical climate (e.g. Vijitj and Dodge-Wan 2019), which experiences two seasons: the northeast monsoon (wet season) and southwest monsoon (dry season). Regional annual temperature ranges are relatively low but orography, geography, atmospheric circulation, and currents in littoral areas influence the spatial heterogeneity of temperature across the island (Sa'adi et al. 2020).

El Niño–Southern Oscillation (ENSO) is the most dominant source of tropical annual climatic variability (e.g. Kripalani and Kulkarni 1997), causing extreme weather conditions with changes in the intensity of ENSO events. Prolonged dry seasons in Borneo associated with El Niño events often lead to devasting consequences (Department of Statistics Malaysia 2022). For instance, fires often set for agricultural purposes become severe and uncontrollable with the delay of the monsoon season (e.g. Hendon 2003). Although the most recent El Niño events occurred in 2018–19 and 2023–2024, the strong El Niño conditions of 2015–16 severely exacerbated the fire environment, making the release of haze the most severe in over two decades (Field et al. 2016). The ENSO fluctuates between irregularly warm (El Niño) and cooler (La Niña) periodic variations, recurring every 2 to 7 years (e.g. McPhaden et al. 2006). It is suggested that global warming will significantly modify ENSO events, although how it will be impacted is uncertain (Collins et al. 2010).

2.1.2 Rainfall

Borneo is perhumid and characterized by high precipitation throughout the year (e.g. Ichikawa and Yansunari 2006). Although rainfall averages 3000 mm annually (Hamada et al. 2002), it greatly deviates between regions. Higher rainfall generally occurs in coastal regions and areas strongly influenced by high land mass, such as the northwest and central mountain ranges, whilst the lowlands of the southeast and northeast experience less rainfall (Vijitj and Dodge-Wan 2019). Whilst El Niño is associated with drought, La Niña events typically cause the opposite, bringing prolonged rainfall (Department of Statistics Malaysia 2022).

2.1.3 Topography

The land and ocean geography of Borneo is complex (Ichikawa and Yansunari 2006). It is surrounded by the Sulu, Celebes, Java and South China Seas, whilst Philippine and Indonesian islands are situated on its outskirts, and the Indochina peninsula is located to its northwest. Historically, Borneo was adjoined to the Sundaland landmass before separation during the last ice age as sea level increased.

Borneo's mountain ranges extend from southwest to northeast across much of the island and include the island's highest peak, Mount Kinabulu (4,095 m), situated in Sabah at the world heritage site Kinabalu Park. However, low elevations dominate much of the south of the island and coastline.

2.1.4 Land use

In 1973, 75.7% of Borneo's land area was estimated as forest (558,060 km^2); however, by 2010 this declined by 30.2% due to industrial agriculture and logging (Gaveau et al. 2014). Sabah and Kalimantan are amongst the worst affected regions of the island, with 39.5% and 30.7% respectively of total forest area lost between 1973 and 2010 (Gaveau et al. 2014). Plantation industries (predominately oil palm and pulpwood) are principal drivers in the deforestation of Malaysian Borneo over the last 40 years, whilst rapid conversion of forest to plantation has increased extensively since 2005 in Indonesian Borneo (Gaveau et al. 2016).

2.2. Sabah

The Malaysian state of Sabah is situated on the northeast of Borneo, covering a land area of 73,904 km^2 (Department of Statistics Malaysia 2022), located just north of the equator. Sabah shares terrestrial borders with both Sarawak (southwest) and North Kalimantan (southeast). It is the third most populous Malaysian state, with 3.9 million people, exceeded only by Selangor and Johor (Department of Statistics Malaysia 2022).

The entire coastline of Sabah is located within the Coral Triangle, a region with extremely biodiversity rich marine waters (e.g. Veron et al. 2009). Sabah's coasts extend a distance of 4,328km (including islands and lagoons), encompassing over 300 villages and four population growth centres, including the state capital Kota Kinabalu (Figure 2.2) (Jakobsen et al. 2007). Many coastal villages are dependent on fisheries for income and tourism is emerging as important for future economic growth (Jakobsen et al. 2007).

Three ecosystems dominate the coasts of Sabah: wetlands, coral reefs and seagrasses (Jakobsen et al. 2007). The coastline of east Sabah is dominated by the former, which comprises swamps, mangroves and mudflats, primarily in turbid waters, whilst coral reefs and seagrasses are usually characterised by clear, low turbid waters (Jakobsen et al. 2007).

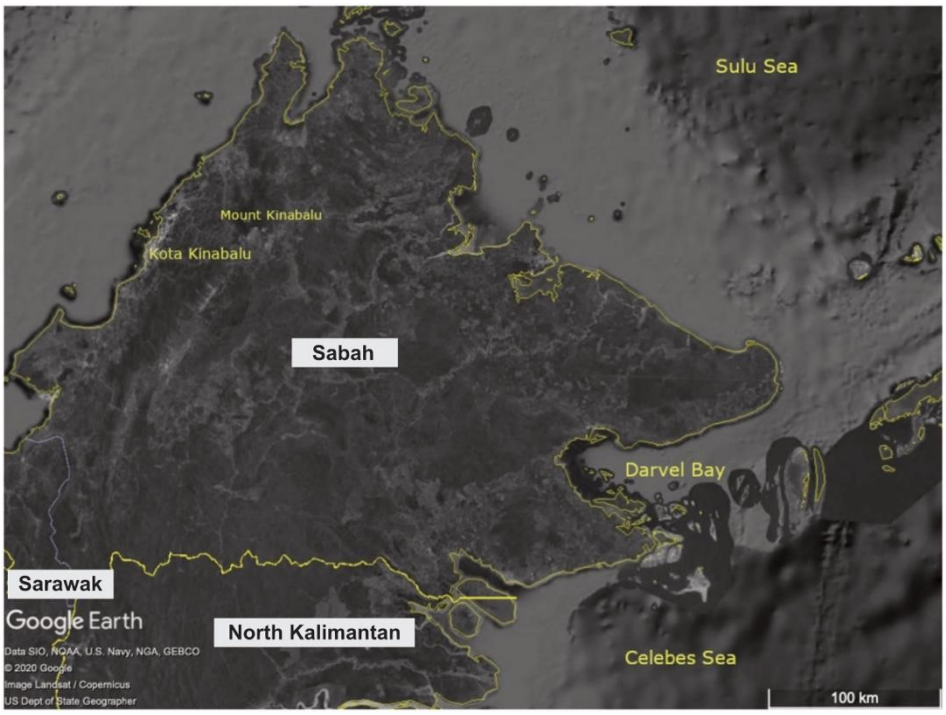

Figure 2.2. **Map of northern Borneo, showing Sabah and the two states it shares a border with (North Kalimantan and Sarawak). Darvel Bay, Mount Kinabalu and Kota Kinabalu situated within Sabah are designated. Modified from: Google Earth Pro.**

2.2.1 Temperature

Sabah experiences its lowest temperatures from December to February during the wet season and its warmest in May in the dry season (Department of Statistics Malaysia 2022). Whilst the wet season extends from around November to March and brings strong winds that blow across Sabah from the northeast Pacific, the dry season is from May to September and is subject to winds from the southwest Pacific (Montagne et al. 2013). Mean annual coastal temperatures are approximately 27°C, 1 to 3°C warmer than areas further inland due to the influence of the coastal climate (Department of Statistics Malaysia 2022). Although there is generally little seasonal temperature variability, El Niño events may bring high temperature anomalies, the most widespread in recent times concurring with the 1983 El Niño event, reflecting across the whole of Sabah (Department of Statistics Malaysia 2022).

2.2.2 Rainfall

In general, annual mean rainfall in Sabah is between approximately 2500 to 3500 mm, although some areas greatly deviate from this due to coastal and land-mass influences (Figure 2.3) (Department of Statistics Malaysia 2022).

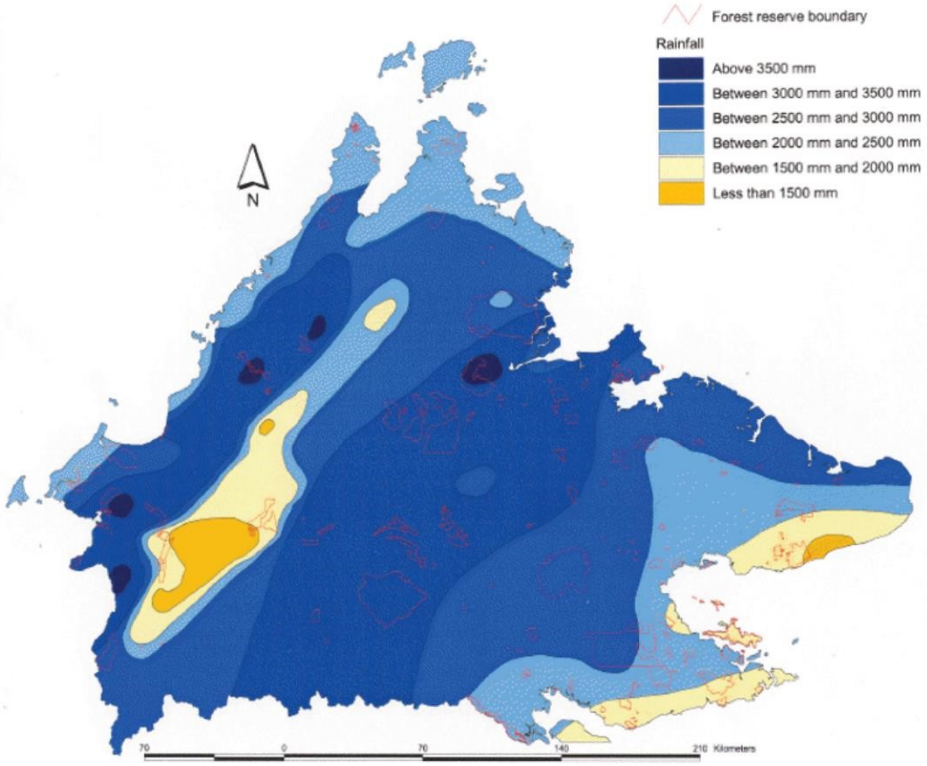

Figure 2.3. **Annual mean rainfall map of Sabah. Source: Sabah State Government.**

2.2.3 Tropical cyclones

Although few tropical cyclones reach land in Malaysian Borneo, tail effects of storms may impact eastern Malaysia due to its geographical location and orography (Tan et al. 2013). Sabah may experience heavy rainfall and strong winds from cyclones formed in the western Pacific Ocean that move northwest, depending on the intensity, position and movement of the storm (Tan et al. 2013). In recent decades, only two tropical cyclones have made landfall: Tropical Storm Greg in 1996 and Typhoon Vamei in 2001 (Chang et al. 2003). Others such as Typhoon Utor and Tropical Storm Jangmi have passed within close proximity to Sabah's coastline.

2.2.4 Land use

As Sabah has developed, more forest has been harvested and cleared for conversion to agriculture (Latip et al. 2015). The loss of forest cover experienced in Sabah is the most severe of the whole of Borneo (Gaveau et al. 2014). Oil palm is the main crop

covering Sabah, which provides a significant source of income to the state, being its main export product and biggest contributor to Sabah's economy (Latip et al. 2015). Total oil palm area in Sabah has increased to 1.4 million hectares and the state produced 5.3 million tons of crude palm oil in 2010 (Latip et al. 2015).

2.3 Study localities

2.3.1 Darvel Bay

The Coral Triangle region of northeast Sabah is a particularly favourable area for the study of turbid reefs in this thesis because turbid reefs occupy about 30% of reefs within the region (Sully and van Woesik 2020). This study investigates six diverse reef sites in Darvel Bay (Figure 2.4, 2.5; Table 2.1), characterized by turbidity (section 2.10 for more information). Two of the six reef sites, Baik and Triangle (Figure 2.5), were chosen as key study sites because of their contrasting environments and the collection of live giant clam shells (section 2.4 and 2.10 for more information).

Darvel Bay (4° 5356′ N, 118° 2646′ E) is the largest semi-enclosed bay on the eastern coast of Sabah and is connected to the Pacific Ocean through the Sulawesi and Celebes deep basins, separated by the Sulu ridge (Figure 2.2). It is within the northern corner of the Coral Triangle and noted for its high levels of marine biodiversity and endemism (Ditlev et al. 1999; Veron 2000; Ditlev 2003). Most coral reefs in Darvel Bay are dominated by small patch and fringing reefs developed around the coastline and its numerous islands (Ditlev et al. 1999) (Figure 2.4). The brown turbid waters and muddy, silty bottoms that prevail in the inner part of the bay (Ditlev 2003) on nearshore reefs is due to high terrigenous input, greatly reducing water clarity (Waheed and Hoeksema 2013). Several coral species within the region are presumed to be regional endemics that are subject to limited distributions, considered to be well adapted to sheltered habitats with high organic contents (Veron 2000; Ditlev 2003). The bay is approximately 55 km wide at its mouth (measured across from Bum Bum Island, off Semporna with Google Earth Pro). Several islands are situated within the bay; the largest, Timbun Mata (26 km long, 10 km wide), dominates the south side and is separated from the main coastline only by a single shallow channel. Climatic

conditions are controlled by the Indo-Australian monsoon system, divided into the southwest monsoon between May to September (dry season) and northeast monsoon from November to March (wet season) (Saleh et al. 2007). The tidal range is mesotidal (between 2 and 4 m) (Santodomingo et al. 2021).

Currents are complex due to the area's uneven bathymetry (Figure 2.6), islands and coastal morphology (Saleh et al. 2007). Strong tidal currents play a key role in water circulation and freshwater runoff within Darvel Bay (Saleh et al. 2007). Freshwater inputs mainly originate from the Silabukan and Tingkayu rivers, situated at the northern and southwestern parts of the bay, respectively (Saleh et al. 2007). These freshwater inputs play important roles in carrying wastewater discharge and land-based pollutants into the coastal area (Saleh et al. 2007). Current velocities range from 0.001 to 0.68 m/s and are faster at the northern part of the Bay near Sakar Island; however, current velocity does not significantly change with season and daily tides are more important (Saleh et al. 2007). During flood tides, currents flow westward along the coastal area from Bakapit towards Sakar Island and Kunak, before returning to the open sea at the bay's southern end during ebb tides.

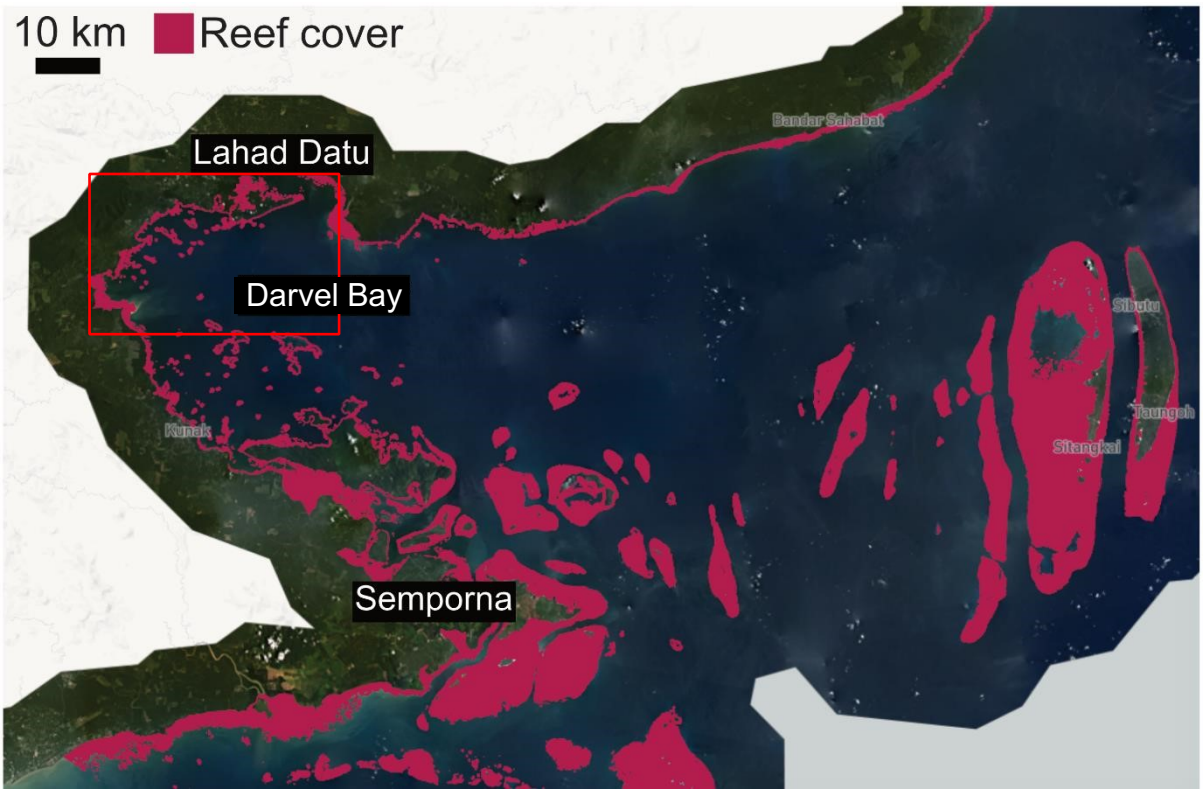

Figure 2.4. **Reef extent in northeastern Sabah, highlighting Lahad Datu city, Darvel Bay and Semporna. Modified from: Allen Coral Atlas. Red rectangle over the Darvel Bay area refers to area shown in Figure 2.5.**

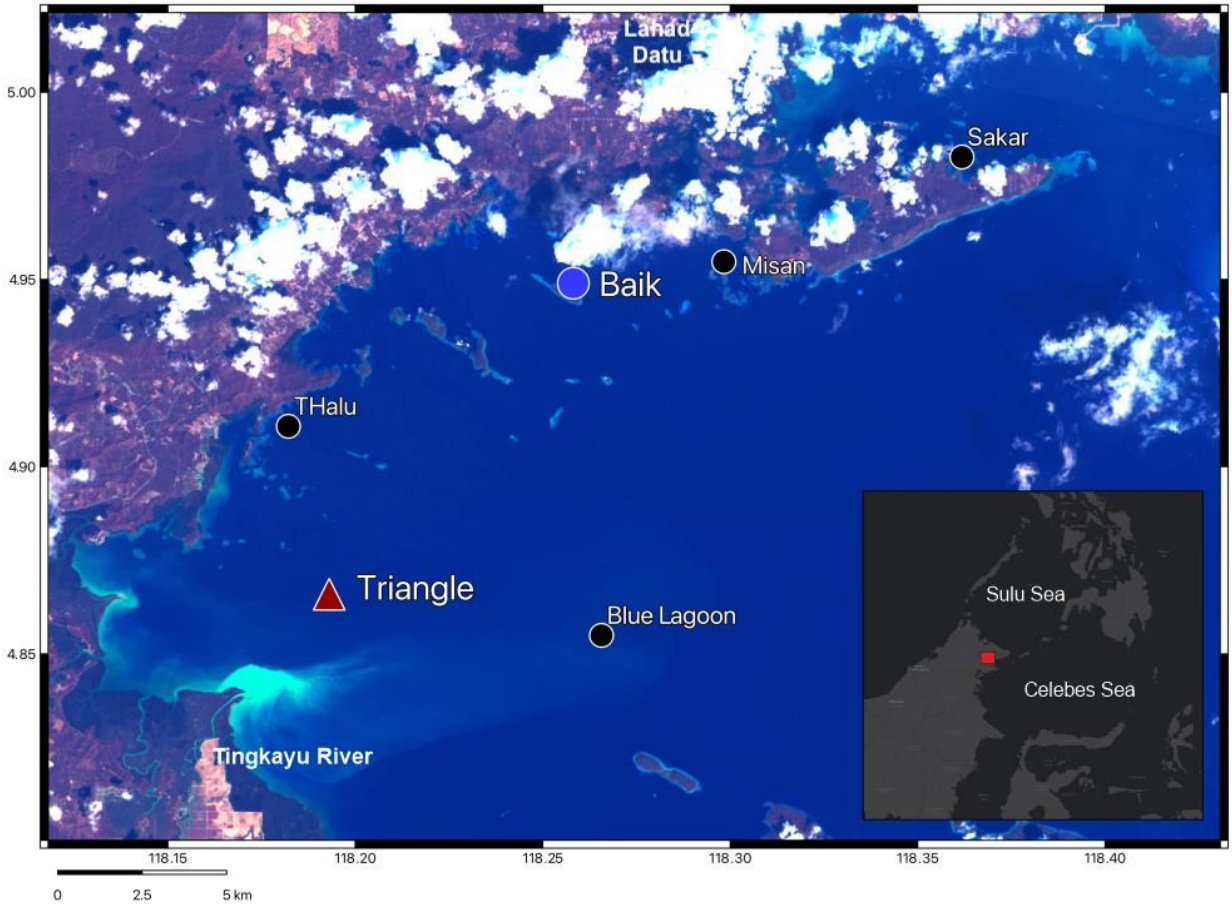

Figure 2.5. **Location of six sampling sites in Darvel Bay (Sakar, Misan, Baik, THalu, Triangle, Blue Lagoon) and nearby urban centre, Lahad Datu. Map shows false colour composite image (bands 7/4/2) of sample sites in wet season, highlighting water turbidity and delineation of the water body. Enlarged points correspond to key localities at Baik (low turbid) and Triangle (high turbid) reefs, where *Tridacna squamosa* were collected alive. River plume originating from the Tingkayu river near Triangle highlighted in bright blue.**

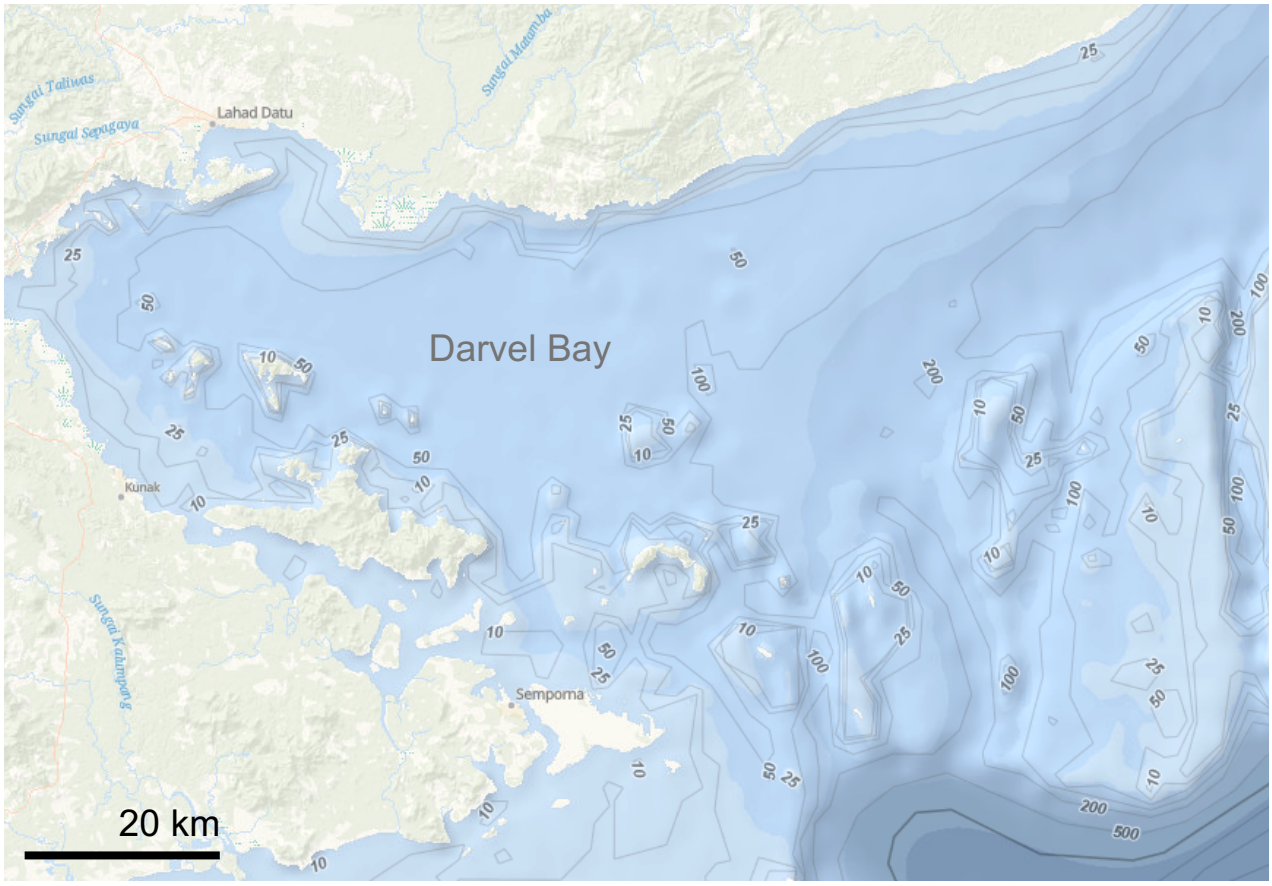

Figure 2.6. **Bathymetry of Darvel Bay and Semporna region. Modified from: National Oceanographic and Atmospheric Administration (NOAA) bathymetric data viewer.**

2.3.1.1 Triangle

Triangle reef (Figure 2.7, 2.8) is approximately 3.5 km from the outlet of the Tingkayu river (Figure 2.5), which discharges sediment to the site at low tide. During an ebb tide, freshwater carrying sediment loads from the river are directly discharged seaward to the reef at the surface, while density gradients generating two-layer circulation patterns move saltwater landward at the bottom (Saleh et al. 2007). Due to the influence of the river, sediment input is likely land derived particulate organic matter from the river basin produced by different mechanisms (e.g. freshwater productivity and remains of plants and microorganisms) and mineral sediment (Bainbridge et al. 2018). The basin around the Tingkayu is covered by thick vegetation and the area is subject to little anthropogenic influence. Triangle shows a high abundance of leather corals (*Sinularia* and *Lobophytum* spp.) (Santodomingo et al. 2021).

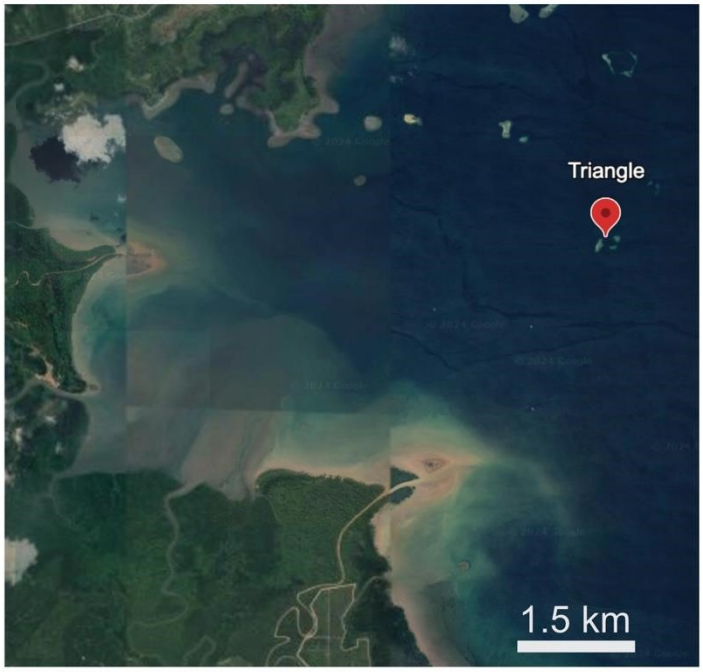

Figure 2.7. **Location of 'high turbid' Triangle Reef sampling site (4° 51'57.2′ N, 118°11'34′ E) and river mouth influence of River Tingkayu. Source: Google Earth.**

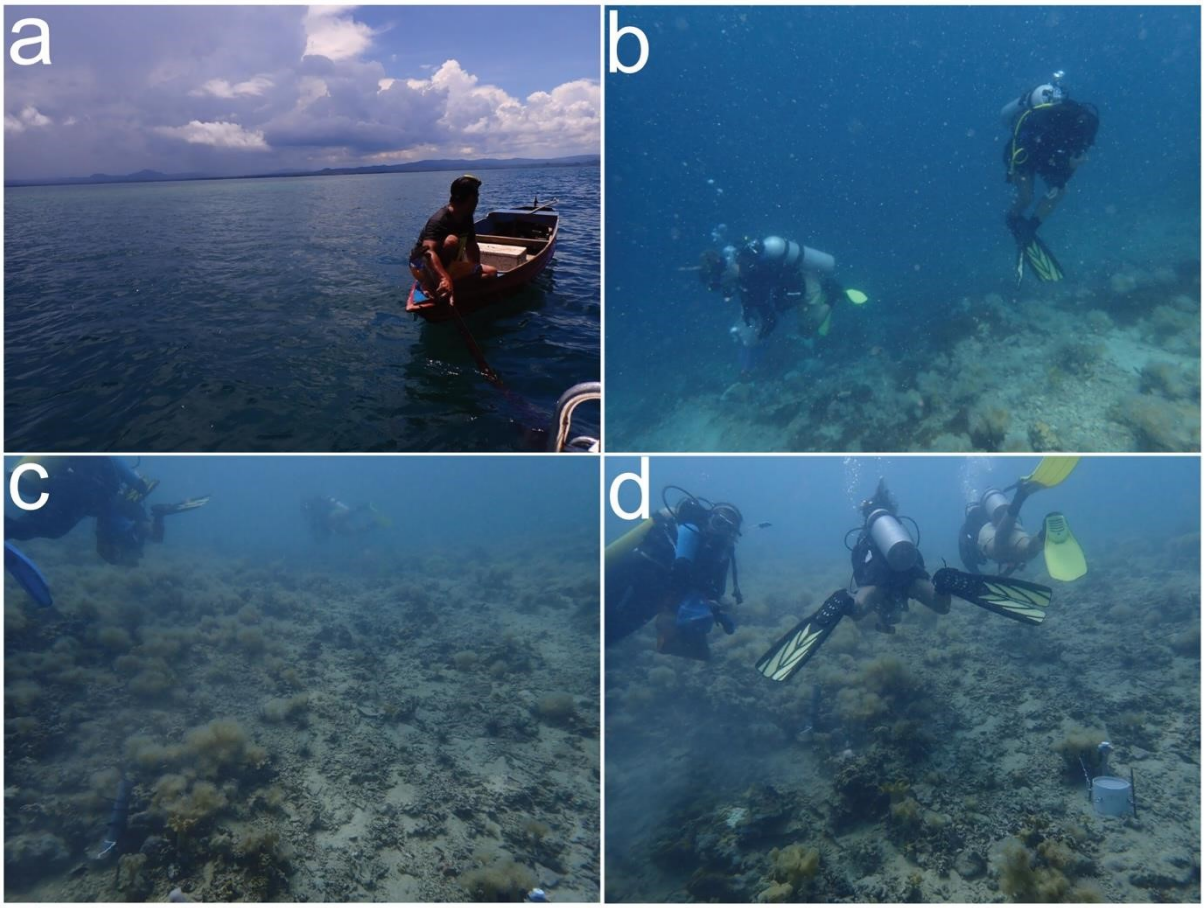

Figure 2.8. **Images taken in 2019 from Reefugia expedition to Triangle Reef. (a) View from boat above dive site. (b–d) Demonstrating the silty bottom of the reef.**

2.3.1.2 Baik

Baik (Figure 2.9, 2.10) is proximal to a fish farm, and activities at the site include recreational diving and fishing for tourism. Baik has the highest live coral cover of all six sites at 46–51% and branching *Porites* corals are common (Santodomingo et al. 2021). It has low sediment input year-round and is indicative of a low turbid reef (Santodomingo et al. 2021). The reef is situated off Baik Island (Figure 2.5, 2.9), approximately 2.5 km south of mainland Borneo. The estimated terrain elevation of Baik Island is 54 metres above sea level.

Figure 2.9. **Location of 'low turbid' Baik sampling site off Baik Island (4° 56'56.4″ N, 118° 15'29.4″ E) and nearby fish farm. Source: Google Earth.**

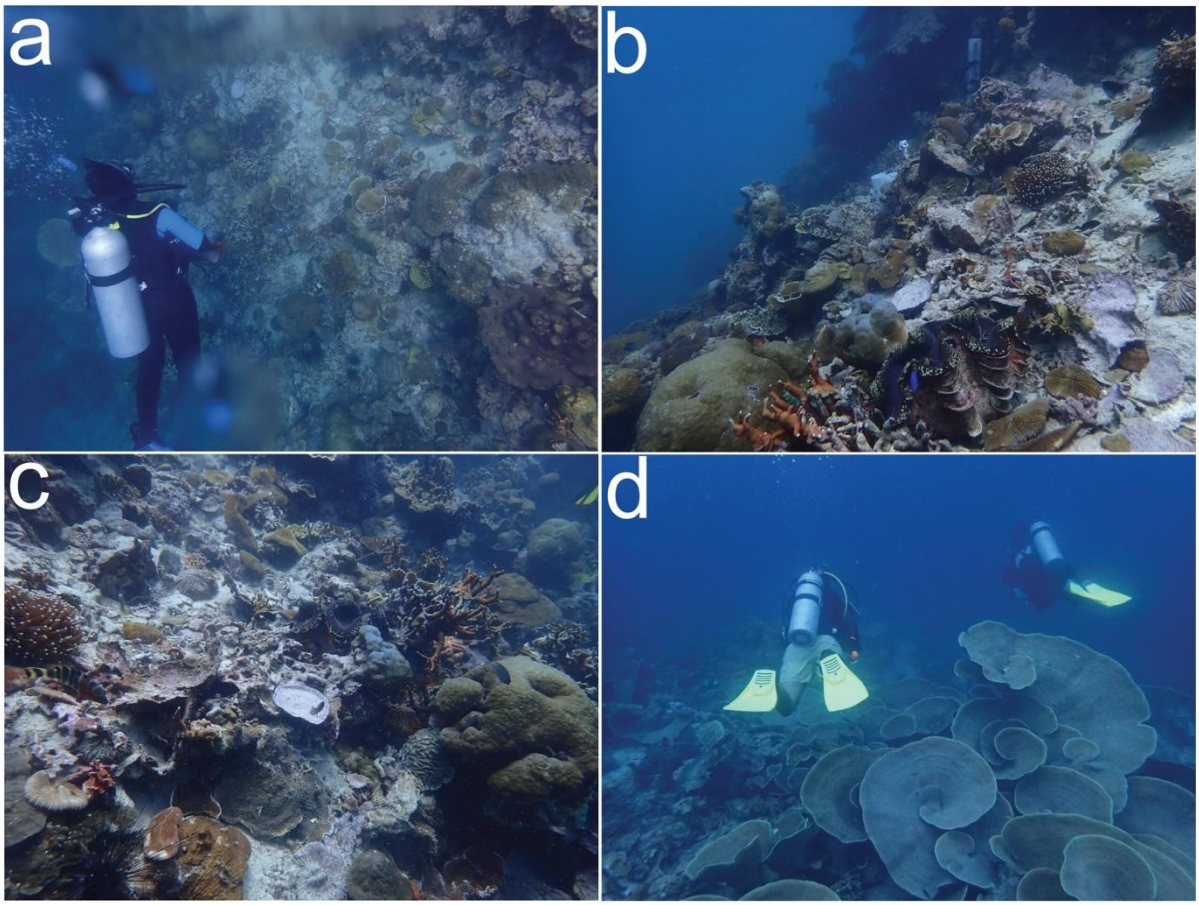

Figure 2.10. **Images taken in 2019 from Reefugia expedition to Baik Reef. (a–d) High and diverse coral cover at Baik. (b) *Tridacna squamosa* in foreground of image.**

2.3.1.3 THalu

THalu (Tamanong Halu; Figure 2.11, 2.12) is approximately 0.8 km from mainland Borneo (Figure 2.5), experiencing influence from coastal run off. Large colonies of blue coral *Heliopora* and branching *Porites* are common in THalu (Santodomingo et al. 2021). The adjacent coastal environment consists predominately of mangroves and vegetation. In recent years, Silam Coast Conservation Area (SCCA) was founded along a small proportion of coastline directly adjacent to THalu, with the aim of rehabilitating the area and ensuring less sediment flow into the sea. The recently created conservation area, which is located between urban centres Lahad Datu and Kunak, is expected to promote geotourism around two coastal geosites (Asis et al. 2017; Isnain et al. 2017).

Figure 2.11. **Location of Tamanong Halu (THalu) sampling site (4° 54'38.8′ N, 118° 10'55.7′ E), with coastal runoff influence. Source: Google Earth.**

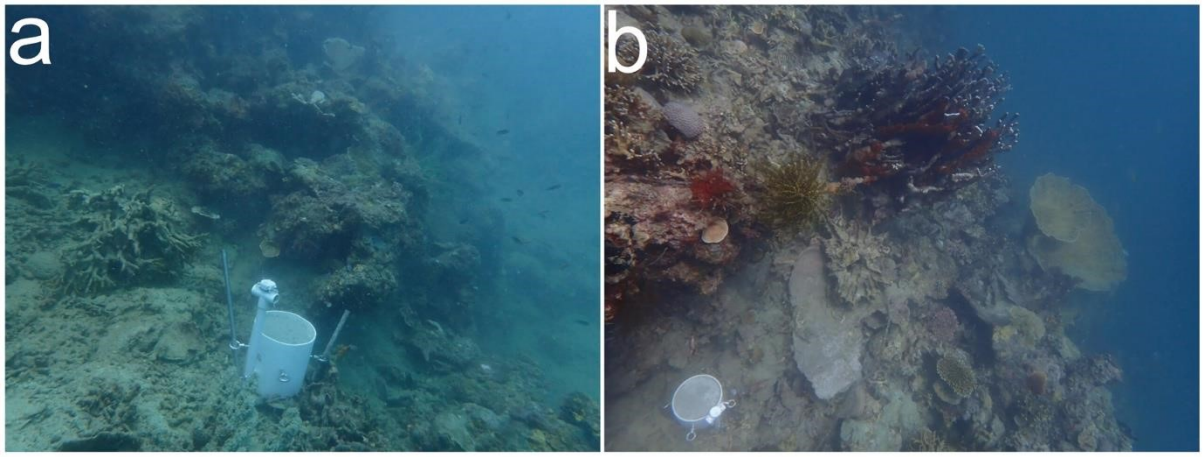

Figure 2.12. **Images taken in 2019 from Reefugia expedition to THalu Reef.**

2.3.1.4 Sakar

Sakar (Figure 2.13, 2.14) is a highly turbid urban reef situated 5 km south of a main urban settlement, Lahad Datu, which is a rapidly developing city along the bay (Saleh et al. 2007). *Leptoseris* spp. corals with foliose and platy growth forms constitute the predominant coral cover in Sakar (Santodomingo et al. 2021). Although coral cover at Sakar is the lowest of all six reef sites in Darvel Bay at 33–39% (Santodomingo et al. 2021), it has been demonstrated to be significantly resistant to bleaching events

compared to the low turbid reefs (Rosedy et al. 2023). Main economic activities around the area include small-scale fisheries and oil palm plantations.

Figure 2.13. **Location of Sakar North (Sakar) sampling site (4° 58'57.7′ N, 118° 21'42.5′ E) south of the rapidly developing urban centre Lahad Datu. Source: Google Earth.**

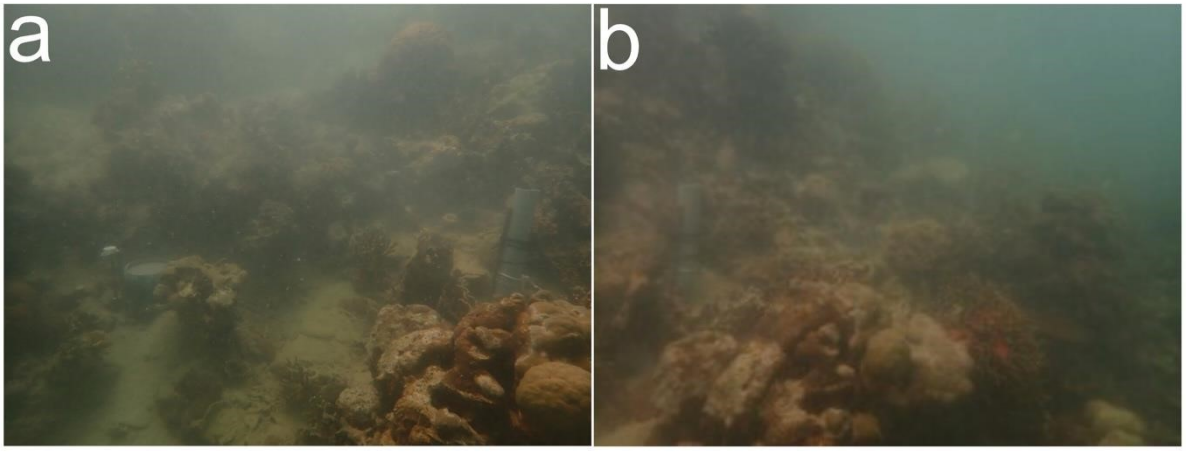

Figure 2.14. **Images taken in 2019 from Reefugia expedition to Sakar Reef, demonstrating waters with highly reduced water clarity.**

2.3.1.5 Misan

Misan (Figure 2.15, 2.16) is south of Sakar but is still within close proximity of the urban centre Lahad Datu (Figure 2.5). There is a narrow channel running between

Sakar and Misan, which is dominated by a mangrove canal with estuarine waters. The reef site is approximately 0.7 km from the mainland and coral cover is dominated by branching *Porites* corals (Santodomingo et al. 2021).

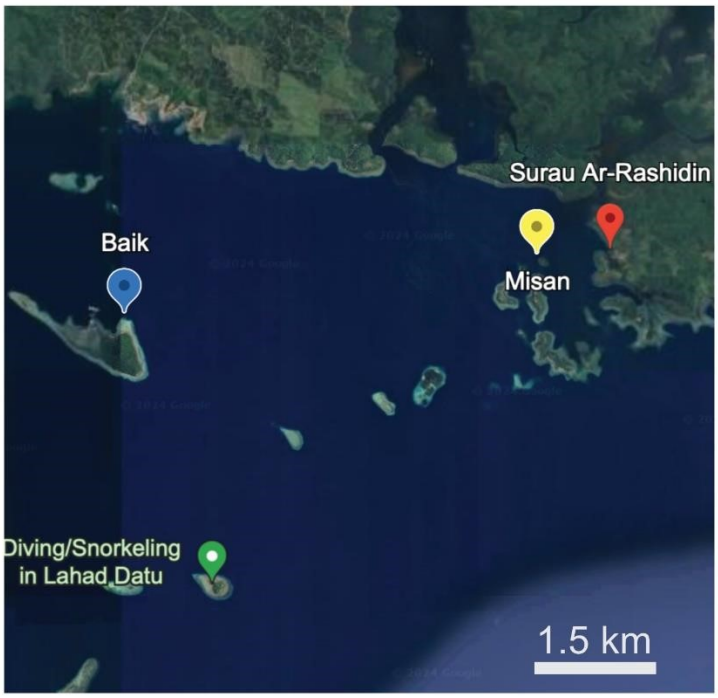

Figure 2.15. **Location of Sakar South Misan (Misan) sampling site (4° 57'17.0′ N, 118° 17'53.9′ E) subject to mangrove and canal influence. Source: Google Earth.**

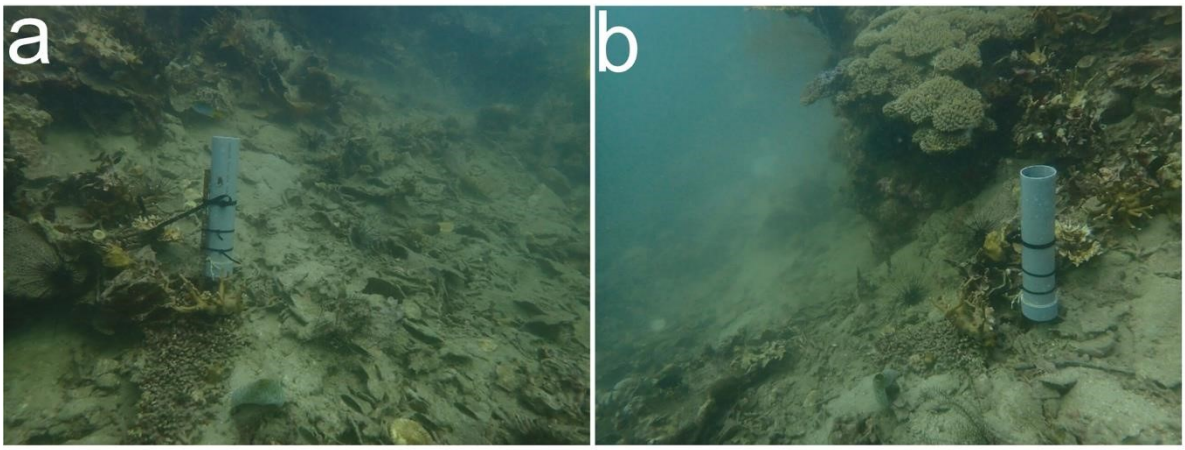

Figure 2.16. **Images taken in 2019 from Reefugia expedition to Misan Reef.**

2.3.1.6 Blue Lagoon

Blue Lagoon (Figure 2.17, 2.18) is a semi-atoll offshore reef, located approximately 11 km from the mainland (Figure 2.5). The main activity at the reef is tourism through recreational diving, owing to the site's clear waters. The shallow waters of Blue Lagoon

are dominated by large branching and table acroporid corals (Santodomingo et al. 2021), but it is known to suffer severely in bleaching events, with 46–53% coral colonies severely bleached during a 2020 bleaching event (Rosedy et al. 2023).

Figure 2.17. **Location of Blue Lagoon offshore clear water sampling site (4° 51'17.7′ N, 118° 15'56.4′ E). Source: Google Earth.**

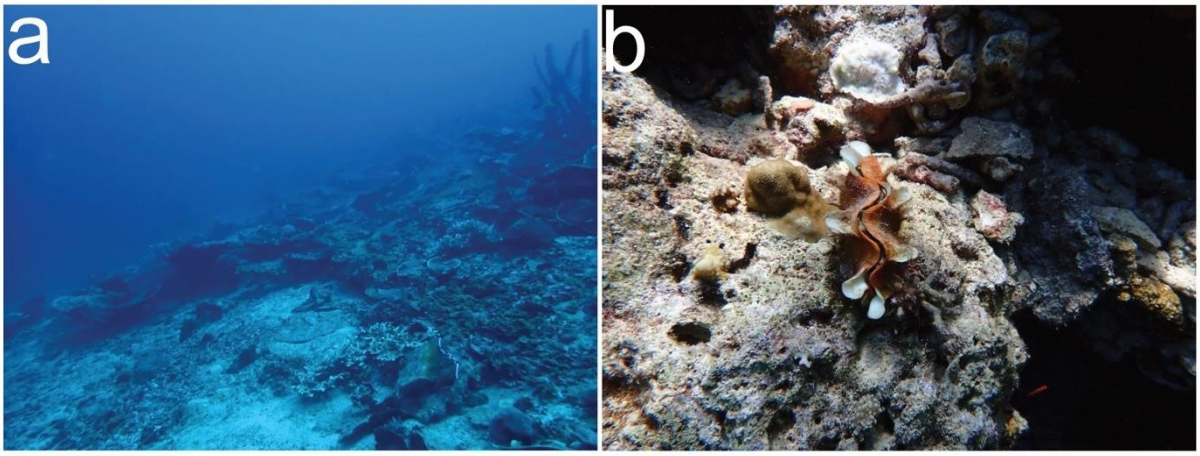

Figure 2.18. **Images taken in 2019 from Reefugia expedition to Blue Lagoon reef. (a) Demonstrating comparatively high water clarity. (b) *Tridacna squamosa* situated on sea floor.**

2.3.2 Semporna Region

Semporna is a town situated south of Darvel Bay (Figure 2.4). Its main activities include recreational diving around its islands and ecotourism within the Semporna region (e.g. hawksbill turtle and green turtle nesting sites). To broaden the region of investigation in this study beyond Darvel Bay, I also include samples from the Semporna region (section 2.4 for information).

Table 2.1. **Summary of nearby coastal environment and human activities of modern coral reef (Baik, Triangle, Blue Lagoon, THalu, Misan, Sakar and Semporna) and fossil sampling sites (east Lahad Datu and east Bontang) in eastern and northeastern Borneo.**

Site	Adjacent coastal environment/human activities
Baik	Fish farm/recreational diving
Triangle	Near Tingkayu river outlet
Blue Lagoon	Semi-atoll/recreational diving
THalu	Mangroves/conservation area (SCCA)
Misan	Mangroves/estuary
Sakar	Mangroves/urban centre influence
Semporna reefs	Recreational diving, ecotourism
east Lahad Datu	Stratigraphic formation, clay-rich outcrop in quarry
east Bontang	Stratigraphic formation, clay-rich outcrop in quarry

2.3.3 Stratigraphic formations

In addition to the seven aforementioned reef sites in Darvel Bay and Semporna, this study also investigates two rocky outcrops in eastern Borneo. One outcrop is situated in a quarry to the east of Lahad Datu, east Sabah, Malaysia (5° 22'3.36′ N, 119° 14'20.4′ E) and the other a quarry close to the city of Bontang in East Kalimantan, Indonesia (0° 11’7.08′ N, 117° 26’40.92′ E) (Figure 2.19). Both outcrops contain reef associated fossil fauna in clay-rich stratigraphic formations. Fine grained clay minerals provide high fidelity of preservation in a range of organisms (e.g. Wacey et al. 2014) because they are pore-filling and have low permeability (e.g. Bjørlykke 1997). These characteristics often help facilitate excellent fossil preservation.

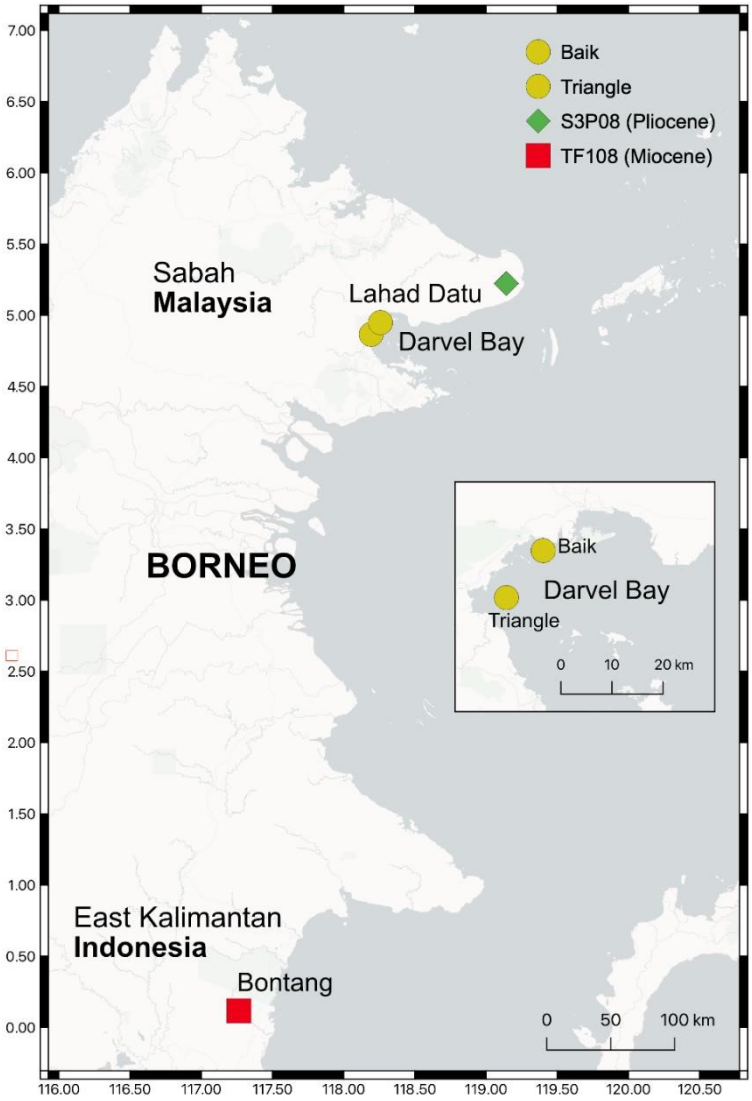

Figure 2.19. **Location of studied fossil sample sites in eastern and northeastern Borneo, showing collection localities of key modern *Tridacna squamosa* shells collected alive in Darvel Bay (Triangle and Baik reefs) relative to fossil *Tridacna* spp. shells retrieved from stratigraphic formations in eastern Sabah, Malaysia (S3P08) and eastern East Kalimantan, Indonesia (TF108).**

2.4 Study samples

Within this study, a total of 16 shell valves of giant clams were used for analysis (Table 2.2), collected either alive, dead from the seafloor, or as fossils from rocky outcrops. Eleven *T. squamosa* and one *H. hippopus* were collected from the six reef localities in Darvel Bay, either alive or dead, while two *T. squamosa* were collected from the Semporna region with unknown collection status. Two additional specimens were retrieved from clay-rich formations in eastern Sabah and eastern East Kalimantan. All specimens are either housed at the School of Earth and Environmental Sciences, Cardiff University, at the collections at the Natural History Museum, London (NHM) or at Amgueddfa Cymru—National Museum Wales (NMW).

2.4.1 Modern shells

Four modern *T. squamosa* shells were extracted alive at the key Baik and Triangle reefs on 16th and 17th April 2019 (SS_BAIK and SS_CT, respectively) and 24th and 22nd February 2020 (NS207 and ZW156, respectively) on two separate field excursions made by the Reefugia project (Figure 2.20, Table 2.2). Animals were collected with SCUBA equipment at shallow depths between 5 and 8.5 m. Shell height ranged between 14.7 cm and 26.9 cm and shell width between 21.5 cm and 40.0 cm.

In addition, eight shells were collected dead from the seafloor at Baik (SS01B_BT), Triangle (SS03B_CT, SS02B_CT), Sakar (SS02A_SN, SS01B_SN), Misan (SS01A_SM), THalu (SS01A_TH) and Blue Lagoon (SS01A_BH) between the 13th and 17th April 2019 (Figure 2.20, Table 2.2). These shells were collected at minimum depths of 5 m and maximum depths of 15 m. It is important to note that the differences in collection depths across these locations could potentially influence the observed variation highlighted in this thesis through differences in light penetration. Shell heights ranged between 10.8 cm and 23.1 cm and shell widths 15.5 and 31.5 cm.

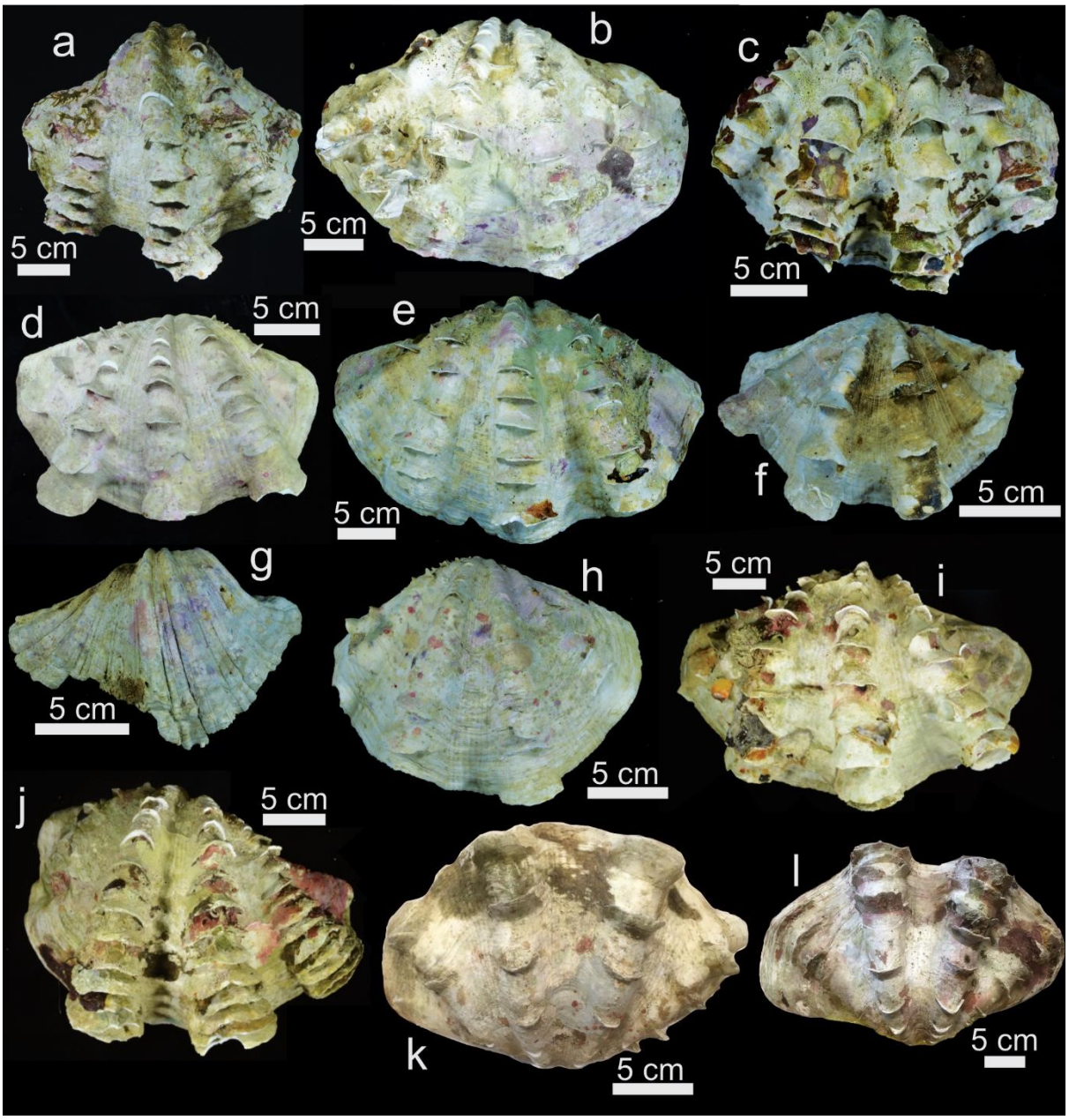

Figure 2.20. **Dead collected giant clams from Blue Lagoon (SS01A_BH, *T. squamosa*) (a); Baik (SS01B_BT, *T. squamosa*) (b); Misan (SS01A_SM. *T. squamosa*) (c); Triangle (SS03B_CT; SS02B_CT, *T. squamosa*) (d, e); Sakar (SS02A_SN, *T. squamosa*; SS01B_SN, *H. hippopus*) (f, g); THalu (SS01A_TH, *T. squamosa*) (h). Live collected giant clams from Triangle (SS_CT, *T. squamosa*) (i) and Baik (SS_BAIK, *T. squamosa*) (j) in 2019 and Triangle (ZW156, *T. squamosa*) (k) and Baik (NS207, *T. squamosa*) (l) in 2020.**

To broaden the comparison to a wider geographical area outside of Darvel Bay, an additional two small *T. squamosa* shells from the Semporna region (SEM_A, SEM_B) (Figure 2.21) situated south of Darvel Bay (Figure 2.4) were obtained from the Sue Fielding collection held at NMW (N.B. original accession numbers are NMW.Z.2007.032.00501.a for SEM_A and NMW.Z.2007.032.00501.b for SEM_B).

The precise collection location is unidentified, and there is no recorded information regarding whether the shells were collected in a living or deceased state. Notes associated with the collection specify that the shells were collected in the early 1960's (c. 1961–1963) in a remote area of Semporna. Many of the coral sites in proximity to the collection area are now thought to be inaccessible due to piracy or destroyed from dynamite fishing. Due to the preservation of macro-features on the inner shell surface, including a pearly white appearance free from microboring or colonization by other organisms such as alga, the current author presumes shells were collected alive.

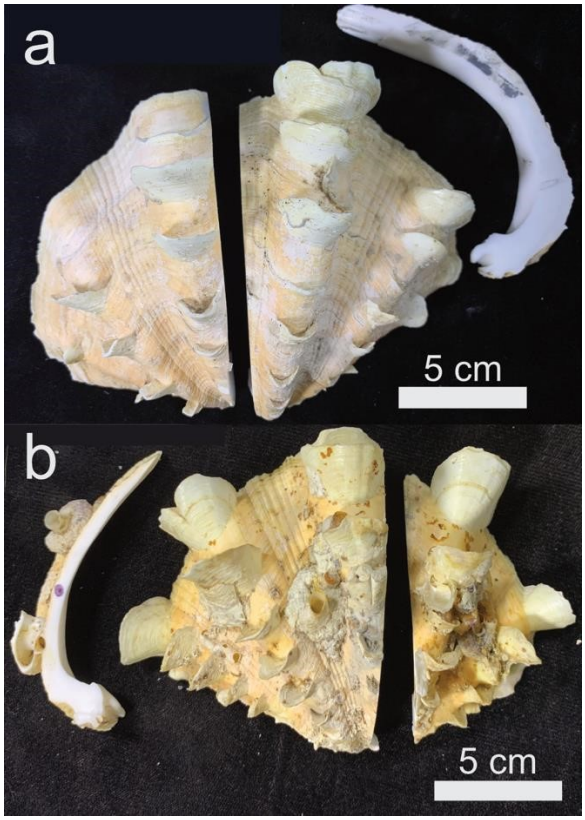

Figure 2.21. **Two giant clam *Tridacna squamosa* shells from the Semporna region south of Darvel Bay: SEM_A, (a); SEM_B (b). Slices from the maximum growth axis used for thin section analysis are shown adjacent to each shell.**

2.4.2 Fossil shells

Two fossil *Tridacna* spp. shells were previously collected in December 2010 (TF108_BW4B) and September 2012 (S3P08), respectively (Figure 2.22). TF108_BW4B was retrieved from a quarry close to the city of Bontang in eastern East Kalimantan (Figure 2.19, section 2.3.3 for more information) and estimated at 9.4 Ma with errors of +0.39/-0.37 (Miocene epoch) using strontium isotope stratigraphy (SIS) (Renema et al. 2015; Warter et al. 2015). Another part of a different valve of the same shell has been previously studied in Warter et al. (2015, 2017). Sample S3P08 was collected from a quarry to the east of Lahad Datu, Sabah (Figure 2.18, section 2.3.3 for more information) and estimated at 3.4 Ma with errors of +1.08/1.44 (Pliocene epoch) with SIS (Saw et al. 2019). Sample S3P08 was retrieved from the collections at NHM as a slice, rather than a whole shell valve (Figure 2.21b).

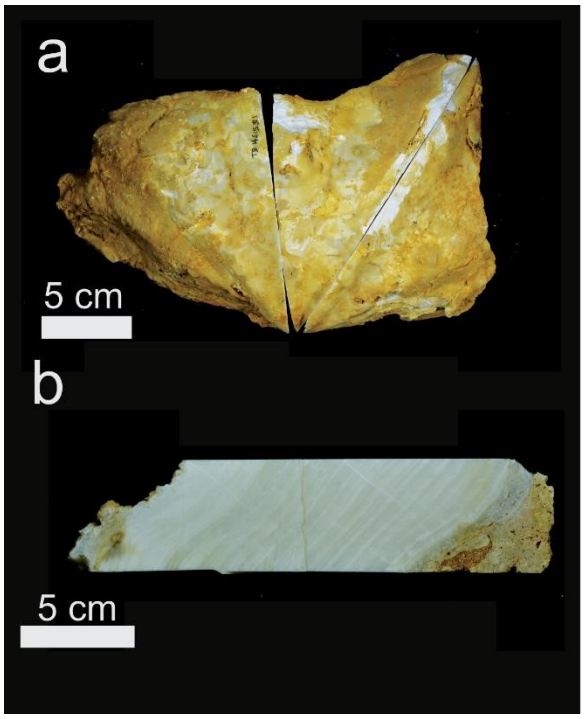

Figure 2.22. **Two giant clam *Tridacna* spp. fossil shells from clay-rich rocky outcrops in East Kalimantan (a) and eastern Sabah (b): TF108_BW4B (a); S3P08 (b).**

Table 2.2. **Giant clam specimens used in this thesis. Most specimens are from six study sites within Darvel Bay, although additional modern shells from the Semporna region and fossil specimens from Malaysia and Indonesia are used for comparison. Collection status: L = live, D = dead, F = fossil, U = unknown. Collection depth in metres (m). Institution: NHM = Natural History Museum, NMW = National Museum Wales. Light source used for thin section light microscopy: T = transmitted light, R = reflected light.**

Site	Specimen no.	Modern/Fossil	Species	Collection status	Collection Depth (m)	Institution	Light source
Blue Lagoon	SS01A_BH	modern	*T. squamosa*	D 2019	5–15	NHM	T
Baik	SS01B_BT	modern	*T. squamosa*	D 2019	5–15	NHM	T
Misan	SS02B_SM	modern	*T. squamosa*	D 2019	5–15	NHM	T
Triangle	SS03B_CT	modern	*T. squamosa*	D 2019	5–15	NHM	T
Triangle	SS02B_CT	modern	*T. squamosa*	D 2019	5–15	NHM	T
Sakar	SS02A_SN	modern	*T. squamosa*	D 2019	5–15	NHM	T
Sakar	SS01B_SN	modern	*H. hippopus*	D 2019	5–15	NHM	T
THalu	SS01A_TH	modern	*T. squamosa*	D 2019	5–15	NHM	T
Triangle	SS_CT	modern	*T. squamosa*	L 2019	5	NHM	R
Baik	SS_BAIK	modern	*T. squamosa*	L 2019	7	NHM	R
Triangle	ZW156	modern	*T. squamosa*	L 2020	5	NHM	R
Baik	NS207	modern	*T. squamosa*	L 2020	8	NHM	R
Semporna	SEM_A	modern	*T. squamosa*	U 1961–1963	NA	NMW	R
Semporna	SEM_B	modern	*T. squamosa*	U 1961–1963	NA	NMW	R
east Bontang	TF108_BW4B	fossil (Miocene)	*Tridacna* sp.	F 2010	NA	NHM	R
east Lahad Datu	S3P08	fossil (Pliocene)	*Tridacna* sp.	F 2012	NA	NHM	R

2.4.3 Sample preparation procedure

For all samples, the exterior of each shell valve was thoroughly rinsed and gently scrubbed to remove dirt and debris from the outer surface, before being air-dried. Afterward, valves were cut along the axis of maximum growth (longitudinal from umbo to upper shell margin) (Figure 2.23a) with a HC Evans and Son (Eltham) LTD circular saw (250 mm blade, 1 mm thickness) or Logitech GTS1 Thin Section Cut-Off diamond saw (Figure 2.24) depending on shell size, to obtain two halves of each valve. A slice approximately 1–2 cm thick (Figure 2.23b) was cut from the middle of one half and used to prepare thin sections (approximately 60 μm thickness) of the inner- and outer shell layers perpendicular to the direction of growth (Figure 2.23c). Slices from the middle of each shell valve were used because this represents the fullest record of growth of the animal (e.g. Liu et al. 2022) and is the thickest part of the shell. To prepare slices to be made into thin sections, one side of each slice was ground flat using silicon carbide 1000 grit. This side of the slice was then washed, dried and stuck to a 28×48 mm frosted glass slide using Araldite 2020 epoxy resin. Excess sample was cut from the slides leaving a 500–1000 μm slice stuck to the glass. Slides were then lapped on a Logitech LP50 lapper using 600 silicon carbide grit to leave samples at a thickness of around 100 μm. Afterward, the slides were lapped by hand using 1000 silicon carbide grit until the required sample thickness was reached. Slides were washed in an ultrasonic bath and polished on a Logitech PM5 lapper with 0.3 μm Aluminium oxide. After polishing slides, they were again washed in an ultrasonic bath. To improve visibility of growth banding (Figure 2.23d) and biomineral units, slides were finally weakly etched with 0.5% hydrochloric acid (HCl) for 15 seconds.

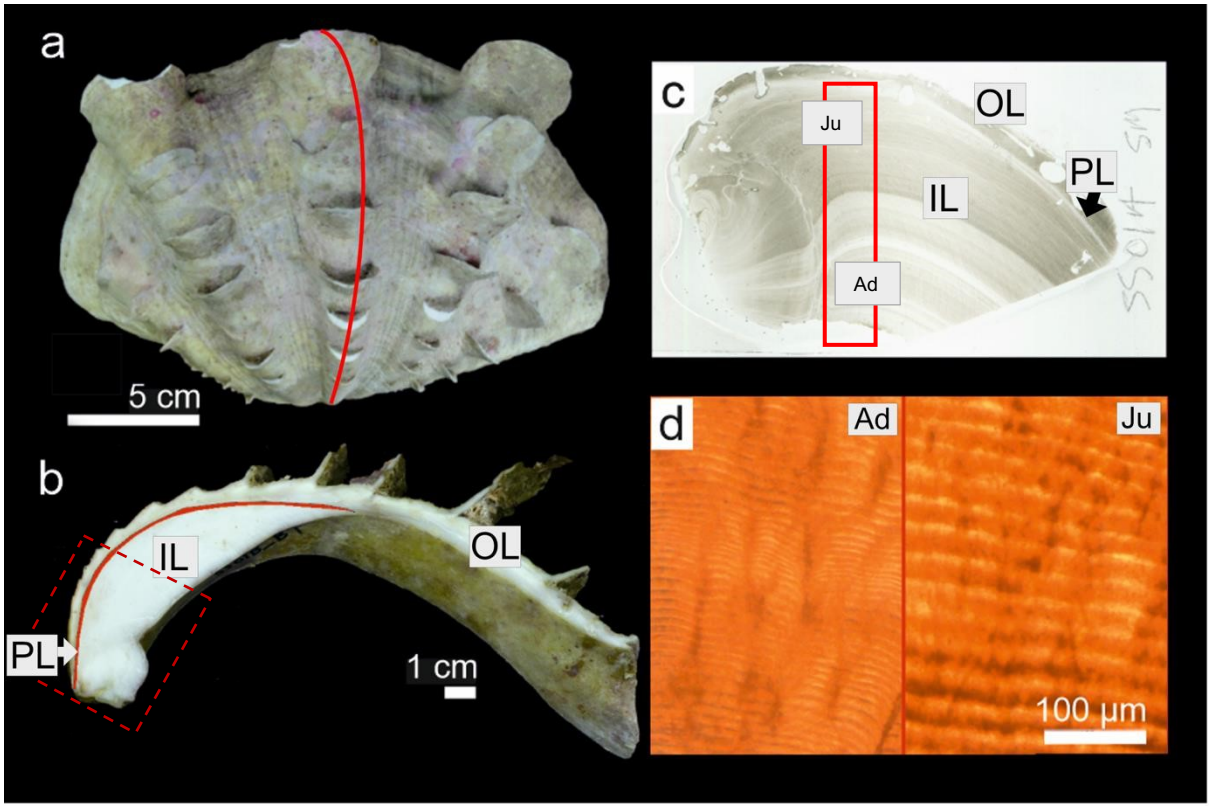

Figure 2.23. **Sample preparation procedure for giant clam shells. (a) Valve of *Tridacna squamosa* with red vertical line indicating initial location of saw cut along axis of maximum growth. (b) Longitudinal slice taken from initial saw location in (a), showing the inner shell layer (IL), outer shell layer (OL) and pallial line (PL), dividing the IL and OL. (c) Thin section taken from red dashed rectangle in (b), denoting the IL, OL, PL and first growth (juvenile growth, Ju) and last growth (adult growth, Ad). Long red rectangle denotes region of shells investigated with light microscopy and scanning electron microscopy, representing the height of the inner layer. (d) Daily growth bands under transmitted light microscopy (20x magnification) from first (Ju) and last growth (Ad), demonstrating difference in band width between different stages of life.**

***Figure 2.24. Tridacna squamosa* shell valve on platform of diamond saw apparatus, in preparation for cutting longitudinally along the axis of maximum growth.**

2.5 Imaging analysis

2.5.1 Light microscopy

Thin section light microscopy using a stereomicroscope (Leica MZ16) or compound microscope (Leica DMR) equipped with a digital camera was used to image daily growth bands in giant clam shells at the School of Earth and Environmental Sciences, Cardiff University. Micrographs between 10–40x magnification were taken across entire section lengths vertically from the inner shell layer (IL) to the outer shell layer (OL) (an area with height ~30 mm, width ~1 mm), providing sets of TIFF images that encompassed growth throughout the entirety of lifespan. Markers, or features, were noted for each image (e.g. a speck of dust on image, microstructural variation, conspicuous growth band), so images could be assembled into larger composites of whole thin section heights (Figure 2.25).

Each daily growth band consists of a ‘couplet’ of a light (transparent) and dark (opaque) region (Figure 2.23d, 2.25), which changes opposingly under transmitted and reflected light, the former source showing denser bands as darker and the latter as lighter

(Warter et al. 2015). It is important to ascertain the transparency of bands accurately because band lightness aids the delineation of each day of growth and additionally gives qualitative information on density of the shell material. In this study, both transmitted and reflected light were tested to ascertain the source that provided the most discernible daily banding patterns, with the final light source used varying between each specimen (Table 2.2).

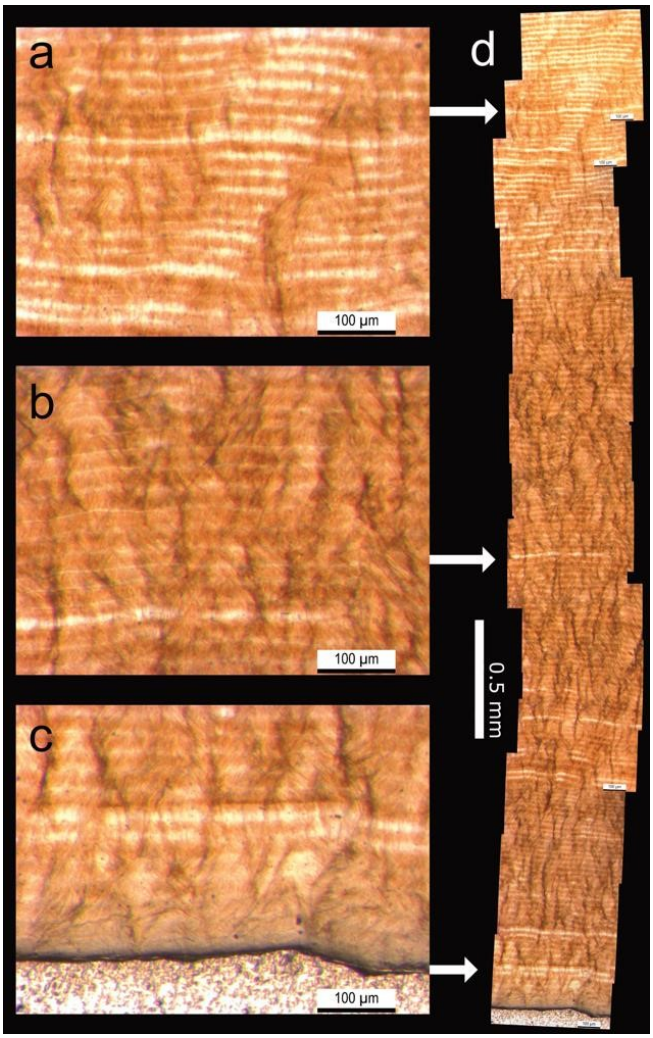

Figure 2.25. **Examples from a set of transmitted images (45 total) of *Tridacna squamosa* sample SS03B_CT (a–c). Images were assembled into larger composite images based on unique features from each image in the stack (d).**

Each daily 'couplet' was counted and measured with the image processing software ImageJ 1.53 (Schneider et al. 2012) to determine age of the specimen and daily growth rate (DGR) in micrometres (µm) and millimetres (mm). Before recording each growth band, spatial calibration was carried out using the 'set scale' function and measuring the scale bar associated with the set of images. The line tool was used to measure the

width of each subsequent growth band from the IL edge (Figure 2.26a) to the pallial line, where the OL begins (Figure 2.26b). The IL region was chosen because growth bands were clearer and could regularly be counted in this region of the shell in the selected species. The IL also showed minimal microboring, in comparison to the edge of the OL in some shells. Measurements were saved as an overlay and the data exported to a .csv file for further interpretation and data processing. Specimens that were collected alive (i.e. from the key Baik and Triangle reefs in Darvel Bay: SS_CT, SS_BAIK, NS207, ZW156) and used as a primary focus for comparison in this study were additionally counted by a secondary person on ImageJ to reduce subjective results. A 'semi-automatic' approach, which included using an autoplace function and subsequently checking measurements, was also trialled with the dendrochronological software CooRecorder 9.8 (Cybis) (Maxwell and Larsson 2021). However, this was only successful in specimens with extremely clear daily growth bands throughout the whole shell, largely unobstructed by other features. A comprehensive overview of counts per sample, offsets between counts and measurements is given in chapter 3 and in Mills et al. (2023).

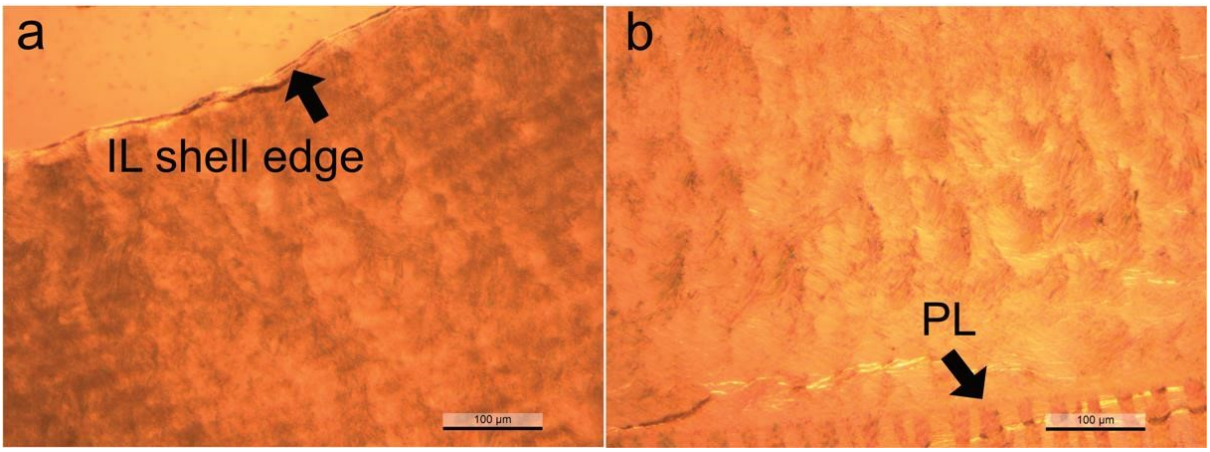

Figure 2.26. **The inner shell layer (IL) edge for *Tridacna squamosa* sample SEM_B, perpendicular to the direction of growth, where counting and measuring growth bands commenced (a). The pallial line (PL) demarcating the end of the IL and beginning of the outer shell layer, where counting stopped (b). Reflected light used.**

2.5.2 Scanning electron microscopy (SEM)

A Zeiss Sigma HD field emission gun SEM at the School of Earth and Environmental Sciences, Cardiff University (Figure 2.27) was also used to image daily growth bands on the same thin sections (chapter 3 and Mills et al. (2023) for more information). SEM focuses a high energy beam of electrons onto the surface of a sample, where secondary electrons (i.e. those originating from the sample, as opposed to backscattered electrons from the electron beam) are ejected, forming images which reveal surface topography. Electrons have a shorter wavelength than visible light, allowing SEM to provide higher resolution images than light microscopy, generally down to the range of tens of nanometres. As SEM is capable of extracting only information on the sample surface, rather than the entire thickness of the section, shell regions for which growth bands are indiscernible under light microscopy may be observable. Moreover, the boundary between the OL and IL is often clearly definable under SEM (Faylona et al. 2011), something which is not always apparent when using light microscopy.

To prepare samples for SEM, the polished and etched sections were gently cleaned with alcohol wipes and surfaces sprayed with air duster compressed air to remove dust/dirt. Samples must be made conductive prior to SEM imaging to prevent charge build up on the sample surface, which repels the electron beam and distorts the image. Hence, each section was sputter coated with 20 nm gold-palladium (Au-Pd) alloy using a BIO-RAD SC500 sputter coater at the School of Earth and Environmental Sciences, Cardiff University. Samples were also held in the SEM with copper clasps to further diminish charging (Figure 2.27b). Growth bands were observed between 500x and 2500x magnification under high vacuum with an acceleration voltage of 10 kV, aperture size of 30 μm, nominal beam current of 210 pA, pixel dwell time of 10 μs and working distance of approximately 9.5 mm. Images were set up to be automatically captured and montaged into larger composites using Oxford Instruments Aztec 6.0 software.

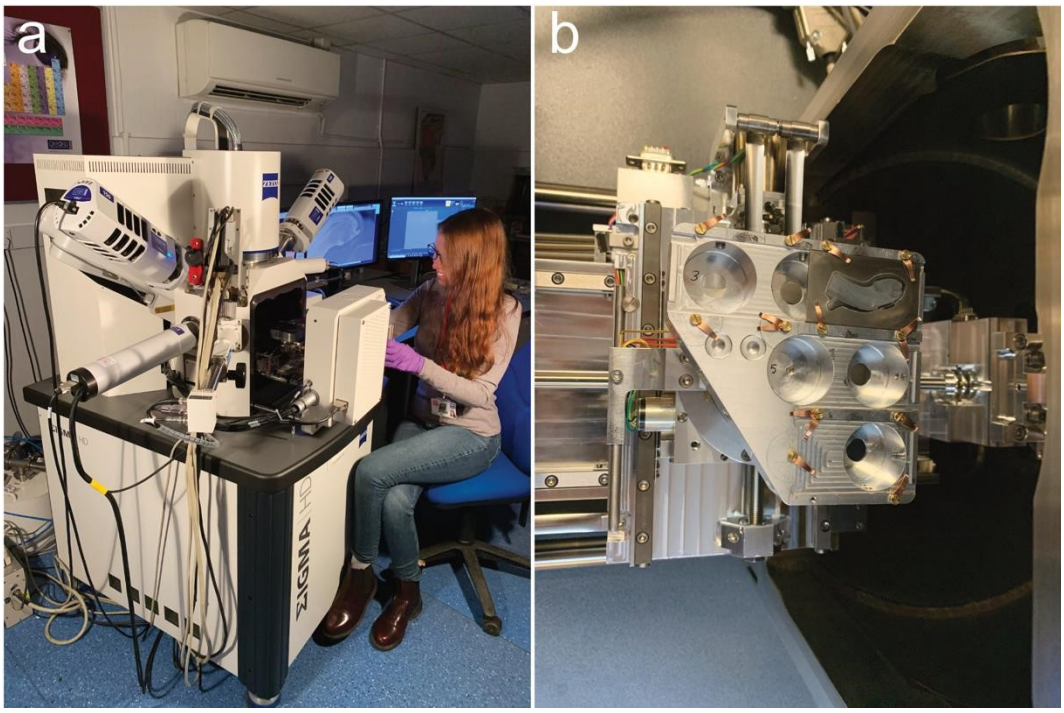

Figure 2.27. **Author operating Zeiss Sigma HD field emission gun SEM (a). Sample chamber inside SEM, showing sample holder for giant clam thin sections with sample loaded in upper right corner (b).**

Secondary electron imaging was also used for preliminary assessment of microstructural variation in shells. It was used to qualitatively investigate the microstructure of biomineral units across the entirety of the height of the IL of samples (red rectangle in Figure 2.23), using the same operating parameters as for investigation of growth bands. In modern specimens, investigation focused on differences in the type of microstructure at an intra- and intershell scale (findings in chapters 3 and 5). In fossil giant clams, microstructure was compared to modern shells and screened for signs of diagenetic alteration (findings in chapter 6). Images were taken under a wide range of magnifications, ranging from 500x to 50,000x, allowing the observation of differences in the hierarchical structure of shells (i.e. first-, second-, third-order lamellae and nanograins).

2.5.3 Electron backscatter diffraction (EBSD)

EBSD experiments were performed on the same Zeiss Sigma HD FEG-SEM, equipped with a Nordlys-2 EBSD detector at the School of Earth and Environmental Sciences, Cardiff University. A selection of sections used for light microscopy and

SEM imaging, chosen based on variation in microstructure, were used for EBSD analysis. EBSD is an SEM-based technique used to gain precise and quantitative crystallographic information on materials. It allows for the identification of characteristics of individual grains across a sample, such as grain orientations, boundaries, size, distribution and phase identification. The collected data are spatially distributed and may be viewed as microstructural maps. Further, crystal orientations extracted for each grain identified can be plotted on pole figures in 3D space (i.e. stereographic projection of the poles of planes used to represent the orientation of crystals) to quantify differences between distinct areas of growth bands in a sample.

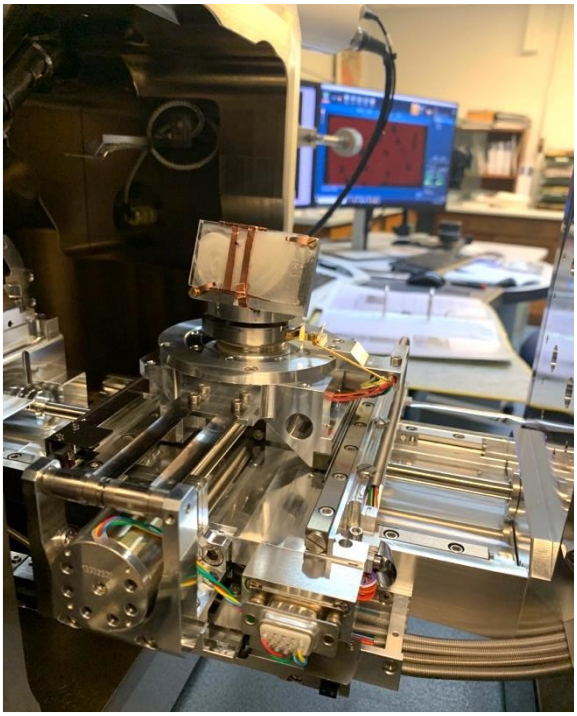

Figure 2.28. **Sample chamber inside the SEM, showing the EBSD sample holder for giant clam thin sections, with the sample loaded at a 70° angle.**

EBSD involves the interaction of an electron beam with a tilted crystalline sample at a 70° angle (Figure 2.28). Backscattered electrons leaving the sample may exit and travel in such a way that their energy and direction satisfy the Bragg condition:

$$2d\sin\theta = n\lambda$$

Where d is the interplanar spacing between lattice planes, θ is the Bragg angle, λ is the wavelength of the radiation used (i.e. electron beam) and n is an integer, referred to as the order of diffraction.

Electrons that meet the Bragg condition when they scatter produce what are known as backscatter Kikuchi patterns (BKP). These patterns, also referred to as EBSD patterns, are essentially electron scattering patterns that directly reflect the arrangement of lattice planes within the crystal undergoing diffraction. BKP are captured on a phosphor screen positioned near the tilted sample (Figure 2.29) and are automatically analysed by EBSD software using the Hough transformation (i.e. used to detect linear features in the diffraction pattern), generating crystallographic orientation measurements.

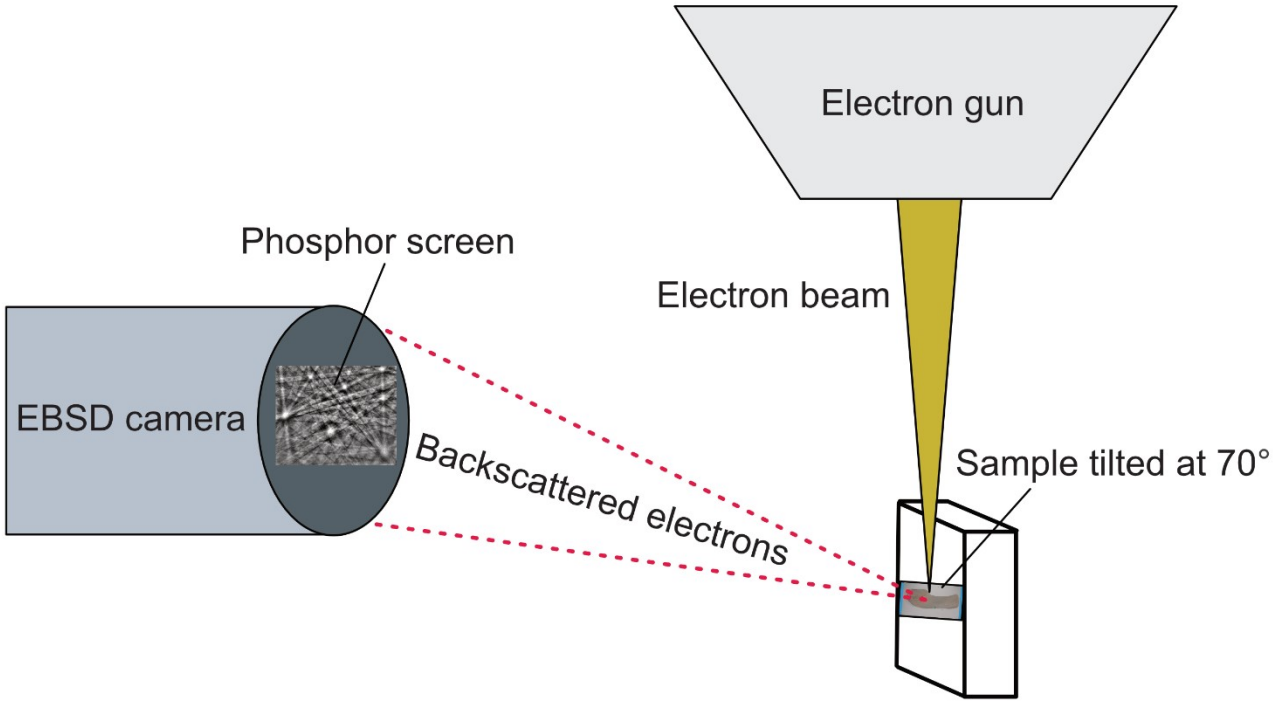

Figure 2.29. **Simplified schematic of experimental set-up for electron backscatter diffraction (EBSD) data collection. A beam of electrons is directed at the titled sample surface from an electron source. These electrons interact with atoms within the sample and some 'scatter' in different directions, i.e. backscattered electrons. The pattern of backscattered electrons depends on the arrangement of atoms in the crystal lattice of the material. A phosphor screen**

on an EBSD camera is used to capture these backscattered electrons, forming Kikuchi patterns.

EBSD is a surface technique and requires a finely polished, flat sample surface to achieve the best results. Given the significant role of EBSD in this thesis (refer to chapters 5 and 6) and considering previous studies' failure to characterize aragonite crystals in giant clam shells using EBSD (Gannon et al. 2017), a thorough examination of data processing techniques is conducted in methods chapter 4 and Mills et al. (2024).

2.6 Electron probe microanalysis (EPMA)

EPMA is a powerful geochemical technique commonly employed in materials sciences to determine the elemental composition of solid samples at very fine scales (nano- to micrometers). In EPMA, a high-energy electron beam is focused onto the sample surface, causing interactions with the atoms in the material. These interactions result in the emission of characteristic X-rays that are excited by electrons, with energies specific to the elements present in the sample. By analysing the energy and intensity of emitted X-rays, EPMA can identify the elements present in the sample and quantify their concentrations down to trace levels (100s ppm). EPMA allows the distribution of chosen elements to be visualized due to its mapping capabilities, which is key to understanding localized elemental properties of samples and their relation to other characteristics of the material, such as structure and texture.

In this study, the geochemical concentrations of giant clam shells collected alive in 2019 were measured on a JEOL 8530F field-emission electron microprobe equipped with five wavelength dispersive spectrometers (WDS) at the Electron Microbeam Suite, University of Bristol, UK. Targeted regions of thin sections previously used in light microscopy, SEM and EBSD were repolished and fragmented by hand into approximately 6 x 6 mm pieces with a diamond tipped scribe at the School of Earth and Environmental Sciences, Cardiff University. Each fragment was finished on a grinding machine equipped with a CUTROCK horizontal diamond wheel. To make samples conductive, fragments were coated with a thin layer of 10 nm of silver (Ag) at Bristol University to minimize beam damage and ensure sample stability.

EPMA maps were acquired for Mg using TAP and TAPH crystals and Sr using a TAP crystal with the following parameters: 15 kV accelerating voltage and 100 nA beam current, with a step size of 0.9 µm and 500 ms dwell time. Spot measurements of 3 µm beam diameter for Mg and Sr were acquired at 15 kV and 100 nA. Measurements for Ca using the PETH crystal were acquired with 3 µm beam diameter at 15 kV and 5 nA. The instrument was calibrated with the following internal standards: Iceland Spar Calcite (ICE) for Ca, MgO for Mg and $SrSO_4$ for Sr. Maps were quantified using CalcImage in Probe for EPMA software package (http://www.probesoftware.com/).

Shell Mg and Sr concentrations were normalized to Ca in Image J 1.53 software (Schneider et al. 2012) and final Mg/Ca and Sr/Ca maps represented as molar ratios. To generate the El/Ca maps, negative Mg values were substituted with half of the minimum value above zero, following Jonkers et al. (2016). This technique was chosen because discarding negative values that may have arisen during measurement leads to loss of information. By substituting negative values with a positive value, some information from the original data is retained. In addition, this method avoids overall distortion of the distribution of data in maps.

The detection limit for Mg for an average of 4 pixels is 0.009 wt% (90 ppm) or for 1 pixel 0.017 wt% (170 ppm) to 2 SD. If wt% Ca = 40, analytical uncertainty at 2 mmol/mol Mg/Ca (close to average map values in chapter 5) for an average of 4 pixels is ~11%; this drops to ~5% when averaging 16 pixels. The detection limit for Sr for an average of 4 pixels is 0.037 wt% (370 ppm) or for 1 pixel 0.073 wt%, 730 ppm to 2 SD. If wt% Ca = 40, analytical uncertainty at 3 mmol/mol Sr/Ca (close to average map values in chapter 5) for an average of 4 pixels is ~10%; this drops to ~5% if 16 pixels are averaged. To achieve similar uncertainty at lower El/Ca ratios, more pixels need to be averaged. For example, Mg/Ca analytical uncertainty at 1 mmol/mol for an average of 4 pixels is ~21% and this drops to 10% if 16 pixels are averaged.

2.7 X-ray diffraction (XRD)

XRD is a non-destructive technique used to determine the phase of crystalline materials through investigation of atomic and molecular structure. In powder XRD, a

finely ground powdered sample is exposed to a beam of monochromatic X-rays that interact with the atoms in the sample's crystal lattice. This interaction causes X-rays to scatter in different directions, producing a diffraction pattern that is collected and analyzed. By measuring the angles and intensities of diffracted X-rays, d-spacings are evaluated (i.e. the distance between planes of atoms) according to Bragg's Law (see section 2.5.3). Phase identification can be performed by comparing and matching Xray diffraction patterns obtained from the sample of interest to patterns in a reference database.

I used bulk powder XRD for preliminary identification of phase in modern and fossil giant clam shells, with the expectation that modern shells would be 100% aragonite, while fossil *Tridacna* shells may show some transformation to calcite. To achieve a fine-grained powder from slices of shells taken adjacent to thin sections, samples were ground by hand in an agate mortar and pestle. Mineralogical composition was analyzed using a Philips PW 1820 diffractometer located at the School of Earth and Environmental Sciences, Cardiff, employing Cu Kα radiation (λ = 1.54056 Å) with an X-ray tube voltage of 35 kV and a current of 40 mA. Each sample ran for 27 min, with a step size of 0.020°, time per step of 0.5 sec and scan speed 0.040°. Following analysis, the Rietveld refinement method (Rietveld 1969) was conducted using Profex 5.0.2 software (Doebelin and Kleeberg 2015). This method allows for the precise determination of the crystal structure and phase composition of the samples by fitting the observed diffraction pattern with a calculated pattern generated from a structural model (Rietveld 1969). This minimizes the difference between the observed and calculated patterns.

2.8 Raman spectroscopy

Raman spectroscopy is a spectroscopic technique used to study vibrational, rotational, and other low-frequency modes in a material. It enables non-destructive determination of shell preservation by the scattering of monochromatic light by a sample from a laser source, which leads to shifts in energy due to the vibrational modes of the sample's molecules. These energy shifts, known as Raman shifts, provide information about the chemical composition, molecular structure, and bonding within the sample.

A Raman spectrum consists of intensity peaks corresponding to specific vibrational modes, uniquely characteristic of the sample, providing insight into its mineral phase. It may be used with, or instead of, XRD, a method more widely utilized to test the preservation of giant shell material (Belda et al. 1993a, b; Watanabe et al. 2004; Asami et al. 2015; Ayling et al. 2015; Warter et al. 2015; Arias-Ruiz et al. 2017; Yan et al. 2020). Raman Spectroscopy is generally advantageous to XRD due to its higher sensitivity, enabling micrometre-scale details to be extracted with very small amounts of sample (Rondahl et al. 2018).

In this study, preservation of dead collected and fossil shells were investigated with Raman spectroscopic analysis, carried out on a Renishaw in Via Raman microscopy with green argon laser (λ = 540) at the School of Chemistry, Cardiff University. Raman spectra were acquired at specific points of interest across the same thin sections as used from light microscopy, SEM and EBSD. For each spectrum, 20 accumulations were integrated with 5 s exposure time at 10% laser power. Focus was placed on the calcium carbonate “lattice mode” (100-400 cm^{-1}) and the in-plane bend (v_4) internal mode (700–720 cm^{-1}), effective for the discrimination between aragonite and calcite (e.g. Urmos et al. 1991; Parker et al. 2010). In particular, the lattice mode was investigated for low frequency measurements at 150 and 210 cm^{-1} and strongest v1 peaks near 1085 cm^{-1}, which indicate aragonite opposed to calcite (Urmos et al. 1991; Decarlo 2018) (Figure 2.30).

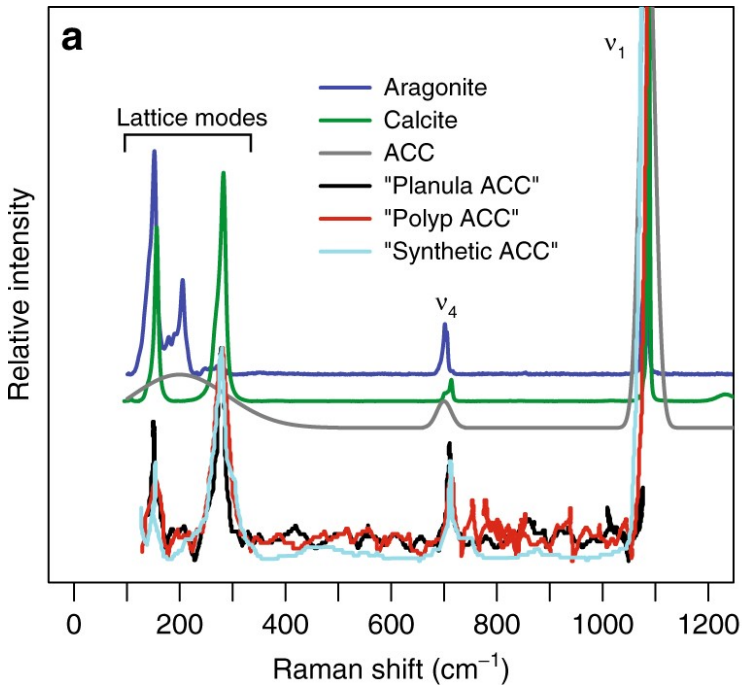

Figure 2.30. **Relative intensity versus Raman shift (cm^{-1}) of typical Raman spectra of calcium carbonate ($CaCO_3$) minerals (taken from: Decarlo 2018). A broad spectrum from 0 to 1300 cm^{-1} is shown, including both lattice and internal modes. Reference Raman spectra of aragonite in blue and calcite in green.**

2.9 Loss on ignition (LOI)

LOI is a technique that can quantify the amount of volatile organic components present in a material. In the giant clam shells in this study, bulk LOI measurements were used to identify the amount of organic components between modern and fossil samples. During LOI, the organic matter within shells combusts and volatilizes, leaving behind inorganic $CaCO_3$ residue, constituting the mineral portion of the shell. By measuring the change in mass before and after ignition, the amount of organic material present in the sample can be calculated.

To conduct bulk LOI, shell slices taken from areas adjacent to where thin sections were prepared were manually ground into a fine powder using an agate mortar and pestle. A total of 5g of powdered shell material representing the height of the IL was dried at 105°C for 1 hour to remove water contents (e.g. Santisteban et al. 2004). Samples were then inserted into a Vecstar chamber furnace at 360°C ± 30°C for 1 hour for decomposition of organic macromolecules (e.g. Neves and Mano 2005). The mass of samples was measured on scientific high-precision scales before and after both

temperature treatments and three replicates for each sample were taken and data averaged for each shell (results in chapter 6).

2.10 Environmental data

2.10.1 *In situ*

In situ environmental data from the six diverse reef sites in Darvel Bay (Figure 2.5) was collected by the Reefugia Project between April 2019 and January 2022. In the Triangle and Baik key reefs where giant clams were collected alive, sea surface temperature (SST) and lux data were collected every 10 min using HOBO temperature and light loggers deployed at 5 and 10 m. 5 m data was used for Triangle due to shallower collection depths and 10 m used for Baik (section 2.4). In addition, *in situ* measurements of water clarity at every site was estimated with a Orion^{TM} Aquafast Turbidity Meter (Nephelometric Turbidity Units: NTU) and Secchi disc in the dry season of 2019. Unfortunately, prolonged drought experienced throughout southeast Sabah during early 2019 (Payus et al. 2020) meant that measurements were atypically low. Therefore, turbidity is defined herein based on the amount of suspended particles using the diffuse attenuation coefficient of spectral irradiance at 490 nm wavelength K_d(490) from remote sensed data (see section 2.10.2). The following water nutrient concentration measurements were also recorded once in April and October 2019: total suspended solids (TSS), total dissolved solids (TDS), total volatile solids (TVS), total volatile dissolved solids (TVDS) and total solids (TS-DU) (dissolved and undissolved). *In situ* tidal data were sourced from the Sea Level Monitoring Station Facility at Lahad Datu (station ms006).

2.10.2 Remote sensed data

In situ measurements were supplemented with the extraction of remote sensing datasets. Cloud cover, salinity, chlorophyll-*a*, K_d(490), rainfall and additional SST data for 2018–2019 before HOBO loggers were deployed were sourced from the Google Earth Engine (GEE) code editor or the National Oceanic and Atmospheric Administration (NOAA) database (Table 2.3) and used to compliment *in situ* data.

***Table 2.3. In situ* (logger depths 5 for Triangle and 10 m for Baik) and remote sensed derived products used in this study. BA = Baik; TR = Triangle; BL = Blue Lagoon; TH = THalu; MI = Misan; SA = Sakar; SEM = Sempora region. GEE = Google Earth Engine; NOAA = National Oceanic and Atmospheric Administration database. NOAA CDR PATMOSX = Cloud Properties, Reflectance, and Brightness Temperatures, Version 5.3; HYCOM = Hybrid Coordinate Ocean Model, Water Temperature and Salinity; MODIS Aqua = Ocean Colour SMI: Standard Mapped Image MODIS Aqua; VIIRS = NOAA Visible Infrared Imaging Radiometer Suite; CHIRPS = Climate Hazards Group InfraRed Precipitation with Station data.**

Environmental Factor	Site	Data Period	Data Type	Source	Spatial Resolution	Temporal Resolution
SST	BA, TR	2019–2020	*In situ*	This study	NA, HOBO logger at site	10 min
Lux	BA, TR	2019–2020	*In situ*	This study	NA, HOBO logger at site	10 min
Cloud Cover	BA, TR	2018–2020	Remote sense	GEE; NOAA CDR PATMOSX	0.08° x 0.08°	Daily
Salinity	BA, TR	2018–2020	Remote sense	GEE; HYCOM	0.08° x 0.08°	Daily
SST	BA, TR	2018–2019	Remote sense	GEE; MODIS Aqua	0.05° x 0.05°	Daily
K_d(490)	BA, TR, BL, TH, MI, SA, SEM	2018–2020	Remote sense	NOAA; VIIRS	0.05° x 0.05°	Daily
Chlorophyll-*a*	BA, TR	2018–2020	Remote sense	NOAA; VIIRS	0.05° x 0.05°	Daily
Rainfall	BA, TR	2018–2020	Remote sense	NOAA; CHIRPS	0.05° x 0.05°	Daily

2.10.2.1 Remote sensed validation

To validate satellite data, a comparison between *in situ* and remote sensed data was made. This was only possible with SST for 2019–2020 because this was the only variable which had both remote sensed and *in situ* data with overlapping time periods. The Pearson correlation coefficient was used to measure the degree of association between monthly averaged *in situ* HOBO and MODIS Aqua data for the key reef sites Triangle and Baik (Figure 2.31). The correlation coefficients of 0.83 for Triangle and 0.86 for Baik indicate a strong positive relationship between the HOBO logger and MODIS SST measurements. However, it is noteworthy that although trends are similar between both datasets and capture seasonal variability well, MODIS SST is consistently higher than the HOBO data (mean offset of 0.9°C).

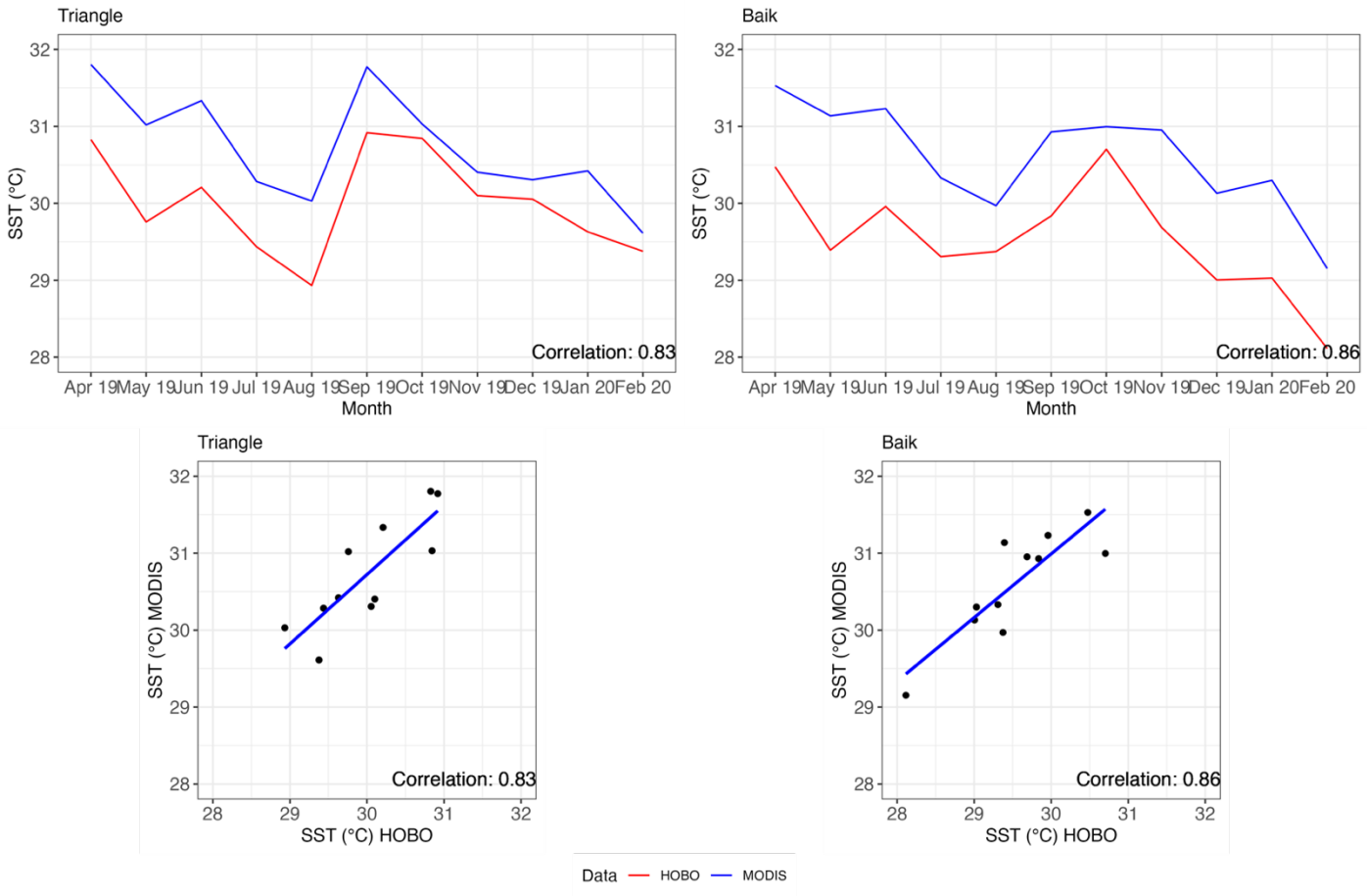

Figure 2.31. **Line graphs of SST from *in situ* HOBO loggers (red line) and MODIS remote sensed (blue line) data from key reef sites Triangle (top left) and Baik (top right). Respective linear regression lines represent the degree of association between MODIS and HOBO data. Pearson correlation coefficient values (correlation) show high association between MODIS and HOBO data.**

2.10.3 Characterization of environment

2.10.3.1 Turbidity

I characterized each site based on turbidity using $K_d(490)$ (Table 2.4). $K_d(490)$ is a measurement that quantifies how much light at a wavelength of 490 nm is attenuated or scattered as it penetrates through the water. This choice is supported by Loiola et al. (2019) and Hennige et al. (2008), who used remote sensed $K_d(490)$ values as robust indicators of differences in turbidity on coral reefs in the Abrolhos Archipelago off Brazil and Indonesia, respectively. Hennige et al. (2008) highlighted that recorded variation in $K_d(490)$ between reef sites was in line with measurements of turbidity along a natural environmental gradient. In this study, I define low turbidity as mean annual $K_d(490) < 0.2$ m^{-1} and the turbidity threshold for more turbid waters in Darvel Bay as mean annual $K_d(490) > 0.2$ m^{-1} (e.g. Zhang and Fell 2007; Yu et al. 2016). This parameter was interpreted alongside the *in situ* HOBO measurements of lux and total solids content, as well as with remote sensed chlorophyll-*a* concentrations, often shown to be controlled by river runoff in the wet season (Chen et al. 2007).

To further elucidate the implications of my methodology in characterizing turbidity, it is essential to span out and examine global variations in $K_d(490)$ values. A study by Shi and Wang (2010) highlights the range of turbidity gradients across the world's oceans and coastal regions: a 'clear' water, with $K_d(490)$ values < 0.1 m^{-1} dominates roughly 95.67% of the global ocean. Low to moderate turbid waters, with $K_d(490)$ values between 0.1 to 0.3 m^{-1} cover around 3.59% of the ocean, split between 5.12% in summer and 3.07% in winter. Extremely high turbid waters, exceeding 0.3 m^{-1}, are primarily found in coastal areas, river estuaries, and inland lakes, constituting about 0.74% of the global ocean and comprising 8% to 12% of the total continental shelf area. The Amazon River Estuary stands out as the most turbid region globally, with a mean $K_d(490)$ value of approximately 5 m^{-1}.

Table 2.4. **Coral reef sampling sites surveyed in Darvel Bay (East Sabah, Malaysia) and mean annual K_d(490) (2019–2020).**

Site	Annual mean K_d(490)
Baik	0.09
Triangle	0.30
Blue Lagoon	0.08
THalu	0.13
Misan	0.10
Sakar	0.39
Semporna region	0.06

2.10.3.2 Monthly analysis of environmental parameters at Baik and Triangle

To characterise the environment of key reef sites Baik and Triangle, I used monthly environmental parameters. In Figure 2.32, I show an overview of monthly averaged environmental data for Baik and Triangle over a two-year period. I work back from the last *Tridacna* collection date at the end of February 2020. Investigation for one year between 2019–2020 showed mean SST at Baik and Triangle was 29.53°C and 30.01°C, respectively. Throughout the year, monthly SST varied between 28.11°C and 30.47°C at Baik and 28.93°C and 30.91°C at Triangle, peaking at the end of the dry season and generally dropping towards the end of the wet season (Figure 2.32a). Light intensity (lux) corresponded with SST in Baik and showed a peak in October, varying between monthly lux of 7122.50 and 16444.75 throughout the year, compared to 7285.83 lux and 13705.91 lux for Triangle (Figure 2.32b). However, it is important to consider that we could not retrieve data for lux between August and October for Triangle, as the HOBO logger was lost and not reinstalled until November. Precipitation showed a bimodal distribution pattern, with maximum rainfall towards the beginning of the dry- and mid-wet season in both sites (Figure 2.32f). Chlorophyll-*a* (Figure 2.32d) generally corresponded to K_d(490) (Figure 2.32c) in both sites, but mean monthly values were higher at Triangle (4.19 mg m^{-3}, 0.51 m^{-1}, respectively) than Baik (1.06 mg m^{-3}, 0.14 m^{-1}, respectively). Cloud cover was similar between sites (Figure 2.32e), peaking in June and dropping during the late wet season in March. Although patterns were similar in 2018–2019, prolonged drought in early 2019 revealed atypically low

cloud cover (51%, both sites) and rainfall (62.98 mm Baik; 43.35 mm Triangle) in February 2019. Sea surface salinity (SSS) showed a partial inverse behaviour with rainfall (Figure 2.33) but was only investigated for Darvel Bay and not for individual sites because information was not available for the Triangle reef.

To summarise key differences between both reef sites, Triangle has overall warmer SST's, less variability in lux, and notably higher turbidity and chlorophyll-*a*. Baik has marginally lower SST's, higher variability in lux and lower turbidity and chlorophyll-*a* year-round.

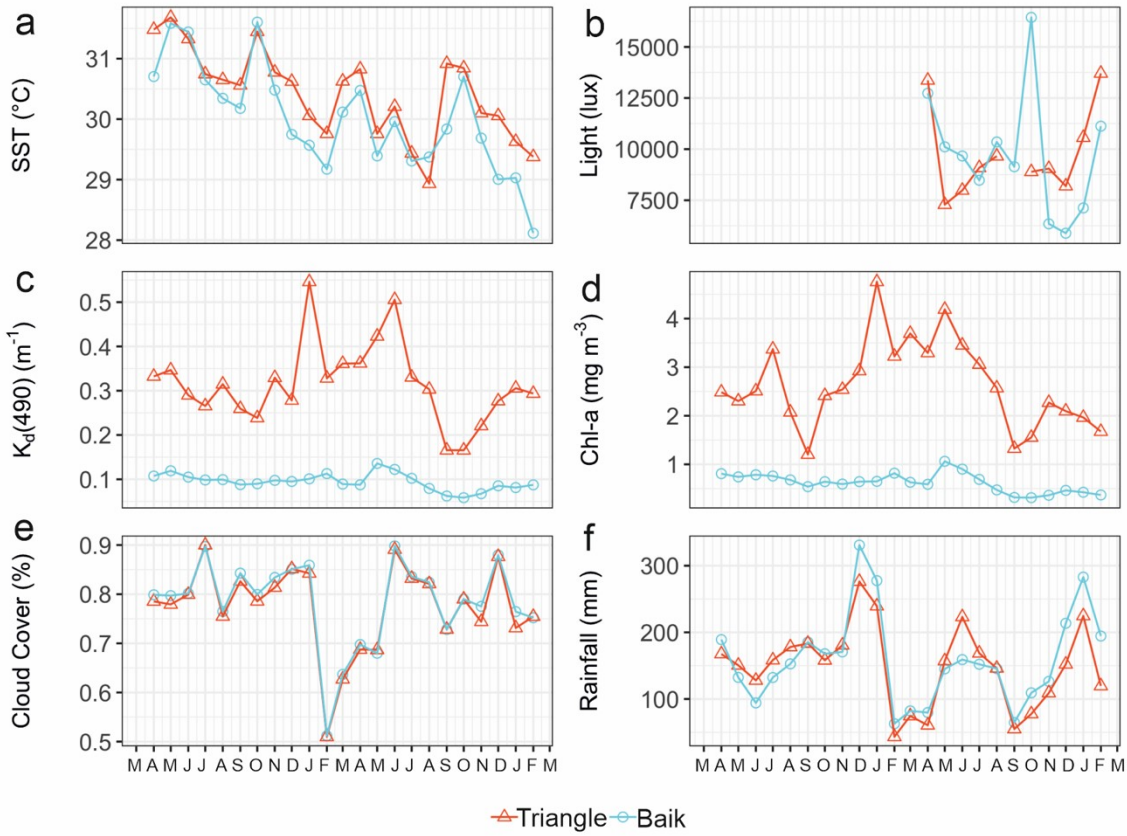

Figure 2.32. **(a) Monthly average sea surface temperature (SST), (b) light (lux), (c) K_d(490) (m^{-1}), (d) chlorophyll-*a* (mg m^{-3}), (e) cloud cover (%) and (f) rainfall (mm) from Baik and Triangle reefs in Darvel Bay for 2018–2020. Environmental data shown relates to last year of growth (LYOG) for samples collected live in April 2019 and February 2020.**

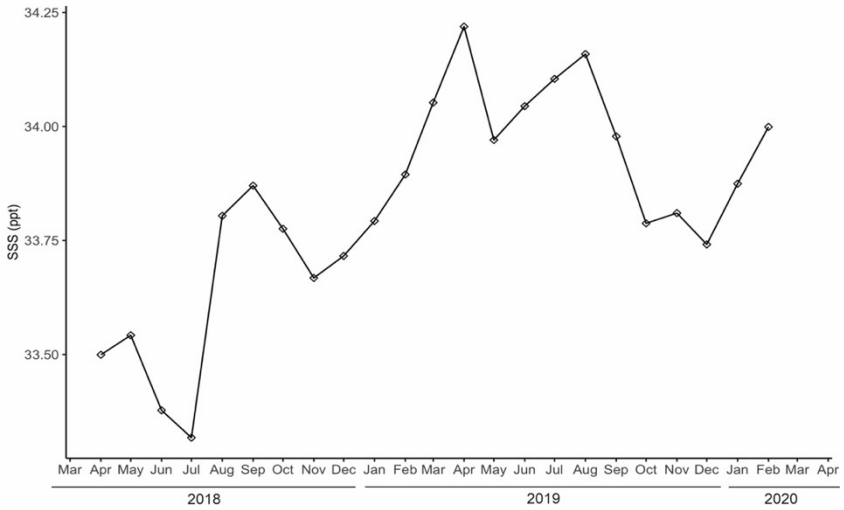

Figure 2.33. **Monthly variation of sea surface salinity (SSS) in Darvel Bay for 2018–2020. Data are for period of last year of growth (LYOG) for 2019 and 2020 live collected shells.**

2.10.3.3 High resolution analysis of sea surface temperature and lux at Baik and Triangle

In both Triangle and Baik, I also analysed representative 10-minute resolution HOBO data from November 2019 (early wet season) and May 2019 (early dry season). Both sites displayed daily cycles in SST and lux, with lux cycles more distinct due to the day/night cycle. During the wet season (Figure 2.34), mean SST was relatively similar between the two locations, although Triangle exhibited slightly higher temperatures (30.08°C) and a narrower range (1.57°C) compared to Baik (mean 29.64°C; range 1.91°C). Similarly, mean lux was comparable between sites, with slightly higher lux at Triangle (7285.83) compared to Baik (6344.90). In the dry season (Figure 2.35), mean SST was 29.35°C for Baik and 29.76°C for Triangle, with mean lux values of 10111.74 and 9048.06, respectively. The range of SST was similar for Baik (2.37°C) and Triangle (2.20°C). However, range of lux was notably higher in Triangle (21097.31) during the dry season compared to Baik (14010.28).

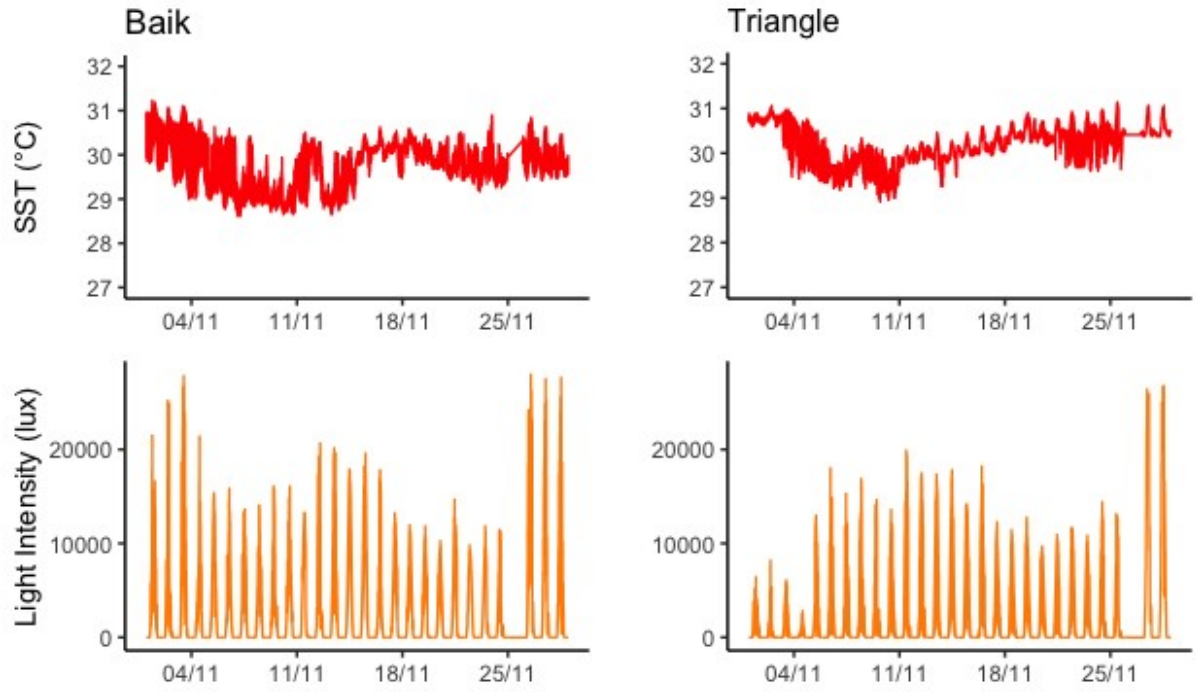

Figure 2.34. **10-min sea surface temperature (SST) and light (lux) HOBO data from Baik (left-hand column) and Triangle (right-hand column) key reef sites in Darvel Bay for November 2019, representative of the early wet season.**

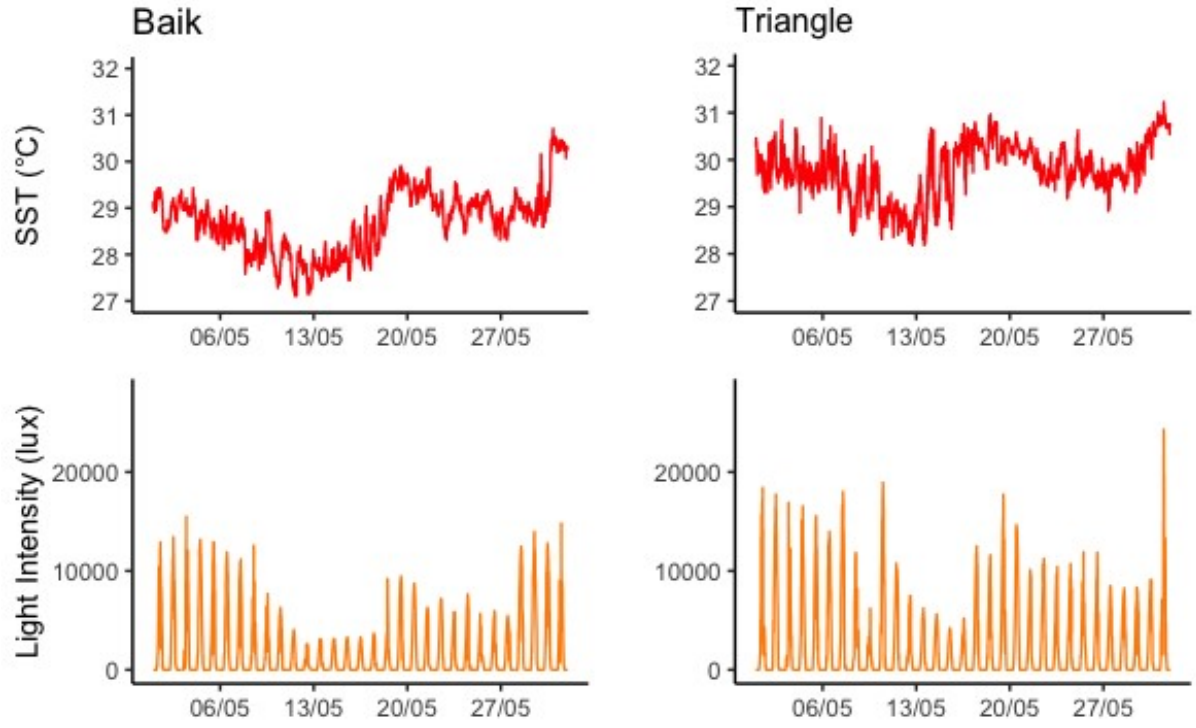

Figure 2.35. **10-min sea surface temperature (SST) and light (lux) HOBO data from Baik (left-hand column) and Triangle (right-hand column) key reef sites in Darvel Bay for May 2019, representative of the early dry season.**

2.10.3.4 Tidal data at Lahad Datu

I used the *in situ* tidal data obtained from the Sea Level Monitoring Facility to investigate mean tide and tidal range within Darvel Bay. Lahad Datu (station ms006) served as the nearest available tidal monitoring station to our designated reef sites, enabling the extraction of one year's worth of tidal data spanning from 2020 to 2021 (Figure 2.36), despite some gaps in the database. Raw data was extracted as hourly readings taken with a pressure sensor and mean (m) tide in Figure 2.36 refers to the averaging of hourly readings over a 24-hour period, while max (m) and min (m) refer to the maximum and minimum tidal height for one day respectively. Analysis revealed daily maximum tide of 3.07 meters and daily minimum tide of 1.47 meters. These findings indicate that Darvel Bay is best classified as mesotidal, typified by coastal areas where the tide typically ranges between 2 to 4 meters (e.g. Santodomingo et al. 2021).

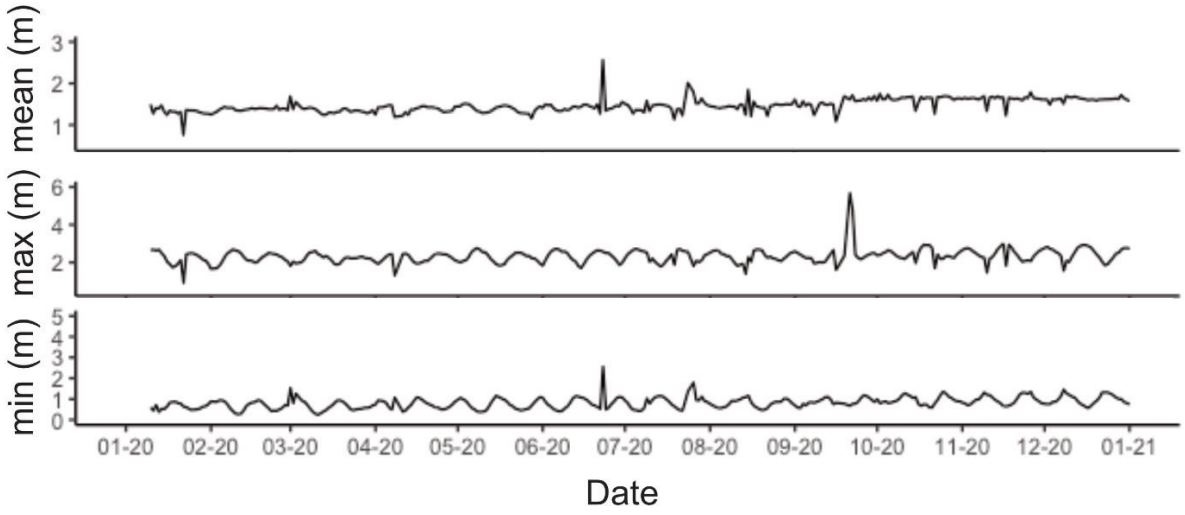

Figure 2.36. **Tidal data for Lahad Datu (station ms006), showing mean daily tidal height (m), maximum tide (m) and minimum tide (m) between 2020 and 2021.**

2.10.3.5. Total solids content

Between Baik and Triangle, variation in total suspended solids (TSS) concentrations were notably more pronounced after the wet season in April 2019 compared to after the dry season in October 2019 (Table 2.5), suggesting greater divergence among sites during and after periods of heightened precipitation. There is no data available for measurements of total volatile dissolved solids (TVDS) and total solids (dissolved

and undissolved) (TSDU) in April 2019, but there was similarity in both TVDS and TSDU at Baik and Triangle in October 2019 after the dry season. The largest disparity lies in total volatile solids (TVS) in April 2019, where measurements were 45.35 mg/L in Triangle and 5.06 mg/L in Baik, which may reflect high run-off from the Tingkayu river near Triangle after the wet season. These observations prompt the hypothesis that environmental shifts during and after the wet season may exert more pronounced effects on growth and microstructure, potentially altering biomineralization pathways, compared to the dry season. However, it's crucial to acknowledge the limitations of relying solely on single measurements per season, highlighting the need for complementary data analysis.

Table 2.5. **Total solids content in milligrams per litre (mg/L) for key reef sites Baik and Triangle. TSS = total suspended solids; TDS = total dissolved solids; TVS = total volatile solids; TVDS = total volatile dissolved solids; TS = total solids (dissolved and undissolved). Largest seasonal difference between reefs is highlighted in grey and occurs for TVS in April 2019, after the wet season.**

Parameter	Date	Site	Content
TSS	April 2019	Triangle	14.87
TSS	October 2019	Triangle	0.45
TSS	April 2019	Baik	8.73
TSS	October 2019	Baik	0.42
TDS	April 2019	Triangle	N/A
TDS	October 2019	Triangle	37.22
TDS	April 2019	Baik	N/A
TDS	October 2019	Baik	37.03
TVS	April 2019	Triangle	45.35
TVS	October 2019	Triangle	11.12
TVS	April 2019	Baik	5.06
TVS	October 2019	Baik	11.16
TVDS	April 2019	Triangle	N/A
TVDS	October 2019	Triangle	6.15
TVDS	April 2019	Baik	N/A
TVDS	October 2019	Baik	5.98
TS-DU	April 2019	Triangle	N/A
TS-DU	October 2019	Triangle	43.20
TS-DU	April 2019	Baik	N/A
TS-DU	October 2019	Baik	43.13

2.11 Data analysis

The majority of data analysis throughout this thesis was carried out in RStudio Version 4.0.3 (R Core Team 2020) or MATLAB R2022b (The MathWorks Inc. 2022), unless otherwise specified. Detailed methods of data analysis are included in each chapter. R or MATLAB scripts corresponding to specific chapters are available in appendices A–D.

3. Growth responses of giant clam shells to turbid reefs

3.1 Abstract

Increasing evidence suggests that nearshore turbid coral reefs may mitigate bleaching of reef building calcifiers and play a critical role in the future of marine biodiversity in coastal areas. However, biomineralization processes on turbid reefs are relatively understudied compared to clear water counterparts and most published work focuses on corals. Here, I investigate how the mixotrophic giant clam *Tridacna squamosa*, a bivalve with ecological, cultural and economic significance, grows across a mosaic of low turbid to high turbid reefs in the Coral Triangle. I construct growth chronologies from live and dead collected shells by measuring daily growth bands with petrography and scanning electron microscopy (SEM) to gain insight into growth rate on daily, seasonal and annual scales. I find annual growth is not significantly different across a turbidity gradient when scaled to ontogeny, while seasonal growth highly varies. K_d(490) (a measurement positively correlated with turbidity) and chlorophyll-*a* are likely important factors driving seasonal growth on a turbid reef near a river, compared to sea surface temperature (SST), cloud cover and rainfall on a low turbid reef. On a daily scale, I investigate growth band microstructure and spectral characteristics of chronologies, finding a relationship between tidal range and daily bands. Overall, results indicate that light-enhanced calcification may be most important in the low turbid reef, compared to heterotrophic feeding in the turbid reef. The trophic plasticity of *T. squamosa* may allow for its sustained growth in marginal conditions, supporting evidence that these habitats serve as important conservation hotspots for diverse reef building taxa.

3.2 Introduction

Coral reefs deliver critical ecosystem goods and services to millions of people worldwide but are under threat due to multiple anthropogenic stressors acting at a local to global level (Hughes et al. 2017). Recently, turbid nearshore reefs have shown resilience in the face of increasing ocean warming and have been hypothesized to be important ecological refugia (Cacciapaglia and van Woesik 2016; Zweifler et al. 2021). However, aside from corals (e.g. Anthony 2000; Fox et al. 2018), little is understood about the capabilities of other key reef building organisms to calcify in turbid reefs. A robust understanding of different organisms and functional groups is required because individual responses result in ecosystem-wide effects (Bainbridge et al. 2018).

Giant clams are large and long-lived symbiont bearing bivalves, distributed throughout the Indo-Pacific (Rosewater 1965). They fulfil critical roles in tropical reef communities due to their contributions to the structure, complexity and ecology of reefs (Neo et al. 2015). Their rapid (daily band widths of 5–60 µm) and continuous shell growth (Ma et al. 2020) has long been attributed to the photosynthetic rate of their endosymbiotic zooxanthellae (Klumpp and Griffiths 1994). Therefore, changes in growth are expected to be sensitive to external environmental conditions that directly or indirectly alter light exposure (Sano et al. 2012). In some species, translocated photosynthates from endosymbionts satisfy all daily metabolic energy requirements (Jantzen et al. 2008). However, tridacnids are mixotrophs and like many bivalves, take up particulate organic matter (POM) (Klumpp et al. 1992) through filter-feeding. The balance of autotrophy and heterotrophy to total energy requirements changes depending on inter- and intraspecific differences in size, photosynthetic potential (Jantzen et al. 2008), and ontogeny (Klumpp and Griffiths 1994). Compared to most tridacnids, *Tridacna squamosa* (fluted giant clam) is a 'true mixotrophic species' due to its reduced photosynthetic activity, showing a stronger reliance on a heterotrophic strategy to satisfy its metabolic needs within its range (Tedengren et al. 2000; Jantzen et al. 2008). Indeed, the survival of *T. squamosa* may be comparable or even higher under turbidity relative to clearer water (Guest et al. 2008; Yong et al. 2022). However, how the growth and biomineralization processes of *T. squamosa* vary between turbid and clear waters and external mechanisms controlling these processes are not understood. Increasing

understanding of how giant clams respond to local stressors is required for conservation strategies under continued environmental change (Watson and Neo 2021).

Petrographic microscopy, scanning electron microscopy (SEM) and laser scanning confocal microscopy (LSCM) methods have revealed daily growth banding in both the inner- (Watanabe et al. 2004; Aubert et al. 2009; Elliot et al. 2009; Schwartzman et al. 2011; Sano et al. 2012; Ayling et al. 2015; Hori et al. 2015; Warter et al. 2015; Arias-Ruiz et al. 2017; Gannon et al. 2017; Warter and Müller 2017; Ma et al. 2020; Yan et al. 2020; Yan et al. 2021; Zhao et al. 2021; Liu et al. 2022; Zhao et al. 2023) and outer layers of giant clam shells (Duprey et al. 2015; Komogoe et al. 2018; Killam et al. 2021). Shell growth chronologies constructed from these daily bands, or increments, are important alongside powerful geochemical techniques (e.g. LA-ICPMS) in reconstructing highly time-resolved profiles of water temperature (e.g. Arias-Ruis et al. 2017), productivity (e.g. Elliot et al. 2009), paleoweather (Komagoe et al. 2018; Yan et al. 2020) and diurnal light cycles (Sano et al. 2012), among others. The refinement of identification of growth bands is important in different environments and ensures accuracy of time-series analysis (Warter and Müller 2017). Yet, the environmental controls on their variation are little understood and the potential of tridacnid shell growth chronologies in (paleo)environmental reconstruction on their own remains largely untapped (Zhao et al. 2021).

In this work, I investigate the growth rate of *T. squamosa* in turbid and clear reefs on annual, seasonal and daily scales. I focus on measuring daily band widths and investigate their microstructure in shells collected alive from two contrasting reef sites in eastern Sabah—a high turbid reef near a river outlet (Triangle) and a low turbid reef (Baik). To disentangle potential external environmental drivers of growth between the high turbid and low turbid reef, I compare shell growth chronologies and their spectral characteristics with *in situ* and remote sensing environmental data. I further investigate growth across a gradient of turbidity by exploring growth trends in shells collected dead at four additional reef sites, characterized by different turbidities.

3.3 Methods Summary

I carried out an in-depth comparison of daily growth rate for four *T. squamosa* shells collected alive at two key reef sites in Darvel Bay—Baik (low turbid) and Triangle (high turbid) (SS_BAIK, NS207; SS_CT, ZW156, respectively) (Table 2.2). An additional seven shells collected dead from the seafloor at Baik (SS01B_BT), Triangle (SS03B_CT, SS02B_CT) and four additional locations across a gradient of turbidity ((Sakar (SS02A_SN); Misan (SS01A_SM); THalu (SS01A_TH); Blue Lagoon (SS01ABH)) were also investigated. To broaden the comparison to a wider region, another two shells from Semporna reefs (SEM_A, SEM_B, with unknown collection status) situated south of Darvel Bay were further studied.

3.3.1 Diagenetic screening

3.3.1.1 SEM

Prior to analysis, the nine dead collected/unknown collection status shells were investigated for diagenesis using scanning electron microscopy (SEM). Using SEM, I scanned across the inner shell layer (IL) of shell surfaces (etched 0.5 % HCl for 15 sec) where counting of growth bands took place and investigated visual characteristics that indicate deviation from original aragonite arrangements (Taylor et al. 1969). The following characteristics that may indicate alteration were searched for: irregular shaped crystals with irregular intercrystalline boundaries, coarsening of crystal size (Hou et al. 2020); fusion of platelets (Hou et al. 2020); lack of consistency in size of lamellae (supplemental in Killam et al. 2021).

3.3.1.2 Raman spectroscopy

Preservation of dead collected shells was further investigated using Raman spectroscopic analysis. Raman spectra were acquired for three areas across shells in the same position as acquired images for growth chronologies, corresponding to the edge of the inner layer, representing the region of last growth, the middle inner layer, representing the region of mid to first growth and the outer layer. For each spectrum, 20 accumulations were integrated with 5 s exposure time at 10% laser power. Focus

was placed on the calcium carbonate “lattice mode” (100-400 cm^{-1}) and the in-plane bend (v_4) internal mode (700–720 cm^{-1}), effective for discrimination of aragonite and calcite (e.g. Urmos et al. 1991; Parker et al. 2010).

3.3.2 Environmental data

I used *in situ* and satellite remote sensed data to characterize environmental factors for the last year of growth (LYOG) in shells collected alive from Baik and Triangle in 2019 and 2020. Sea surface temperature (SST) and light intensity (lux) were characterized *in situ*. Cloud cover, salinity, chlorophyll-*a*, K_d(490), rainfall and additional SST data for 2018–2019 were extracted from Google Earth Engine (GEE) or the National Oceanic and Atmospheric Administration (NOAA) database. A full overview of environmental data analysis is given in chapter 2.

3.3.3 Construction of mean shell growth chronologies

Shell growth chronologies were assembled from the daily bands of thirteen *T. squamosa* shells (i.e. four collected alive and nine collected dead/unknown collection status) to determine age and daily growth rate. I used a mixed-method approach to image growth bands of thin sections with light microscopy and SEM at the School of Earth and Environmental Sciences, Cardiff University (refer to chapter 2). Images were obtained along the entire height of the inner layer and final mean shell growth chronologies were compiled from multiple counts that met certain criteria, which was based on how many bands could be defined and their clarity. Overall visibility across the IL of each shell obtained with SEM and petrography were accessed and rated from very low (VL) (> 30% of increments clear), low (L) (> 60% of increments clear), medium (M) (> 75% of increments clear), high (H) (> 90% of increments clear) or very high (VH) (> 95% of increments clear) (Table 3.1). To compile final mean shell growth chronologies, combined chronologies that were rated L or higher were fitted with locally weighted least squares regression (loess line). Mean lifespan and growth (mm/yr) were calculated from final chronologies (Table 3.2).

For some counts, the autoplace tool was used in Coorecorder 9.8 (Cybis) (Maxwell and Larsson 2021), which automatically places points at growth line borders (denoted as ‘automated’ or ‘A’ as opposed to ‘manual’ or ‘M’ in Table 3.1). Although other studies have successfully determined growth banding in giant clams using Coorecorder (Liu et al. 2022), due to the highly topographic microstructure of most samples herein, this tool was deemed unreliable in most cases and created large offsets. For this reason, I only incorporated these measurements into final mean chronologies in samples whose daily growth lines were highly identifiable across the whole IL of the shell.

3.3.4 Data analysis

The R code for data analysis carried out in this chapter is available from the Mendeley Data Repository given in Appendix A. I used a dimensionless standardized growth index (SGI) to control for ontogenetic decelerated growth rates throughout lifespan (e.g. Jones et al. 1986). Widely used in studies of bivalves (e.g. Butler et al. 2013), including giant clams (Zhao et al. 2021), the SGI is an estimation of how growth deviates from the average growth trend (Schöne et al. 2005), represented by the equation:

$$SGI = \frac{\frac{measured}{predicted} - \bar{x}}{\sigma}$$

where ‘measured’ is the growth rate of daily bands, ‘predicted’ is the moving average (365 days) of daily bands, $\bar{x}$ is the mean and σ is the standard deviation of the set of growth bands for each sample.

I applied the SGI to my data as ages of samples likely covered life stages from juvenile to adult. I investigated and compared SGI values on daily, seasonal and annual scales.

To examine differences in annual growth, a one-way analysis of variance (ANOVA) and Tukey’s post-hoc test were performed between shells pooled into the seven different reef sites. Assumptions of ANOVA were checked for normality and homogeneity of variance using Shapiro–Wilk's test, QQ (quantile–quantile) plots of standardized residuals and Bartlett's test.

On a monthly scale, SGI values were plotted with monthly averaged environmental data for the LYOG in the shells collected alive at Baik and Triangle. These data were explored as added-variable (AV) plots because they control for the variability of other explanatory variables when plotting the effect of *x* on *y*. They therefore more accurately show relationships because other variables in the model are adjusted for (Draper and Smith 1966). Principal component analysis (PCA) was also performed on environmental data for time periods corresponding to LYOG to explore annual and seasonal relationships, allowing the number of variables under investigation to be reduced.

On a daily scale, I used spectral analysis to investigate daily growth with tidal cycles in frequency space in Baik and Triangle because tidal patterns are thought to be expressed in the daily growth bands of *T. squamosa* (e.g. Evans 1972). Multi-taper method spectral analysis (MTM) (Thompson 1982) was carried out in K-Spectra v.3.9.3 (SpectraWorks) to extract dominant frequencies. Cycles were analysed with significance of spectral peaks at 95–99% compared to red noise background.

Table 3.1. **Raw count data of individual shell growth chronologies for thirteen *Tridacna squamosa*. Shell sample name, reef site, collection status, counting method, technique used to acquire images, image source, estimated lifespan, daily growth statistics, growth band visibility are shown. BA = Baik; TR = Triangle; BL = Blue Lagoon; TH = THalu; MI = Misan; SA = Sakar; SEM = Semporna region. L = live collected shells; D = dead collected shells; U = unknown collection status of shells. PM = primary person manual, measurement tool on Image J; SM = secondary person manual, measurement tool on Image J; PA = primary person automated, autoplace tool on CooRecorder. R = reflected light; T = transmitted light, SE = secondary electron image. LM = light microscopy; SEM = scanning electron microscopy. VH = very high banding visibility; H = high banding visibility; M = medium banding visibility; L = low banding visibility; VL = very low banding visibility.**

Sample	Site	Collection	Counting method	Technique	Image source	Estimated days alive	Mean daily growth (µm)	Standard deviation	Standard error	Range (µm)	Visibility
SS_CT	TR	L 2019	PM	LM	R	1144	14.28	3.78	0.11	21.92	H
SS_CT	TR	L 2019	PA	LM	R	1336	13.88	4.16	0.11	28.00	H
SS_CT	TR	L 2019	PM	SEM	SE	1127	12.86	3.02	0.09	20.03	H
SS_CT	TR	L 2019	SM	LM	R	1107	15.91	4.44	0.13	27.62	H
BB_BAIK	BA	L 2019	PM	LM	R	1186	15.79	6.03	0.18	38.50	M
BB_BAIK	BA	L 2019	PA	LM	R	1081	15.46	6.09	0.18	38.50	M
BB_BAIK	BA	L 2019	PM	SEM	SE	1961	11.86	5.85	0.13	37.25	M
BB_BAIK	BA	L 2019	SM	LM	R	1141	16.70	7.63	0.23	51.79	M
ZW156	TR	L 2020	PM	LM	R	689	21.79	6.37	0.26	43.52	VH
ZW156	TR	L 2020	PA	LM	R	662	25.02	10.21	0.40	49.58	VH
ZW156	TR	L 2020	PM	SEM	SE	684	20.00	7.84	0.30	37.04	VH
ZW156	TR	L 2020	SM	LM	R	681	21.72	8.85	0.34	42.06	VH
NS207	BA	L 2020	PM	LM	R	2508	12.08	5.20	0.10	32.70	L
NS207	BA	L 2020	PM	SEM	SE	2702	9.94	4.46	0.08	21.39	L
NS207	BA	L 2020	SM	LM	R	2441	12.89	5.93	0.12	35.36	L
SS01A_BH	BL	D	PM	LM	T	1093	15.35	7.12	0.21	34.57	H
SS01A_BH	BL	D	PA	LM	T	1055	16.99	7.27	0.22	45.00	H
SS01A_BH	BL	D	PM	SEM	SE	1649	15.68	6.15	0.15	34.72	VL
SS01B_BT	BA	D	PM	LM	T	1899	11.93	3.53	0.12	26.90	L

SS01B_BT	BA	D	PA	LM	T	1518	12.90	4.22	0.11	29.00	L
SS01B_BT	BA	D	PM	SEM	SE	2016	11.75	3.86	0.09	32.70	M
SS03B_CT	TR	D	PM	LM	T	541	20.34	5.62	0.24	31.27	VH
SS03B_CT	TR	D	PA	LM	T	540	19.56	5.37	0.23	28.26	VH
SS03B_CT	TR	D	PM	SEM	SE	537	16.86	6.50	0.28	28.30	VH
SS02B_CT	TR	D	PM	LM	T	1261	12.06	4.63	0.13	22.20	H
SS02B_CT	TR	D	PA	LM	T	1204	11.97	4.78	0.14	25.00	H
SS02B_CT	TR	D	PM	SEM	SE	1251	12.39	4.80	0.14	24.46	H
SS01A_TH	TH	D	PM	LM	T	345	10.46	3.72	0.20	17.62	M
SS01A_TH	TH	D	PA	LM	T	357	10.27	4.09	0.22	19.00	M
SS01A_TH	TH	D	PM	SEM	SE	472	10.90	3.85	0.18	22.81	H
SS01A_SM	MI	D	PM	LM	T	1246	16.13	6.64	0.19	30.56	M/H
SS01A_SM	MI	D	PA	LM	T	1081	16.61	7.28	0.22	39.03	M/H
SS01A_SM	MI	D	PM	SEM	SE	1330	13.87	6.13	0.17	27.55	H
SS02A_SN	SA	D	PM	LM	T	370	10.11	3.41	0.18	16.93	VL
SS02A_SN	SA	D	PM	SEM	SE	284	12.08	3.69	0.22	17.42	L/M
SS02A_SN	SA	D	PM	SEM	SE	262	11.24	3.30	0.21	17.87	L/M
SEM_A	SEM	U	SM	LM	R	371	22.88	4.37	0.23	24.79	M
SEM_A	SEM	U	PA	LM	R	387	23.56	5.37	0.27	28.24	M
SEM_A	SEM	U	SM	SEM	SE	447	20.46	6.12	0.29	28.80	H
SEM_B	SEM	U	SM	LM	R	153	21.38	6.07	0.49	30.23	VL
SEM_B	SEM	U	PA	LM	R	278	20.73	7.69	0.46	34.79	VL
SEM_B	SEM	U	SM	SEM	SE	263	19.27	8.15	0.50	32.89	L

3.4 Results

3.4.1 Diagenetic screening

The detection of original aragonite structures was recorded in all nine shells and alteration to secondary aragonite or calcite was not detected (Figure 3.1). The SEM images showed evidence of original aragonite microstructures across the IL, including sharp boundaries of crystallization, distinguished biomineral units (Figure 3.1a, b) and clear well-defined angles between each first order lamellar (Figure 3.1b, c).

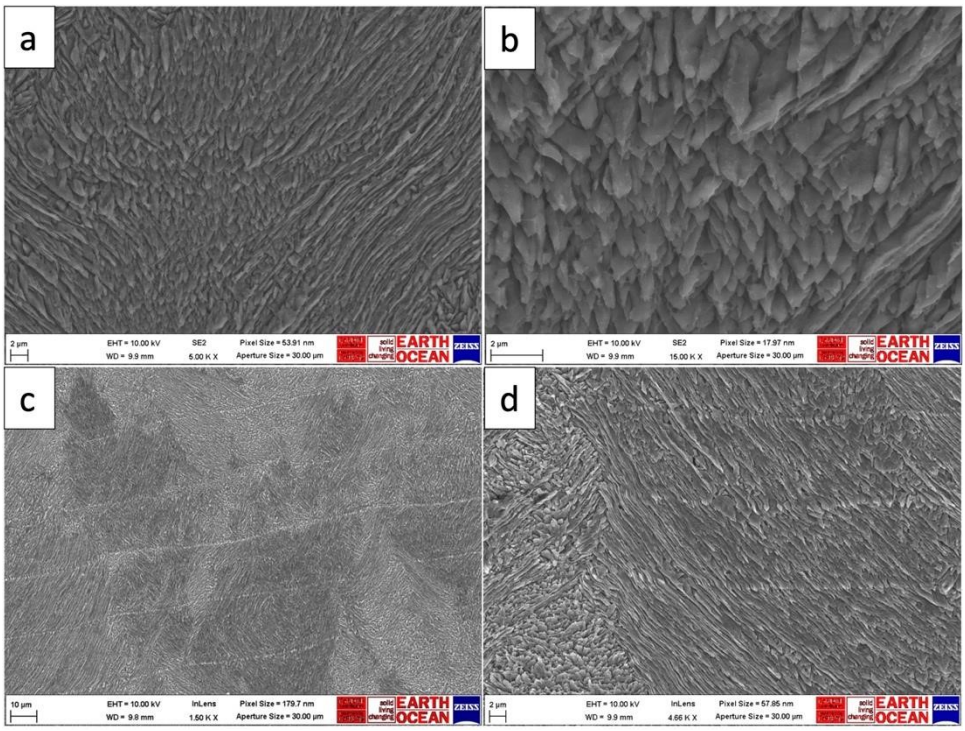

Figure 3.1. **Scanning electron microscopy (SEM) images of *Tridacna squamosa* thin sections showing evidence for original aragonite microstructures: (a, b) strong crystallization boundaries in size and shape of third-order laths (i.e. individual aragonitic crystals) (SS03B_CT); (c, d) well-defined angles between each first-order lamellar in the inner shell growth layer (SEM_A and SEM_B respectively).**

Raman spectroscopy showed aragonite defining peaks at the v4 in-plane bending mode at ~701 and 705 cm^{-1} across shells of all samples (Urmos et al. 1991) (Figure 3.2). The lattice mode showed characteristic low frequency measurements at 150 and 210 cm^{-1} (DeCarlo 2018) and the strongest v1 peaks (Urmos et al. 1991) near 1085

cm^{-1} were displayed, indicating that shells were aragonitic and showed no alteration to calcite at each location investigated.

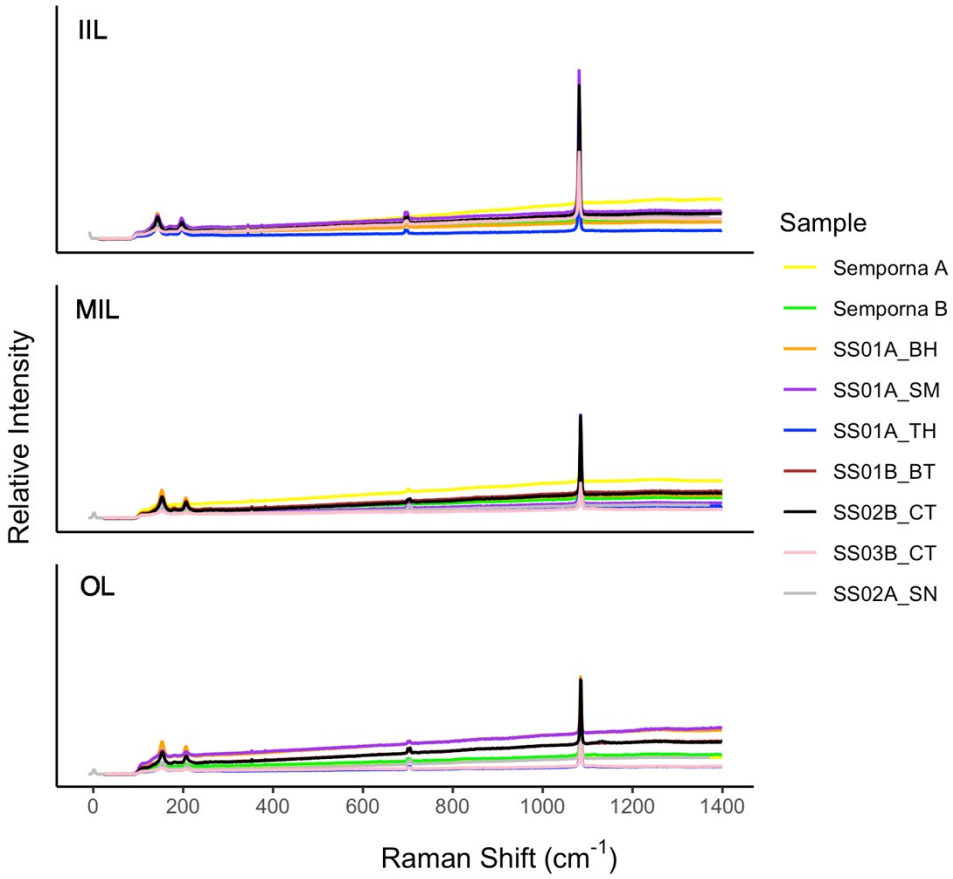

Figure 3.2. **Raman spectra of nine *Tridacna squamosa* shell samples collected dead from Darvel Bay and unknown collection status from Semporna reefs, showing aragonite defining peaks and a lack of calcite defining peaks. (a) IIL = 'inner' inner layer, representing region of last growth at edge of shell; (b) MIL = middle inner layer, representing region of mid to first growth; (c); OL = outer layer.**

3.4.2 Environmental data

I used PCA to further explore relationships between monthly environmental variables at Baik and Triangle reefs. PCA defined two principal components covering 77.1% of the cumulative variance (Figure 3.3). PC1 accounted for 43.9% of variance, with highest negative association of SST and cloud cover and highest positive association of salinity and rainfall, while PC2 accounted for 33.2% of variance and showed highest

negative association of chlorophyll-*a* and K_d(490) and positive association of cloud cover and SST. Baik and Triangle generally clustered into two distinct groups regardless of season. However, two points that represented the dry season of 2019, when an anomalous drought was experienced throughout the region, were positioned in the top left quadrant and did not cluster with others.

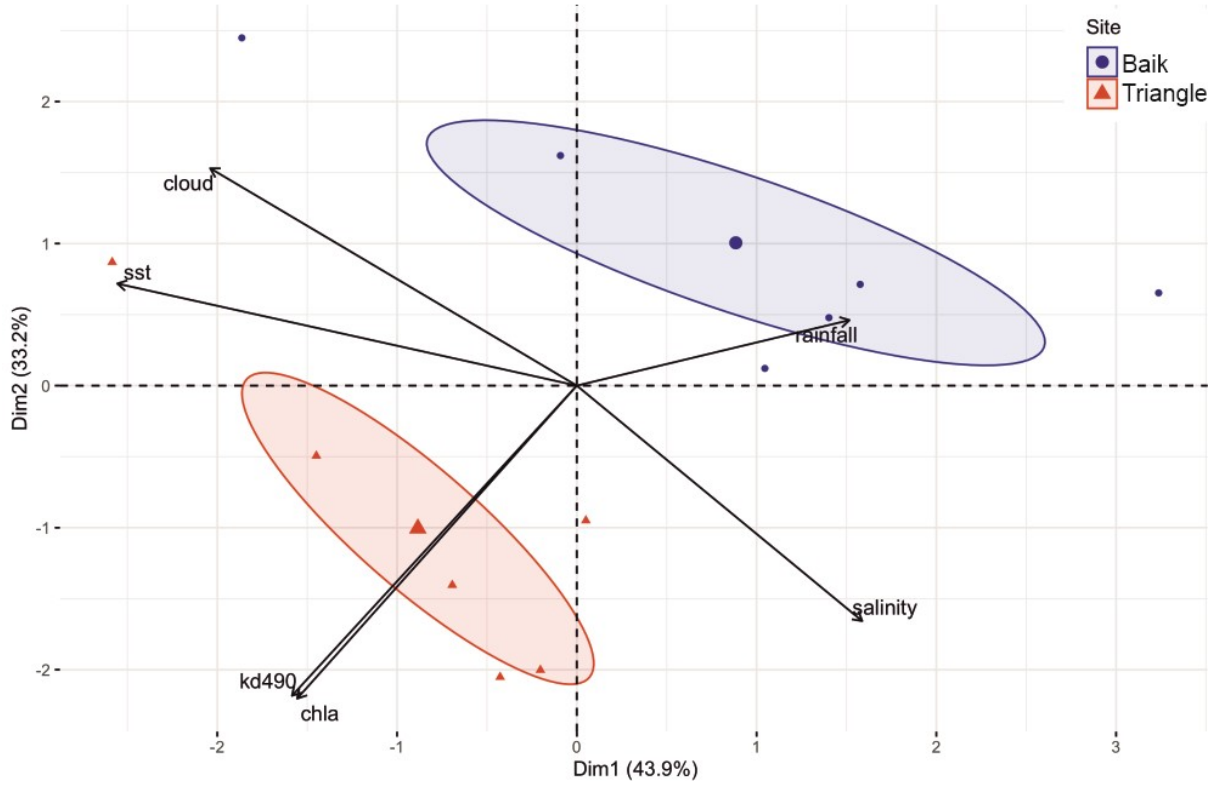

Figure 3.3. **Principal component analysis (PCA) for environmental data: monthly average sea surface temperature (SST), K_d(490) (m^{-1}), chlorophyll-*a* (mg m^{-3}), cloud cover (%) and rainfall (mm) from Baik and Triangle reefs in Darvel Bay, showing the loading of each variable (black arrows) and PCA scores (points) of each season for 2018–2020. Superimposed 95% confidence ellipsoids contain group points. Point sizes represent quality of representation of each individual point.**

3.4.3 Growth band microstructure

The microstructure of daily growth bands in the inner shell layer (IL) varied among the thirteen *T. squamosa* shells depending on collection site. Two distinct microstructures of daily bands were noted: Type 1—paired growth couplets, consisting of a thicker- and thinner layer, delineated by crystalline structure, similar to the thicker prismatic layer and thinner layer with oblique crystals described by Gannon et al. (2017) (Figure 3.4a, c); Type 2—Two adjacent organic rich growth lines delineating a band and

intersecting an irregular or cone complex crossed lamellar microstructure (Taylor et al. 1969) (Figure 3.4b, d). Type 1 was generally found in shells from the Triangle reef, while Type 2 was common in Baik, Blue Lagoon, THalu, Misan, Sakar and Semporna. Despite these differences, broad observations of the outer shell layer (OL) showed an identical microstructure in every specimen that consisted of a simple crossed lamellar arrangement (Taylor et al. 1969).

The microstructure observed in Type 1 showed a stronger delineation than Type 2. Thus, it was easier to observe, measure and count growth bands and in turn, data from shells with Type 1 had lower errors (calculated by value 1 subtracted from value 2, divided by value 1) between individual counts (0.74–2.37%). In contrast, the recorded variability in counting and measuring the least visible bands of Type 2 demonstrates that these were harder to distinguish. A comparison of the relationship between days alive and daily growth (μm) for individual counts that made up final mean growth chronologies of live collected *Tridacna squamosa* shells SS_BAIK (Baik, low turbid, 2019 collected), SS_CT (Triangle, high turbid, 2019 collected), NS207 (Baik, low turbid, 2020 collected) and ZW156 (Triangle, high turbid, 2020 collected) is shown in Figure 3.5, while a comparison between the dead collected shells is given in Figure 3.6. In particular, the SS_BAIK shell showed an extremely large offset of 880 bands between petrographic and SEM approaches (error 44.88%) (Figure 3.5a). However, data were similar between observer counts in the juvenile region of growth.

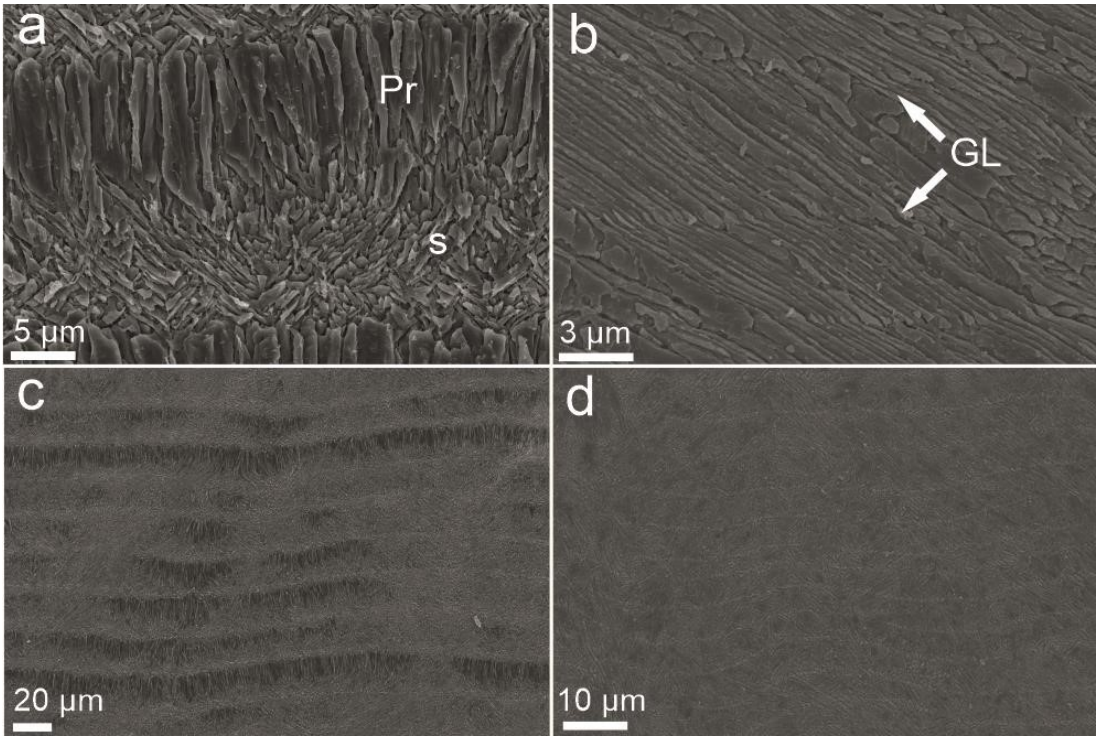

Figure 3.4. **SEM images of the microstructure of paired daily increments in *Tridacna squamosa* from Triangle reef (a, c), consisting of a simple prismatic layer (Pr) and layer with smaller crystals (s). (b, d) In Baik shells, there is a complex crossed lamellar microstructural arrangement with faint growth lines (GL) running perpendicular to first order lamellae.**

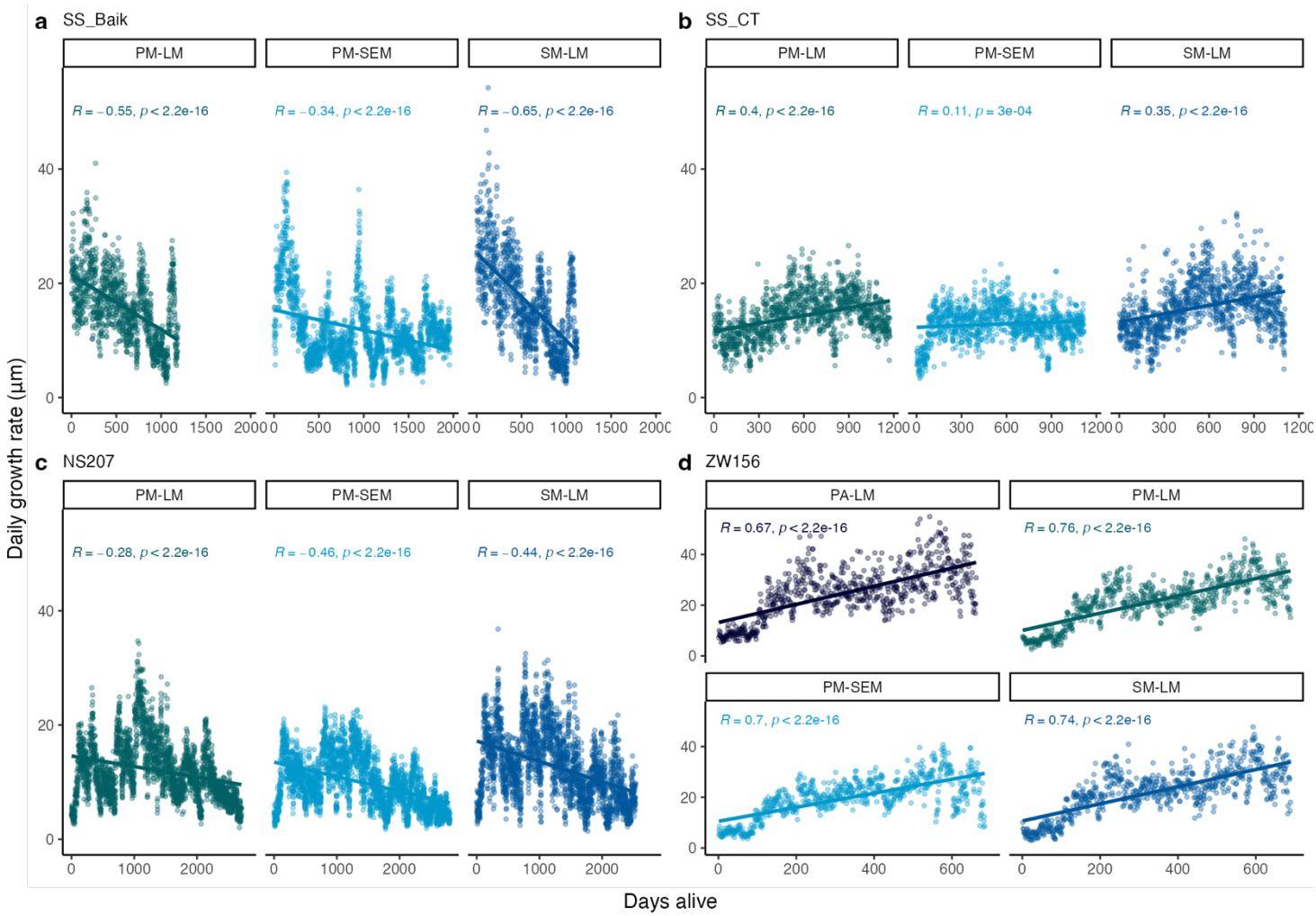

Figure 3.5. **Relationship between days alive and daily growth rate (µm) for individual counts incorporated into final mean shell growth chronologies from live collected *Tridacna squamosa* shells for samples SS_BAIK (Baik, 2019 collected) (a), SS_CT (Triangle, 2019 collected) (b), NS207 (Baik, 2020 collected) (c), ZW156 (Triangle, 2020 collected) (d). PM-LM = primary counter, measurement tool (ImageJ), light microscopy images; PA-LM = primary counter, autoplace function (CooRecorder), light microscopy images; PM-SEM = primary counter, measurement tool (ImageJ), SEM images; SM-LM = secondary counter, measurement tool (ImageJ), light microscopy images. N.B. The number of counts incorporated into final chronologies (i.e. three for SS_BAIK and four for ZW156) are different for each shell because not all counts met specified criteria for inclusion. R is correlation coefficient; *p* is statistical significance (<0.05) of the relationship between variables (days alive and daily growth).**

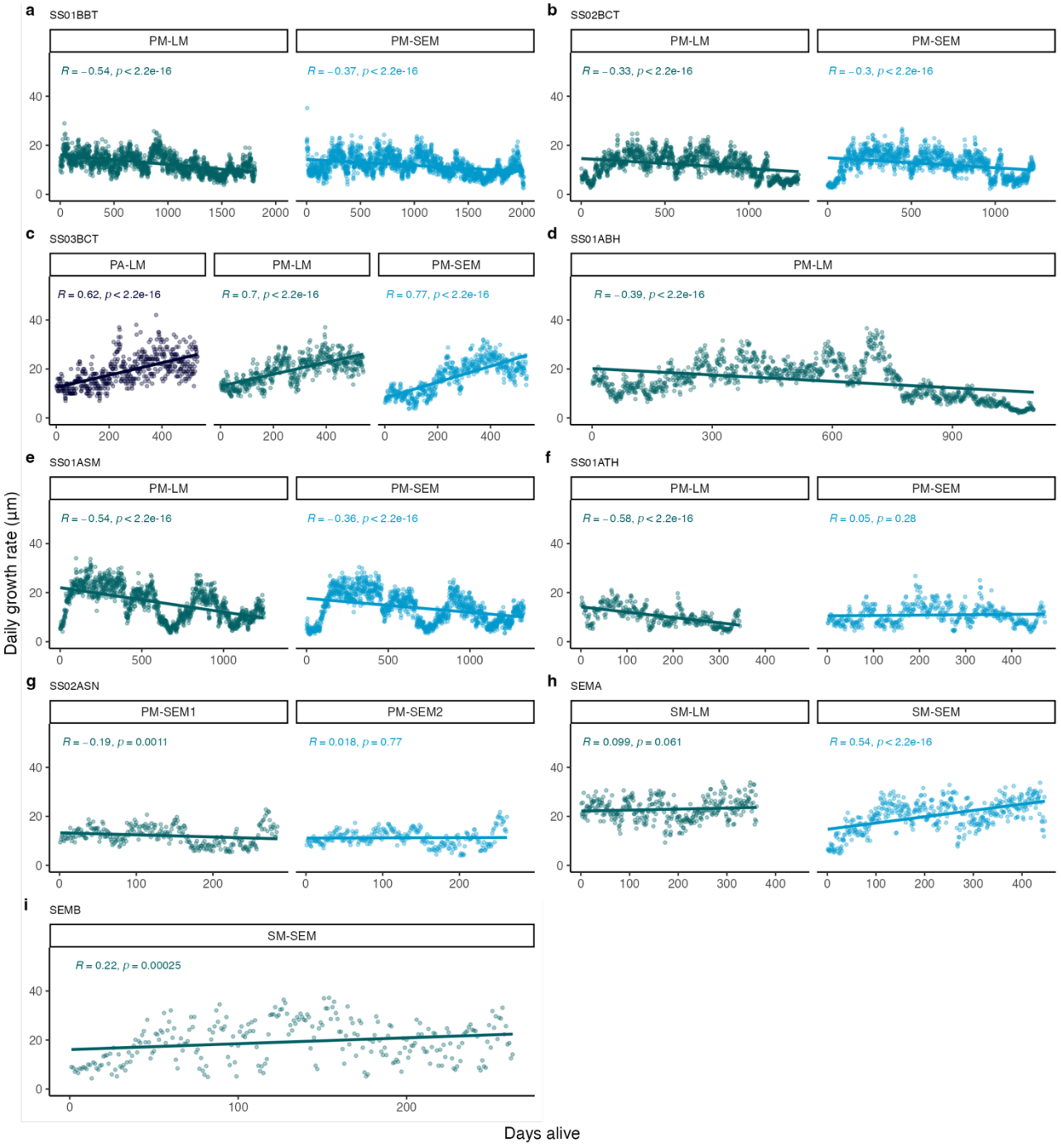

Figure 3.6. **Relationship between days alive and daily growth rate (µm) for individual counts incorporated into final mean shell growth chronologies from dead collected *Tridacna squamosa* shells for samples SS01B_BT (Baik) (a), SS02B_CT (Triangle) (b), SS03B_CT (Triangle) (c), SS01A_BH (Blue Lagoon) (d), SS01A_SM (Misan) (e), SS01A_TH (THalu) (f), SS02A_SN (Sakar) (g), SEM_A (Semporna) (h), SEM_B (Semporna) (i). PM-LM = primary counter, measurement tool (ImageJ), light microscopy images; PA-LM = primary counter, autoplace function (CooRecorder), light microscopy images; PM-SEM = primary counter, measurement tool (ImageJ), SEM images; SM-LM = secondary counter, measurement tool (ImageJ), light microscopy images. N.B. The number of counts incorporated into final chronologies (e.g. one for SEM_B and three for SS03B_CT) are different for each shell because not all counts met specified**

criteria for inclusion. R is correlation coefficient; *p* is statistical significance (<0.05) of the relationship between variables (days alive and daily growth).

3.4.4 Annual shell growth

Lifespan of all thirteen shells was estimated between 0.72 (262 days) and 7.23 (1726 days) years (Table 3.2). Seven shells were under 3 years, which may indicate the juvenile life stage, while six were over 3 years, which may indicate adulthood (Lucas 1994). Shell growth chronologies over 3 years generally showed a concave down shape and could be divided into two broad stages: Stage 1—rapid acceleration at start of life and Stage 2—deceleration in or after 3 years (Figure 3.7). Younger shells that presumably had not reached latter growth stages showed no concavity but continued rapid growth or no relationship with days alive.

Mean shell growth rates over lifespan varied greatly and ranged from 3.91 ± 1.39 to 8.13 ± 3.37 mm/yr (Table 3.2), corresponding to daily band widths between 2.02 and 41.40 µm (mean 14.90 µm/day). In all shells, mean annual growth in the first year of life was 6.28 mm/yr ($n = 11$), 5.51 mm/yr ($n = 7$) in 0–2 yr, 5.18 mm/yr ($n = 2$) in 2–4 yr, 3.58 mm/yr ($n = 1$) in 4–6 yr, following age-related deceleration of growth. Shells from Semporna ($n = 2$) showed pooled fastest overall mean annual growth (7.46 mm/yr), followed by those from Triangle ($n = 4$) (6.16 mm/yr), Misan 5.41 mm/yr ($n = 1$), Baik 4.61 mm/yr ($n = 3$), Sakar 4.26 mm/yr ($n = 1$), and THalu 3.91 mm/yr ($n = 1$). Among individual shells, ZW156 from Triangle showed fastest mean growth (21.55 µm/day), while SS01ATH from THalu (10.72 µm/day) grew slowest.

SGI values (i.e. chronologies corrected for ontogenetic growth trends) revealed strikingly contrasting results to raw growth rates and showed more similar minimum and maximum values between all *T. squamosa* shells irrespective of site or age (Figure 3.7c, d). One-way ANOVA and post hoc Tukey test confirmed no significant differences in SGI over lifespan between shells from different sites (one-way ANOVA, $F(6) = 0.964$, $P > 0.05$, pairwise comparisons with Tukey HSD test) (Table 3.3).

Table 3.2. **Individual growth chronologies incorporated into combined final growth chronologies, approximate age (yr) and annual mean growth rate (mm/yr) for *Tridacna squamosa* shells. BA = Baik; TR = Triangle; BL = Blue Lagoon; TH = THalu; MI = Misan; SA = Sakar; SEM = Semporna reefs. N = number of counts incorporated into final chronologies. PM-LM = primary counter, measurement tool (ImageJ), light microscopy images; PA-LM = primary counter, autoplace function (CooRecorder), light microscopy images; PM-SEM = primary counter, measurement tool (ImageJ), SEM images; SM-LM = secondary counter, measurement tool (ImageJ), light microscopy images.**

Sample	Site	N	Incorporated chronologies	Age (yr)	Overall mean growth (mm/yr)	Mean growth 0–1 yr (mm/yr)	Mean growth 0–2 yr (mm/yr)	Mean growth 2–4 yr (mm/yr)	Mean growth 4–6 yr (mm/yr)
SS_BAIK	BA	3	PM-LM (1), PM-SEM (1), SM-LM (1)	3.40	5.20 ± 2.48	6.01 ± 2.63	5.48 ± 0.006	-	-
SS_CT	TR	3	PM-LM (1), PM-SEM (1), SM-LM (1)	3.10	5.24 ± 1.46	4.91 ± 1.35	5.40 ± 1.43	-	-
NS207	BA	3	PM-LM (1), PM-SEM (1), SM-LM (1)	7.23	4.21 ± 1.95	4.66 ± 2.05	4.30 ± 1.73	5.82 ± 1.81	3.58 ± 1.46
ZW156	TR	4	PM-LM (1), PM-SEM (1), SM-LM (1) PA-LM (1)	1.86	8.13 ± 3.37	6.51 ± 3.09	-	-	-
SS01A_BH	BL	2	PM-LM (1), PA-LM (1)	2.95	5.90 ± 2.66	6.31 ± 1.97	7.14 ± 2.15		
SS01B_BT	BA	2	PM-LM (1), PM-SEM (1)	5.23	4.43 ± 1.40	5.06 ± 1.40	5.01 ± 1.31	4.53 ± 1.31	-
SS03B_CT	TR	3	PA-LM (1), PM-LM (1), PM-SEM (1	1.48	6.82 ± 2.21	6.02 ± 2.05	-	-	-
SS02B_CT	TR	2	PM-LM (1), PM-SEM (1)	3.41	4.44 ± 1.72	4.68 ± 1.86	5.01 ± 1.62	-	-
SS01A_TH	TH	2	PM-LM (1), PM-SEM (1)	1.19	3.91 ± 1.39	4.00 ± 1.43	-	-	-
SS01A_SM	MI	2	PM-LM (1), PM-SEM (1)	3.53	5.41 ± 2.36	6.94 ± 2.53	6.22 ± 2.46	-	-
SS02A_SN	SA	2	PM-SEM (2)	0.74	4.26 ± 1.29	-	-	-	-
SEM_A	SEM	2	SM-LM (1), SM-SEM (1)	1.11	7.87 ± 2.02	7.73 ± 2.02	-	-	-
SEM_B	SEM	1	SM-SEM (1)	0.72	7.04 ± 2.98	-	-	-	-

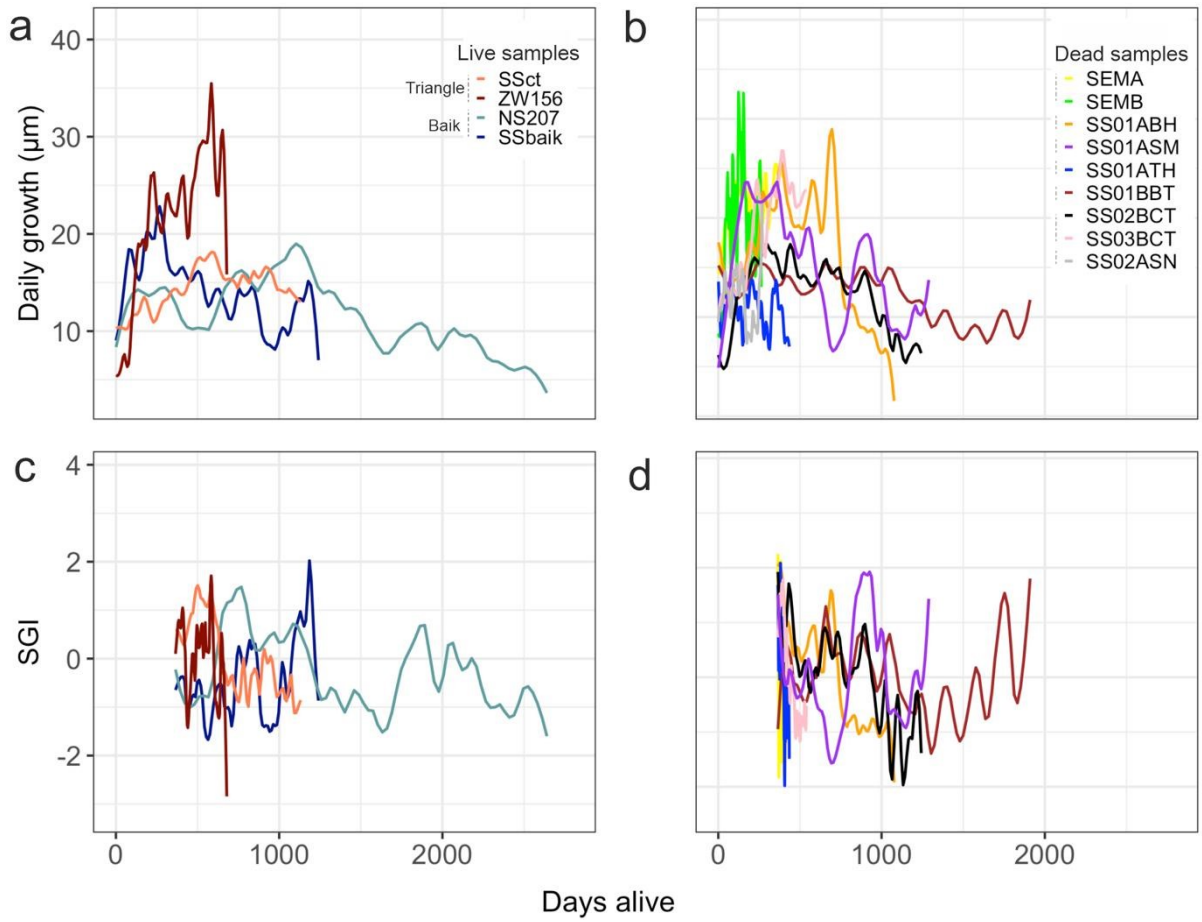

Figure 3.7. **All mean shell growth chronologies derived from daily growth increment bands of live (a, c) and dead (b, d) collected *Tridacna squamosa* for comparison of shell growth over lifespan. Measurements are presented by rate of daily growth (µm) (a, b) and detrended growth rates shown in the dimensionless unit of the standardized growth index (SGI) (c, d). Lines are smoothed (span 0.1) and colours represent different samples. Shells younger than 365 days are excluded from SGI values due to the 365 moving averages used.**

Table 3.3. **Tukey HSD test for differences in SGI growth rate between pooled shells from different sites in Darvel Bay and Semporna. Upper matrix reports *p* values between sites. Lower matrix is the difference (lower-upper values).**

	Sakar	Triangle	THalu	Misan	Baik	Blue Lagoon	Semporna
Sakar		0.54	0.89	0.76	0.36	0.82	0.90
Triangle	-1.27 (-3.65-1.12)		0.99	0.97	0.99	0.99	0.99
THalu	-0.97 (-3.89-1.95)	-0.29 (-2.68-2.09)		0.99	0.99	0.99	0.98
Misan	0.99 (-1.39-3.37)	-0.28 (-1.96-1.41)	0.02 (-2.36-2.40)		0.36	0.99	0.99
Baik	1.38 (-0.80-3.57)	0.12 (-1.28-1.51)	0.41 (-1.77-2.60)	1.38 (-0.80-3.57)		0.97	0.99
Blue Lagoon	0.97 (-1.55-3.50)	-0.29 (-2.18-1.59)	0.01 (-2.53-2.53)	-0.02 (-1.90-1.87)	0.41 (-1.22-2.04)		0.82
Semporna	-0.95 (-3.87-1.97)	-0.32 (-2.70- 2.07)	-0.02 (-2.94-2.90)	0.04 (-2.34-2.42)	0.43 (-1.76-3.57)	0.02 (-2.50-2.55)	

3.4.5 Seasonal shell growth and environmental relationships

Distinct temporal patterns that were most prominent at a seasonal level were revealed in live collected shell chronologies where exact dates of death were known. The most striking difference was seasonal acceleration of growth that generally occurred in the wet season for low turbid Baik (Figure 3.8a, c), particularly in shell SS_BAIK, while a seasonal trend in high turbid Triangle was less clear (Figure 3.8b, d). The undated SGI chronologies from dead collected shells at the same sites revealed similar seasonal acceleration in Baik (Figure 3.9e), while Triangle showed what appeared to represent shorter-term cycles throughout the year (Figure 3.9f).

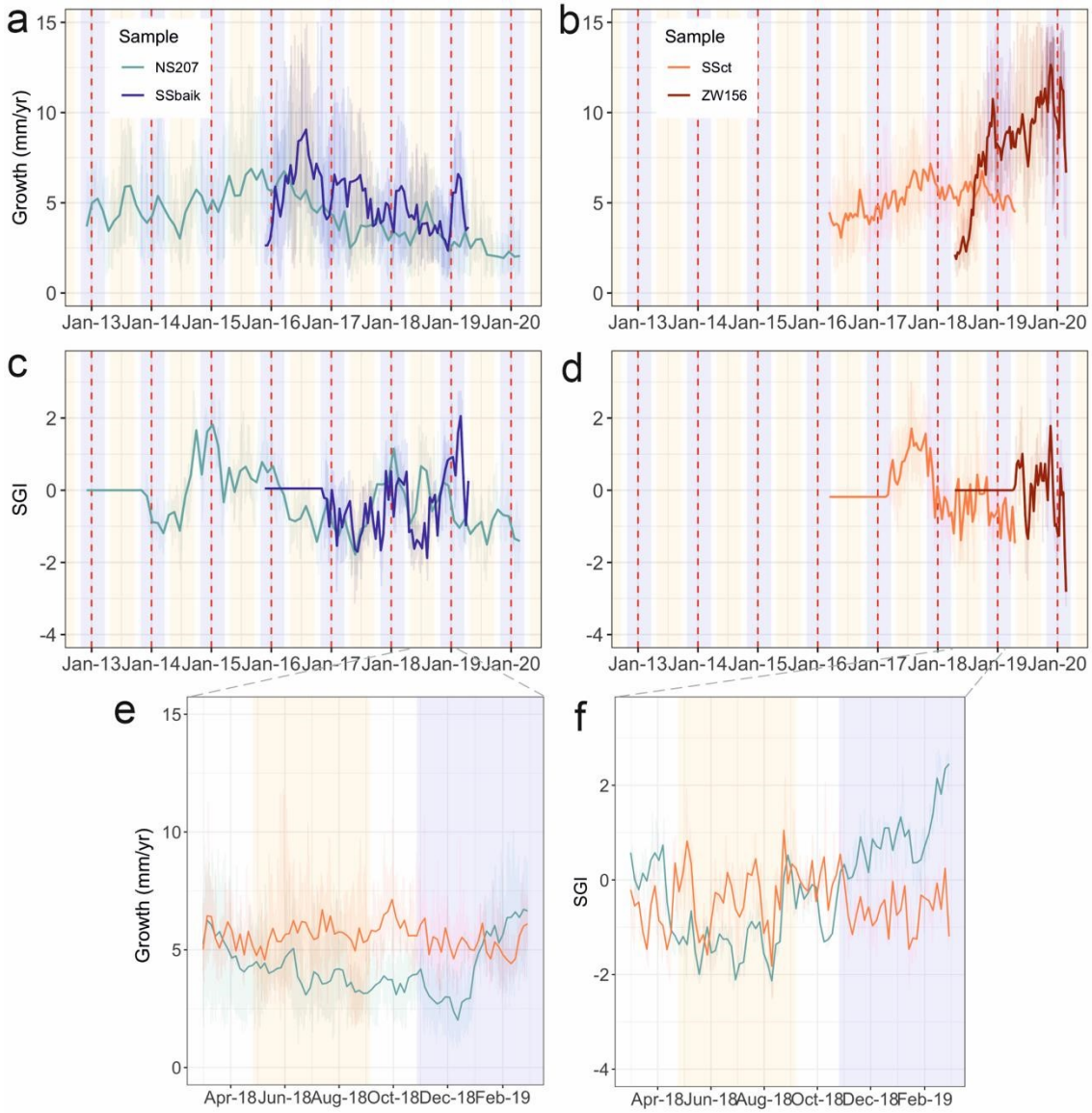

Figure 3.8. **Dated mean shell growth chronologies derived from daily growth increment widths for *Tridacna squamosa* collected from Baik (blue lines) (a, c) and Triangle (red lines) (b, d) reefs in 2019 (SS_CT, SS_BAIK) and 2020 (ZW156, NS207). Measurements from raw data are presented in mm/yr (a, b) and detrended growth rates shown in the dimensionless unit of the standardized growth index (SGI) (c, d). Red dashed vertical lines represent one year of growth and purple and orange bars represent wet and dry seasons respectively. Raw growth (e) and SGI chronologies (f) showing only last year of growth (LYOG) in Baik (SS_BAIK) (blue line) and Triangle (SS_CT) (red line) reveal seasonal variation between the two sites. Raw data is represented by pale lines and data after smoothing (span 0.1) is represented by bold lines.**

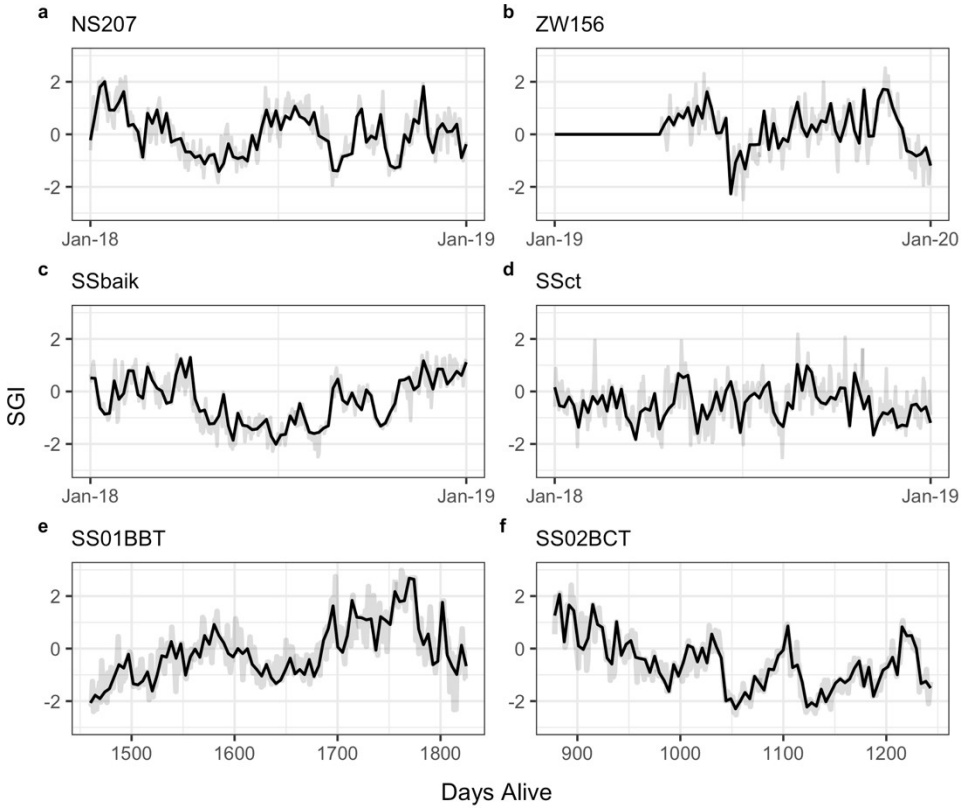

Figure 3.9. **SGI chronologies for last year of growth (LYOG) for *Tridacna squamosa* shells collected alive (a–d) and dead (e, f) from the key reef sites Baik (NS207; SS_BAIK; SS01B_BT) and Triangle (ZW156; SS_CT; SS02B_CT) in Darvel Bay. NS207 (a), ZW156 (b), SS_BAIK (c) and SS_CT (d) are live collected shells and the x-axis correspond to a period of one year of growth that is dated. SS01B_BT (e) and SS02B_CT (f) are dead collected shells from the seafloor and the x-axis correspond to approximate days alive, showing a 365 day period.**

Undated SGI chronologies from dead shells collected at additional sites generally showed a similar seasonal range of SGI values to live collected shells (Figure 3.10). The shell from Blue Lagoon revealed positive SGI values in the second year of growth, compared to only negative SGI values in the third year (Figure 3.10 a), while the shell from Misan showed a distinct peak in the third year of growth (Figure 3.10 d). Younger shells at THalu, Triangle and Semporna that were under 3 years showed a short deceleration in the second year of growth before death (Figure 3.10 c, e, g respectively).

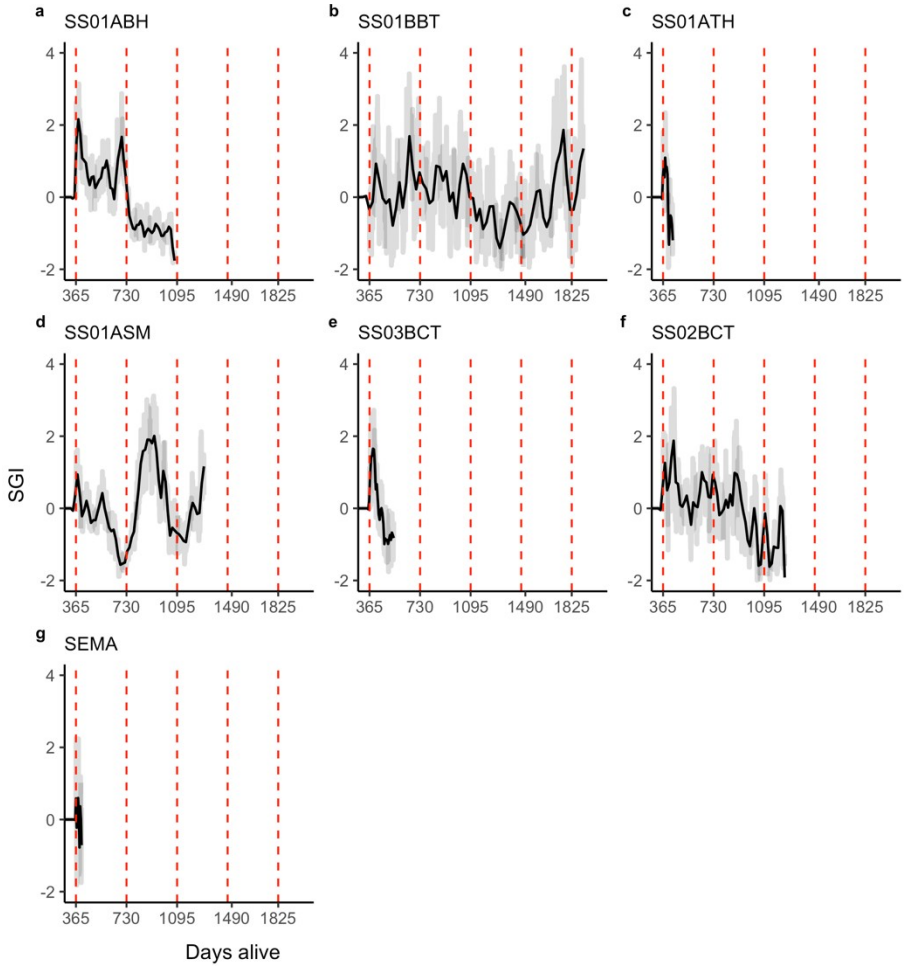

Figure 3.10. **Floating SGI chronologies for dead collected *Tridacna squamosa* shells from Darvel Bay at Blue Lagoon (SS01A_BH) (a), Baik (SS01B_BT) (b), THalu (SS01A_TH) (c), Misan (SS01A_SM) (d), Triangle (SS03B_CT, SS02B_CT) (e, f) and Semporna (SEM_A) (g) showing growth in relation to approximate days alive. Shells younger than 365 days are excluded from analysis. Red dashed vertical lines represent one year of growth.**

AV plots revealed significant relationships between monthly SGI and cloud cover ($p < 0.05$) and SST ($p < 0.05$) in one Baik shell (SS_BAIK) (Figure 3.11) and salinity ($p < 0.01$) and rainfall ($p < 0.01$) in the additional older Baik shell (NS207) (Figure 3.12). In contrast, shells from Triangle (SS_CT; ZW156) showed no significant correlation between tested environmental variables and SGI values (Figure 3.13; 3.14). Nonetheless, I did note a degree of synchronization with bimodal chlorophyll-*a* and K_d(490) peaks in ZW156 from Triangle, while growth appeared relatively consistent year-round in SS_CT (Figure 3.15).

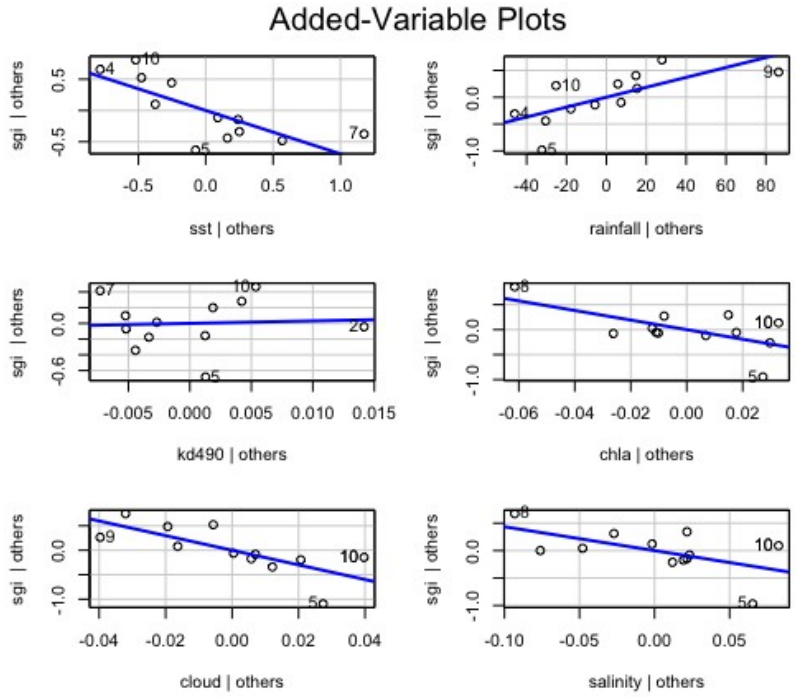

Figure 3.11. **Added-variable plots of individual explanatory variables versus dependent shell SGI for period corresponding to last year of growth (LYOG) for sample SS_BAIK (Baik, 2019).**

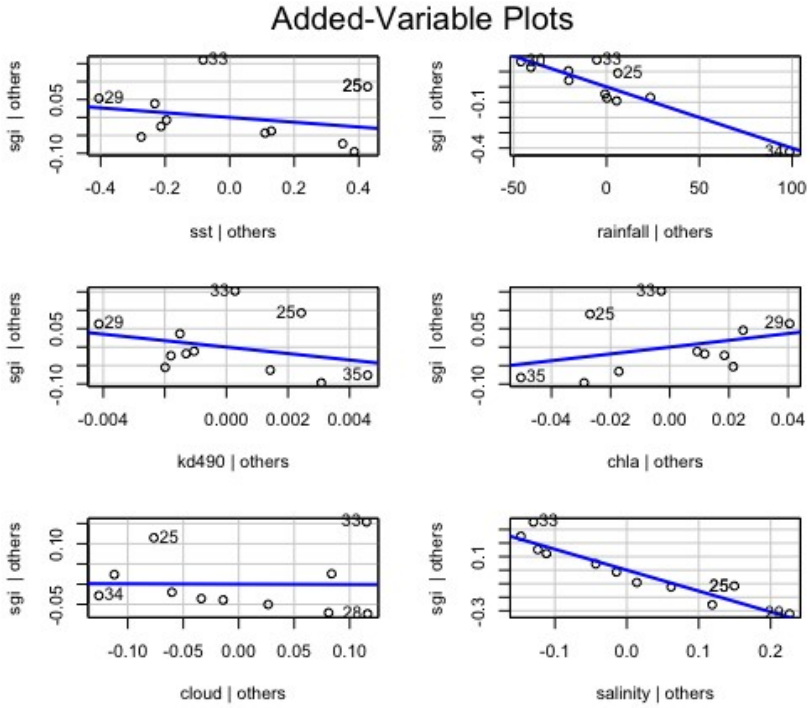

Figure 3.12. **Added-variable plots of individual explanatory variables versus dependent shell SGI for period corresponding to last year of growth (LYOG) for sample NS207 (Baik, 2020).**

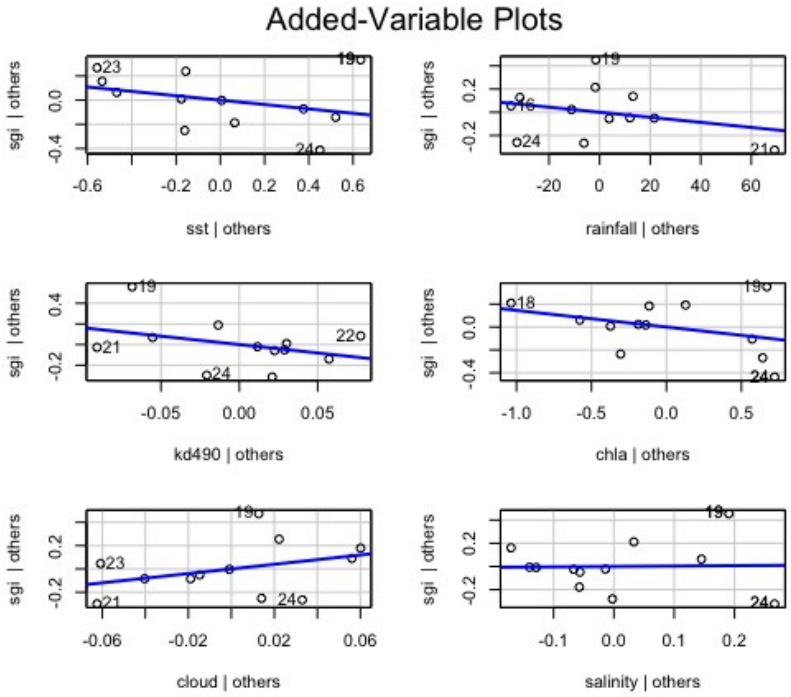

Figure 3.13. **Added-variable plots of individual explanatory variables versus dependent shell SGI for period corresponding to last year of growth (LYOG) for sample SS_CT (Triangle, 2019).**

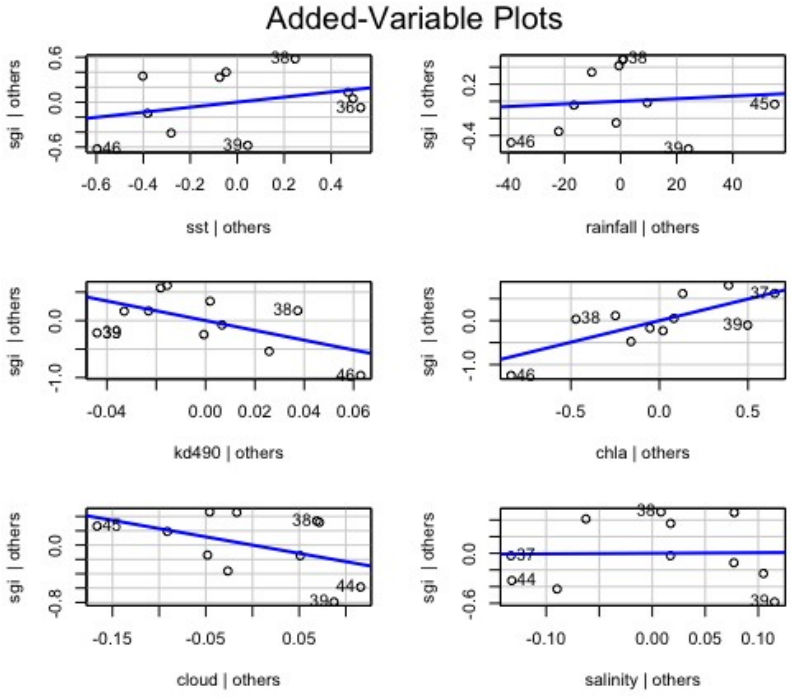

Figure 3.14. **Added-variable plots of individual explanatory variables versus dependent shell SGI for period corresponding to last year of growth (LYOG) for sample ZW156 (Triangle, 2020).**

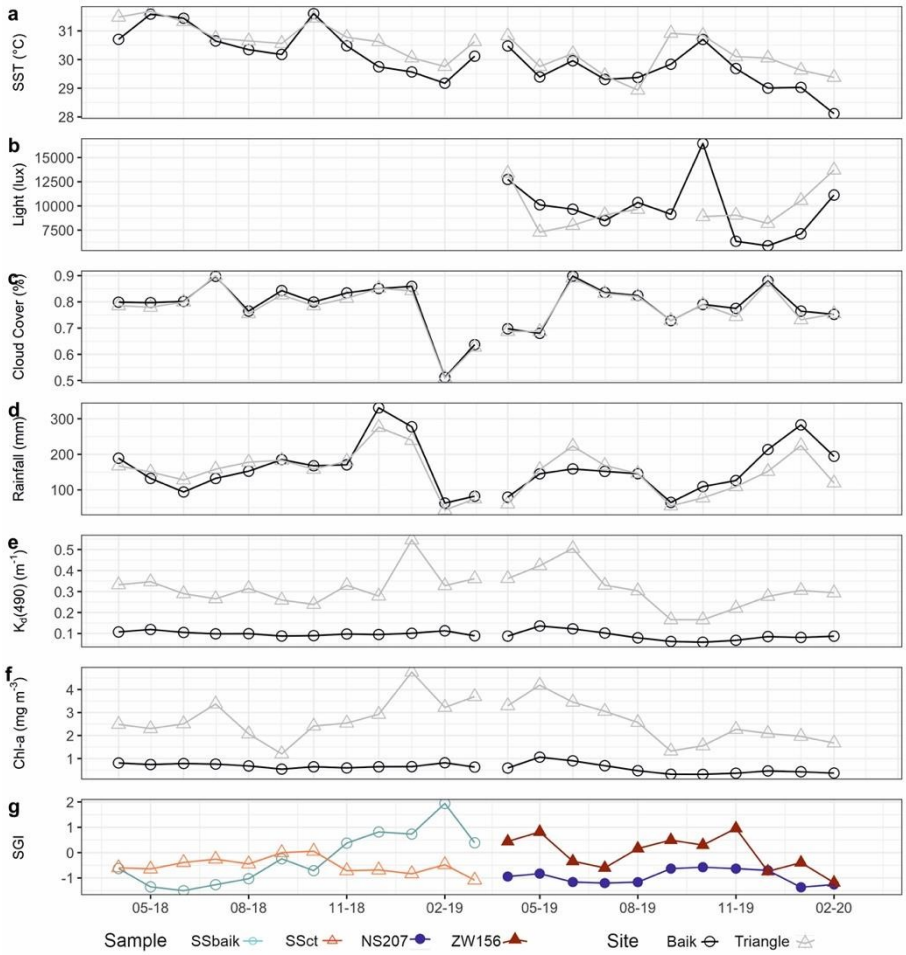

Figure 3.15. **Comparison of monthly growth pattern for last year of growth (LYOG) in shells collected alive from the Baik (SS_BAIK, NS207) and Triangle (SS_CT, ZW156) reefs, with monthly sea surface temperature (SST) (a), light (lux) (b), cloud cover (%) (c), rainfall (mm) (d), $K_d(490)$ (m^{-1}) (e), chlorophyll-*a* ($mg\ m^{-3}$) (f) and monthly SGI (g).**

3.4.6 Daily shell growth using spectral analysis

Multi-taper method (MTM) spectral analysis (Thomson 1982) was applied to daily SGI values and tidal range to search for similarity of periodicities in frequency space. Daily growth bands in high turbid Triangle shells were characterized by high-frequency significant peaks corresponding to periods of ~2–3 days and spectra revealed several similarities with daily maximum sea level. Sample ZW156 from Triangle shared the most similarity with maximum tide (Figure 3.16). However, significant peaks in low turbid Baik shells occurred over a wider range of frequencies corresponding to periods of ~2–6 days and showed less similarity with tidal spectra (Figure 3.17c, d).

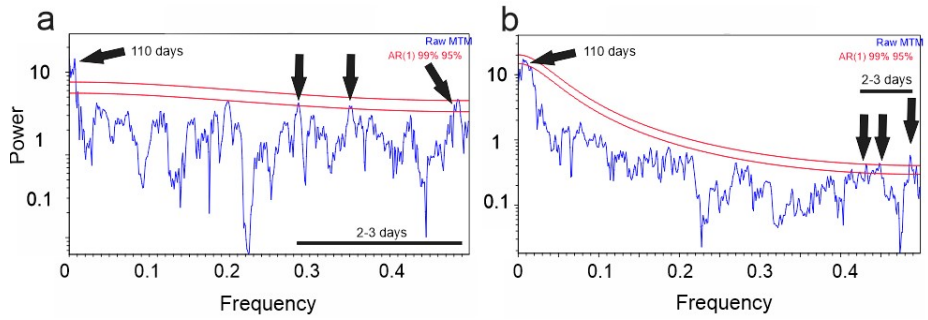

Figure 3.16. **Multi-taper method (MTM) power spectra of (a) daily maximum tide (m) and (b) daily SGI growth chronology of Triangle reef shell ZW156 in frequency space. AR(1) significance peaks are set to 95% and 99% and represented to a red noise background. Significant peaks labelled with arrows and identified in approximate days in relation to frequency (1/day).**

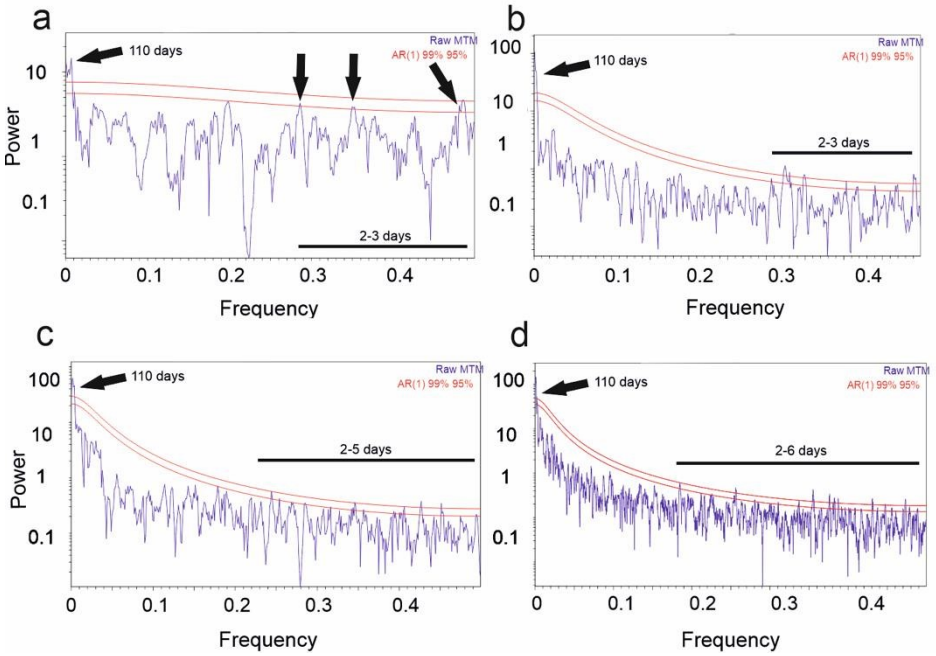

Figure 3.17. **Multitaper method (MTM) power spectra of (a) daily maximum tide (m), and SGI chronologies (b) SS_CT (Triangle reef), (c) SS_BAIK (Baik reef) and (d) NS207 (Baik reef) in frequency space. AR(1) significance peaks are set to 95% and 99% and represented in respect to red noise background. Significant peaks are labelled with arrows and/or horizontal bars and identified in approximate days in relation to frequency (1/day).**

3.5 Discussion

3.5.1 Multi-method approach to sclerochronology in giant clams

In this study, I established shell growth chronologies for thirteen giant clam shells based on counting and measuring widths of daily growth bands with a mixed-method approach (light microscopy and SEM). To reduce uncertainty, bands were counted multiple times with different software and live collected shells cross-checked by a secondary person. However, large offsets existed between counts in some samples, which could be attributed to either differences in microstructure that reduced growth band visibility or visualization of bands between approaches.

Molluscan shell microstructure is strongly underpinned by genetic and biophysiological mechanisms but is further influenced by external environmental factors (Clark et al. 2020). Size and shape of biomineral units may change depending on temperature (Milano et al. 2017; Höche et al. 2020), light attenuation (Pätzold et al. 1991) and food supply (Clark et al. 2020). Here, I found two distinct microstructures of daily bands for the inner shell layer (IL) of *T. squamosa:* Type 1 in the Triangle reef, which consisted of paired daily growth couplets with a thicker- and thinner layer delineated by crystalline structure and Type 2 in other reef sites, with two adjacent growth lines cutting a complex crossed lamellar microstructural arrangement that was either irregular or cone (Taylor et al. 1969) and running perpendicular to first order lamellae (Agbaje et al. 2017). Delineation of bands from Type 1 shells was clearer than Type 2, and this was reflected in the differences between individual counts. Distinctly demarcated paired increments that vary in morphology along one growth band like Type 1 have previously been recorded for *T. gigas* (Pätzold et al. 1991; Gannon et al. 2017) and are presumably driven by the daily light cycle (Sano et al. 2012). The thicker prismatic layer is thought to be deposited in the daytime when symbiotic algae allow light-enhanced calcification, while the thinner layer may calcify at night when less light is available for photosynthetic processes (Sano et al. 2012). Although Pätzold et al. (1991) described a similar microstructure with faint growth bands like Type 2, they only reported its occurrence near the umbo and not throughout other regions of the shell. I found Type 2 to be common in early stages of growth when growth was faster, presumably a continuation of the simple crossed lamellar microstructural arrangement

of the outer shell layer. Although this concurs with reports of less defined crystalline boundaries indicating faster deposition of microstructural components (Gannon et al. 2017), Type 2 continued into adulthood in many shells and Type 1 only recorded in Triangle, which may relate to tidal rhythm (discussed below).

Apart from microstructure, differences in visibility of daily growth bands in giant clam shells have also been attributed to method specific issues. For example, changes in focal length and low fluorescence of shell material under LSCM (Zhao et al. 2021). I used high-resolution SEM imaging across the entirety of the IL of each shell because this method allows singular daily bands to be revealed in detail in secondary electron images (Welsh et al. 2011). Shell regions whose daily bands remained unclear under SEM are likely a true feature of the sample instead of an artefact of sampling technique. I additionally found the boundary between the OL and IL (i.e. the pallial line) distinct under SEM (Figure 3.18), similar to other studies (Gannon et al. 2017; Ayling et al. 2017). Yet, this was sometimes unclear under light microscopy, which may be attributed to variation in focal length due to the presence of a highly topographic complex crossed lamellar microstructural arrangement. These results emphasize the importance of applying a multi-method approach in counting daily growth increments of giant clams because large unveiled offsets could severely obstruct interpretation for high-resolution studies.

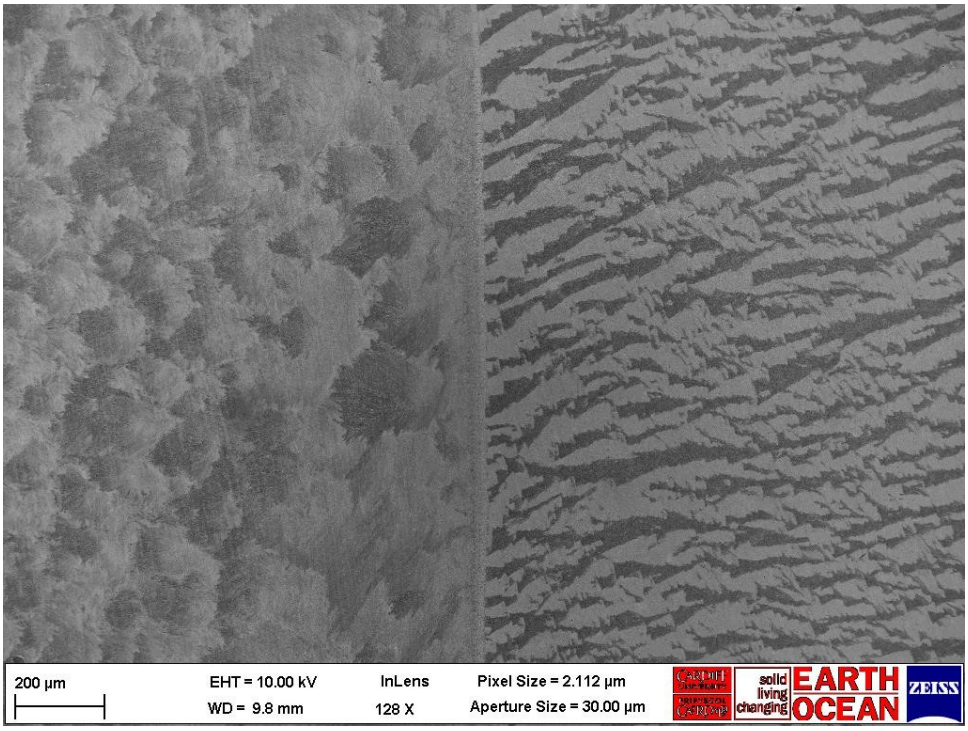

Figure 3.18. **SEM image of the outer- (right) and inner shell layer (left) of *Tridacna squamosa* (SS_BAIK), clearly demarcated by the pallial line running vertically down the middle of the image.**

3.5.2 Shell growth mediated by ontogeny

A challenge in the study of sclerochronology is to disentangle vital effects and externally forced growth signatures (e.g. temperature) (Schöne 2003). As for many bivalves, physiological processes of tridacnids change with the onset of sexual maturity and energy priorities switch between growth and reproduction (Jones et al. 1986). Over time, growth bands become tightly packed and rate and year to year amplitude of growth decreases (Romanek and Grossman 1989; Arias-Ruiz et al. 2017; Zhao et al. 2021). In this study, shell growth chronologies accounting for ontogenetic growth were investigated before applying the SGI. I found most shells over approximately three years old demonstrated rapid acceleration at the beginning of life and reduction in growth in or after three years. Although delayed onset of sexual maturity (approximately 10 years) and subsequent deceleration of growth has been recorded for *Tridacna maxima* (Jones et al. 1986; Romanek et al. 1987; Chambers 2007) and *T. gigas* (Klump and Griffiths 1994; Lucas 1994), the switch between juvenile and adult growth phases may occur earlier in other species (Lucas 1994). While the shells used herein are young (~1–7 yr) relative to the natural lifespan of

Tridacna spp. (several decades) (Rosewater 1965), growth curves in some samples may indicate early onset maturity for *T. squamosa.*

3.5.3 Environmental influences on shell growth

My results revealed mean shell growth rates from seven reefs that ranged from 3.91 ± 1.39 to 8.13 ± 3.37 mm/yr (10.71 ± 3.81 to 22.26 ± 9.23 μm/day), corresponding to individual daily band widths that ranged between 2.02 and 41.40 μm (mean of 14.90 μm/day). Despite shells being collected from a range of reefs subject to varying turbidity, results were generally consistent with those in the literature for modern and cultured shells, showing mean daily widths of 3–32.7 μm for measurements of the IL of *T. squamosa* and other Tridacnidae (Aubert et al. 2009; Elliot et al. 2009; Schwartzmann et al. 2011; Arias-Ruiz et al. 2017; Gannon et al. 2017; Yan et al. 2020; Zhao et al. 2021) (Figure 3.19). Moreover, removal of ontogenetic growth signals using the SGI revealed no significant differences across annual growth rate from shells at any of the sites over lifespan. However, I do caution the uncertainties of the interpretation of the dead collected shells from the seafloor and it is possible that they were translocated post-mortem.

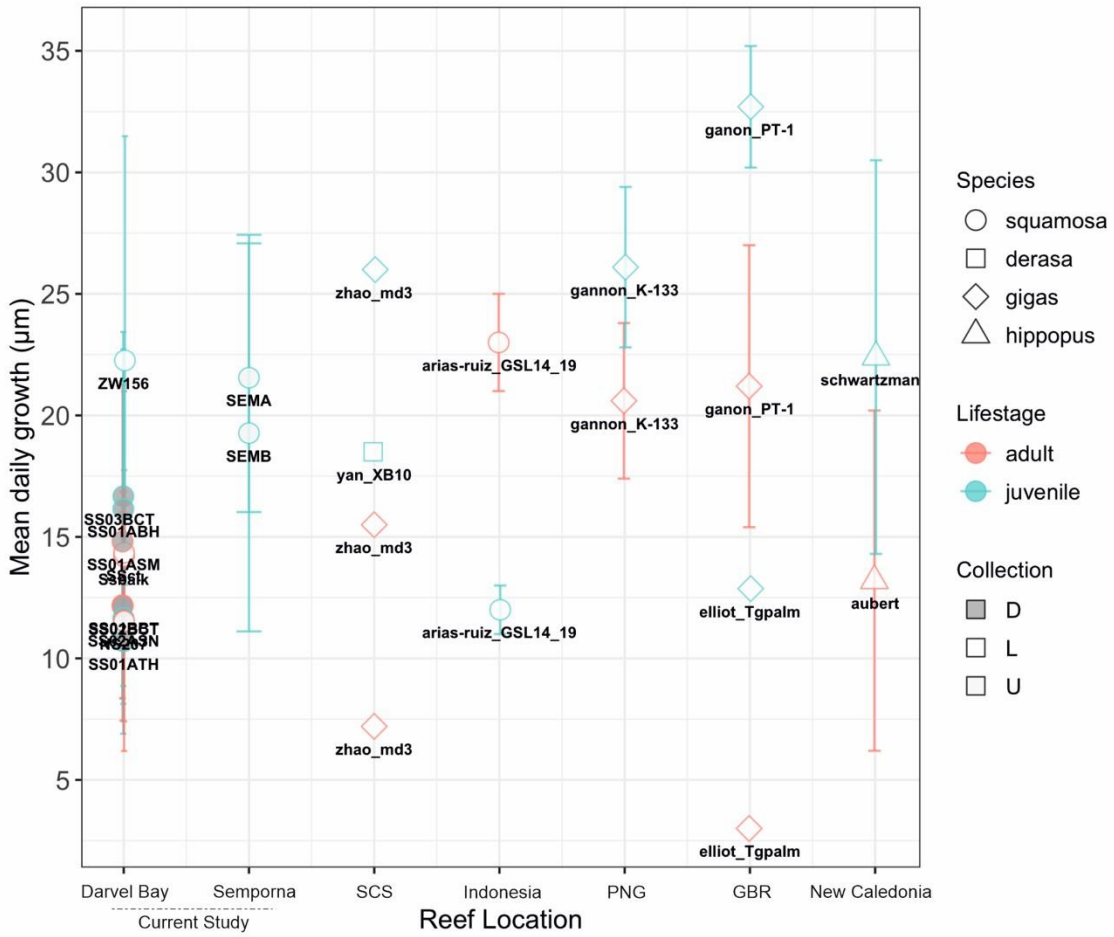

Figure 3.19. **Mean daily growth rate (µm) of the inner shell layer for Darvel Bay and Semporna Tridacnidae (current study) compared to published growth values. Reef location *SCS* Southern South China Sea, *PNG* Papua New Guinea, *GBR* Great Barrier Reef. Sample zhao_md3 = Zhao et al. (2021); yan_XB10 = Yan et al. (2020); arias-ruiz_GSL14_19 = Arias-Ruiz et al. (2017); gannon_K-133 = Gannon et al. (2017); gannon_PT-1 = Gannon et al. (2017); elliot_Tgplam = Elliot et al. (2009); schwartzman = Schwartzmann et al. (2011), aubert = Aubert et al. (2009). Error bars represent standard deviation, if available.**

3.5.3.1 Influences on annual shell growth

One explanation for similar annual SGI values across sites may be related to the trophic plasticity documented for *T. squamosa*. Unlike some giant clam species who are functional autotrophs, *T. squamosa* has a photoautotrophic range that is extended by heterotrophy (Jantzen et al. 2008). Although contributions of heterotrophy to total energy requirements in tridacnids change depending on ontogenetic stage and size (Fisher et al. 1985; Klump et al. 1992; Klumpp and Griffiths 1994; Yau and Fan 2012), *T. squamosa* is unusual because it has significantly lower photosynthetic potential irrespective of age and is more reliant on filter-feeding (Jantzen et al. 2008). It is known

to increase rates of filter-feeding with depth (Tedengren et al. 2000) and is common on the deeper fore-reef compared to other species, which are abundant in shallow (< 3 m) reef flat (Roa-Quiaoit 2005). My results lend weight to *T. squamosa* surviving and potentially thriving in turbid reefs and concur with other studies (Guest et al. 2008; Yong et al. 2022), who reported the species can survive well and even accelerate growth on impacted reefs.

3.5.3.2 Influences on monthly shell growth

On the contrary, at a seasonal level I found substantial site-to-site variability between the shells collected alive from Baik and Triangle, indicating that different environmental factors may play some role in regulation of intra- annual growth trends. At the low turbid reef Baik, growth generally accelerated seasonally and monthly SGI values negatively correlated with temperature, cloud cover, rainfall and salinity. Although in previous studies of giant clams increment widths positively correlate with SST (Aubert et al. 2009; Duprey et al. 2015; Komagoe et al. 2018; Zhao et al. 2021), the negative correlation found between SGI and temperature in Baik may relate to depressed growth above a thermal tolerance threshold of 27 °C (Schwartzman et al. 2011; Killam et al. 2021). As monthly SST varied between 28.11 °C and 30.47 °C at Baik, band thickness could become erratic and a stress reaction initiated (Schwartzman et al. 2011). Another explanation may be the small variation in SST throughout the year (~2°C), considered negligible in terms of contribution to growth rate (Gannon et al. 2017). As such, SST may play an indirect role in modulation of growth of shells herein due to its relationship with light. A positive correlation between light and growth has been observed in several tridacnid species on diurnal- (Sano et al. 2012; Yan et al. 2021) to seasonal scales (Lucas et al. 1989). Yan et al. (2021) found co-variance of daily growth rate with outgoing longwave radiation (OLR), but no significant correlation with SST for *Tridacna derasa*, indicating local effective solar radiation, is more important than SST in determination of band width. My results of an inverse relationship between monthly SGI and cloud cover may indicate at least some light dependence on growth in Baik caused by photosynthetic activity of endosymbionts.

Seasonal rainfall within Darvel Bay is enhanced by southwest (dry season) and northeast (wet season) monsoons. Rainfall may indirectly influence growth by washing

particulate matter into the region, increasing local turbidity and impeding photosynthetic processes (Gannon et al. 2017). High-resolution paleoweather reconstructions show abrupt decreases in daily increment thickness due to cold upwelling and strong wave action from typhoon and tropical cyclone activity (Komagoe et al. 2018; Yan et al. 2020). Monthly SGI in Baik shows a negative relationship with rainfall, but periods of accelerated growth in the mid to late wet season observed in some years may be attributed to enhanced vertical mixing after increased rainfall, bringing nutrient rich sub-surface waters to the surface, coupled with subsequent increased solar irradiance (Gannon et al. 2017; Yan et al. 2020). While Baik is indicative of a low turbid reef and K_d(490) and chlorophyll-*a* do not increase to the same extent as Triangle, I propose that a sequence of events similar to those recorded by Gannon et al. (2017), following: (1) higher rainfall during the early wet season, (2) resultant elevated K_d(490) and chlorophyll-*a*, (3) increased sunlight, which may result in favourable growing conditions.

Unlike Baik, shells from Triangle lacked any statistically significant relationship between monthly SGI and environmental variables. Yet, I did note a positive association between SGI and chlorophyll-*a* and K_d(490) in some months of the year. Triangle is a naturally turbid reef situated around 3.5 km from the mouth of the river Tingkayu, which discharges sediment to the site at low tide. Sediment input is likely land derived POM produced in the river basin by different mechanisms (e.g. freshwater productivity and remains of plants and microorganisms) and mineral sediment (Bainbridge et al. 2018). In similarity to mixotrophic corals (Fox et al. 2018), elevated chlorophyll-*a* concentrations at Triangle may indicate *T. squamosa* utilises chlorophyll-*a* as a key contributor towards metabolic requirements in reduced photic depth. Local irradiance may be of less importance for *T. squamosa* compared to other giant clam species as it can sustain growth in turbid reefs if a suitable local food source is available.

3.5.3.3 Influences on daily shell growth

At a daily scale, spectral characteristics of SGI chronologies revealed similarities with tidal range at Triangle. Significant spectral peaks occurred at around two to three days corresponding closely to peaks in maximum daily tide. Tidal rhythms are known to leave characteristic daily growth or geochemical patterns in many bivalves, such as differentiation of band widths that relate to spring-neap variability or daily tidal emergence (Goodwin et al. 2001) and trace element cyclicity (Warter and Müller 2017; de Winter et al. 2023). It has recently been suggested that under natural conditions the circadian clock genes of some bivalves may also run at tidal frequency, indicating behavioural patterns relating to a circadian cycle can be modulated by tidal rhythm (Tran et al. 2020). Based on this hypothesis, the presence of paired daily growth bands observed in the Triangle shells may relate to reef sediment flux controlled by a circadian rhythm paced to tides that result in variable light intensities. The thicker prismatic layer presumably related to higher irradiance may be accreted during flood tide, when clear water is transported offshore to the reef. At ebb tide when suspended sediment is transported to the reef lowering photic depth, smaller crystals could be deposited. However, more work is needed to elucidate the relationship between short-term tidal cycles and daily growth increments in tridacnids.

3.5.4 Conclusion

In this study, I provide the first assessment of growth in giant clams from turbid reefs using a mixed method approach. I investigated daily growth bands in thirteen *Tridacna squamosa* shells from different coral reef sites with varying degrees of turbidity. Similarities were found in annual growth rate between clear and turbid reefs, while there were differences in seasonal growth trends, indicating that an interplay of different environmental factors may regulate intra-annual growth between reefs. At a daily scale, I found differences in microstructure and spectral characteristics of daily bands, which may relate to tidal variability at the turbid site near a river source. These results do not indicate that turbidity negatively influences growth but are consistent with sustained growth, which may relate to the trophic plasticity of *T. squamosa*. This work supports growing evidence that resilient marginal habitats with elevated turbidity may serve as important conservation hotspots and my results are useful in the context

of management and conservation for *T. squamosa* under changing future oceanic conditions. Although encouraging, I cannot ascertain what this may mean for other parameters important for survival, such as skeletal biomechanical properties. Further work is needed on different tridacnid species to better understand the multiple environmental and physiological influences of turbidity.

4. Improving electron backscatter diffraction (EBSD) data in giant clams by post-acquisition refinement

4.1 Abstract

Electron backscatter diffraction (EBSD) is an important SEM-based microscopic technique that characterizes the crystallography of biominerals. It has shown great promise in the detection of finescale (nano- to microscale) variation in the carbonate skeletons of corals and bivalves, which can be used to understand biomineralization pathways and high-resolution environmental change, such as ocean temperature and acidification. However, many aragonite bivalve shells show an absence of EBSD diffraction patterns and low diffraction intensity, presenting a difficulty in understanding the crystallographic texture of shell aragonite due to poor data quality. Here, I aim to enhance EBSD data quality in the shells of two species of giant clam, *Tridacna squamosa* (fluted clam) and *Hippopus hippopus* (bear paw clam). I focus on post acquisition reanalysis of saved EBSD patterns, including optimizing band detection and the number of reflectors, to improve EBSD indexing rate. My results show an increase in indexing of the aragonite fraction by approximately 8% compared to default selection of parameters. The enhanced quality of the EBSD maps allows detailed investigation of crystallographic arrangements otherwise undetected, such as grain boundary misorientation or characterization of material properties (e.g. Young's Modulus). This optimized method for accurate EBSD data collection can be applied to other aragonitic biogenic carbonates and is applicable to samples with biomineral crystal sizes down to 1 μm, including many species of coral and gastropod. The optimization of EBSD data has broad implications for better understanding shell growth and biomineralization mechanisms in the fields of structural biology and (paleo)environmental reconstruction.

4.2 Introduction

Marine calcifiers, organisms that produce calcium carbonate ($CaCO_3$) biominerals, are increasingly under threat from a range of anthropogenic stressors acting at a local to global scale, such as ocean warming and acidification (e.g. Hoegh-Guldberg et al. 2007). To understand the future effects of such stressors on key calcifying biota, such as corals and bivalves, it is crucial to investigate their biomineralization response to periods of environmental change in the past (e.g. Allemand et al. 2011). Determining the crystalline structures of shell biominerals at a finescale (i.e. nano- to microscale level) is important because these relate directly to localized growth and material properties (e.g. hardness or Young's Modulus) of crystals (e.g. Kamaya 2009), providing insights into mechanisms of mineralization and the defensive capability of shells (Moynihan et al. 2021).

Electron backscatter diffraction (EBSD) is a scanning electron microscope (SEM) based crystallographic technique, involving an interaction of beam electrons with a tilted (at 70°) crystalline surface. It is commonly used in the fields of materials science and geology, but recently has been applied to a number of studies investigating the crystallographic arrangements of marine carbonates, including bivalve and brachiopod shells, corals, foraminifera and bryozoans (e.g. Ye et al. 2018; Coronado et al. 2019; Crippa et al. 2020; Pabich et al. 2020; Farfan et al. 2022; Grenier et al. 2023). It is one of few imaging techniques that allows precise and detailed mapping of crystallographic orientations at high spatial resolutions (sub-micron scale), which is required for determining localized changes of skeletal organization at a fundamental level (i.e. individual biomineral units). While other techniques such as X-ray diffraction (XRD) are also capable of providing information about crystal lattice orientation and structure (e.g. Iwase and Mori 2020), they lack the spatial resolution and ability to characterize microstructural features offered by EBSD. EBSD allows areas on the scale of hundreds of microns to be obtained rapidly (within minutes to hours depending on spatial resolution when using a CMOS sensor) and automatically, enabling the generation of rich microstructural maps with thousands of grains representing different periods of growth. Each grain mapped, or indexed, provides a wealth of information on mineral phase, crystalline structure, and orientation, which can be used together with other powerful high-resolution techniques, such as trace element geochemistry

using electron probe microanalysis (EPMA), or laser ablation inductively coupled plasma mass spectrometry (LAICPMS). The combination of crystallographic and geochemical methods can help us understand the impact of biomineralization on shell geochemistry, and vice versa.

In the past, some bivalve shells have shown low diffraction intensity or even complete absence of diffraction (e.g. Checa et al. 2019), hindering the interpretation of crystallographic texture due to poor data quality. Indexing for shell aragonite has proven challenging compared to calcite for several reasons. It suffers from issues of pseudo-symmetry, a phenomenon where a crystal structure belongs to one crystal symmetry group, e.g. orthorhombic, but shares many characteristics with a group of higher symmetry, e.g. monoclinic (e.g. Lenthe et al. 2019). This is compounded by high rates of twinning, where two or more crystal domains share some of the same crystal lattice points in a symmetrical manner (Bragg 1924). Furthermore, poor indexing success rates may be attributed to sample specific characteristics, such as the presence of a different mineral phase to the one being studied (e.g. calcite rather than aragonite), small grain sizes in the range of or below 1 μm, rough and irregular surface morphology, and the presence of non-crystalline phases, such as organic material or amorphous $CaCO_3$ (e.g. Dalbeck and Cusack 2006; Cusack et al. 2008). In giant clams, an absence of diffraction has been recorded for multiple specimens of *Tridacna gigas* (Gannon et al. 2017). To date, data has only been successfully acquired for a singular shell of *Tridacna derasa* (Agbaje et al. 2017) and *T. gigas* (Gannon et al. 2017), revealing a highly orientated crystallographic structure with superior mechanical properties (Agbaje et al. 2017). Variation in the crystallographic features of their biominerals between different environments is not understood, important because their shells are frequently used as high-resolution (paleo)environmental proxies (e.g. Aubert et al. 2009; Duprey et al. 2014; Arias-Ruiz et al. 2017).

In this study, I focus on the optimization of EBSD data quality for two giant clam species (*Tridacna squamosa* and *Hippopus hippopus*) by assessing and producing steps of EBSD data collection and post-processing reanalysis to increase indexing success rates. I characterize the microstructure and crystallographic texture of shells and highlight the use of analytical microscopy techniques such as EBSD to understand biomineralization and crystallographic change at a nano- to microscopic scale.

4.3 Methods

Two modern giant clam shells, *T. squamosa* (SS02B_CT) and *H. hippopus* (SS01B_SN) were collected from Darvel Bay within the Coral Triangle region of northeast Borneo (Sabah, Malaysia) in April 2019. The exterior of one valve of each shell was thoroughly rinsed and scrubbed to remove dirt and debris, before being left to air-dry. Afterward, valves were cut into ~1–2 cm thick slices along the axis of maximum growth (longitudinal from umbo to upper shell margin) and prepared as polished thin sections on glass slides (Figure 4.1), according to the preparation methods in chapter 2.

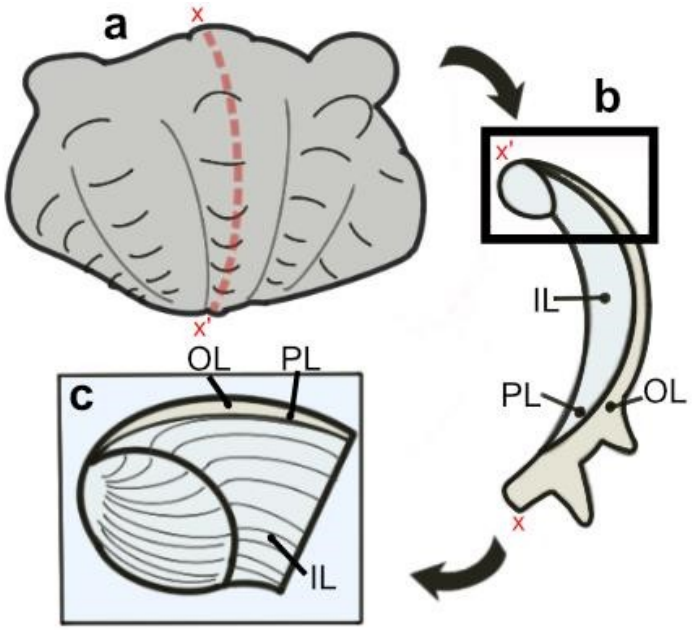

Figure 4.1. **Schematic showing section location of a giant clam shell along the maximum growth axis. (a) Shell valve with red vertical line indicating longitudinal cut along center. (b) Longitudinal shell slice from umbo to upper shell margin highlighting the inner layer (IL), outer layer (OL) and pallial line (PL). Bold rectangle highlights region in (c). (c) Thin section (approximately 60 µm thickness). Transect x-x' shows how cut location in image (a) relates to shell slice in (b).**

4.3.1 SEM

I used SEM for preliminary characterization of aragonitic microstructures within *T. squamosa* and *H. hippopus* shells. Giant clams have two shell layers—the inner shell layer (IL) and outer shell layer (OL), separated by the pallial line (PL). I focused on imaging the IL of sections because this layer is generally better preserved (e.g. Elliot et al. 2009) and is frequently used for high resolution analysis of (paleo)environment and climate. Polished thin sections were weakly etched with 0.5 % hydrochloric acid (HCl) for 15 sec to improve visibility of biominerals and then rinsed for 1 min with deionized water. Samples were dried by gently spraying a canister of compressed air across the surface of sections. Afterward, samples were sputter coated with gold palladium alloy (Au-Pd) and SEM was used to obtain in-lens secondary electron (SE) images of different microstructures at the School of Earth and Environmental Sciences, Cardiff University (chapter 2 for more information).

4.3.2 EBSD

4.3.2.1 Sample preparation

Areas of thin sections selected for crystallographic characterization with EBSD were based on prior identification of microstructure with SEM. Sections were repolished and subjected to several sequential mechanical grinding and polishing steps. This included first grinding with 600 silicon carbide grit, followed by a finer 1000 grit, a polish with 0.3 micron Aluminium oxide fine powder and a final polish with Logitech SF1 Polishing Fluid of colloidal silica, using a Logitech PM5 automatic polisher (70 rpm rotation, 2 x 10 min cycles). Afterward, copper tape was applied in rectangles around selected areas of samples for EBSD mapping to assist with locating areas of interest in the SEM and to help eliminate electron charging within the high-vacuum chamber (Figure 4.2). Samples were coated with a thin uniform layer of 3 nm carbon (Pérez-Huerta and Cusack 2009) using an Agar Turbo Carbon Coater. The fraction of the indexed pattern for aragonite (%) was tested with layers of carbon thickness between 2–6 nm, but 3 nm provided the strongest diffraction signal with negligible charging of the sample.

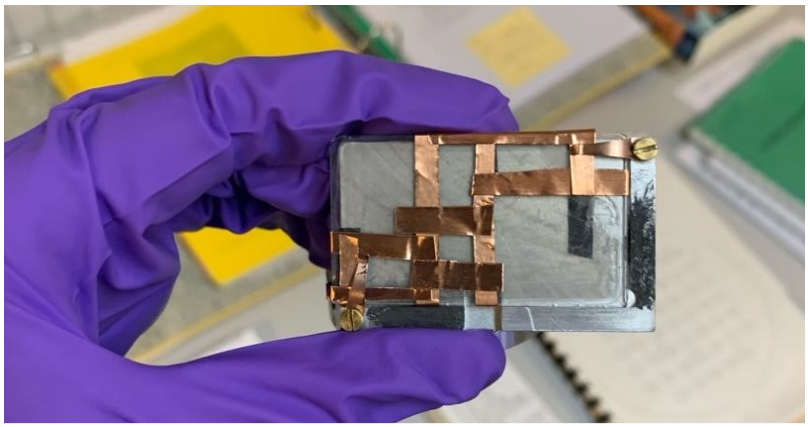

Figure 4.2. **Thin section showing rectangles of copper tape to help eliminate charging and to assist with targeting specific areas of the sample for EBSD mapping.**

4.3.2.2 Data acquisition

EBSD data acquisition involves directing an electron beam onto a sample surface to produce diffraction patterns from backscattered electrons. Such patterns can be indexed by the software and translated to crystallographic orientation. Acquisition was carried out using a Zeiss Sigma HD SEM equipped with a Nordlys-2 EBSD detector at the School of Earth and Environmental Sciences, Cardiff University. In the SEM, samples were tilted at an angle of 70° using a pre-tilted holder with ~10 mm working distance and ~193–194 mm detector insertion distance. Diffraction patterns were collected at a resolution of 0.5 µm step size, 20 kV accelerating voltage, 60 µm aperture in high current mode with a 2.7 nA nominal beam current and 2 x 2 camera (320 x 240 pixels) binning. Total acquisition time was approximately 27 hours for *H. hippopus* (SS01B_SN) and 12 hours for *T. squamosa* (SS02B_CT), with map dimensions of 1024 x 768 pixels and 681 x 510 pixels respectively. Exposure time was 96.8 ms for SS01B_SN and 127.58 ms for SS02B_CT.

Electron backscatter patterns (EBSP) were indexed using Oxford Instruments AZtec 6.0 software. Parameters chosen for the indexing of the aragonite unit cell were the OINA database *a* = 4.9614 Å, *b* = 7.9671 Å, *c* = 5.7404 Å space group 62 Pmcn (de Villiers 1971). Aragonite indexed with the OINA database provided pole figures with a preferred crystallographic orientation of the [001] axis (*c*-axis) orthogonal to growth bands, commonly reported for bivalves in previous literature (e.g. Frýda et al. 2010). The use of other available databases within the software such as the HKL database is

possible, and produces similar index rates (see results), but switches crystal axes to *a* = 5.7407 Å, *b* = 4.9611 Å, *c* = 7.9673 Å so that the [100] axis (*a*-axis) becomes orthogonal to growth lines instead of the [001] axis.

4.3.2.3 Post-acquisition refinement

EBSD post-acquisition refinement is a set of techniques applied to enhance and improve the quality of the EBSD data obtained after the initial data acquisition phase. While initial acquisition provides raw data on crystallographic orientations, grain boundaries, and phase, post-acquisition refinement aims to correct errors in indexing and increase indexing success rate, to extract more detailed insights from the acquired data.

Post-acquisition refinement to optimize index rates of aragonite was performed on data with EBSD patterns stored at indexing using AZtec 6.0 software (Oxford Instruments). Maps were reanalysed changing (1) the number of reflectors, (2) band detection mode, (3) Hough resolution and (4) area of interest (AOI). (1) Reflectors are specific Kikuchi bands (i.e. diffracting planes of backscattered electrons) to be considered in the indexing process. Changing the number of reflectors varies which Kikuchi bands in the EBSD pattern are correlated to the diffracting lattice planes of the crystal structure in the software. (2) Band detection mode changes the detection of band positions and hence indexing success. Hough-based band detection converts the image from the EBSD camera to Hough space by identifying the positioning of Kikuchi bands using the Hough transform (i.e. representation of lines in polar coordinates ρ, θ, where ρ is the perpendicular distance from the line to origin, and θ is the angle made with the x-axis), assuming bands are linear (e.g. Thomsen et al. 2013). Refined Accuracy band detection utilizes a secondary band refinement step in addition to Hough-based detection, which fits the simulated band to the true band recorded as an EBSP, while also considering the width and curve of the band (e.g. Thomsen et al. 2013). (3) Hough resolution relates to the angular resolution and accuracy of orientation data (e.g. Winkelmann et al. 2020). A dataset with very low angle boundaries between grains (e.g. <1° misorientation angle) will require a higher Hough resolution to resolve, but data acquisition will take longer. (4) The AOI is the defined area of the EBSP used for band detection, which is set by a given band detection area x, area y and area radius.

A larger AOI will include more of the EBSP in indexing. Higher priority is given to bands at or near the centre of the AOI (Aztec EBSD User Guide). Thus, bands which are more reliably detected are used in indexing, making the process of indexing more robust.

4.3.2.4 Data analysis

Data analysis was carried out in MTEX toolbox 5.7.0 for MATLAB R2022b (Mainprice et al. 2011). The raw EBSD files and MATLAB code for data analysis carried out in this chapter are available from the Mendeley Data Repository given in Appendix B. Grain boundaries were defined by using a threshold misorientation angle of 2° with adjacent grains and minimum grain size was set to 3 pixels, in comparison to 10 pixels previously used for giant clam aragonite (Agbaje et al. 2017) because grain sizes were notably small (around and under 1 μm) in some areas. Points with mean angular deviation (MAD) over 1° were discarded due to low indexing confidence between the measured and the calculated angles between bands, and remaining grain boundaries were smoothed. Zero solutions, defined as missing data from parts of the sample that showed an absence of diffraction, were not interpolated or filled with a 'fill' command to avoid over-simplification of the dataset in the presence of small grains.

EBSD band contrast images, EBSD colour-coded orientation maps (inverse pole figure maps) and pole figures for *T. squamosa* and *H. hippopus* were assembled using MTEX. Pole figures were plotted on a lower hemisphere projection in the Y-X projection plane, with spread of the poles controlled by half-width (e.g. Crippa et al. 2020), which controls the span of the EBSD data. An optimal half-width of approximately 4° for the data was computed based on the mean orientation of grains using the kernel function for orientation distribution function (ODF) estimation in MTEX. The strength of the crystallographic preferred orientation was derived from the maximum intensity of contoured pole figures and statistically represented as multiple of uniform density (MUD) values. MUD values quantify the sharpness of texture and a strong crystal co-orientation will have a higher MUD value than a low or random coorientation (e.g. Casella et al. 2018a, b; Crippa et al. 2020).

4.4 Results

4.4.1 Microstructure

The preliminary characterization of microstructure of the IL in *H. hippopus* and *T. squamosa* is shown in Figure 4.3. The *T. squamosa* shell showed a complex crossed-lamellar microstructure (Figure 4.3b), intersected by thin bands that were presumed to be daily growth bands. In *T. squamosa*, individual biomineral units resembled lath-like structures (i.e. third order laths) (Figure 4.3d). In comparison, the *H. hippopus* shell consisted of wider daily growth bands that consisted of a layer of triangular prismatic crystals, adjacent to smaller biomineral crystals (Figure 4.3c).

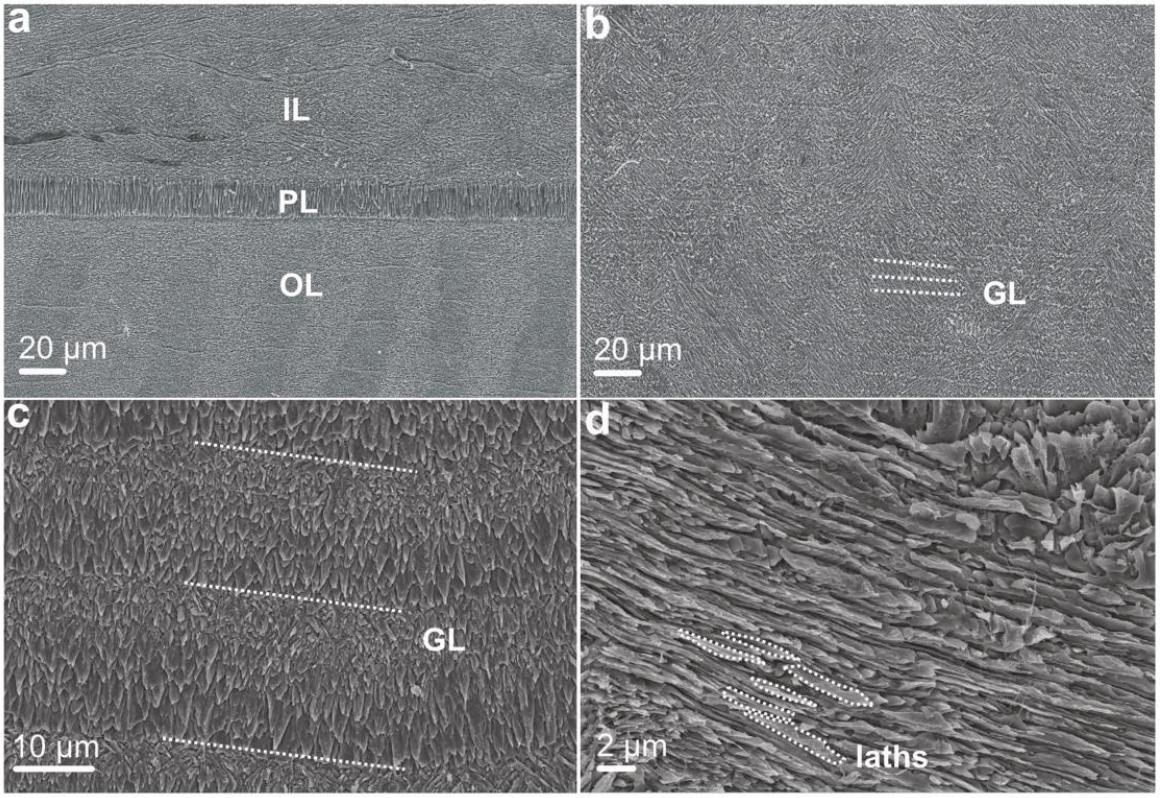

Figure 4.3. **SEM in-lens secondary electron images showing the microstructure of the giant clam shells. IL: inner shell layer; OL: outer shell layer; PL: pallial line; GL: growth lines, or bands. (a) OL and IL divided by prismatic PL (specimen SS02B_CT, *Tridacna squamosa*); (b) daily GL in IL running perpendicular to the direction of growth in complex crossed-lamellar microstructure (specimen SS02B_CT, *Tridacna squamosa*); (c) paired daily GL in IL that consist of a prismatic type layer adjacent to smaller crystals (specimen SS01B_SN, *Hippopus hippopus*); (d) third order laths (biomineral units) that stack into larger layered structures (specimen SS02B_CT, *Tridacna squamosa*).**

4.4.2 EBSD post-acquisition refinement

Post-acquisition refinement of stored EBSD patterns was used to optimize index rates of aragonite. Manual selection of the number of reflectors (i.e. list of Kikuchi bands to be considered in the indexing process) within the OINA and HKL databases ranged between 2 to 82 reflectors. The relationship between fraction of indexed pattern for aragonite (%) and number of reflectors peaked at 67 reflectors in the OINA database and 63 reflectors in the HKL database (Figure 4.4; 4.5). This increased indexing by 5% compared to default selection of 49 reflectors, while keeping mean angular deviation (MAD) under 1°. Refined accuracy band detection mode compared to routine Hough-based indexing further increased indexing by approximately 3% and an example is shown by the grey point in Figure 4.4. Despite further investigation of Hough resolution (Table 4.1) and area of interest (AOI) (Table 4.2), alteration of these parameters only marginally increased the percentage of the indexed pattern of aragonite (~0.2%).

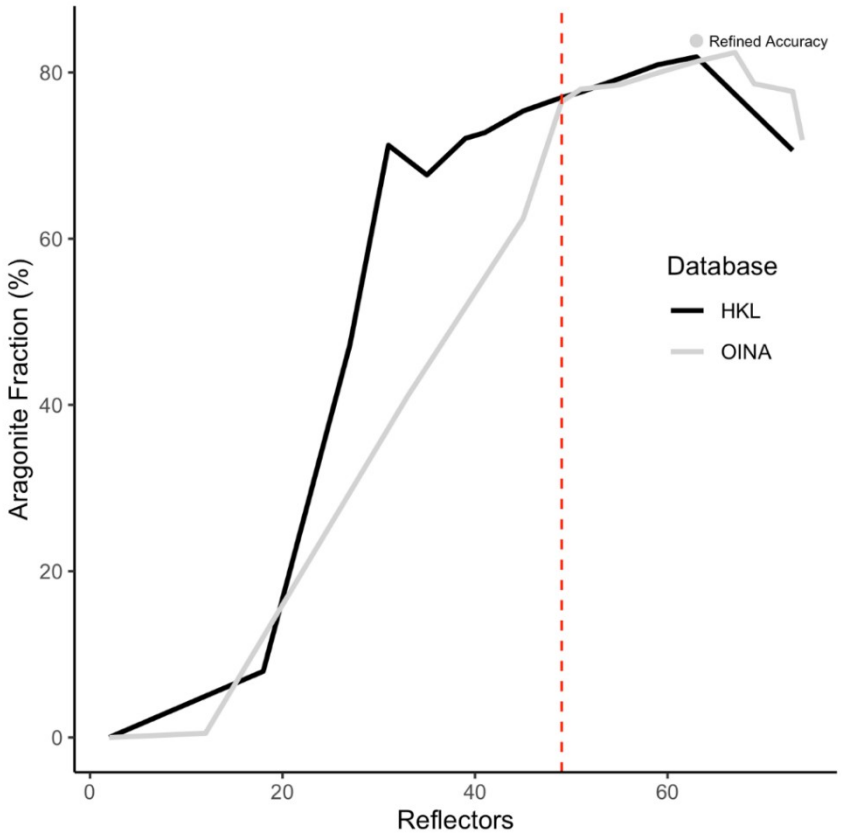

Figure 4.4. **Relationship between fraction of indexed patterns for aragonite (%) and manual selection of number of reflectors for aragonite in SS02B_CT within the OINA and HKL databases in AZtec 6.0 software (Oxford Instruments). Parameters used for the indexing of the aragonite unit cell were the orthorhombic symmetry system from the OINA database (space group 62 P n m a) *a* = 4.9614 Å, *b* = 7.9671 Å, *c* = 5.7404 Å and HKL database (space group 62 P n m a) *a* = 5.7407 Å, *b* = 4.9611 Å, *c* = 7.9673 Å. Single grey point is an example of indexing improvement of the refined accuracy band detection approach at 63 reflectors compared to routine Hough-based indexing. Dashed red vertical line indicates the default number of reflectors (49) the software selects for aragonite.**

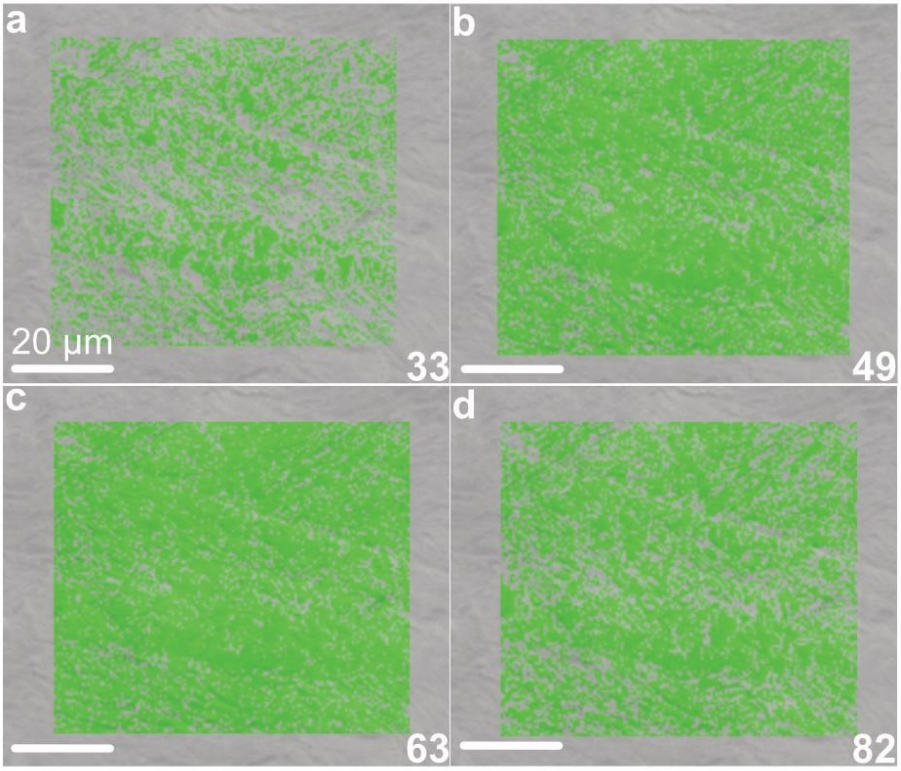

Figure 4.5. **Fraction of indexed pattern for aragonite (%) in SS02B_CT using standard Hough based detection by manually selecting the number of reflectors for orthorhombic aragonite with the HKL database in AZtec 6.0 software (Oxford Instruments). Patterns indexed had a mean angular deviation (MAD) below 1°. (a) 33 reflectors (41.06% aragonite); (b) 49 reflectors (76.48% aragonite); (c) 63 reflectors (81.31% aragonite); (d) 82 reflectors (64.66% aragonite). Scale bars = 20 µm.**

Table 4.1. **Hough resolution and indexed fraction of aragonite (%) for *T. squamosa* (SS02B_CT) using the HKL database. Grey shaded cells represent default selection of parameters by the software.**

Hough resolution	Aragonite fraction (%)
40	80.82
50	84.14
60	83.91
70	79.82
80	84.15
90	77.64
100	80.40

Table 4.2. **Area of interest (AOI) parameters (X, Y and radius) and indexed fraction of aragonite (%) for *T. squamosa* (SS02B_CT) using the HKL database. Grey shaded cells represent default selection of parameters by the software.**

BD Area X	BD Area Y	BD Area Radius	Aragonite Fraction (%)
0.50	0.38	0.45	82.55
0.50	0.38	0.40	79.42
0.45	0.38	0.45	81.40
0.40	0.38	0.40	76.35
0.50	0.38	0.50	84.15
0.55	0.43	0.55	82.63
0.60	0.48	0.60	83.07
0.45	0.33	0.45	80.60
0.40	0.28	0.40	72.84

4.4.3 EBSD crystallographic texture in *H. hippopus* and *T. squamosa*

EBSD band contrast (BC) images are presented with associated pole figures in Figure 4.6. BC images are greyscale EBSD images that represent signal intensity of each data point measured. When the electron beam scans over an area with high organic content or another factor impeding diffraction, the signal is absent and the BC datapoint is black. When the mineral is hit by the electron beam, a stronger diffraction signal is obtained and the BC datapoint is lighter/brighter. Hence, dark pixels represent poor pattern quality and bright pixels represent high pattern quality. Associated pole figures of BC images are a stereographic projection (lower hemisphere projection) of aragonite planes and enable the distribution of 3D orientation data to be visualized in 2D by the conversion of crystallographic directions to points. Pole figure axes are defined by an external reference frame (X, Y, Z correspond to E-W, N-S and out of plane, respectively), showing clustering of points around specific direction(s) (i.e. pole maxima).

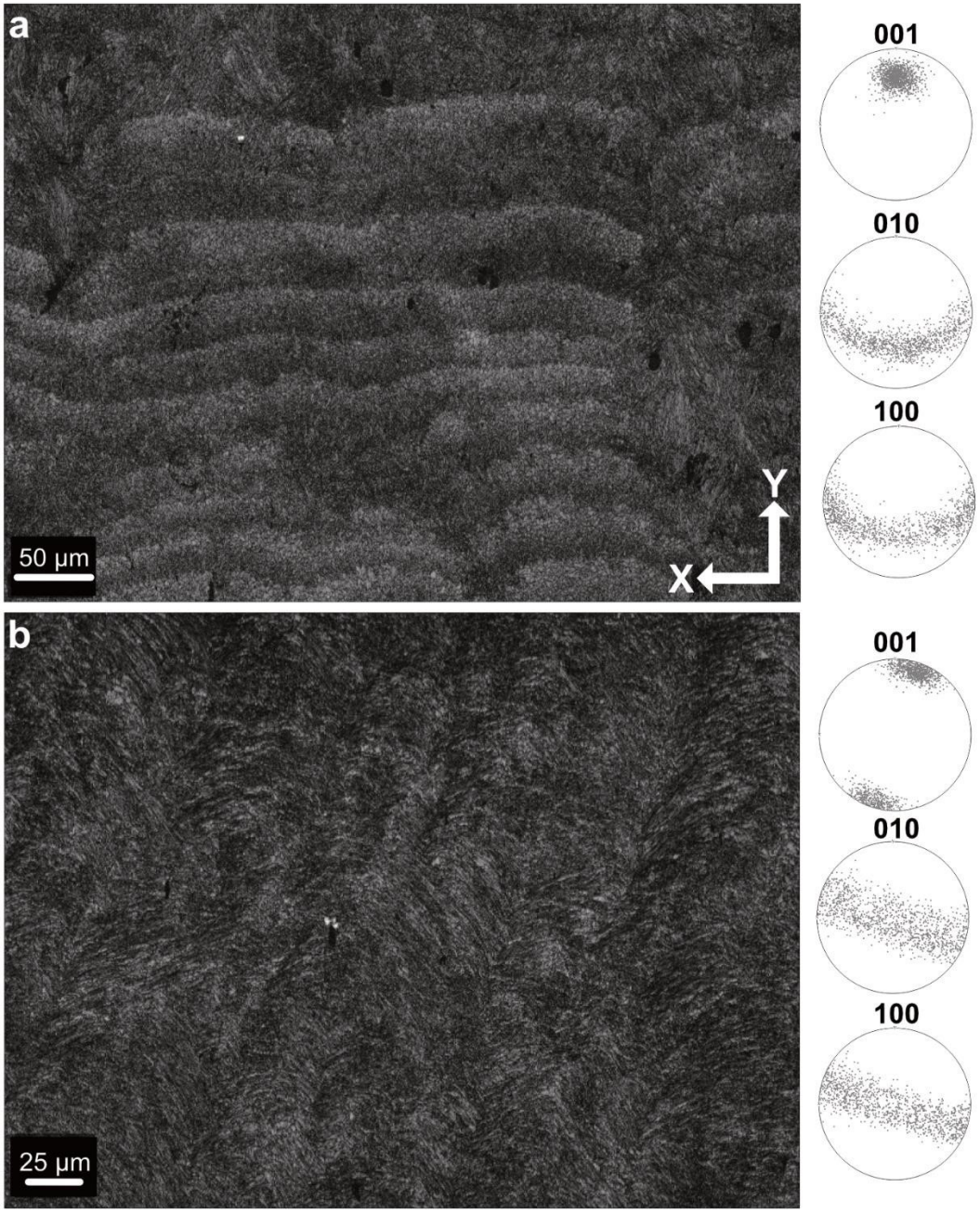

Figure 4.6. **EBSD band contrast (pattern quality) images of the inner shell layer in giant clam shells. (a) Paired daily growth lines of *Hippopus hippopus* (SS01B_SN) that correspond to the IPF-Y map in Figure 4.7 and the highlighted microstructure in Figure 4.3c; (b) complex crossed-lamellar microstructure of *Tridacna squamosa* (SS02B_CT) that correspond to the IPF-Y map in Figure 4.8 and highlighted microstructure in Figure 4.3b. Associated adjacent pole figures display density distribution for image (a) and (b), respectively. Pole figures show indexed aragonite points with a preferred crystallographic orientation of the [001] axis approximately orthogonal to growth lines.**

EBSD crystallographic preferred orientation (CPO) data are represented as colour-coded orientation maps and are shown with corresponding contoured pole figures that represent the density distribution of indexed data points in Figure 4.7 for *H. hippopus* and Figure 4.8 for *T. squamosa*. Orientation maps are coloured according to the inverse pole figure (IPF) colour key for aragonite referenced to the Y direction of the external reference frame (shown on Figures 4.7; 4.8), where similar coloured grains relate to similar crystallographic orientations. Grains represented in red/pink have their [001] axis pointing in the X direction, whereas green tones represent the [010] axis and blue tones the [100] axis orientated in the Y direction. The strength of the CPO is quantified using multiple of uniform distribution (MUD) values, which are derived from the maximum intensity of contoured pole figures of crystallographic axes (*a*-axis, [100]; *b*-axis, [010]; *c*-axis [001]). A higher MUD value represents a stronger co-orientation strength, indicating an organized crystallographic texture that is highly orientated, while a random orientation of crystallographic distribution will have an MUD of 1 or below (e.g. Crippa et al. 2020).

Assessment of the crystallographic texture of the *H. hippopus* and *T. squamosa* shells revealed a coherent crystallographic preferred orientation of the aragonite [001] axis in both samples, showing one strong pole figure maximum (Figure 4.7; 4.8). Both samples showed a belt-like distribution of the [100] axis and [010] axis around the [001] axis, with [001] parallel to the growth direction and [100] and [010] weakly parallel to growth bands. Despite this similarity, MUD values derived from pole figures showed variation between the two shells, which likely reflect the differences in microstructural arrangements identified with SEM. The prismatic-type microstructure documented in *H. hippopus* (S001B_SN) showed a higher crystal co-orientation strength with MUD of 34, compared to MUD of 23 in *T. squamosa* (SS02B_CT).

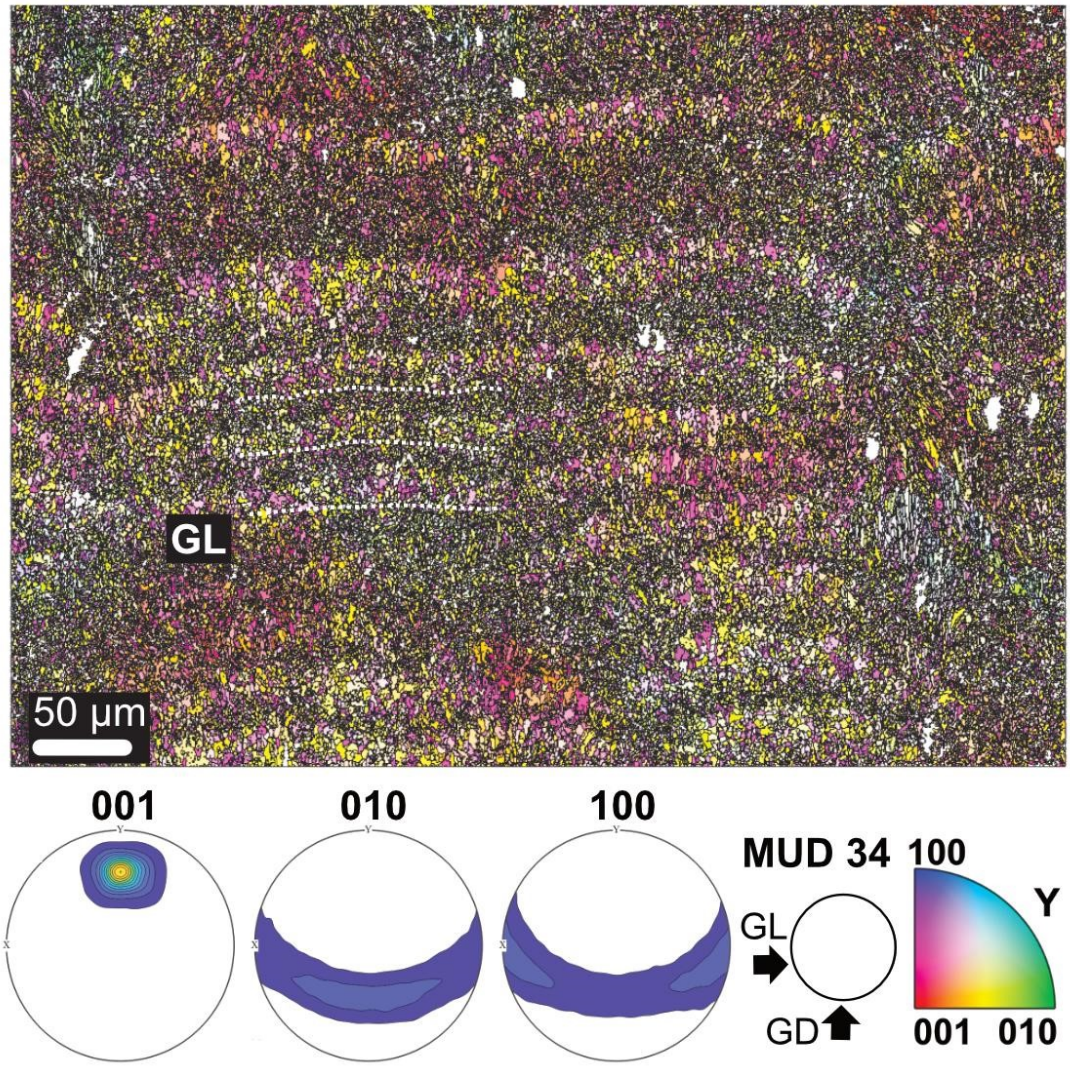

Figure 4.7. **EBSD inverse pole figure (IPF-Y) map showing the microstructure and texture of paired daily growth lines within the inner layer of a *Hippopus hippopus* shell (SS01B_SN), corresponding to band contrast image in Figure 4.6a. Contoured pole figures show density distribution of all points indexed as aragonite and preferred crystallographic orientation of the [001] axis. GL: growth lines, GD: growth direction. Aragonite co-orientation strength has an MUD value of 34.**

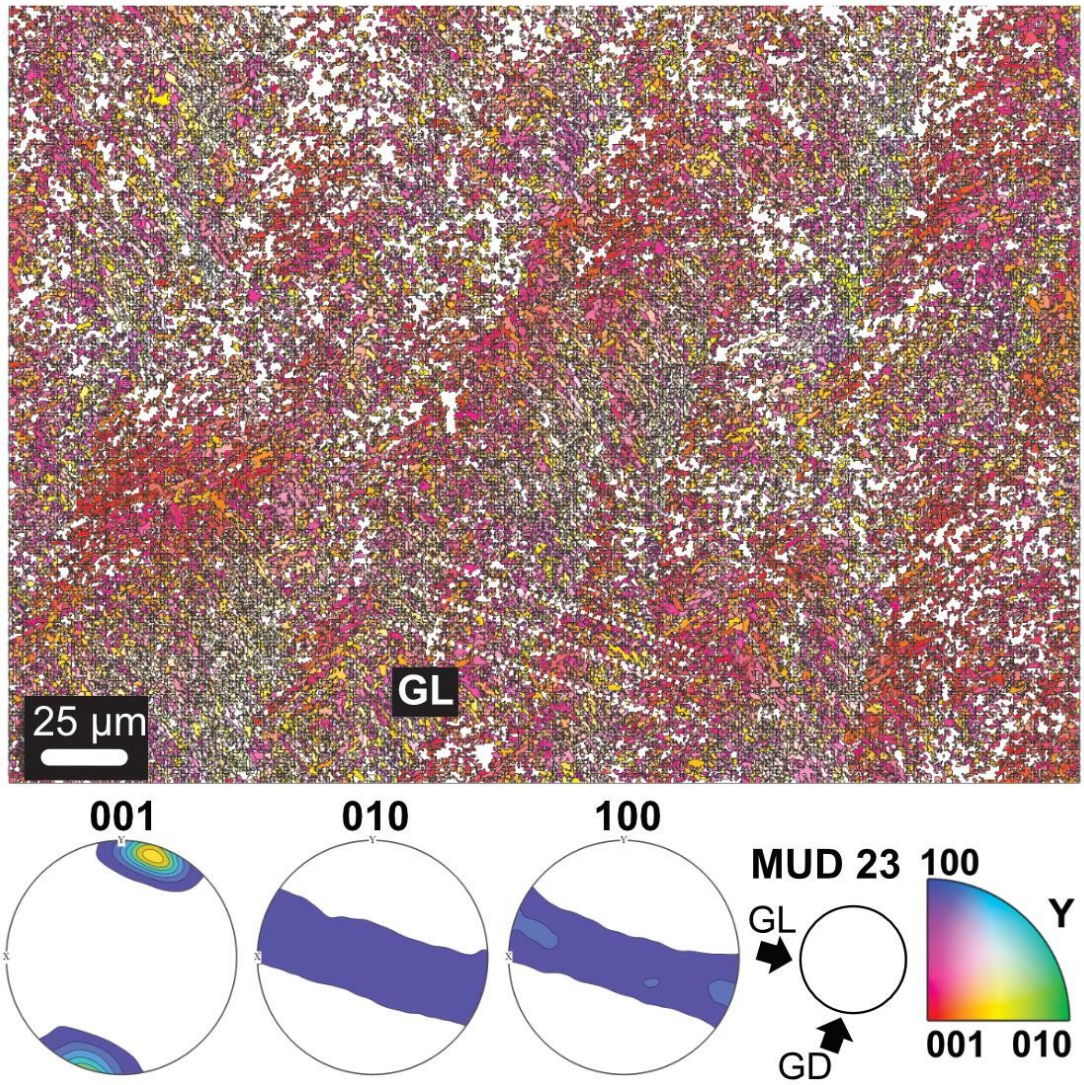

Figure 4.8. **EBSD inverse pole figure (IPF-Y) map showing the complex crossed lamellar microstructure and texture of the inner layer of a *Tridacna squamosa* shell (SS02B_CT), corresponding to band contrast image in Figure 4.6b. Contoured pole figures show density distribution of all points indexed as aragonite and preferred crystallographic orientation of the [001] axis. GL: growth lines, GD: growth direction. Aragonite co-orientation strength has an MUD value of 23.**

4.5 Discussion

In this chapter, I aimed to optimize the parameters related to EBSD data collection in two species of aragonitic giant clam (*T. squamosa*; *H. hippopus*). I focused on using post-acquisition reanalysis of saved EBSD patterns to improve indexing success rate, which represents the percentage of diffraction patterns that can be successfully matched to crystallographic orientations in the sample. My results showed an increase in indexing of the aragonite fraction by approximately 8% compared to default parameters selected by the software. Manually changing the number of reference reflectors produced the largest difference in indexing, with an improvement of 5%. This was followed by the selection of refined accuracy band detection mode compared to Hough based detection, with a further increase of approximately 3%. Although the indexing success rate of biogenic carbonates is rarely reported, the improvement of my data to over 80% is in line with (Wichern et al. 2023) or higher (Moreno-Azanza et al. 2013; Coronado et al. 2019; Negrini et al. 2022) than raw EBSD data from previous studies. In complex non-biogenic structures, an indexing rate of approximately 90% has been classified as 'particularly good' (e.g. van de Moortèle et al. 2010). Yet, considering the highly heterogenous nature of biogenic materials and variation of organic material between crystals, I propose that above 80% is a robust value to obtain reliable and accurate results in the crystallographic characterization of biominerals.

At current, there is an overreliance on EBSD image cleaning, through (1) removal of wild spikes, related to exclusion of single indexed points not surrounded by similar orientations and (2) nearest neighbour extrapolation, involving reducing the number of non-indexed points by interpolation of surrounding neighbour grains (e.g. Li et al. 2023). However, it is easy to misapply these steps so that the EBSD data is no longer a true representation of the sample, and many authors perform this data modification routinely, often with little transparency regarding data cleaning steps (Brewer and Michael 2010). Such treatment of image data is not accepted in other fields, and should be relied upon less with EBSD, especially as detector accuracy, sensitivity and speed improves with the advent of CMOS detectors. I propose instead of rigorous clean up procedures, similar significant gains in data quality may be achieved with relatively minor adjustments of acquisition settings, such as those provided in this article.

With robust data collection, EBSD is a promising technique for understanding the impact of environmental and climate change on biomineralization, and by extension the biomechanical properties of calcifying taxa. Microstructural and crystallographic behaviours are at the most fundamental level of skeletal organization and are key to understand biomineralization scenarios (e.g. Mastropietro et al. 2017). Several recent studies of corals and molluscs have showcased their application as sensitive proxies of the surrounding environment, demonstrating variation in crystallographic organization in response to changing ocean temperature and acidification, for example (Wolfe et al. 2013; Fitzer et al. 2014; Hennige et al. 2015; Fitzer et al. 2016; Coronado et al. 2019; Knights et al. 2020). However, the use of crystallographic features as tracers of the environment is still in its infancy. More data is needed to advance our current understanding of how crystal growth dynamics reflect changing environmental conditions in marine calcifiers.

In giant clams, most previous work has focused on how shell growth rate (e.g. Zhao et al. 2021) or geochemical tracers in shells (e.g. Elliot et al. 2009) can be used to track environmental changes. However, how their shell crystallographic properties might decode environmental signals is not known. EBSD data has been previously difficult to acquire in giant clams, and an absence of diffraction reported, likely owing to microstructural type, small grain sizes and presence of organic material between and on the surface of biominerals (Gannon et al. 2017). Previous studies have only reported results for singular individuals of *T. derasa* and *T. gigas* (Agbaje et al. 2017; Gannon et al. 2017), demonstrating a highly co-orientated crystallographic texture with a common preferred orientation of the [001] axis. This is the most common orientation in biogenic aragonite (Checa and Rodrıgueź -Navarro 2005), caused by the accumulation of charged ions on the [001] plane (Addadi and Weiner 1992). Yet, coorientational order on the [001] axis shown by pole figures reveal important differences, such as crystallographic co-orientation strength, represented by MUD statistics (e.g. Crippa et al. 2020). Moreover, the [010] and [100] axes provide information on orientation around the [001] axis (e.g. Agbaje et al. 2017). Although the focus of this study was to optimize EBSD data with post-processing methods and not interpretation of the data, the two EBSD maps showcased herein reveal clear differences in MUD values and orientation properties, which warrant future investigation. Despite previous difficulties, it has been demonstrated that careful

optimization of beam and software parameters to individual sample requirements mean a plethora of information on giant clam biomineralization responses have the potential to be unlocked.

4.5.1 Conclusion

In this study, I provided first overview of the optimization of EBSD maps in giant clam shells, allowing detailed investigation of their crystallographic arrangements. EBSD imaging provides quantitative information on mineral phase, crystalline structure and orientation of the grain. Mapping these features across a sample surface can be used to detect variation in crystallographic texture, which in turn can be linked to environmental change (e.g. modification to the orderliness of crystals under changing temperatures and acidification). The value of the EBSD method has so far been shown for diverse calcifying taxa, including bivalves and corals, enabling novel insights in paleoenvironmental research such as providing unprecedented detail on skeletal organization. Resolving the nano- to microscale signatures of how giant clams grow using EBSD could further our understanding of the current and future effects of a rapidly changing ocean, but also help to elucidate the mechanism of shell mineralization. This optimized method for accurate EBSD data collection should be employed instead of relying on image cleaning and smoothing, which is widely used and leads to misrepresentation of data. A similar strategy can be applied to other biogenic carbonates and is applicable to samples with biomineral crystal sizes down to 1 µm.

5. Biomineralization plasticity in giant clam shells from turbid reefs: integrating physical and geochemical pathways

5.1 Abstract

Coral reefs are highly vulnerable to a multitude of global to local stressors associated with anthropogenic change and are declining at an alarming rate. Understanding the biomineralization of reef-building animals in different reef environments is key to unravelling how they respond to a rapidly changing ocean. One unexplored aspect is their biomineralization in turbid coral reefs, which are forecast to increase throughout the 21st century and are resilient conservation hotspots. Here, I map the nano- to microscale architectural and chemical features of the shell biominerals of an important marine calcifying bivalve — the mixotrophic giant clam *Tridacna squamosa* — along a turbidity gradient in a locality at the Coral Triangle. I investigate microstructure, crystallographic texture, and microspatial distribution of element-to-calcium ratios (magnesium/calcium, strontium/calcium) to understand how both physical and geochemical signatures are modified by turbid reefs. I reveal variation in microstructure and crystallographic organization with significant differences in both Mg/Ca and Sr/Ca between high turbid and low turbid reef environments. My results demonstrate shells formed in a turbid reef generally have paired daily growth increments with a highly organized crystalline structure and significantly lower Mg/Ca and Sr/Ca, hinting at biomechanically superior shells compared to low turbid reefs. I hypothesize that observed variations may be related to differences in mixotrophic feeding between reefs, representing compensatory responses for increased resilience to turbidity. Overall, this work suggests that the environmental conditions present on turbid reefs may be a key driver in shaping biomineralization plasticity in giant clams, important in anticipating species resilience in the face of a changing world.

5.2 Introduction

Tropical coral reefs are highly vulnerable to the impacts of anthropogenic change (e.g. Reid et al. 2009), already experiencing system-wide declines in many locations around the world due to large-scale coral bleaching from global warming, disease, and overexploitation (e.g. Bellwood et al. 2009). Comprehensive understanding of how reef building species make their biomineral skeletons in the face of future climate change can help understand their sensitivity to changing oceanic conditions (Tambutté et al. 2011). It is crucial to understand skeletal formation processes and how these translate to resilience in turbid coral reefs because turbidity caused by anthropogenic activity is forecast to increase throughout the 21st century (Zweifler et al. 2021).

Similar to many reef species, giant clams are threatened by a multitude of local to global stressors, including suffering from mass bleaching events due to thermal stress (e.g. Junchompoo et al. 2013; Apte et al. 2019). However, it can be challenging to disentangle how changes in their shells correlate to their surrounding environment because, like all biogenic carbonates, they are affected by both environmental factors and physiological adjustments (vital effects) governed by the organism (Urey et al. 1951). Giant clams are unique among bivalves in hosting zooxanthellae symbionts in their outer shell mantle, which adds further complexity to the interpretation of biomineralization because symbionts undergo unique light dependent physiological responses (Ip and Chew 2021). As such, the physiology of not only the host, but also the activity of symbionts (family Symbiodinaceae) (e.g. Pätzold et al. 1991; Lucas 1994) must be considered as a factor in biomineral production.

So far, work exploring differences in the balance between autotrophy and heterotrophy has shown that the fluted giant clam *Tridacna squamosa* can sustain similar rates of growth in turbid and low turbid reefs, likely due to compensatory heterotrophic feeding under turbidity (refer to findings of chapter 3, Mills et al. 2023). It is highly mixotrophic and has a photoautotrophic range extended by heterotrophy (Jantzen et al. 2008). Relative contributions of autotrophy versus heterotrophy are likely particularly dynamic for *T. squamosa* from turbid environments with diverse food resources (refer to findings of chapter 3, Mills et al. 2023), in similarity to corals with high mixotrophic capacity

(Fox et al. 2018; Travaglione et al. 2023). Yet, to understand how its biomineralization changes in response to turbidity, more information aside from growth rate is needed, especially in relation to the properties of shell biominerals that are important for health and survival of the organism.

Microstructural and crystallographic arrangements (i.e. shell architecture) are the fundamental building blocks of skeletal organization and strongly influence shell biomechanical properties (Moynihan et al. 2021). They are known to vary in response to changing environmental conditions in many marine calcifiers, such as corals and bivalves (e.g. Fitzer et al. 2014; Hennige et al. 2015; Coronado et al. 2019; Knights et al. 2020). In giant clams, experimental studies have shown microstructural variation in relation to light (Warter et al. 2018), warming and pCO_2 (Brahmi et al. 2019), suggesting these parameters modify biomineralization pathways. In the natural world, an environmental gradient dictated by nutrient flux has also proven to be a key factor in modifying daily to seasonal scale microstructure (Gannon et al. 2017). At current, associated crystallographic properties of microstructures are only known from studies of singular giant clam shells and show a strong preferred crystallographic orientation on the [001] axis and highly organized biomineral units (Gannon et al. 2017; Agbaje et al. 2017), contributing to the optimization of the organism's protective shell capacity (Agbaje et al. 2017). To date, however, it has not been investigated how shell microstructure and crystallography change across a natural environmental gradient, which offers insight into the ability of giant clams to make protective shells under changing oceanic conditions and identify the resilience of species.

The geochemical fingerprint of shells is thought to underpin biomineral design, associated crystallographic properties and their relationship to the environment because geochemical variations play a key role in the dictation of mineral formation (e.g. Armstrong et al. 2022). However, giant clams show heterogenous composition of trace and minor elements including strontium (Sr), magnesium (Mg) and barium (Ba) between (Elliot et al. 2009) and within their aragonite shell layers (Warter et al. 2018; de Winter et al. 2023). Even on subdaily temporal scales, there are large variations in El/Ca that are likely strongly related to diurnal cyclicity and inherent biological rhythm (de Winter et al. 2023). In the past, Mg/Ca and Sr/Ca have been particularly difficult to interpret because they are hypothesized to be under strong biophysiological control by

the organism (Elliot et al. 2009; Sano et al. 2012; Hori et al. 2015; Warter et al. 2015; Arias-Ruiz et al. 2017; Warter et al. 2018; de Winter et al. 2023). Mg has been shown to be highly associated with the organic components of the shell (e.g. Yao et al. 2019) and is often substantially elevated near the organic-rich daily growth lines in giant clams, revealing daily Mg cyclicity (e.g. Warter et al. 2018). Similarly, Sr cyclicity has been observed at a daily scale, but is associated with active transport mechanisms such as the calcium pump Ca^{2+}-ATPase at mantle epithelia running on a diurnal cycle (Sano et al. 2012; Hori et al. 2015).

To better understand the fundamental mechanisms of biomineralization in giant clams, and how shell construction changes with environmental conditions, I investigate the distribution of microstructure, crystallographic texture and element-to-calcium ratios (Mg/Ca; Sr/Ca) of biominerals in fluted giant clams *Tridacna squamosa*. Firstly, I assess crystallo-chemical variation at the intra-shell scale by analyzing different shell layers (i.e. inner shell layer, outer shell layer and the myostracum, involved in shell muscle attachment). Secondly, I compare features between shells collected from high turbid and low turbid coral reefs in Sabah to understand the impact of turbidity on biomineralization. I build upon previous studies and discuss the potential role of the environment and physiology on (1) the giant clam host and (2) associated photosymbionts, with a focus on potential relative contributions from mixotrophy. Overall, this study has implications for how giant clams build their protective shells under changing oceans and pinpointing plasticity in biomineralization responses.

5.3 Methods Summary

This study was performed on four modern *T. squamosa* giant clam shells collected alive from the Baik (low turbid) and Triangle (high turbid) reefs (Triangle: SS_CT, ZW156; Baik: SS_BAIK, NS207) in Darvel Bay. In chapter 2, it was determined that key environmental differences between these reefs are K_d(490) (indicator of turbidity within the water column), chlorophyll-*a* and total suspended solids, which are elevated year-round in Triangle compared to Baik. Lifespan was estimated by counting daily growth bands (refer to chapter 3 and Mills et al. (2023)) and ages ranged between approximately 1.86 and 7.23 years (Table 5.1). Two of the four specimens sampled

had a comparable lifespan of around 3 years and were collected at each site one day apart, allowing for direct comparison. Analysis was carried out in ontogenetic years 1, 2 and 3 for SEM and EBSD and ontogenetic year 2 for EPMA.

Table 5.1. **List of four studied samples of *Tridacna squamosa* from Baik (low turbid) and Triangle (high turbid) reefs in Darvel Bay. BA = Baik; TR = Triangle. Estimated age calculated from daily growth increments in chapter 3. Collection status: L = shells collected alive in either 2019 or 2020. SEM = scanning electron microscopy; EBSD = electron backscatter diffraction; EPMA = electron probe microanalysis.**

Site	Species	Sample ID	Collection Status	Estimated Age	Mean growth (mm/yr)	Method
TR	TS	SS_CT	L 2019	3.40	5.24 ± 1.46	SEM, EBSD, EPMA
BA	TS	SS_BAIK	L 2019	3.10	5.20 ± 2.48	SEM, EBSD, EPMA
TR	TS	ZW156	L 2020	1.86	8.13 ± 3.37	SEM, EBSD
BA	TS	NS207	L 2020	7.23	4.21 ± 1.95	SEM, EBSD

5.3.1 SEM

Whole shell valves were prepared as thin sections (refer to chapter 2) and the microstructure of the entire height of the inner shell layer (IL) and outer shell layer (OL) was investigated with scanning electron microscopy (SEM) at the School of Earth and Environmental Sciences, Cardiff University. Secondary electron images (SE) were acquired at a range of magnifications to approximately 50,000x, allowing detailed observation of differences in the structure of shells at all hierarchical levels of organization (i.e. first-, second- and third-order lamellae).

5.3.2 EBSD

Areas of thin sections chosen for EBSD were based on preliminary identification of microstructure with SEM. For the IL, at least two EBSD maps were acquired for each different microstructure observed in each sample. For the OL and myostracum, one EBSD map for each sample was used for representation because microstructure was observed to be highly conserved in these regions of the shell.

Thin sections previously used for SEM were prepared for EBSD according to the steps in chapter 4 and Mills et al. (2024). Briefly, a range of mechanical grinding and polishing steps were applied to sections, with a final polish of colloidal silica, ensuring a smooth and damage free sample surface. Samples were then coated with a thin layer of carbon to avoid charging. EBSD was carried out at the School of Earth and Environmental Sciences, Cardiff University using data collection and post-acquisition refinement protocol in chapter 4.

EBSD data is shown as inverse pole figure maps (IPF), which show crystallographic preferred orientation. Each grain in the IPF maps is colour-coded based on crystallographic orientation that is relative to a specific sample direction (e.g. Y, X, or Z). Corresponding contoured pole figures provide crystallographic co-orientation statistics derived from pole figure maxima (multiple of uniform density (MUD) values) of crystallographic axes (a-axis, [100]; b-axis, [010]; c-axis [001]). A higher MUD value indicates a stronger co-orientation strength, which is indicative of an organized texture that is highly orientated, while a random orientation of crystallographic distribution will have an MUD of 1 (e.g. Crippa et al. 2020).

5.3.3 EPMA

Geochemical concentrations were measured with EPMA according to protocol in chapter 2. One thin section of *T. squamosa* collected in 2019 from both the Baik and Triangle reefs, previously used for SEM and EBSD, was prepared for EPMA (Table 5.1). Three 6 x 6 mm squares of each section were obtained (refer to chapter 2) that corresponded to periods of growth from (1) the OL, (2) the IL in the wet season

(~December 2017) and (3) the IL in the dry season (~August 2018). 100 x 100 µm maps of Mg/Ca and Sr/Ca were acquired for all six squares using the software package CalcImage in Probe for EPMA (http://www.probesoftware.com/). A table of the El/Ca values used in this chapter are available from the Mendeley Data Repository given in Appendix C.

5.3.4 Data analysis

To test for significant differences between the means of Sr/Ca and Mg/Ca in different EPMA maps, a one-way analysis of variance (ANOVA) test was conducted. Tests were assessed for normality and homogeneity of variances using Shapiro-Wilk's test, QQ (quantile-quantile) plots of standardized residuals and Bartlett's test. Assumptions of ANOVA were satisfied for Sr/Ca, but not for Mg/Ca, and the nonparametric Kruskal-Wallis test was used. Differences between groups were investigated using either Tukey's post-hoc test (ANOVA) or Dunn's multiple comparisons test (Kruskal-Wallis test).

5.4 Results

5.4.1 Microstructural features

This research identified fine-scale skeletal structures from four giant clam shells in two reef sites: Triangle reef (high turbid) and Baik reef (low turbid). Giant clams have a two layered shell, consisting of an inner shell layer (IL) and outer shell layer (OL), demarcated by the pallial myostracum (or pallial line) (Figure 5.1). Identified aragonitic microstructural arrangements from the OL to the IL consisted of: crossed-lamellar (CL) in the OL (Figure 5.1b), irregular complex crossed-lamellar intersected with simple irregular or regular prisms (CCL-P) (Figure 5.1d, e) and irregular complex crossed lamellar with an absence of prisms (CCL-I) in the IL (Figure 5.1f, g).

The OL, composed of CL (Figure 5.1b), was identical in all shells regardless of collection locality. The three hierarchical structural orders of lamellae in this microstructure were markedly clear: first-order lamellar, which in turn comprised

second-order lamellae, made up of nanoscale third-order biomineral units (e.g. Agbaje et al. 2017; Agbaje et al. 2019; Hou et al. 2020; Höche et al. 2020).

In contrast, the IL consisted of CCL that showed fine-scale skeletal variation among reefs (Figure 5.1d–g). Two regular morphologies of daily growth bands that intersected lamellae were defined: 1. CCL-P in Triangle, composed of frequent irregular or regular simple prisms coupled with a thinner layer of smaller, oblique crystallites (Gannon et al. 2017; refer to findings of chapter 3, Mills et al. 2023), varying in length and masking the underlying CCL microstructure (Figure 5.1d, e); 2. CCL-I in Baik, composed of adjacent growth lines cutting through the CCL structure (Figure 5.1f, g). Shells collected from the Triangle reef showed CCL-P in latter shell regions only (i.e. mid shell to IL edge) and CCL-I in juvenile portions of the shell adjacent to the pallial myostracum, suggesting some age-related influence.

Myostraca are sites of attachment for bivalve soft tissues to the mineral shell surface (Dong et al. 2022). The pallial myostracum separates the IL and OL, and at the studied shell region (~4 mm along from the hinge) comprised elongate regular simple prisms (Figure 5.1c). Bivalves also have adductor and pedal retractor myostraca, of which the former is a local thickening of the pallial myostracum (Taylor et al. 1969). When traced from the umbo to upper shell margin, the width of the pallial myostracum progressively increased and crystal morphology changed, with single rows of elongate prisms modified to rounded polygonal sheet like rows of prisms of the adductor myostracum (Figure 5.1h).

Noteworthy, at higher resolution, a nanoscale composite granular assembly typical of amorphous calcium carbonate precursor phases of biomineralization (Mastropietro et al. 2017; Gilbert et al. 2019) covered the surface of biominerals across shells. Nanograins ~80 nm in size (Figure 5.2) with an irregular rounded shape were present in all microstructures.

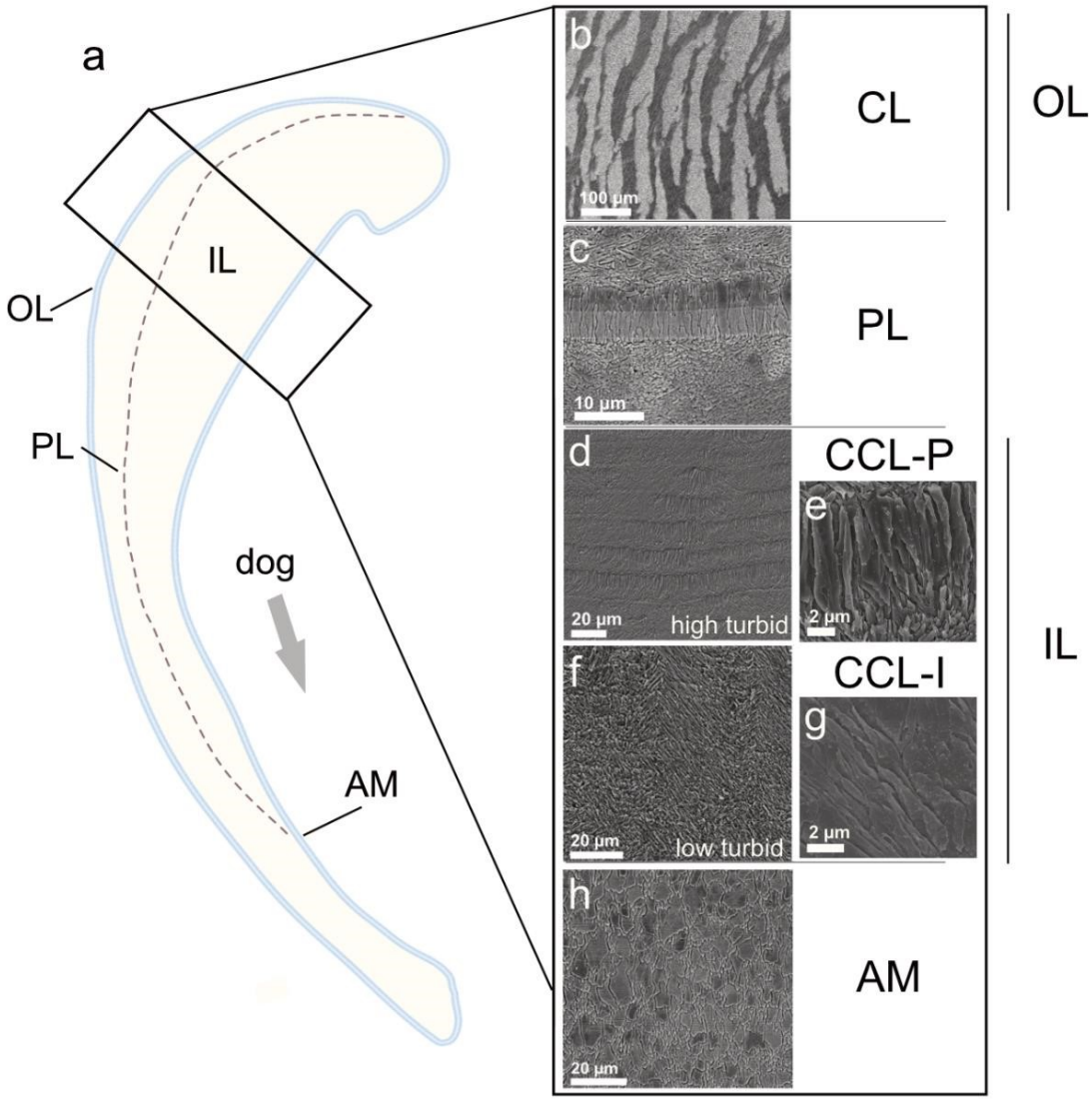

Figure 5.1. **Microstructure of high turbid and low turbid giant clam shells. (a) Schematic longitudinal slice of the shell of *Tridacna squamosa* highlighting the inner layer (IL), outer layer (OL), pallial line (PL) and adductor myostracum (AM). Black rectangle denotes location of analysis for the IL, OL and PL. (b–h) SEM images of the different layers and associated microstructures throughout high turbid (Triangle reef) and low turbid (Baik reef) shells: (b) crossed lamellar microstructure (CL) in the OL (SS_CT); (c) PL separating the IL and OL (SS_CT); (d, e) complex crossed lamellar microstructure with prisms in high turbid shells (SS_CT); (f, g) irregular complex crossed lamellar microstructure in low turbid shells (SS_BAIK); (h) rounded polygonal prisms of the AM (SS_CT). dog = direction of growth.**

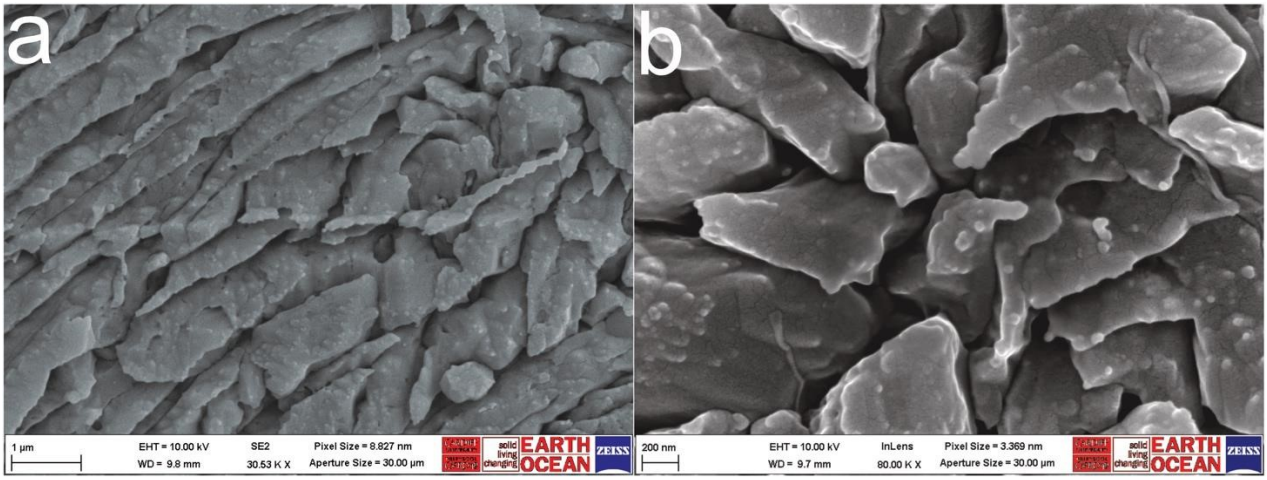

Figure 5.2. **(a, b) Representation of nanograins on the surface of shell biominerals in the inner shell layer of *Tridacna squamosa* (specimen SS_BAIK), shown as lightly colored irregular rounded nanoscale 'bumps'.**

5.4.2 Crystallographic features

Investigation of crystallographic texture of the *T. squamosa* shells with EBSD revealed a coherent crystallographic preferred orientation of the aragonite [001] axis in all samples, showing one strong pole figure maximum (Figure 5.3). However, multiple of uniform density (MUD) values derived from pole figures, which represent crystal coorientation strength, showed variation across different microstructures. The CL microstructure associated with the OL showed MUD values between 27–30. Sets of alternating first-order lamellae ~15–30 µm wide were apparent and showed a belt-like distribution of the [100] axis and [010] axis around the [001] axis. However, I caution the low diffraction quality of CL and fewer aragonite points were indexed compared to the IL (compare Figure 5.3c, d to Figure 5.3a, b), likely related to its small grained composition, below ~1 µm.

The IL had larger grain sizes that were generally above 1 µm and showed a higher indexing of aragonite points. Areas of first shell growth in the IL adjacent to the pallial line with a CCL-I arrangement shared microtextural continuity with the OL (i.e. lamellae carry over from the OL) (Figure 5.3). Away from the pallial line and OL, a stronger intensity of fabric developed in shells from Triangle that showed the CCL-P arrangement (Figure 5.3), with a clear one-dimensional orientational order, where [100] and [010] axes formed a continuous girdle around the [001] axis. CCL-I had a wider belt-like distribution of the [100] and [010] axes and more scattered [001]

maxima. Accordingly, co-orientation strength between CCL-I and CCL-P showed MUD values of 16–24 and 45–48, respectively. The adductor myostracum, imaged further up the shell section nearer to the ventral margin had the largest grain sizes (~5–20 μm) and highest MUD of 88–89 (Figure 5.3).

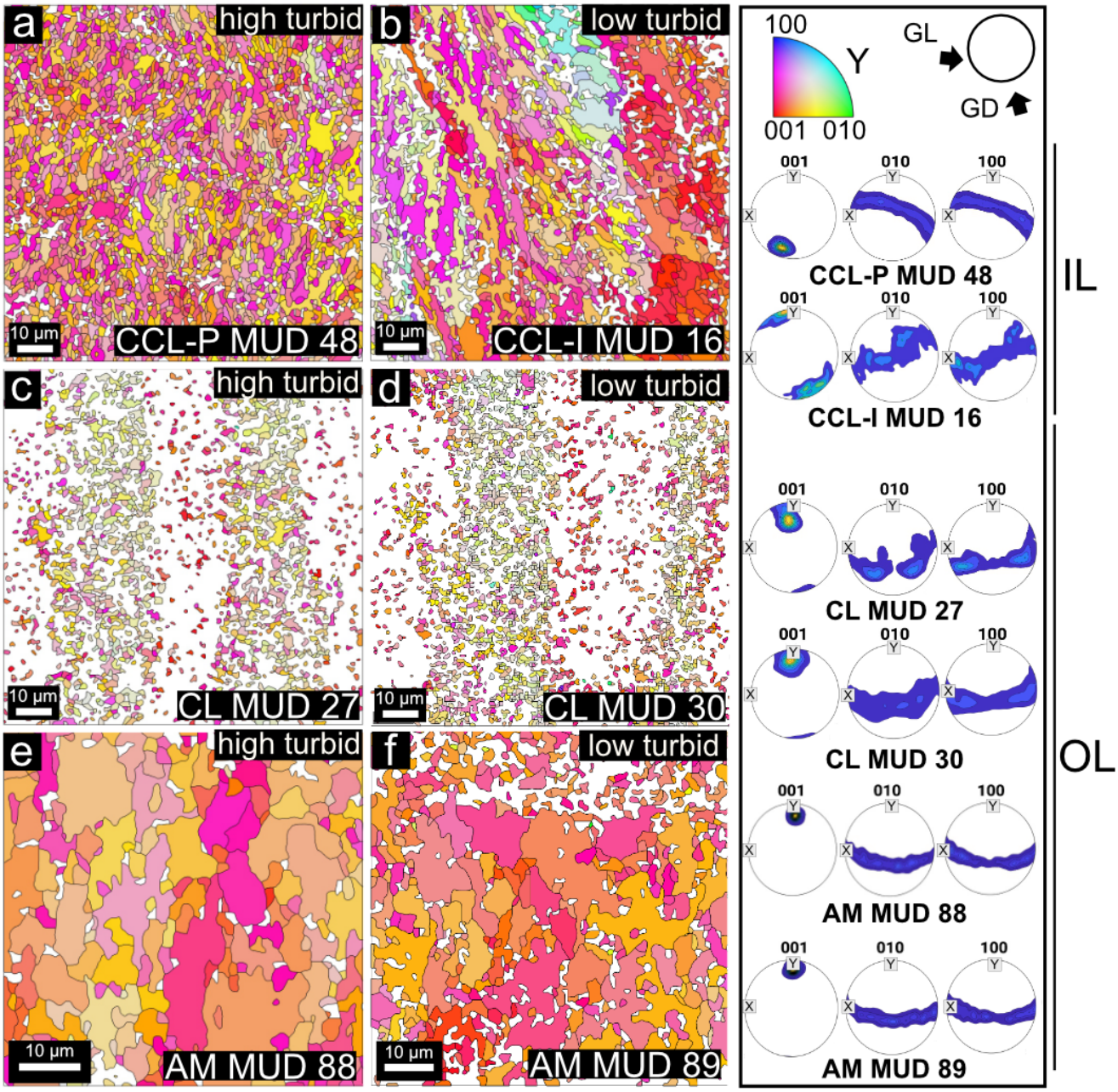

Figure 5.3. **Crystallographic texture of high turbid and low turbid giant clam shells. EBSD inverse pole figure maps (IPF-Y) and corresponding contoured pole figures representative of different layers and associated microstructures in high- (Triangle) and low (Baik) turbid giant clam shells. (a) aragonitic arrangements of complex crossed lamellar microstructure with prisms in the IL of turbid shells (MUD 48) (SS_CT). (b) irregular complex crossed lamellar microstructure with lower crystallographic orderliness (MUD 16) (SS_BAIK) in the IL of low turbid shells. Near identical arrangements of (c, d) crossed lamellar (MUD 27, 30) (SS_CT and SS_BAIK, respectively) and (e, f) adductor myostracum (MUD 88, 89) (SS_CT and SS_BAIK, respectively) present in the OL of both high and low turbid shells. Contoured pole figures show a common preferred crystallographic orientation of the [001] axis in all identified microstructures. The MUD values associated with each pole figure indicate different co-orientation strengths between the IL in high and low turbid shells, as well as**

between different regions of the shell. Reference pole figure shows orientation of GL (growth lines, or bands) and GD (growth direction).

5.4.3 Geochemical features

EPMA was used to investigate Mg/Ca and Sr/Ca ratios of shells on a comparable scale to the SEM and EBSD data collected from high turbid (Triangle: SS_CT) and low turbid (Baik: SS_BAIK) reef localities. In the IL, thin (~8 μm) high Mg and Sr banding showed daily periodicity, cohering with daily growth banding (Figure 5.4a–d). Mean Mg/Ca and Sr/Ca ratios taken from transects (white dashed line on Figure 5.4a indicates location) between high turbid and low turbid reefs varied from 0.90 ± 0.55 to 1.56 ± 0.66 mmol/mol and 2.09 ± 0.70 to 2.95 ± 0.58 mmol/mol, respectively (Figure 5.4e–h). In the OL, collection of EPMA data from the Triangle reef was unsuccessful due to microboring of the shell surface (Figure 5.5). However, the OL for Baik showed minimal alteration and mean Mg/Ca and Sr/Ca ratios taken from a transect were similar to the IL (1.42 ± 1.29 mmol/mol and 2.09 ± 1.20 mmol/mol, respectively) (Figure 5.6). High Mg and Sr bands presumably relating to growth bands also occurred in the OL in similarity with the IL (Figure 5.6).

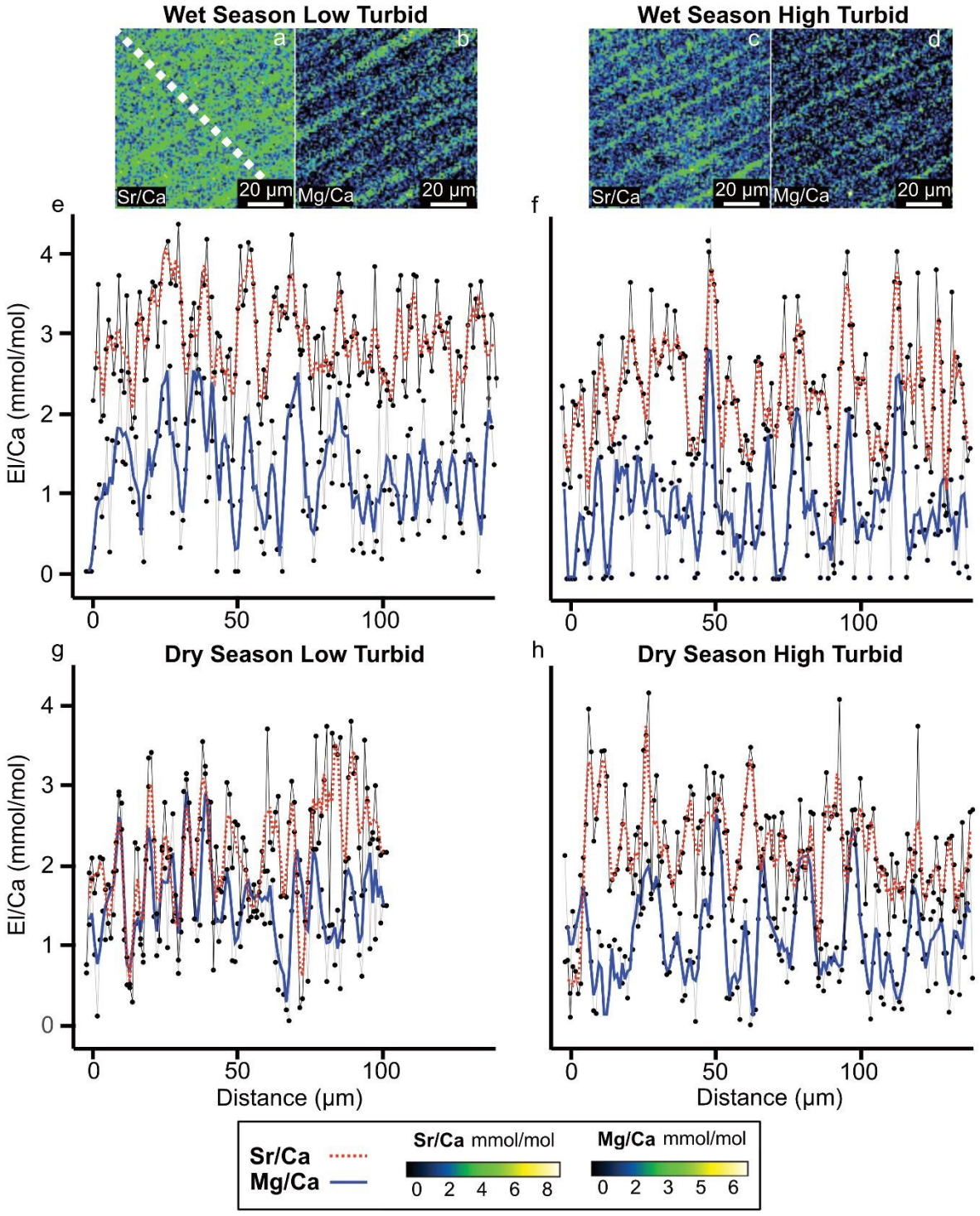

Figure 5.4. **Geochemical profiles of element-to-calcium ratios for high turbid and low turbid giant clam shells. (a–d) Sub-daily resolved EPMA maps for the inner shell layer of high turbid (Triangle: SS_CT) and low turbid (Baik: SS_BAIK) giant clams within a region of shell growth corresponding to the wet season. White dashed diagonal line in (a) denotes transect measurement locations of maps for corresponding profiles for Sr/Ca and Mg/Ca shown in (e–h). (e) Sr/Ca and Mg/Ca profiles for a portion of growth in the low turbid shell collected in 2019 corresponding to the wet season. (f) portion of growth in the high turbid shell collected in 2019 corresponding to the wet season. (g) portion of growth in the low turbid shell corresponding to the dry season. (h) portion of growth of the**

high turbid shell corresponding to the dry season. Colour bars below profiles show concentrations of element-to-calcium ratios in mmol/mol corresponding to maps in (a–d). Grey lines on profiles show raw EPMA data. Red dashed (Sr/Ca) and solid blue lines (Mg/Ca) provide a 3-point rolling mean of the raw data.

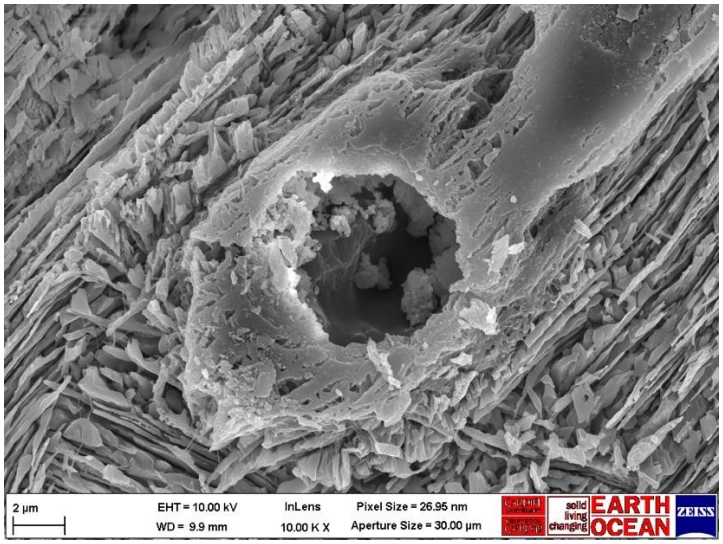

Figure 5.5. **Example of a microboring hole present in the outer shell layer of *Tridacna squamosa* (specimen SS_CT) from high turbid reef Triangle.**

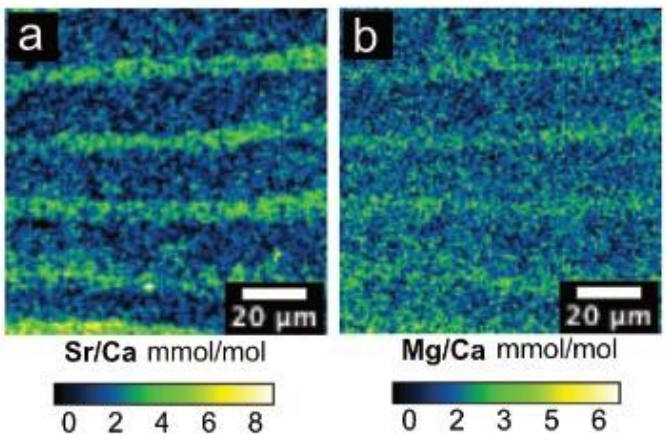

Figure 5.6. **Sub-daily resolved EPMA maps for (a) Sr/Ca and (b) Mg/Ca in a region of the outer shell layer in the low turbid giant clam (specimen SS_BAIK) shell. Colour bars below maps show concentrations of element-to-calcium ratios in mmol/mol.**

I focused on Mg/Ca and Sr/Ca measured from regions of shell growth that corresponded to the wet- and dry seasons in my study locality (Figure 5.4e–h). At an intershell level, median Mg/Ca from the low turbid shell was significantly elevated in the dry- and wet season (Kruskal-Wallis, $\chi2(3) = 40.7$, $P < 0.05$, pairwise comparisons with Dunn's multiple comparisons test) compared to the high turbid shell, while mean Sr/Ca from the low turbid shell was significantly elevated in the wet season only (one-way ANOVA, $F(3) = 43.58$, $P < 0.01$, pairwise comparisons with Tukey HSD test) (Table 5.2; 5.3). At an intrashell level, Sr/Ca and Mg/Ca from the low turbid shell significantly varied between seasons (one-way ANOVA, $F(3) = 43.58$, $P < 0.01$, pairwise comparisons with Tukey HSD test; Kruskal-Wallis, $\chi2(3) = 40.7$, $P < 0.05$, pairwise comparisons with Dunn's multiple comparisons test, respectively), while the high turbid shell showed no significant difference in Sr/Ca or Mg/Ca between the wet- and dry season (one-way ANOVA, $F(3) = 43.58$, $P > 0.05$, pairwise comparisons with Tukey HSD test; Kruskal-Wallis, $\chi2(3) = 40.7$, $P > 0.05$, pairwise comparisons with Dunn's multiple comparisons test, respectively) (Table 5.2; 5.3). However, it is important to acknowledge the uncertainties of interpreting this data on a seasonal scale because of the small areas of shells sampled with EPMA, which is a trade off with the high spatial resolution of the data.

Table 5.2. **Post hoc Tukey HSD test results for Sr/Ca between shells from the Triangle (SS_CT) and Baik (SS_BAIK) reefs in the wet season (WS) and dry season (DS). Upper matrix reports *P*-values (<0.05 in bold). Lower matrix is the difference.**

	SS_BAIKWS	SS_BAIKDS	SS_CTWS	SS_CTDS
SS_BAIKWS		**<0.01**	**<0.01**	**<0.01**
SS_BAIKDS	0.86		0.33	0.90
SS_CTWS	-0.62	0.24		0.12
SS_CTDS	-0.80	0.06	0.18	

Table 5.3. **Pairwise comparison of Mg/Ca between shells from the Triangle (SS_CT_ and Baik (SS_BAIK) reefs in the wet season (WS) and dry season (DS). *P*-values (<0.05 in bold) are adjusted with the Benjamini-Hochberg (BH) method.**

Comparison	*P*-value (BH adjusted)
SS_BAIKWS-SS_BAIKDS	**0.02**
SS_CTDS-SS_BAIKDS	**<0.01**
SS_CTWS-SS_BAIKDS	**<0.01**
SS_CTDS-SS_BAIKWS	**0.03**
SS_CTWS-SS_BAIKWS	**<0.01**
SS_CTWS-SS_CTDS	0.16

5.5 Discussion

The findings of this study show that the mixotrophic giant clam *Tridacna squamosa*, an important reef-dwelling bivalve from both an ecological and palaeoceanographic perspective, exhibits plasticity in biomineralization pathways between high turbid and low turbid nearshore coral reefs. For the first time, I highlight fine-scale variations in the microstructure, crystallographic coorientation and minor and trace element geochemistry of shell biominerals, which are not resolvable at coarser sampling resolutions. I find that shells formed in the turbid reef situated near a river source have a different shell microstructure in the inner shell layer (IL), consisting of paired daily growth increments with higher crystallographic co-orientation and lower Mg/Ca and Sr/Ca, compared to lower crystallographic co-orientation and higher Mg/Ca and Sr/Ca in the low turbid reef. Key environmental differences between the two reef localities are K_d(490), total suspended solids and chlorophyll-*a*, which are elevated in the high turbid reef (refer to chapter 2). I hypothesized in chapter 3 and Mills et al. (2023) that elevated concentrations of these parameters year-round may suggest *T. squamosa* can utilize different relative contributions of feeding type to total organismal energy requirements. These environmentally driven changes to physiological machinery may imprint on its biomineralization pathways and hence architecture and geochemistry of shells. This is the first study to show that differences exist in the biomineralization of giant clams on turbid reefs, important because knowledge of giant clam physiological responses to different anthropogenic stressors is vital for conservation strategies under a rapidly changing ocean (Watson and Neo 2021).

5.5.1 Shell architecture

The microstructural changes identified for *T. squamosa* display variation of daily bands within the IL between reefs, with irregular complex crossed-lamellar (CCL-I) in the low turbid reef and paired daily growth couplets with a thinner layer of small crystals and larger prisms (CCL-P) (Pätzold et al. 1991; Gannon et al. 2017) in the turbid reef. Both microstructures show a common preferred crystallographic orientation of the [001] axis roughly perpendicular to growth bands and parallel to the growth direction, similar to previous EBSD studies of *Tridacna gigas* (Gannon et al. 2017) and *Tridacna derasa* (Agbaje et al. 2017). However, crystal co-orientation, or organization, measuring how

orientated crystals are relative to one another, is higher for CCL-P (MUD 45–48) compared to CCL-I (MUD 16–24). This is higher than other tridacnids (Agbaje et al. 2017, MUD of 12), but within the realm of other bivalves with similar microstructural arrangements, such as *Glycmeris glycmeris* (Crippa et al. 2020).

Despite the recorded variability in the IL, the OL and myostracum microstructures are identical in all shells from both high turbid and low turbid reef sites. The myostracum is known to be highly conserved and universal across most of the phylum Mollusca (Dong et al. 2022) and may either grow homoepitactically on top of the OL (Crippa et al. 2020) or directly attach to underlying muscle fibers by adhesive epithelial cells (Norton et al. 1992). While our results for the OL concur with a previous study showing that *T. gigas* has an identical microstructure between different reef sites (Gannon et al. 2017), the authors in this study suggested that the OL is under tight biological control due to a similar mineralization mechanism across individuals. However, I offer an alternative hypothesis based on our observations of fine-scale variation in the IL — that the IL is under high biological control, regulated by complex physiological machinery that is reflected in microstructure. This may be underpinned by: (1) The IL is situated further away from the external environment and may be less open to seawater (Figure 5.7a); (2) The inner mantle is always in direct contact with the extrapallial fluid in the IL compared to the outer mantle (Ip et al. 2017) (Figure 5.7a, b); (3) Mantle epithelial cells lining the IL may be more tightly packed than the OL (Norton et al. 1992), which could minimize paracellular diffusion and leakage. It may be that biophysiology takes precedence in the determination of microstructure between reefs, indirectly influenced by different environmental parameters (Coronado et al. 2019).

5.5.2 Shell geochemistry

The outlined variations observed in the architecture of the IL are also reflected in the elemental distribution of shells. However, it is important to acknowledge the caveat that due to the small areas sampled for each shell with EPMA (100 x 100 µm maps), only a snapshot in time on the scale of days is captured for each reef site. The following observations warrant further expansion in the future and there are uncertainties when discussing this data on a seasonal scale. Nevertheless, the key focus of this study was

the investigation of geochemical data on a comparable (sub-micron) scale to microstructural and crystallographic data.

Mean concentrations of El/Ca shown in the EPMA maps reveal that in the low turbid reef with CCL-I microstructure, there is significantly higher Mg/Ca compared to the high turbid reef with CCL-P. On a daily scale, Mg/Ca is elevated at the boundary between daily growth bands regardless of reef environment. In biogenic aragonite, Mg is associated with the organic or highly disordered amorphous calcium carbonate (ACC) phase because its small cationic radius does not favor incorporation into the orthorhombic structure of aragonite (Yoshimura et al. 2015; Yao et al. 2019) (Figure 5.7a). Although shell organics represent a small portion of total shell weight equating to around 1% in giant clams (Agbaje et al. 2017), their presence likely plays an important role in relation to the concentration of Mg/Ca. For instance, elevated Mg/Ca is linked to increased organic contents at the boundary between growth bands in many aragonitic bivalves (e.g. Schöne et al. 2010). Beyond the amount of organics, the composition of organics also plays an important role in determining Mg signature. For example, different relative concentrations of peptides, short chains of amino acids, have been demonstrated to change Mg concentration in a study by Stephenson et al. (2008). Stephenson et al. (2008) showcased that the addition of simple hydrophilic peptides with the same carboxyl-rich characteristics as calcifying macromolecules within the calcifying fluid elevated Mg concentration. These findings relate to kinetic measurements of step propagation rates, which changes the density of kink sites on crystals and the probability of Mg attachment to a site (Stephenson et al. 2008). Hence, the higher mean Mg/Ca concentrations in the low turbid reef herein may relate to the prevalence of certain types of peptides known to elevate Mg/Ca signal (i.e. simple hydrophilic peptides) (Stephenson et al. 2008), which changes the ability of Mg to bind to crystals. I base this hypothesis on research for corals, in which the balance between heterotrophy versus autotrophy changes relative abundance of type of amino acids in the organic matrix (e.g. Muscatine et al. 2005). I propose a similar mechanism for *T. squamosa*, whereby environmental differences between sites change feeding activity of the host and symbionts (e.g. phytoplankton availability), which may in turn alter amino acid composition and Mg/Ca concentration. Similarly, juvenile tridacnids are known to show more reliance on heterotrophy than adults (Klumpp and Griffiths 1994; Killam et al. 2023), so ontogenetic changes related to feeding could explain lifetime

trends in Mg/Ca that have been previously recorded (e.g. Elliot et al. 2009; Warter et al. 2015). This work highlights the high-level role organics may play in relation to biogeochemical processes and how these parameters could be related to the feeding mechanism in giant clams.

In contrast to the association between Mg and organics, strontium is instead substituted for Ca^{2+} within the aragonite lattice and may predominantly enter the extrapallial fluid to the site of calcification through active transport mechanisms at the mantle epithelia, most notability Ca^{2+}-ATPase (Ip and Chew 2021) (Figure 5.7a). In both reef sites and all shell regions mapped, *T. squamosa* shows daily cyclicity in Sr/Ca. However, in relation to mean Sr/Ca values from maps, Sr/Ca concentration in the low turbid reef is significantly elevated in wet season maps compared to the high turbid reef. Previous work has reported an inverse relationship with Sr and insolation in giant clams (Sano et al. 2012; Yan et al. 2020), thought to reflect diurnal cyclicity related to the light enhanced calcification mechanism (Sano et al. 2012). During light enhanced shell formation in the daytime, a lower Sr/Ca concentration is recorded because light dependent active transport of calcium into the extrapallial fluid by Ca^{2+}ATPase is enhanced, lowering the ratio of Sr/Ca (Ip and Chew 2021). This is in line with our findings not only on a daily scale, but also on a seasonal scale, where mean Sr/Ca is highest in the wet season, with the lowest levels of light. However, it is known a strong biological control exists on Sr incorporation into the shell and individuals kept under continuous illumination (Warter et al. 2018) or alternatively under a sunshade (de Winter et al. 2023) still exhibit Sr/Ca cyclicity. Overall, external environment does seem to play an indirect role in Sr/Ca concentrations; yet it is clear from our data there is a physiological control, in line with previous studies (Elliot et al. 2009; Warter et al. 2015; Warter et al. 2018; de Winter et al. 2023).

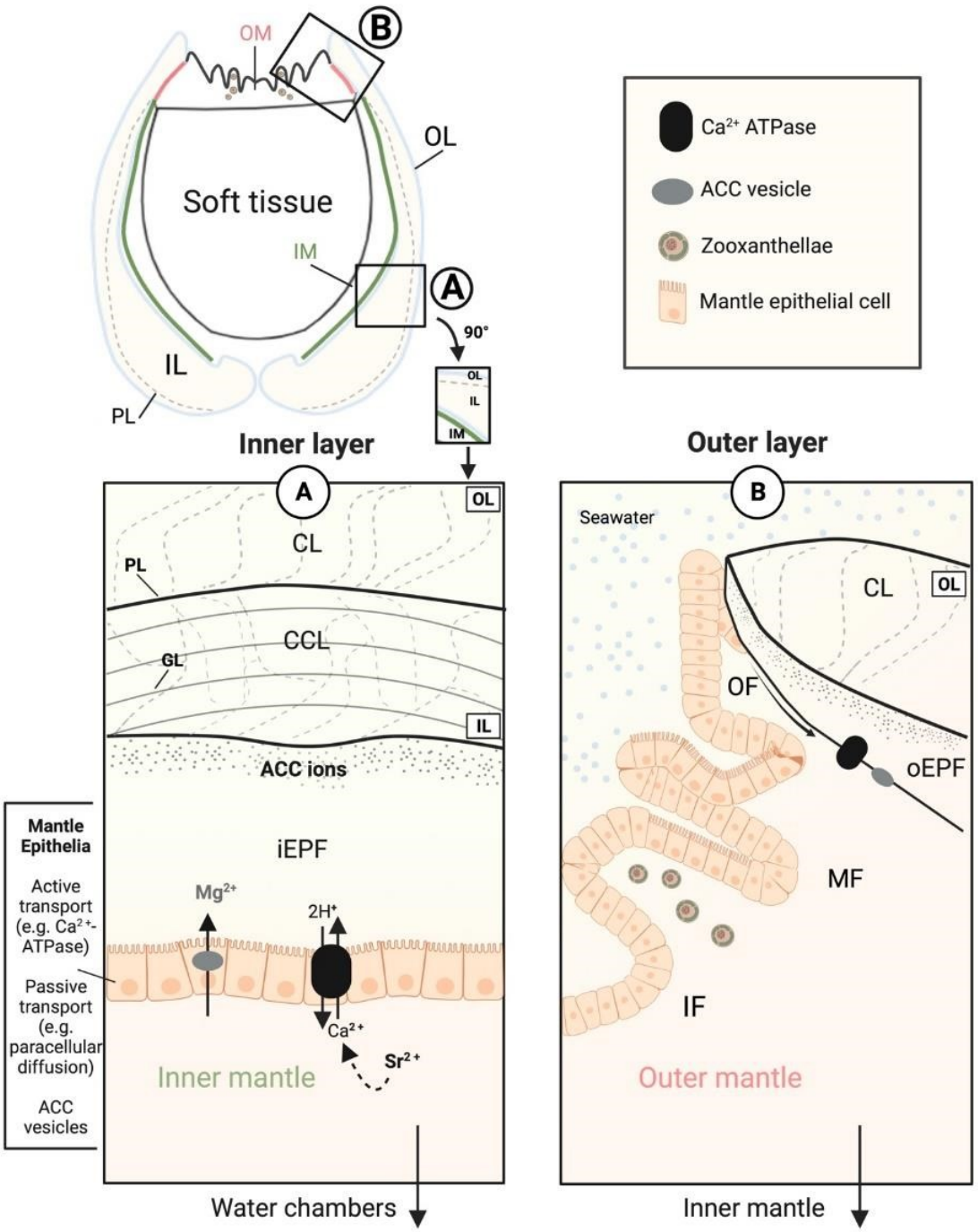

Figure 5.7. **Simplified conceptual representation of the biomineralization mechanism in tridacnid giant clams. Not to scale. Shell mineralization pathways for each shell layer in relation to the inner, or lateral shell mantle (IM) and outer, or siphonal shell mantle (OM) shown. Formation of the shell (Ca^{2+} + HCO_3^- ➔ $CaCO_3$ + H^+) takes place in an extracellular privileged space, commonly known as the extrapallial fluid (EPF) (e.g. Gilbert et al. 2022). The inner shell layer (IL), with a complex crossed lamellar microstructure (CCL) (a) forms from the inner EPF (iEPF) and the outer shell layer (OL), with a crossed lamellar microstructure (CL) (b) from the outer EPF (oEPF). The IL and OL are demarcated by the pallial line (PL). The EPF is partially open to surrounding seawater but is chemically different from seawater due to biological processes, or 'vital effects' tightly**

controlled by the organism (Urey et al. 1951). Transport of Ca^{2+} to the EPF occurs at the mantle epithelium through active (e.g. Ca^{2+} ATP-ase) (e.g. Ip and Chew 2017) and potentially passive (e.g. paracellular diffusion) transport mechanisms (Tambutté et al. 2011). Organic and Mg rich amorphous calcium carbonate (ACC) vesicles, or granules, also cross the mantle epithelial cell membrane, and are transported to the calcification front. ACC particle attachment and subsequent ion attachment occur at the biomineral growth front and crystallize into aragonite (e.g. Gilbert et al. 2022). In relation to the proximity of the IL and OL to seawater, the IL is situated between the IM and OL, in close contact with the iEPF and physically situated further away from surrounding seawater (a). The OL is in direct contact with seawater, where OM specific mechanisms are carried out and the clam undergoes light-dependent physiological phenomena (Ip and Chew 2021). Photosymbionts (zooxanthellae) are housed extracellularly in Z-tubules (not shown) within the inner fold (IF) of the OM and carry out photosynthesis from sunlight to provide nutrition to the clam through an autotrophic feeding pathway (Norton and Jones 1992). The chemical composition of the EPF is highly variable on a fine temporal scale (subdaily) and also varies seasonally. In the case of Mg and Sr, different predominant pathways are responsible for transportation to the site of calcification (a). Mg is associated with the organic or ACC phase because its ionic radius is not favourably substituted in the orthorhombic crystal lattice of aragonite (Yoshimura et al. 2015; Yao et al. 2019). Sr is substituted for Ca within the aragonite lattice due to similar ionic radii and may predominantly enter the EPF through active transport mechanisms such as Ca^{2+} ATP-ase (e.g. Ip and Chew 2021).

Aside from biological control, thermodynamic and kinetic processes may also play a role in understanding elemental concentrations in reef localities. Considering growth rates in both reef localities are similar within shell regions selected for EPMA, it is unlikely that there is a kinetic effect related to growth rate (Gaetani and Cohen 2006). However, it is possible that other kinetic factors related to foreign ion partitioning may indirectly explain variations. For instance, variation in microstructure affects crystallographic orientation, which, under the influence of thermodynamic principles, can impact the amount of minor and trace elements that can be bound to the mineral phase (Füllenbach et al. 2017). Potentially different mineral surface structures could show different affinities for elements that substantially vary across crystal faces (e.g. Paquette and Reeder 1995). Considering the microstructural and crystallographic variability of the IL in this study, it is noteworthy that microspatial differences in the abundance of elements could be constrained by crystal face symmetry and play a role in preferred element incorporation.

5.5.3 Implications for biomechanical properties

My findings on the geochemistry and architecture of shells have important implications for their biomechanical properties (e.g. hardness and elasticity), giving indication of the defense capabilities and resilience of biogenic skeletons (Moynihan et al. 2021; Armstrong et al. 2022). Overall, my results show higher crystallographic orderliness and significantly lower El/Ca ratios in the high turbid site, compared to the low turbid site. Higher crystallographic control (e.g. Beniash et al. 2010) and low Mg/Ca ratios (e.g. Moynihan et al. 2021) are known to indicate superior mechanical properties and increased structural integrity of the carbonate skeleton, suggesting giant clam shells from the high turbid reef are biomechanically superior. These differences have been suggested to be driven by the amount of ACC and organic material, with higher concentrations of organics linked to more Mg and decreased stiffness and hardness (Moynihan et al. 2021). However, a previous study on corals has shown that there is a strong relationship between skeletal embrittlement and high sedimentation rate, finding corals fractured under lower loads and were weaker with high turbidity (Moynihan et al. 2021). It is important to highlight that shells from the turbid reef may show compensatory responses for increased resilience to turbidity by forming biominerals with higher defensive capabilities, although more work is needed to

understand how turbidity impacts embrittlement, hardness and stability of the carbonate skeleton in multiple tridacnid species.

5.5.4 Conclusion

This study highlights plasticity in biomineral formation of giant clam shells between high turbid and low turbid nearshore coral reefs in the Coral Triangle. Fine-scale modifications to the architecture and geochemistry of the inner shell layer are likely sensitive proxies of complex physiological adjustments in response to turbidity and a multitude of accompanying changing environmental factors on turbid reefs. The highlighted differences in microstructure, crystallographic co-orientation and microspatial distribution of Mg/Ca and Sr/Ca between reefs that may relate to energy partitioning and nutritional strategy are highly relevant in a rapidly changing ocean, where turbidity is set to increase due to anthropogenic pressures. The results presented herein suggest that shell formation is modified potentially as a compensatory mechanism in high turbid coral reefs and that they may be suitable habitats for *T. squamosa* and other mixotrophic marine corals and calcifiers under rapid environmental change. Overall, turbid reefs should be considered as important conservation refuge against bleaching and other stressors.

6. Diagenesis in fossil giant clam shells: using crystallographic texture to detect alteration from pristine to secondary aragonite

6.1 Abstract

The carbonate skeletons of marine bivalves are critical bioarchives for understanding paleoceanographic changes. Yet, unlocking environmental signatures stored within their biological hard tissues is only possible when pristine material is clearly distinguished from diagenetically altered features. Giant clams, or tridacnids, show great potential as high-resolution archives (to sub-daily temporal scale) of past coral reef environments because they live long, grow fast and have dense aragonite shells. However, diagenesis is known to impact both physical and geochemical signatures of their shells through recrystallization of aragonite to calcite. A lesser explored, and often overlooked, aspect of their alteration is within-phase transformation from pristine- to altered aragonite. Herein, I compare the structural features of aragonite from *Tridacna squamosa* shells collected alive to fossil *Tridacna* shells derived from natural environments. I identify mineral phase with X-ray diffraction (XRD) and Raman spectroscopy, investigate organic content with loss on ignition (LOI), and use field emission gun scanning electron microscopy (SEM) and electron backscatter diffraction (EBSD) to characterize and quantify shell crystallographic texture. I focus assessment on (1) crystallographic orientation patterns derived from EBSD pole figures, (2) crystallographic co-orientation strength statistics and (3) grain size statistics. My findings show that although most fossil carbonate remains within the aragonite phase, there is widespread textural alteration, which can be classified on an alteration gradient. Grain boundaries first appear to be eliminated by degradation of organic material, initiating a subtle increase in grain size with little change to crystallographic co-orientation strength. Then, major reorganization of aragonite grains and destruction of original microstructure occurs, with larger and highly orientated grains dominating. I demonstrate that methods which detect mineral phase transformation only (e.g. XRD) are not sufficient to identify alteration in giant clams.

EBSD should be routinely implemented because it can quantitatively map and distinguish biogenic from abiogenic aragonite on a spatial scale relevant to which many highly time resolved analyses are undertaken.

6.2 Introduction

The shells of bivalve molluscs are widely employed as valuable records of past environments and climates, playing a significant role in understanding environmental change throughout the Phanerozoic eon (Veizer and Prokoph 2015). Bivalves have an extremely broad geographical and temporal distribution, occurring in most aquatic ecosystems globally (Schöne and Surge 2012). Specimens are easily accessible and can archive a plethora of highly time-resolved environmental information on sub-daily to fortnightly scales (e.g. Evans 1972; Goodwin et al. 2001; Rodland et al. 2006). However, a major obstacle faced when using them as proxies is that they experience diagenetic alteration over time. Diagenetic processes can occur as early as within the lifetime of the animal, proceeding long after its death throughout the geologic record (e.g. Moore 1989). This makes it difficult to identify biotic pristine signatures deposited by the organism compared to those that are diagenetically overprinted, having important implications for reliable proxy reconstruction because interpretation hinges on this separation.

Traditionally, methods to assess diagenetic alteration in bivalve shells include bulk analysis of phase to detect the presence of aragonite or calcite, using techniques such as powder X-ray diffraction (XRD) (e.g. Walls et al. 1977). However, such methodologies do not provide information on localized and structural changes within a sample, along with only being able to detect advanced steps of the alteration process (e.g. Casella et al. 2017; Hou et al. 2020; Forjanes et al. 2022). In recent years, a series of multi-analytical hydrothermal alteration experiments have shown that pairing secondary electron and electron backscatter diffraction (EBSD) imaging is useful for high resolution diagenetic screening in biogenic carbonates (Casella et al. 2017, 2018a, b; Ritter et al. 2017; Pederson et al. 2020; Wichern et al. 2023). Secondary electron imaging enables visual identification of pristine versus altered microstructures and by coupling with analysis of crystallographic texture with EBSD, a conscientious, quantified and unequivocal overview of preservation state can be achieved. Moreover,

by also measuring the organic content within the skeleton, insight can be gained into the fundamental processes that govern the initial stages of diagenesis (e.g. Risk et al. 1996).

So far, these techniques have revealed that diagenesis in various aragonitic bivalve and coral species follows a coherent stepwise process. Firstly, fast decomposition of the organic matrix of the skeleton acts as key impetus for recrystallization. This loss of organic material drives the formation of a pervading network of micro- and nanoinclusions, voids and pores within the material, acting as gateways for percolating aqueous fluids (Casella et al. 2017, 2018a, b; Pederson et al. 2020; Forjanes et al. 2022). These fluids play a key role as a diagenetic medium and mediate fine scale dissolution of biogenic aragonite with concomitant precipitation/infilling of abiogenic aragonite (Pederson et al. 2020). In many types of shell microstructures, a progressive coarsening of crystal size through 'fusion' of original third-order biomineral units is then observed, with an associated rise or fall in crystallographic co-orientation strength (Forjanes et al. 2022). Only within the final step does phase transformation occur, with recrystallization of aragonite to abiogenic calcite (Casella et al. 2017; Forjanes et al. 2022) by a dissolution-reprecipitation mechanism at high temperatures (e.g. exceeding 175°C in experiments using hydrothermal fluids in Casella et al. 2017). These studies reveal that nano- to microscale microstructural and crystallographic analyses are key to understanding within-phase changes associated with early diagenesis, which would be missed at coarser/bulk sampling resolutions or with techniques that only detect phase change.

The study of diagenesis in a laboratory environment reenacts the in-depth pathways of alteration under controlled conditions, which are key to building on our understanding of the mechanism of diagenesis. However, such *ex situ* experiments often take place under different conditions to nature, occurring at higher temperatures, which may accelerate the diagenetic process, and under different fluid chemistries and microbial activities (e.g. no microboring activity) (Casella et al. 2018a, b; Pederson et al. 2020). Hence, studying diagenesis in specimens from the natural environment is essential to build on our understanding of how *in situ* diagenesis in shells excavated for proxy studies differs/correlates with experimental processes.

The present study focuses on the impact of naturally incurred diagenesis on fossil giant clam shells. Despite a high preservation potential (Ayling et al. 2015), diagenesis in giant clams is known to affect shell microstructure and geochemistry through the transformation of pristine aragonite to secondary aragonite or calcite (Faylona et al. 2011; Warter et al. 2015; Hou et al. 2020). Yet, it is common practice in proxy studies of fossil tridacnids to use screening techniques that only consider phase change (i.e. recrystallization from pristine aragonite to altered calcite) rather than alteration within the same phase (i.e. pristine aragonite to altered aragonite), such as bulk XRD and/or Raman spectroscopy (e.g. Hu et al. 2020). Hence, the motivation of this study was to understand and classify transformation from pristine biogenic aragonite to altered abiogenic aragonite. Since giant clams are extensively utilized for ultra-high-resolution temporal analysis of past low-latitude environments with powerful mineralogical and geochemical techniques, such as daily growth band imaging (Zhao et al. 2021; Mills et al. 2023), laser ablation-inductively coupled plasma-mass spectroscopy (LA-ICPMS) (Warter et al. 2018) or electron probe microanalysis (EPMA) (Hori et al. 2015), it is key to understand how localized diagenesis on a nano- to micro spatial scale implicates their use for reliable proxy reconstruction. Moreover, techniques such as bulk XRD do not align with isotope and laser geochemical analyses because sampling occurs on the IL and/or OL along a specific set of track(s).

So far, the investigation of how natural diagenesis impacts structural shell features has been most widely studied with SEM imaging in giant clams (Faylona et al. 2011; Warter et al. 2015; Hou et al. 2020). SEM is useful for visual approximation of potentially altered biominerals within the aragonite phase, but we are limited in our understanding of how alteration impacts shell texture beyond qualitative imaging analysis. Here, I aim to gain a quantitative understanding of alteration from pristine biogenic aragonite to altered abiogenic aragonite in giant clam shells. I use EBSD for quantitative crystallographic evaluation, alongside SEM for characterization of microstructure, loss of ignition (LOI) for investigation of changes to organic shell content, and XRD and Raman spectroscopy for preliminary identification of mineral phase. I compare modern samples that were collected alive in Darvel Bay to fossil giant clam shells retrieved from stratigraphic formations, dated from the Pliocene and Miocene epochs. I describe preservation state between shells to understand how microstructural and crystallographic features may play a role in natural diagenetic alteration. I emphasize

the importance of a multi-method diagenetic screening approach that operates at a similar scale to subsequent geochemical and other high resolution analyses, providing a framework for understanding alteration in giant clam shells.

6.3 Methods Summary

I compared mineralogical and nano- to microscale features from modern giant clam shells extracted alive from the seafloor to fossil giant clam shells derived from stratigraphic formations at rocky outcrops. Four modern *Tridacna squamosa* shells were collected between 2019 and 2020 at two localities (Triangle reef and Baik reef) in Darvel Bay, northeastern Borneo. Two *Tridacna* spp. fossil shells were additionally retrieved from clay-rich stratigraphic formations in eastern Borneo and previously dated with strontium isotope stratigraphy (SIS). One shell (S3P08) was collected from the east of Lahad Datu, Sabah and estimated at 3.4 Ma (Pliocene epoch) (Saw et al. 2019), while a second shell (TF108) was retrieved close to the city of Bontang in East Kalimantan, Indonesia and estimated at 9.4 Ma (Miocene epoch) (Warter et al. 2015).

Giant clam shells are entirely aragonitic and consist of two primary shell layers: an inner shell layer (IL) and outer shell layer (OL), demarcated by the pallial myostracum (or pallial line, PL) (Figure 6.1). Growth lines in the IL are frequently observed at a daily level and are thought to give the most complete record of shell growth (Pätzold et al. 1991). The IL is often better preserved, while the OL may be visibly impacted by bio-erosion and other diagenetic processes (Elliot et al. 2009; Warter et al. 2015). In this contribution, I chose to focus on the IL because it is most widely utilized for proxy use and often *appears* well preserved (Elliot et al. 2009). Hence, diagenesis is usually harder to discern in the IL than the OL (Warter et al. 2015).

6.3.1 XRD

Bulk mineralogical composition was carried out using powder XRD analysis at the School of Earth and Environmental Sciences, Cardiff University. A thin strip that covered the entire height of the IL was cut from the same shell slice as where thin sections were acquired for Raman spectroscopy, SEM and EBSD (see sections below). The strip was ground in an agate mortar and pestle to achieve a fine-powdered

grain size. Each sample was run according to protocol in chapter 2 and the Rietveld refinement method (Rietveld 1969) applied to raw data.

6.3.2 Raman spectroscopy

Phase of fossil shells was also investigated with Raman spectroscopic analysis at the School of Chemistry, Cardiff University. Raman imaging was performed on polished thin sections prepared according to SEM sample preparation protocol (refer to chapter 2). Characterization of $CaCO_3$ was carried out in targeted regions of the IL on thin sections, covering areas that were proximal to the IL edge (area 1 on Figure 6.1), midway along the IL (area 2 on Figure 6.1) and distal to the IL edge (i.e. near the pallial line at the region of first growth) (area 3 on Figure 6.1).

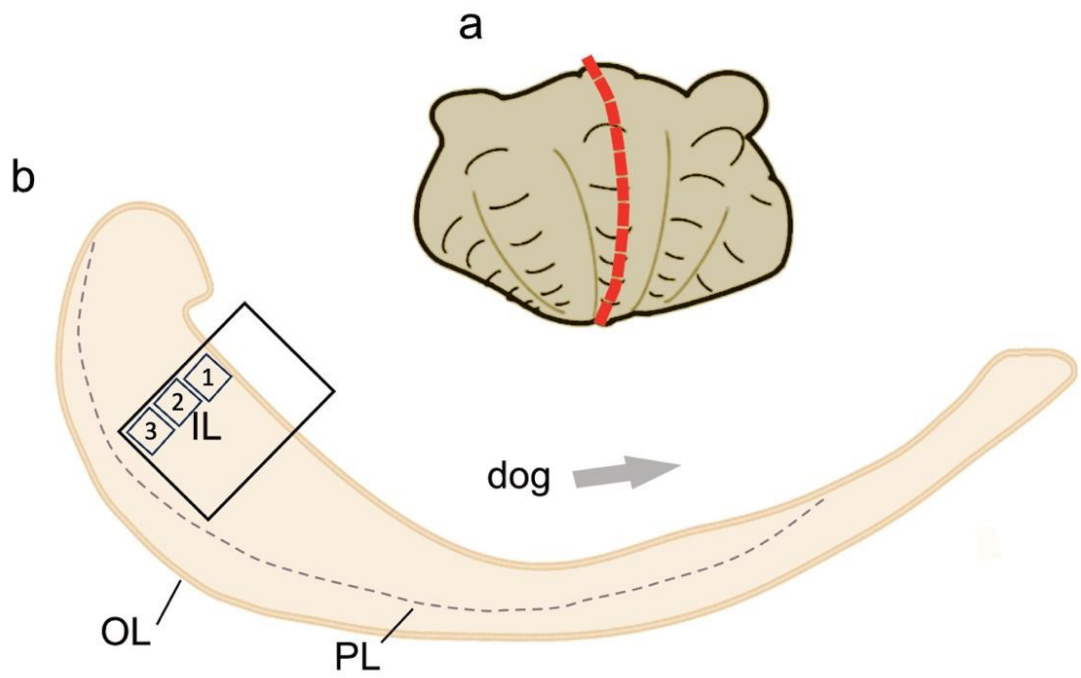

Figure 6.1. **(a) Valve of *Tridacna squamosa*, with red dashed line indicating longitudinal cut from hinge to upper shell margin, where slice in (b) was acquired; (b) Longitudinal shell slice, showing inner shell layer (IL), outer shell layer (IL) and pallial line (PL), demarcating the IL and OL. Three numbered black rectangular regions (1, 2, 3) in IL depicts areas of analysis for Raman spectroscopy, SEM and EBSD.**

6.3.3 SEM

The microstructure of biominerals was investigated using SEM at the School of Earth and Environmental Sciences, Cardiff (chapter 2 for more information). High-resolution in-lens secondary electron images of samples were taken across the height of the IL (i.e. the three rectangular areas on Figure 6.1b) to characterize and identify microstructure.

6.3.4 EBSD

EBSD analyses were performed to map mineral phase, crystallographic orientation, crystallographic co-orientation statistics and grain size distribution statistics. Sections used for SEM were repolished and a thin layer of carbon coat (3 nm) applied, according to protocol in chapter 4 and Mills et al. (2024). EBSD was carried out on the same three rectangular shell regions of the IL as SEM at the School of Earth and Environmental Sciences, Cardiff. The aragonite, calcite and dolomite unit cells were indexed.

The majority of data clean up procedure was kept to a minimum to avoid oversimplification of the data, with the exception being for grain size maps, where nonindexed pixels were interpolated from surrounding indexed pixels. For direct comparison of quantitative data extracted from the EBSD maps (i.e. crystallographic co-orientation strength statistics and grain size statistics), results are reported based on 100 x 100 μm map regions, unless otherwise specified.

The EBSD data is shown as band contrast images (BC), inverse pole figure maps (IPF) demonstrating crystallographic preferred orientation, corresponding contoured pole figures providing crystallographic co-orientation statistics of crystallographic axes (*a*-axis, [100]; *b*-axis, [010]; *c*-axis [001]) and grain size maps that resolve the area (μm^2) of each grain. BC images are greyscale images that visualize microstructure and strength of the diffracted EBSD signal for each data point, where a strong diffraction signal is lighter in colour, and a weaker signal is a darker grey/black. Individual grains in the IPF maps are colour-coded according to crystallographic orientation and relative

to a specific sample direction (e.g. Y, X, or Z), providing information on each crystallographic direction (i.e. [100], [010], [001]). The density distribution of contoured pole figures gives statistics on crystallographic co-orientation strength with multiple of uniform density (MUD) values, derived from pole figure maxima, where a higher MUD value indicates a stronger co-orientation strength (e.g.
Crippa et al. 2020).

6.3.5 LOI

Bulk LOI measurements were performed at the School of Earth and Environmental Sciences, Cardiff University for estimation of organic contents between modern and fossil tridacnid shells. One modern shell was chosen from each reef site (i.e. Triangle, SS_CT; Baik, SS_BAIK) and investigated with the fossil shell from the Miocene (TF108). Powdered shell material was taken from across the entire height of the IL and inserted into a chamber furnace for the decomposition of organic macromolecules (refer to chapter 2 for more information). Three replicates for each sample were taken and data averaged for each shell.

6.4 Results

6.4.1 Nano- to microscale microstructural and crystallographic features

6.4.1.1 Characteristics of modern giant clam shells

The IL of modern *T. squamosa* shells collected alive consist entirely of aragonite, as shown by XRD in Figure 6.2a, b. SEM secondary electron images representative of the IL of *T. squamosa* shells collected from both the Triangle and Baik reefs are shown in Figure 6.3 and highlight characteristic mineral units and their hierarchical assembly. The images show that all shells have a very fine-grained microstructure, with small biomineral units, similar to other pristine aragonitic bivalve shells (e.g. Pederson et al. 2020; Wichern et al. 2023). Biomineral unit shape and crystal packing is highly heterogenous on an intra- and inter-shell level. Microstructure of groups of biominerals can be categorized into irregular complex lamellar arrangements (Taylor et al. 1969) with either an absence (Figure 6.3a, c, e, g) or presence (Figure 6.3b, d, f, h) of simple

elongate regular prisms deposited on a frequent daily scale. The three hierarchical structural orders of lamellae observed in this microstructure are layered first-order lamellae (Figure 6.3c, d), which in turn comprise platelets of second-order lamellae, not always well defined in crossed lamellar microstructures (Crippa et al. 2020), made up of tightly packed third-order biomineral units (Figure 6.3e, f) (e.g. Agbaje et al. 2017; Agbaje et al. 2019; Hou et al. 2020). Nanograins approximately under 100 nm in size are distributed across the surface of third-order biomineral units (Figure 6.3g, h). Bulk LOI measurements carried out adjacent to electron microscopy images demonstrate the IL is composed of approximately 2 wt% of organic material (Table 6.1). However, it is noteworthy that there is high variation between replicates in the modern samples, which may be due to the bulk sampling technique used. This may not capture finescale variation that could be revealed with more localized methods (e.g. TGA).

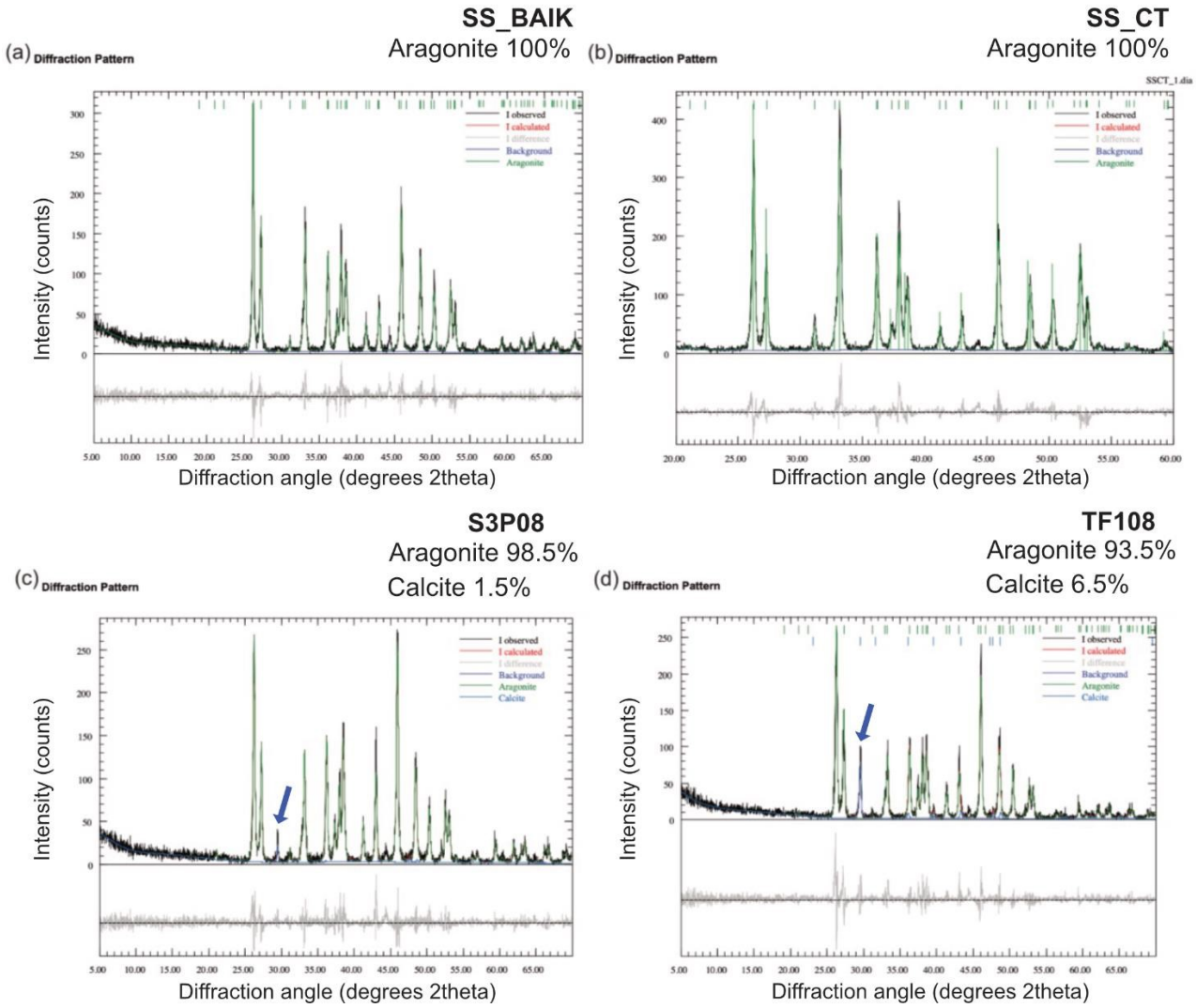

Figure 6.2. **XRD diffractograms of shells of modern *Tridacna squamosa* (a, b) and fossil *Tridacna* (c, d). Modern samples collected alive from Darvel Bay at the Baik (SS_BAIK) (a) and Triangle (SS_CT) (b) reefs show shells are composed of 100% aragonite. Fossil shells dated from the Pliocene (S3P08) (c) and Miocene (TF108) (d) are composed mostly of aragonite, with a small percentage of calcite — 1.5% and 6.5% respectively. Blue arrows indicate calcite defining peaks. Black line is observed measurements, while red line is calculated from the Rietveld refinement. Grey line underneath represents the difference between observed and calculated.**

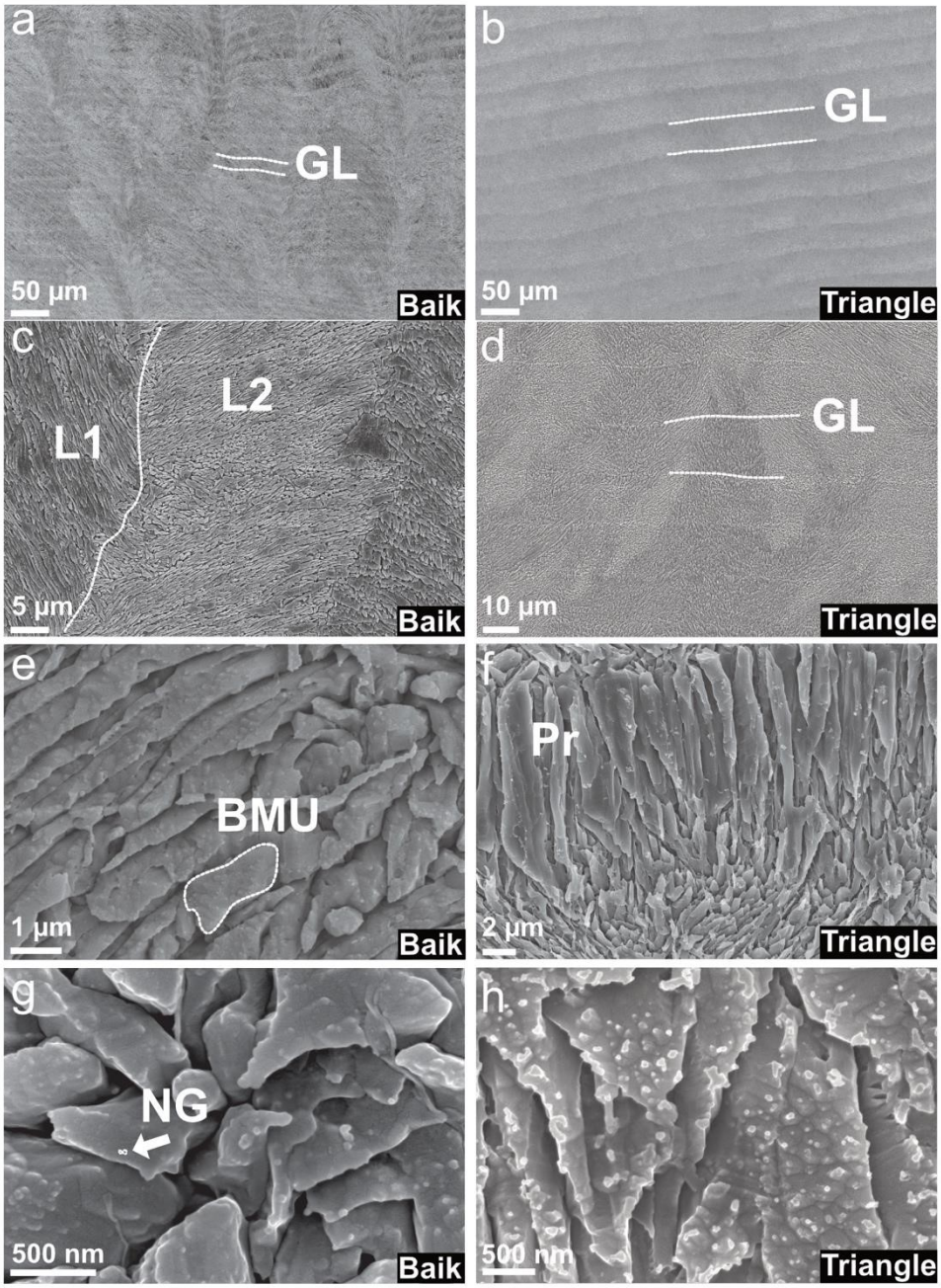

Figure 6.3. **Scanning electron microscopy (SEM) images showing the complex crossed-lamellar microstructure of the inner shell layer (IL) of modern *Tridacna squamosa* shells from Baik reef (a–g) and Triangle reef (b–h). (a, b) Complex crossed-lamellar fabric with regular daily growth lines; (c, d) alternating 'light and 'dark' first-order lamellar (L1, L2); (e, f) third-order biomineral units with varying morphologies: (e) small oblique crystals; (f) rows of simple prisms (Pr) coupled with a layer of smaller crystals, constituting one daily growth increment; (g, h) nanograins (NG) with heterogenous distribution on surface of aragonite crystals. GL = growth line; BMU = biomineral unit.**

Table 6.1. **Bulk loss on ignition (LOI) measurements for the inner shell layer of tested giant clam samples, showing data for modern samples collected alive (Triangle; Baik) and a fossil shell, dated from the Miocene (TF108). Three replicates were taken for each shell (LOI %) and mean LOI (%) given.**

Sample ID	Replicate	LOI (%)	Mean LOI (%)
TF108	1	0.916	0.930 ± 0.014
TF108	2	0.929	
TF108	3	0.944	
SS_CT	1	3.260	2.383 ± 0.766
SS_CT	2	1.845	
SS_CT	3	2.045	
SS_BAIK	1	1.573	2.019 ± 0.586
SS_BAIK	2	2.683	
SS_BAIK	3	1.801	

Crystallographic texture of the microstructures in the modern *T. squamosa* shells reveal a coherent crystallographic preferred orientation of the [001] axis (Figure 6.4), the most common orientation across biogenic aragonite (Checa and Rodríguez-Navarro 2005). Pole figures show one strong maxima on the [001] axes, with the [010] and [100] axes orientated in a continuous belt-like girdle distribution about [001]. Accordingly, on IPF-Y maps, the [001] crystallographic axis of most grains run approximately parallel to the Y axis of the sample reference coordinates (Figure 6.4c, d). MUD values range from 28 to 58 in the IL (Figure 6.4), reflecting the heterogeneity of fine-scale microstructural arrangements, likely dictated by the presence or absence of daily prisms associated with growth bands (chapters 3, 4, 5; Mills et al. (2023, 2024)). *Tridacna squamosa* from the Triangle reef has the highest crystal coorientation strength (MUD 58), compared to *T. squamosa* from the Baik reef (MUD 28), indicative of a more ordered arrangement of biomineral units in the former. Grain size maps are given in Figure 6.4e, f. Grain size distribution, binned into groups based on grain area, is plotted against relative frequency with respect to total number of grains (%) for each EBSD map and shown in Figure 6.5. Total grain area ranges between 0–50 μm^2 for modern samples, but the majority of grains (~90%) are small and within the range of

1–10 μm^2 (Figure 6.5). Grain area data for every grain in the EBSD maps are available from the Mendeley Data Repository and more information is provided in Appendix D.

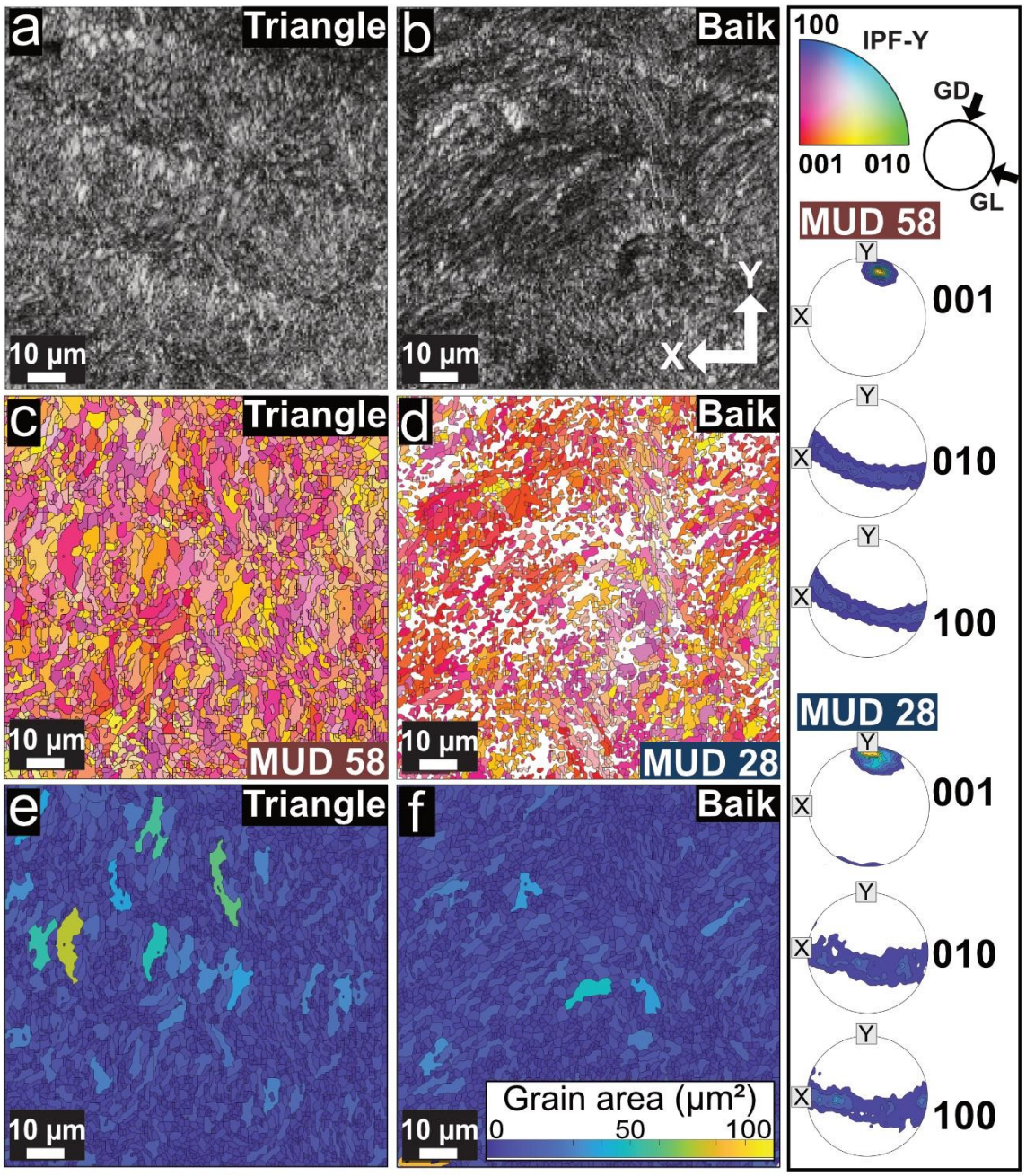

Figure 6.4. **Electron backscatter diffraction (EBSD) maps for modern *Tridacna squamosa* from Triangle (a–e) and Baik (d–f) reefs, showing the orientation of aragonite grains in the complex-crossed lamellar microstructure of the inner shell layer (IL). (a, b) Band contrast (BC) maps; (c, d) inverse pole figure (IPF-Y) maps with corresponding contoured pole figures (Triangle top; Baik bottom); (e, f) grain size distribution maps, showing grain area (µm^2). MUD values indicate a difference in crystal co-orientation strength, with the crystal morphology (prisms and adjacent smaller crystals) from Triangle (c) showing an MUD of 58, compared to 28 in Baik (d). Both samples show a similar grain size distribution (e, f). IPF colour-coded key and reference pole figure indicating estimation of growth direction (GD) and growth lines (GL) in relation to the sample orientation represented in top right-hand corner.**

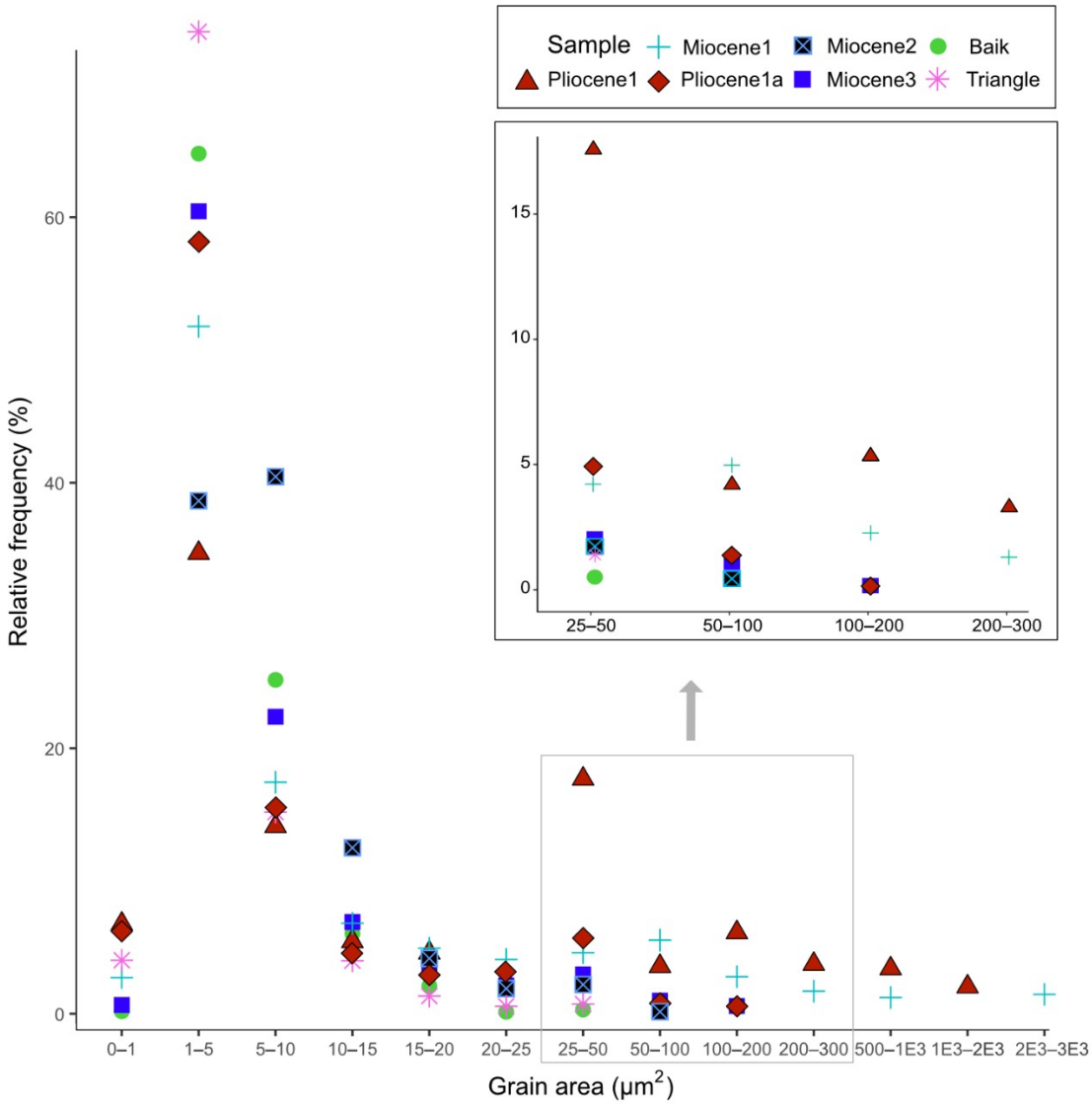

Figure 6.5. **Relative frequency (%) versus distribution of grain area for representative 100 x 100 μm EBSD map regions. Points show data from two modern giant clam shells (Baik; Triangle), which are similar in grain size throughout the IL, and two fossil giant clam shells. Fossil giant clams show large differences in grain size across the IL (Miocene1, Miocene2, Miocene3; Pliocene1, Pliocene1a). In modern *Tridacna squamosa* shells, grain size is small and comparable between individuals, such as grain area does not reach beyond 50 μm^2 and most grains fall between 1–5μm^2. In fossil *Tridacna* shells, grain size distribution in Miocene2 does not reach beyond 100 μm^2 in size, while in Miocene3 and Pliocene1a largest grains are up to 200 μm^2. In areas Miocene1 and Pliocene1, grains are extremely large. Inset of the larger graph highlights variation in largest grain sizes between different shells/regions of shells. 1E3, 2E3 and 3E3 represent 1000, 2000 and 3000, respectively.**

6.4.1.2 Preservation of fossil giant clam shells

XRD and Raman spectroscopy reveal that the fossil giant clam shells consist mostly of aragonite, with a small percentage recrystallized to calcite (Figure 6.2c, d; 6.6a) — 1.5% for the Pliocene shell and 6.5% for the Miocene shell (Figure 6.2c, d). For the Raman spectra, the strongest peaks were v_1 peaks near 1085 cm^{-1}, which indicates aragonite (e.g. Urmos et al. 1991; Parker et al. 2010; DeCarlo 2018). The in-plane bend (v_4) internal mode also revealed peaks around 700–720 cm^{-1} for both shells, with a slight shift to the right in the Miocene shell (TF108). The lattice mode showed characteristic low frequency measurements of aragonite at 150 cm^{-1} and 210 cm^{-1} for the Pliocene shell (S3P08); however, the presence of a small peak at 280 cm^{-1} near the inner layer shell edge/periphery in TF108 is indicative of calcite (Figure 6.6a).

SEM secondary electron images from fossil shells show different microstructures compared to modern samples throughout most of the IL, indicating destruction of original microstructural arrangements (Figure 6.7). First-, second- and third-order hierarchical lamellae are not well defined, in comparison to first- and third-order structures for the modern samples (Figure 6.7). The Pliocene shell shows a consistent level of microstructural alteration across much of the IL, where large aragonitic lathlike crystals (Figure 6.7a, c, e, g) run approximately perpendicular to the IL shell edge. In the Miocene shell, alteration is more variable and some retention of original biominerals are visible (Figure 6.7b, d), particularly away from the shell periphery at the IL edge (i.e. away from region 1 in Figure 6.1b). In region 1, large aragonitic platelet-like crystals completely overprint most of the original structure (Figure 6.7f). The bulk LOI measurements reveal under half of the organic content (<1 wt%) compared with the modern samples (Table 6.1), indicating degradation of the organic matrix. The development of cavities where organic material used to be, predominately associated with daily growth lines (Figure 6.7c), suggest infilling with secondary aragonite cements (e.g. Hou et al. 2020).

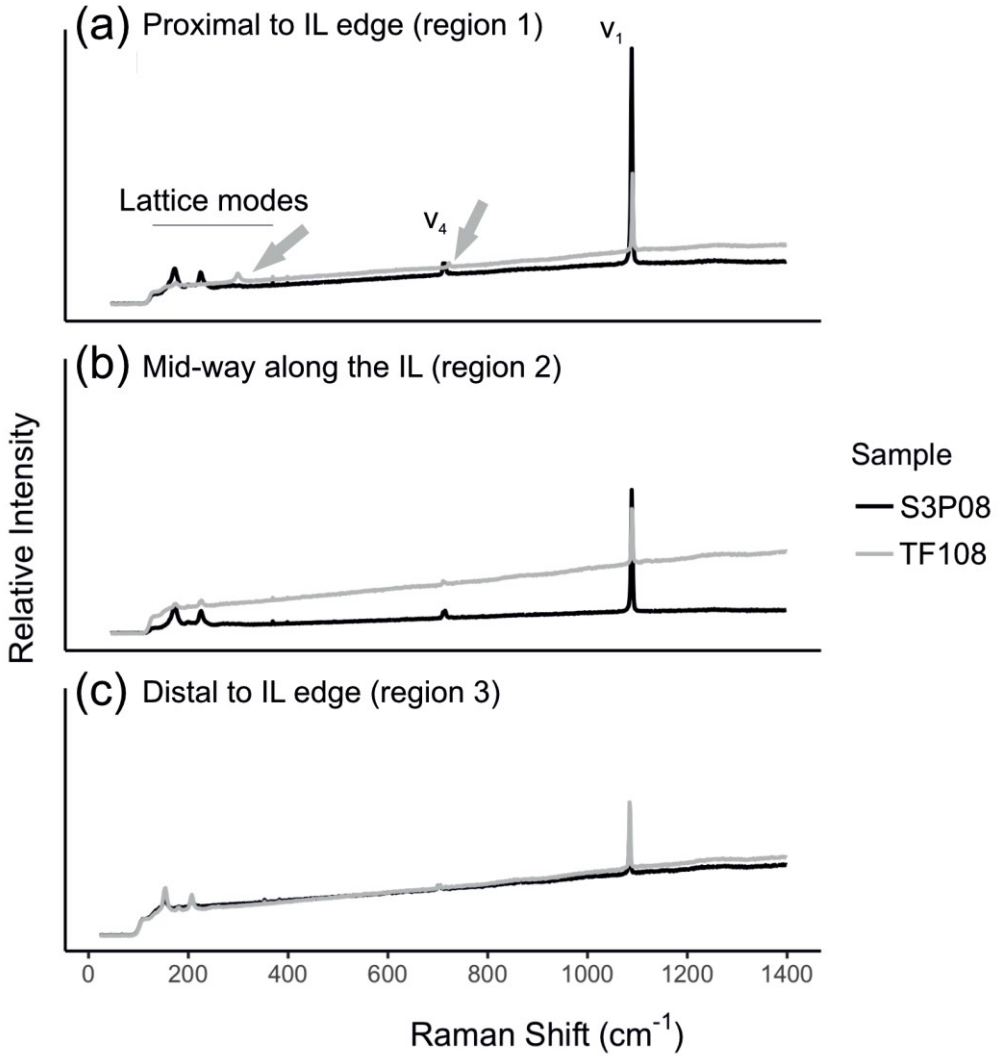

Figure 6.6. **Raman spectra of fossil giant clam shell samples collected from eastern Borneo, showing aragonite defining v_1 peaks near 1085 cm^{-1}, in-plane bend (v_4) internal mode peaks near 700–720 cm^{-1} and lattice modes. The presence of a small peak at 280 cm^{-1} and slight shift of the in-plane bend in shell TF108 (Miocene) is shown in (a), indicating calcite (grey arrows), whereas other shell regions shown in (b, c) indicate aragonite. (a) Analysis carried out proximal to inner layer shell edge/periphery, representing region of last growth before death (rectangle 1 on Figure 6.1). (b) Analysis carried out mid-way along the height of the IL (rectangle 2 on Figure 6.1). (c) Analysis carried out distal to inner layer shell edge/periphery, representing region of juvenile growth (rectangle 3 on Figure 6.1).**

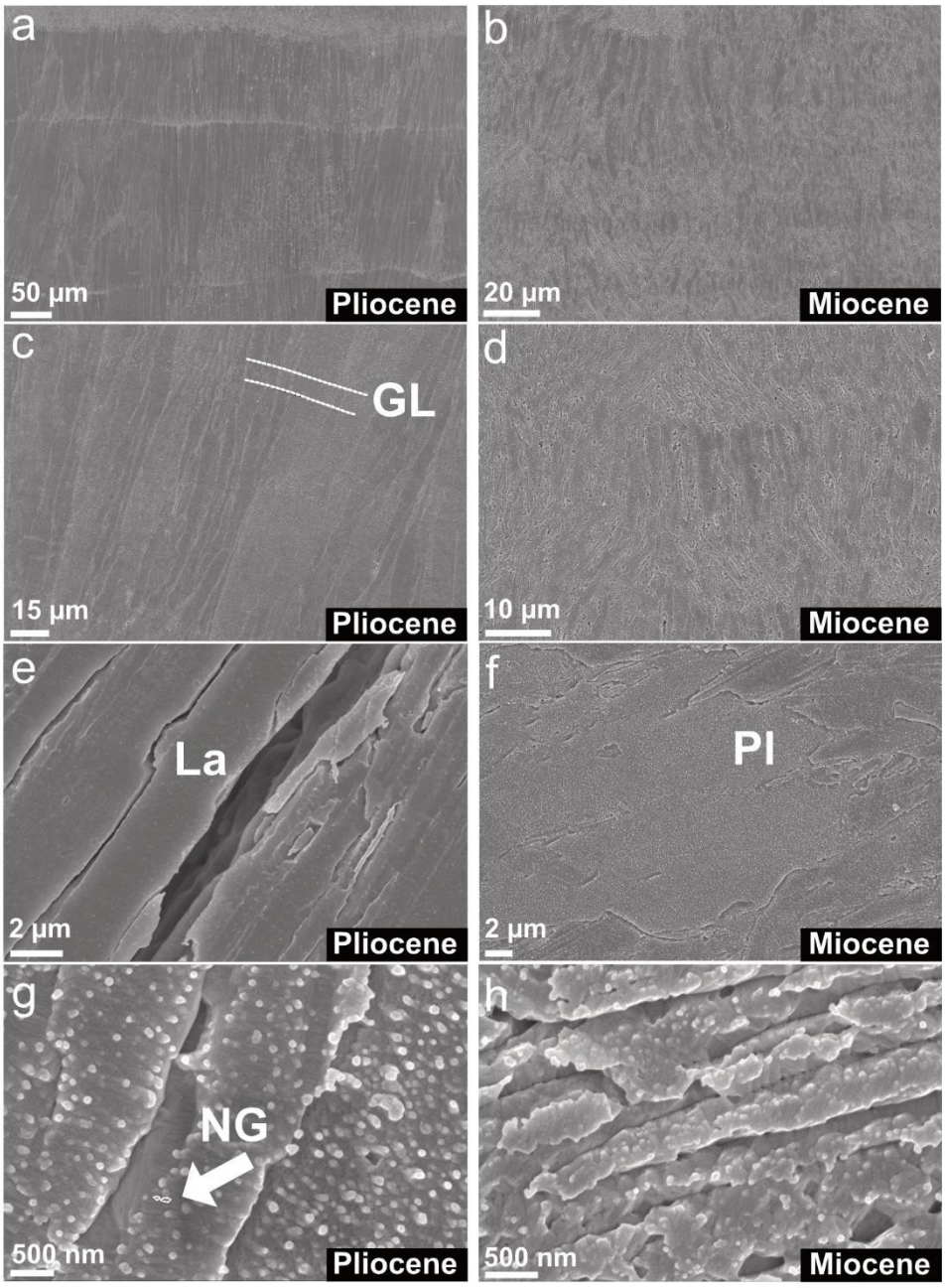

Figure 6.7. **Scanning electron microscopy (SEM) images showing the microstructure of the inner shell layer (IL) for Pliocene (a–g) and Miocene (b–h) fossil giant clam shells. (a, c, e) Large aragonitic lath-like (La) crystals overprint most of the assumed original complex crossed-lamellar fabric within the Pliocene shell, but the faint outline of regular daily growth lines is still observed (c). In comparison, there is notable variation in size of crystals within the Miocene shell, with some smaller crystals directly adjacent to larger crystals with different morphologies (b, d), while large platelet-like (Pl) crystals (f) presumably destroy the retention of original microstructure in other parts of the IL. (g, h) Nanograins (NG) with a heterogenous distribution are still observed on surface of aragonite crystals throughout the IL in both individuals.**

The BC images from the EBSD data for shell regions Miocene1 and Pliocene1 (corresponding to rectangular region 1 on Figure 6.1) (Figure 6.8a, b) reveal a strong intensity signal compared to the modern samples (Figure 6.3a, b), which may be due to a lack of organic content and/or larger grain sizes (e.g. Casella et al. 2017). Contoured pole figures for both samples show preservation of a strong crystallographic preferred orientation on the [001] axes, while the [010] and [100] axes reveal a discontinuous distribution around [001]. A disjointed distribution on [010] and [100] may be related to sampling a smaller number of grains (due to their larger size) in the 100 x 100 μm map areas in Figure 6.8 compared to the modern samples in Figure 6.4. Both samples have notably higher crystal co-orientation strengths (MUD 110–158) and larger grain sizes than modern shells (compare Figure 6.8e, f to Figure 6.4e, f), although approximately 50% of grains remain small, between 1–10 μm^2 (Figure 6.5). The areas of individual grains within the Pliocene1 and Miocene1 EBSD maps range between 0–2000 μm^2 and 0–3000 μm^2, respectively (Figure 6.5).

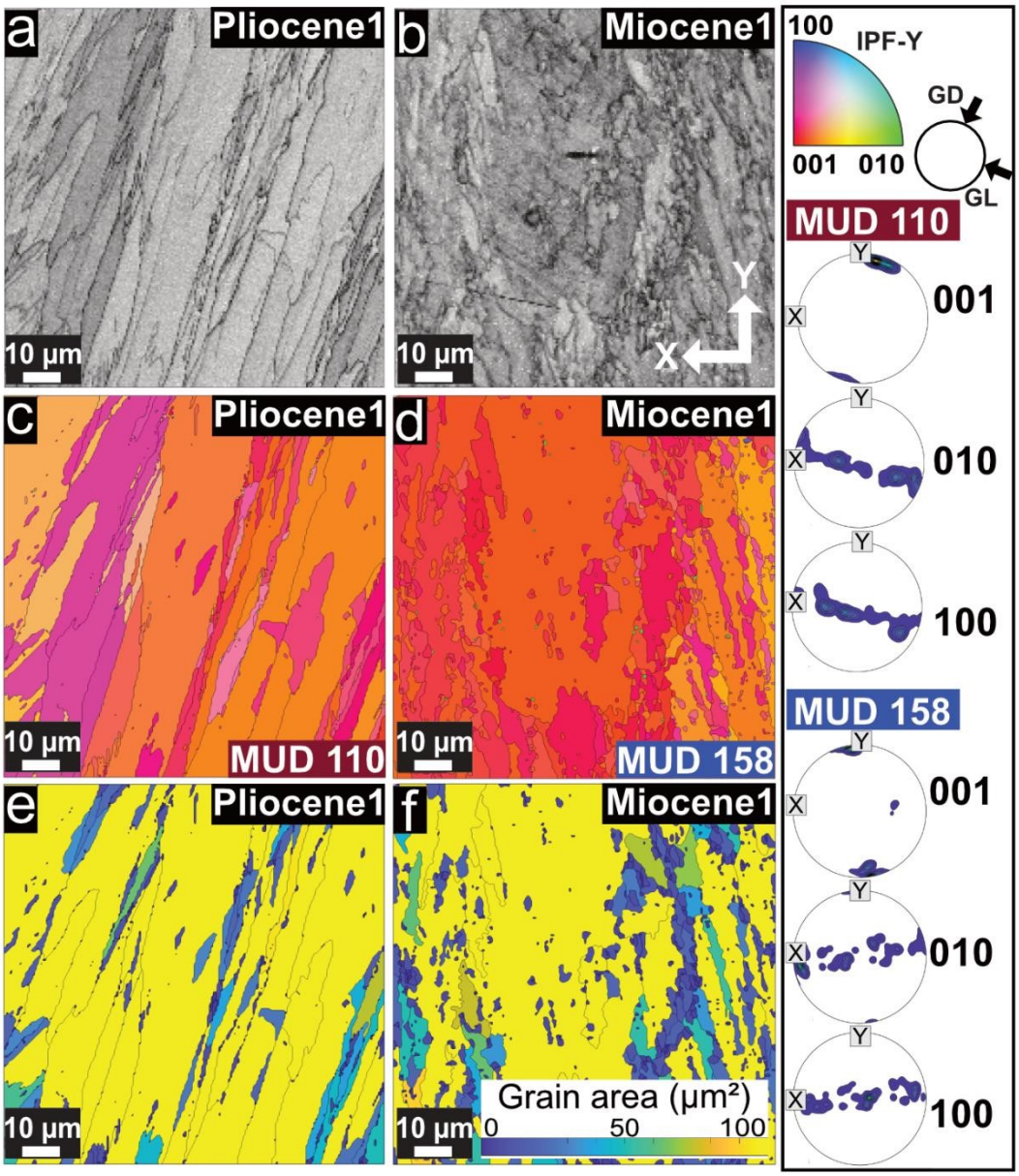

Figure 6.8. **Electron backscatter diffraction (EBSD) maps for fossil giant clam shells from the Pliocene (a–e) and Miocene (d–f), showing areas of shells (Pliocene1; Miocene1) that are most different from modern samples: (a, b) band contrast (BC) images show higher diffraction intensity, such that more grains are 'lighter' grey; (c, d) the orientation of aragonite grains is shown by inverse pole figure (IPF-Y) maps, with corresponding contoured pole figures (Pliocene1 top; Miocene1 bottom). MUD values indicate a much higher crystal coorientation strength, with an MUD of 110 (Pliocene1) and 158 (Miocene1); (e, f) grain size distribution maps demonstrate that grain area (µm^2) is larger in both samples. IPF colour-coded key and reference pole figure indicating estimation of growth direction (GD) and growth lines (GL) in relation to the sample orientation represented in top right-hand corner.**

I consider the EBSD maps in Figure 6.8 the end members of aragonite diagenetic alteration within this study. Although a large proportion of the IL in both fossils is represented by the textures shown in the Miocene1 and Pliocene1 maps in Figure 6.8, it is important to note that textural variation does occur. Some shell regions do appear similar to the texturally pristine modern material and are observed away from the IL shell periphery/edge in the Miocene shell (i.e. rectangular regions 2 and 3 on figure 6.1b). However, subtle crystallographic differences that deviate from the modern material are detected with EBSD statistics, which may hint at early alteration. Figure 6.9 highlights two regions which appear to retain some original crystalline features but show subtle variation in relation to grain size and/or crystallographic orientation. Crystallographic co-orientation statistics for the Miocene2 map (MUD 41) shown in Figure 6.9a, b is comparable to modern shells, but maximum grain size is larger (50–100 μm^2 opposed to 25–50 μm^2) (Figure 6.5), which may indicate either (1) the area is pristine and there is natural variation in biomineral size or (2) early fusion of third-order biomineral units. The Miocene3 map (Figure 6.9c, d) shows a larger maximum grain size (100–200 μm^2) than Miocene2 (Figure 6.9) and a small proportion of pixels are indexed as calcite (1.4%) and dolomite (0.39%) (Figure 6.9b; Figure 6.10 for EBSD phase map). However, mean angular deviation (MAD), which indicates indexing confidence for each phase, was >1.5° for dolomite, suggesting potentially inaccurate measurements and potential EBSD pattern mis-indexing (e.g. Päßler et al. 2018). Pole figures for Miocene3 show scattered girdles on the [010] and [100] axes and crystallographic co-orientation is MUD 25, which falls close to the range of values recorded for modern samples (MUD 28–58).

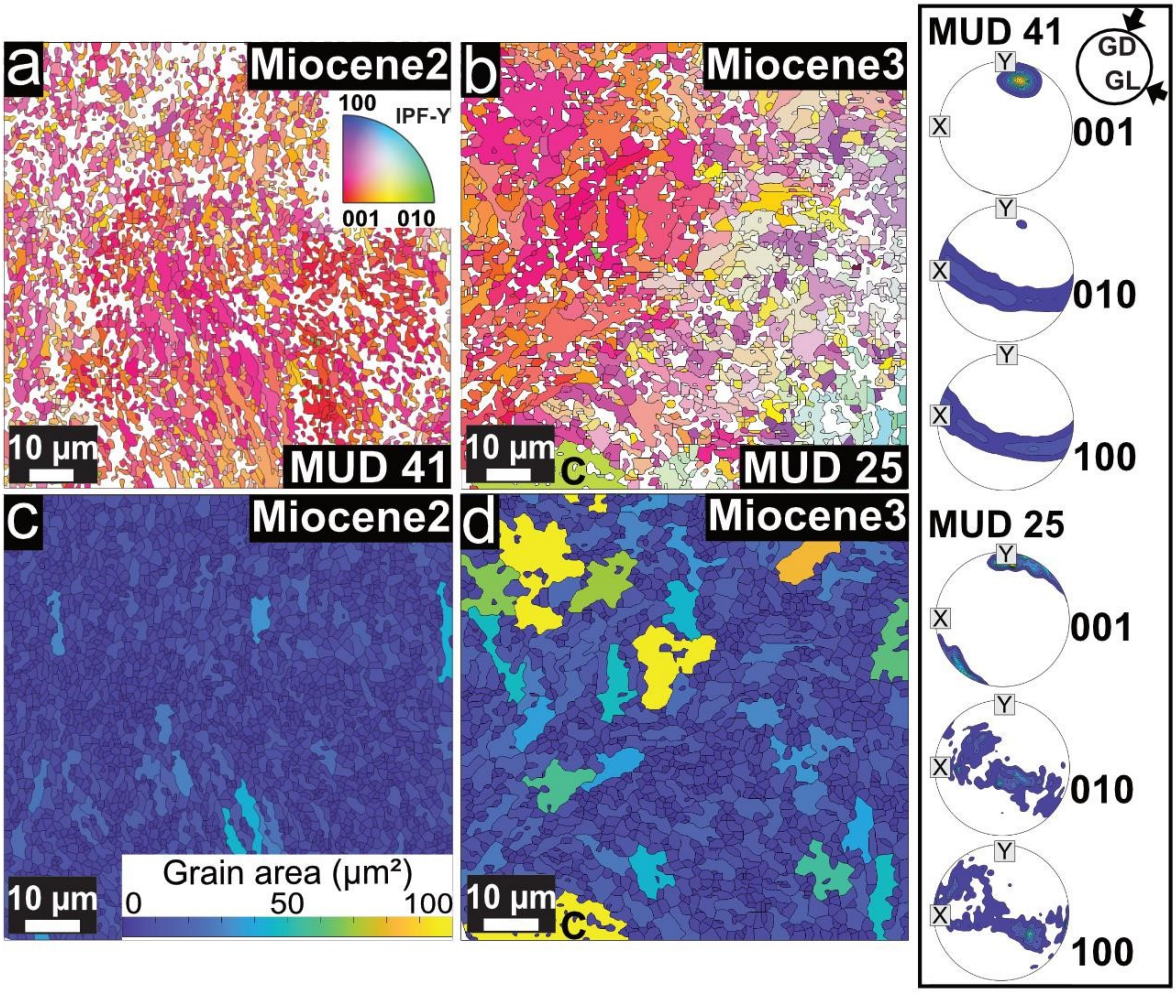

Figure 6.9. **Electron backscatter diffraction (EBSD) maps for the Miocene fossil giant clam, showing different regions of the shell (Miocene2; Miocene3) that moderately vary from modern samples: (a, b) the orientation of aragonite grains is shown by the inverse pole figure (IPF-Y) maps, with corresponding contoured pole figures (Miocene2 top; Miocene3 bottom). MUD values indicate a crystal coorientation strength comparable to modern shells, showing MUD 41 (Miocene2) and MUD 25 (Miocene3); (c) overall grain size distribution of Miocene2 is small and comparable to modern shells; (d) grain size distribution of Miocene3 shows the occurrence of some larger grains than modern shells and Miocene2, in which some aragonitic grains have transformed to calcite (C). IPF colour-coded key given within image (a) and reference pole figure indicating estimation of growth direction (GD) and growth lines (GL) in relation to sample orientation provided in top right-hand corner.**

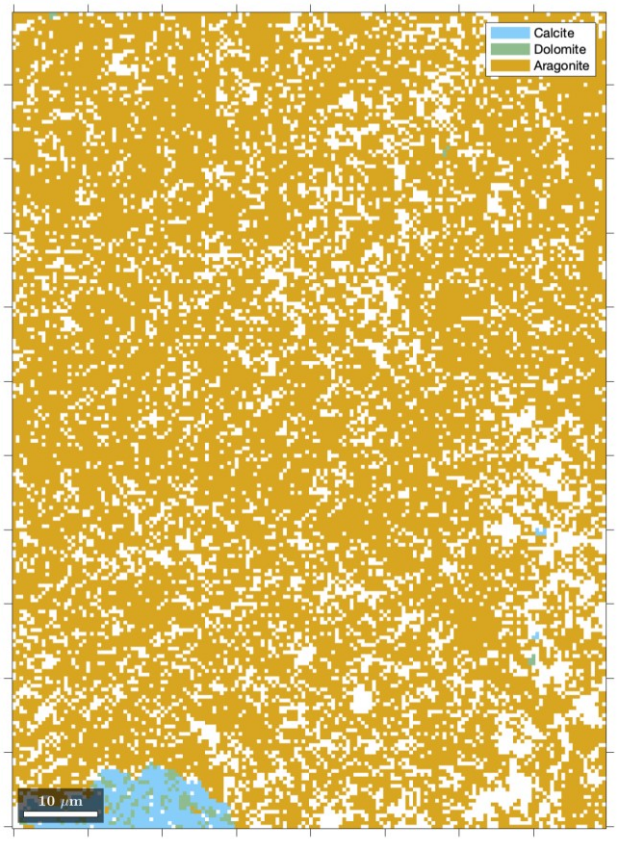

Figure 6.10. **EBSD phase map for area Miocene3 within sample TF108. Small patches of calcite (pale blue) and potentially dolomite (green) are detected between aragonite (orange) grains.**

In comparison to the Miocene shell, the Pliocene shell shows only small textural variation within the IL, with consistently high MUD values and coherent pole figures. However, smaller grain sizes are occasionally detected along the shell periphery (Figure 6.11c) (corresponding to rectangular region 1 on Figure 6.1), albeit still with high crystal co-orientation strength in analyzed 100 x 100 μm map areas (region Pliocene 1a on Figure 6.11c, MUD = 100).

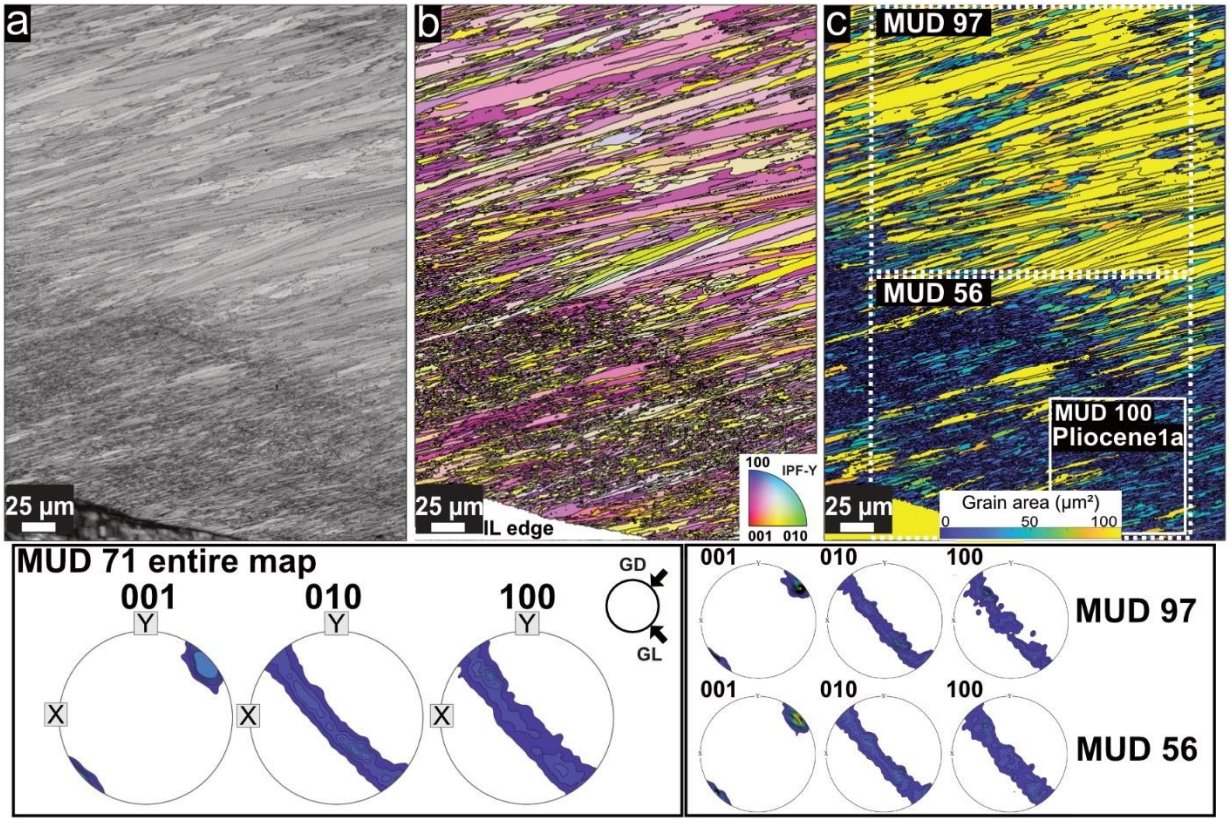

Figure 6.11. **Electron backscatter diffraction (EBSD) map for the Pliocene fossil giant clam, showing a region of the inner layer (IL) shell edge/periphery, where variation in crystal size is observed. (a) band contrast (BC) image showing high diffraction intensity with larger grain size, in which grains are 'lighter' grey; (b) the orientation of aragonite grains shown by an inverse pole figure (IPF-Y) map; (c) grain size distribution map, highlighting that crystal co-orientation strength rises with grain area. The smaller grains closer to the shell periphery (white dashed box at bottom of map) have an MUD value of 56, while adjacent larger grains distal from the shell periphery (white dashed box at top of map) have an MUD of 97. The entire map has a crystal co-orientation strength of MUD 71. Corresponding contoured pole figures are given below the images. The IPF colour-coded key is shown in map (b) and the reference pole figure indicating estimation of growth direction (GD) and growth lines (GL) in relation to the sample orientation is given next to pole figures. The smaller solid white rectangle (Pliocene1a) indicates a 100 x 100 µm region used for direct quantitative comparison with other EBSD maps of the same size.**

6.4.2 Grouping of shell features

I focused the assessment of aragonite alteration in giant clam shells on EBSD data because it is quantifiable and therefore can be measured. By the investigation of crystallographic orientation patterns derived from pole figures, crystallographic coorientation strength statistics (MUD values) and grain size statistics represented by grain area (μm^2), my findings can be classified into four main groupings within the analyzed shell regions (Figure 6.12):

1. **Unaltered shell carbonate reference material from modern shells.** Most crystals are very small (approximately 90% with a grain area of 1–10 μm^2). Maximum crystal size does not exceed 25–50 μm^2. Aragonitic pole figures show a preferred crystallographic orientation of the [001] axis, with the [100] and [010] axes oriented in continuous belt-like gridles around [001]. Crystallographic co-orientation statistics range between MUD 28–58, depending on fine-scale differences in microstructure.

2. **Fossil material largely indicative of reference material in group 1.** Most crystals are very small (approximately 80% with a grain area of 1–10 μm^2). Maximum crystal size does not exceed 50–100 μm^2. Aragonitic pole figures show a preferred crystallographic orientation of the [001] axis, with the [100] and [010] axes oriented in continuous belt-like girdles around [001]. Pole figures show crystallographic coorientation (MUD 41) in line with modern shell values.

3. **Fossil material somewhat indicative of reference material in group 1.** Most crystals are very small (approximately 80% with grain area of 1–10 μm^2). Maximum crystal size does not exceed 100–200 μm^2. Aragonitic pole figures show a preferred crystallographic orientation of the [001] axis, with the [100] and [010] axes oriented in scattered belt-like gridles around [001]. Crystallographic co-orientation is MUD 25. Small calcitic patches are present in between aragonite crystals.

4. **Fossil material not indicative of reference material in group 1.** Some crystals are very small (approximately 50% with grain area of 1–10 μm^2), but other crystals are large aragonite laths or platelets, where maximum crystal size reaches approximately 1000–3000 μm^2. Aragonitic pole figures show a preferred

crystallographic orientation of the [001] axis, with the [100] and [010] axes oriented in discontinuous belt-like gridles around the [001] axis (N.B. likely related to fewer grains than other groups). Pole figures show the highest crystallographic co-orientation, with MUD 100–158.

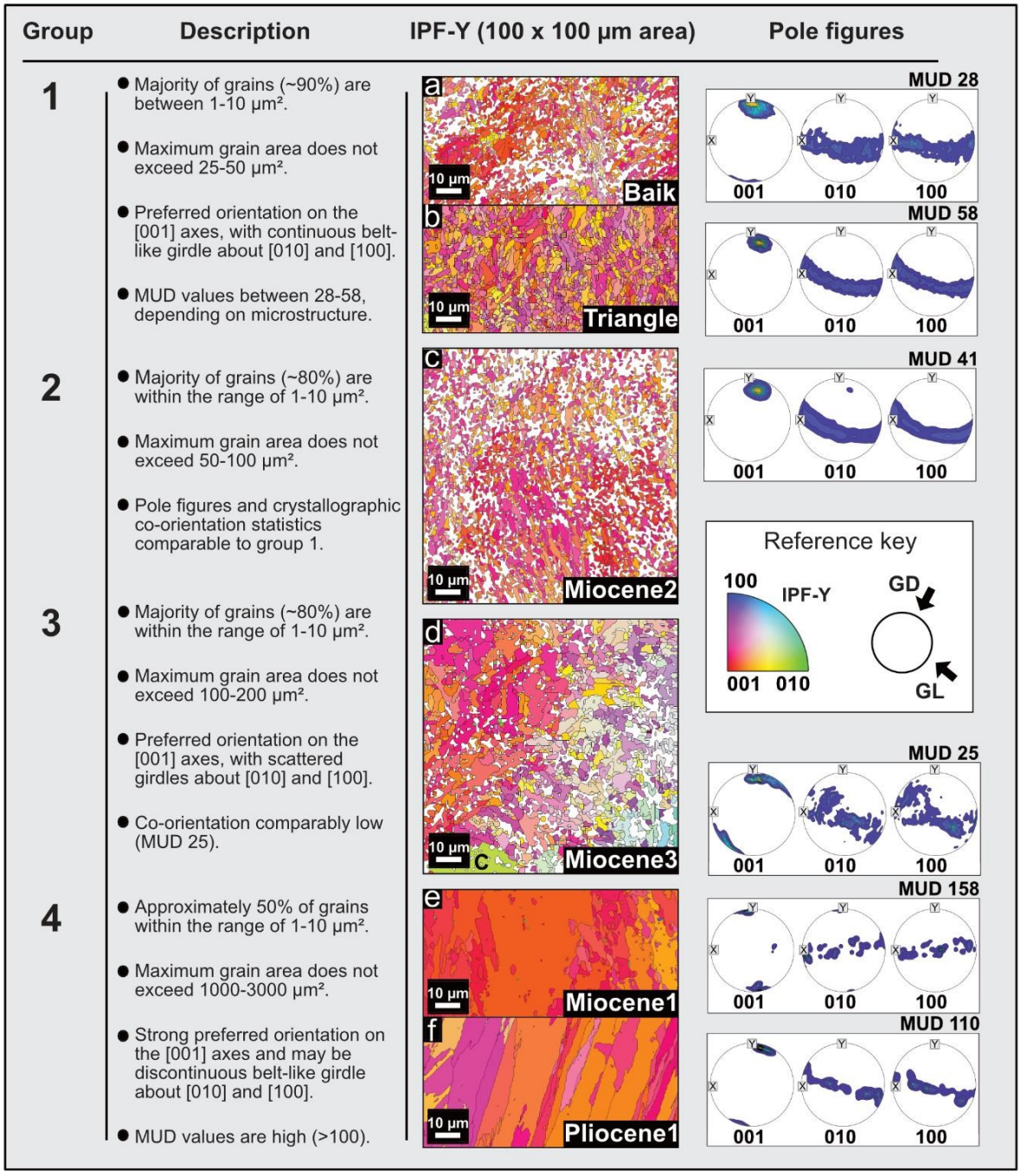

Figure 6.12. **Overview of crystallographic texture from electron backscatter diffraction (EBSD) data of modern and fossil giant clam shells. Variation in the orientation patterns of aragonite is described, based upon 1. arrangement of contoured pole figures, 2. crystallographic co-orientation statistics (MUD values) and 3. grain size distribution statistics, represented by grain area (µm²). I devise a classification scheme using the 100 x 100 µm analyzed shell regions and allocate areas within/between shells into four groups: (a, b) Group 1 is unaltered shell carbonate from modern shells collected alive, used as a reference for other groupings; (c) Group 2 shares many characteristics with group 1 but differs in size of maximum grain area. This area could be due to the early stages of diagenetic alteration, or alternatively may represent pristine**

biogenic carbonate with natural heterogeneity in the size of biomineral deposition; (d) Group 3 is somewhat like group 1; however, maximum grain area is larger, the distribution of data points on the associated pole figure are comparably highly scattered and small patches of calcite are present amongst the aragonite grains. (e, f) Group 4 is most different from group 1, where maximum grain size is extremely large (up to 1000–3000 μm^2), aragonitic pole figures show the strongest preferred crystallographic orientation of the [001] axis and MUD values are highest (100–158).

6.5 Discussion

The skeletons of biogenic carbonates are key to the study of past climates and environments, but they often experience diagenetic alteration post-mortem. It is well documented that metastable aragonitic skeletons can undergo extensive alteration to calcite during diagenesis, the thermodynamically most stable polymorph of $CaCO_3$ near the earth's surface (e.g. Brand 1989; Sandberg and Hudson 1990; Hendry et al. 1995). However, the assumption that the preservation of aragonite unequivocally equals a pristine skeleton is inaccurate (e.g. Marcano et al. 2015).

In this chapter, I carried out structural evaluation of alteration within the aragonite phase in giant clams. I focused on quantitative crystallographic evaluation of giant clam shells with EBSD, alongside complimentary diagenetic screening tools proven to help unveil state of preservation in other bivalve species (Casella et al. 2017, 2018a, b; Pederson et al. 2020; Forjanes et al. 2022). Specifically, I used SEM for preliminary identification of microstructure, LOI for approximate insight into organic matrix degradation between fossil and modern shells, and Raman spectroscopy and XRD for preliminary characterization of phase. I found that the nano- and microtextural and crystallographic characteristics of the inner shell layer (IL) of modern *T. squamosa* giant clam shells collected alive were different to fossil *Tridacna* shells collected from clay-rich outcrops. Preliminary identification of mineral phase with XRD and Raman spectroscopic analyses confirmed modern shells were composed entirely of aragonite, while fossil shells were mostly aragonite with a small percentage of calcite (<7%). SEM revealed that the modern shells showed a complex crossed lamellar assembly typical of many molluscan carbonate tissues (Almagro et al. 2016), with subtle variations observed at a daily scale, consisting of a presence or absence of elongated prisms within daily growth bands, as previously described in chapters 3, 4, 5 and Mills et al. (2023, 2024). However, much of the surface of the IL did not retain these features within either of the fossil shells studied. First- and third-order hierarchical structures clearly observed in modern shells, an indicator of pristine material (Hou et al. 2020), were not identified in the majority of the Pliocene and Miocene shell areas investigated.

SEM imaging has been utilized previously to investigate diagenesis in giant clams and has proven useful for visually assessing potential alterations in structural shell

characteristics. To date, SEM has been used to understand the effects of natural diagenesis on the biominerals in various species of giant clams (Faylona et al. 2011; Warter et al. 2015; Hou et al. 2020). A previous study investigating the microstructure of mid-Holocene *Tridacna maxima* and *Hippopus hippopus* shells (Faylona et al. 2011) found partially dissolved aragonitic biomineral units in prismatic and crossed-lamellar microstructures with SEM, suggesting early diagenesis within the aragonite phase occurred on a finescale that is not visible macroscopically. Warter et al. (2015) also used SEM and cathodoluminescence on the same shell dated from the Miocene as used in the current contribution, but a different valve. Their results concurred with the findings of this study, similarly indicating a crossed-lamellar microstructure comparable to pristine aragonite but showing differences in crystal size and shape on a microscale, with altered crystals being larger, thinner and more porous. Correspondingly, another study on a fossil *Tridacna gigas* collected from the bottom of the South China Sea (Hou et al. 2020) suggested aragonite plate compaction leading to larger crystal sizes based on microstructural identification in SEM images. However, our comprehension of how these alterations influence shell texture extends only as far as qualitative imaging analysis allows prior to this study, as there is a lack of quantitative assessment of diagenetic alteration.

This study built upon previous work by accessing the quantitative crystallographic changes related to diagenesis. I base my analysis on crystallographic orientation patterns derived from pole figures, crystallographic co-orientation statistics represented as multiple of uniform density (MUD) values and grain size distribution statistics. My results showed that all microstructures in modern and fossil shells had a common preferred crystallographic orientation of the [001] axis (or *c*-axis), with the [100] and [010] axes oriented in continuous or discontinuous belt-like gridles around [001], as found in other EBSD studies of modern giant clams, i.e. *Tridacna derasa* and *Tridacna gigas* (Agbaje et al. 2017; Gannon et al. 2017, respectively). In the modern shells, crystal co-orientation strength ranged between MUD 28–58, compared to MUD 100–158 in the most altered areas of fossil shells, showing complete diagenetic overprint. The MUD values from modern shells are higher than that previously recorded for *T. derasa* (MUD 12) (Agbaje et al. 2017), but close to other bivalves with similar complex-crossed lamellar microstructural arrangements, such as *Glycmeris glycmeris* (MUD 42) (Crippa et al. 2020). Crystal co-orientation strength (MUD)

showed a positive relationship with size distribution of grains, which were frequently larger in the EBSD maps from the altered samples relative to those measured in the modern shells. Taken with estimated measurements of organic content (approximately >2 wt% modern; <1 wt% fossil), my results concur with a mechanism of alteration put forward by Hou et al. (2020) for *T. gigas*, following an early loss of organic material and subsequent infilling with abiogenic aragonite, leading to the fusion of original biomineral units and enlargement of grain size (Hou et al. 2020).

In addition to the extensive differences noted between modern shells and much of the IL of fossil shells, I also observed small pockets within the fossil shells which appeared less altered. Inspection of these areas in the Miocene shell revealed remnants of visually pristine or only slightly altered shell carbonate irregularly distributed away from the IL edge, suggesting microspatial zoning of different stages of alteration. In some instances, extremely altered and seemingly slightly altered regions were observed adjacent to one another, only tens of microns apart. I classified this subtle alteration into two groups (Figure 6.12): (1) Areas that appeared pristine upon visual inspection but revealed larger maximum grain sizes than modern shell areas (group 2 on Figure 6.12); (2) Areas that appeared pristine upon visual inspection but revealed larger maximum grain sizes than modern shell areas *and* patches of calcite variegated with aragonitic grains (group 3 on Figure 6.12). These findings underscore the intricate spatial heterogeneity and subtle alterations present within the fossil shells, emphasizing the need to quantitatively map biominerals.

Variation in diagenetic response across small areas of a shell are well documented in other bivalve species (e.g. Pederson et al. 2020) and depend on several contributing factors. For instance, different rates of alteration may reflect the compactness of a microstructure through differences in fluid transmission (e.g. Pederson et al. 2020). For example, the robust and compact skeleton of coral *Porites* sp. acts as a barrier between the interaction of aqueous fluid and organic matter, impeding the initial degradation of organics, compared to the comparatively ‘poorly’ structured bivalve shell of *Arctica islandica* (Forjanes et al. 2022). Accordingly, diagenesis also increases more rapidly where there is an increased presence of organics because a more pervasive network of pores and cavities may be formed, promoting rapid recrystallization through aggressive fluid mobilization (Gaffey et al. 1991). Considering

the highly varied nature of the microstructure of the giant clam samples used in this thesis, variable diagenetic response across small spatial scales due to the differential development of cavities and amount of organic content may be a plausible explanation. However, I do note the caveat that the study of fossil shells from natural settings alone, without the complimentary investigation of experimental alteration, cannot definitively distinguish pristine from altered shell carbonate. Natural variation in the deposition of the size of biomineral units by the organism is inevitable and moving forward, I recommend an experimental study of alteration in giant clam shells to determine these processes *in situ* and compliment current work.

This chapter allowed for the identification of pockets of pristine and altered material in fossil giant clam shells to be revealed in detail at similar scales to high-resolution geochemical approaches, such as EPMA or LA-ICP-MS. Findings show that most shell material is within the aragonite phase and only a small percentage transformed to calcite. Based on hydrothermal studies of other bivalve species (Casella et al. 2017, 2018a, b; Pederson et al. 2020; Forjanes et al. 2022), this suggests that most of the shell IL may be within the early phases of diagenesis. Considering a lead and lag pattern of structural and geochemical alteration has recently been recorded in *Arctica islandica* (Ritter et al. 2017; Pederson et al. 2020), where structural alteration comes first and is decoupled from geochemical changes, geochemical data from structurally altered shells could still be robust. This warrants further investigation in giant clams and more work is needed on the geochemical implications of pristine versus secondary aragonite phases.

6.5.1 Conclusion

In this study, I provided detailed characterization of the microstructural and crystallographic features in modern and fossil giant clam shells. I focused on diagenetic alteration of the inner shell layer (IL) within the aragonite phase, an often overlooked aspect of alteration in studies using giant clam shells as high resolution palaeoceanographic proxies. I presented the first quantified and unequivocal comparison of shell crystallographic texture based on crystallographic orientation patterns derived from pole figures, crystallographic co-orientation strength statistics (MUD values) and grain size statistics. I found that while most of the *Tridacna* shell

fossil carbonate remains within the aragonite phase, there is evidence of extensive textural alteration and crystallographic reorganization. In line with previous findings on experimental alteration in bivalves, my results suggest that natural alteration is a stepwise process, beginning with early degradation of the organic matrix, infilling with secondary aragonite cements that initiates a subtle increase of grain size, followed by a more substantial change in grain size distribution, where large grains are frequent and crystallographic co-orientation strength is correspondingly high. Due to the identification of potential intermediate stages of alteration with EBSD, we can classify the extent of diagenesis from different regions across the IL and show it is highly variable on a microscale. Overall, these results demonstrate the need for the integration of screening tools at a high spatial resolution for reliable interpretation of diagenetic alteration throughout giant clam shells. It is suggested that severe underestimation of the degree of alteration within a shell archive may be assumed if solely relying on bulk screening techniques such as X-Ray Diffraction that detect phase change only. Although I have showcased the usefulness of a multimethod approach for alteration of physical shell features, more work is needed to investigate how recrystallization relates to geochemical measurements within the shell to fully understand the implications of how early diagenesis could impact paleoenvironmental reconstruction.

7. Conclusions and future directions

7.1 Thesis summary and synthesis

Coral reefs are highly vulnerable ecosystems, threatened by both local anthropogenic activity and global impacts such as climate change-induced thermal bleaching events. These pressures affect the growth, health and ultimately survival of reef-building organisms, leading to reduced reef resilience and shifts in ecosystem function. Given the indispensable role that coral reefs play for coastal communities globally, understanding how these ecosystems will respond to ongoing and future stressors is critical. Therefore, understanding the responses of reef-building organisms to a rapidly changing ocean is essential for managing and safeguarding the future of coral reefs.

The Coral Triangle is situated within southeast Asia and is the focal point of marine biodiversity, hosting the highest number of coral species in the world, with a remarkable prevalence of regional endemics (e.g. Reaka et al. 2008). Turbid reefs, characterised by high suspended sediment loads and low light conditions, make up approximately 30% of corals reefs within the Coral Triangle (Sully and van Woesik 2020). They are hypothesized to play a significant role in the future of coastal marine biodiversity because they exhibit exceptional resilience, shielding coral reef organisms from widespread disturbances and thermal bleaching owing to their diminished light levels (Perry and Larcombe 2003; Waheed and Hoeksema 2013; Browne et al. 2019; Sully and van Woesik 2020; Rosedy et al. 2023). Yet, despite their ecological significance, turbid reefs remain comparatively understudied and inadequately managed. Our knowledge of how key reef calcifiers within turbid reef environments respond to turbidity remains rudimentary, requiring comprehensive understanding of the intricate interplay between environmental mechanisms and biomineralization pathways. Investigating such processes is imperative for informed conservation practices, effective management strategies and the preservation of coral reef ecosystems moving forward.

In this thesis, I delved into the biomineralization pathways of giant clam shells (*Tridacna squamosa* and *Hippopus hippopus*) on turbid reefs and the intricate interplay

between external environmental factors and internal biophysiological processes on shell formation. Through a comprehensive multidisciplinary approach integrating advanced high-resolution imaging and geochemical analysis, I explored their shell biomineral growth mechanisms from a holistic viewpoint. My key focus was on modern giant clam shells collected from Darvel Bay, eastern Sabah, Malaysia, spanning a turbidity gradient that encompassed nearshore high turbid reefs to low turbid reefs. Additionally, I undertook comprehensive assessment of fossil giant clam shells retrieved from nearby stratigraphic formations at rocky outcrops in Malaysia and Indonesia, aiming to discern the effects of diagenetic processes on shell structure and uncover implications for proxy interpretation.

7.2 Contribution to knowledge

The four research chapters presented in this thesis successively complement each other. In chapter 3, my research generated time-resolved records of giant clam shell growth using daily, monthly and annual growth rates from shell banding. I highlighted differences in the patterns of growth on daily and seasonal timescales, yet did not find a significant difference in annual growth rate between reefs on a turbidity gradient. I built upon these findings in chapter 5 by incorporating advanced analysis of crystallographic texture with EBSD and investigation of element-to-calcium (El/Ca) ratios using EPMA. Integrated investigation of shell architecture and geochemistry showed that changes to biomineral crystallographic organization concurred with modifications in concentrations of Mg and Sr, which were significantly different between low turbid and high turbid reefs. Chapter 6 used our improved understanding of microstructural and crystallographic shell characteristics gained from previous chapters as a basis to investigate how diagenetic alteration changes physical shell signatures and implications for (paleo)environmental reconstruction. A multi-method screening approach demonstrated that early alteration is highly localized and transformation from pristine to secondary aragonite may be subtle, requiring the detection of fine scale changes to crystallographic organization and crystal size. Chapter 4 is a methods chapter and demonstrated how EBSD data quality can be improved in giant clam shells with post-acquisition refinement techniques. The results of this optimized EBSD method are extensively showcased throughout chapters 4, 5,

6, and in the associated publication Mills et al. (2024), with the further intention of providing a robust guide for future researchers to enable acquisition of high quality EBSD data without excessive clean-up procedures.

Below, the key questions outlined in chapter 2 of this thesis are addressed in relation to the contribution to knowledge. Key findings and conclusions for each question are highlighted.

1. **Are biomineralization pathways of giant clams (structural and geochemical properties of shells) different in clear versus turbid reefs?**

Chapter 3 showed that *T. squamosa* modified its shell growth patterns between high turbid and low turbid coral reefs within Darvel Bay. Detailed analysis of growth chronologies from shells collected alive or dead from the seafloor, undertaken with light- and scanning electron microscopy, revealed that seasonal growth varied between reef environments, primarily accelerating in the wet season in turbid reefs subject to nearby riverine input. Investigation of daily growth using spectral characteristics of chronologies also revealed differences, showing a relationship between tidal range and daily bands in the high turbid reef, but not in the low turbid reef. However, despite the specified differences in growth on shorter time scales, I found that annual growth was not significantly different across a turbidity gradient when scaled to ontogeny. This indicates that *T. squamosa* can grow at similar rates overall regardless of reef environment.

Chapter 5 found variation in the microscale physical and geochemical signatures of shell biominerals between a high turbid and low turbid reef in Darvel Bay. In the high turbid reef, there were distinct differences in microstructure and crystallographic organization of shell biominerals. Daily growth bands with paired daily growth increments related to the day-night cycle and a highly organized crystalline structure were observed. This is compared to a complex-crossed lamellar structure that did not show day-night differences and had lower crystallographic organization in the low turbid reef site. Modifications to shell architecture were coupled with significant differences in El/Ca, with results overall demonstrating lower Mg/Ca and Sr/Ca in the turbid site.

Together, these results support the finding that biomineralization pathways in giant clams are modified between high turbid and low turbid reef environments. Our results indicate sustained shell growth in turbid conditions, but with differences in intra-annual growth patterns, microstructure, crystallographic organization, and geochemical signatures. Although our findings of sustained growth support evidence that these habitats may be suitable conservation hotspots for giant clams because they can grow at similar rates in relation to their low turbid counterparts, the differences found in architecture and geochemistry raise questions related to fitness and structural capabilities of shells. For example, previous evidence investigating coral growth show that rate of linear extension does not make skeletons more robust or healthy (e.g. Edinger et al. 2000). In fact, faster linear growth has negative implications for skeletal density (Highsmith 1979), making corals more vulnerable and susceptible to breakage. However, the differences found for giant clams in this thesis, especially in relation to crystallographic organization, hint at biomechanically superior shells in high turbid reefs compared to low turbid reefs, which could represent compensatory responses for increased resilience to turbidity. Overall, these observations hint that environmental factors play a crucial role in shaping the physical and geochemical characteristics of shells, indicating a link between environment and biomineralization pathways.

2. **What are the physiological and environmental controls on biomineralization pathways in giant clam shells in clear and turbid reefs?**

The research in this thesis highlights that environmental variations modify biomineralization pathways in giant clams between high turbid and low turbid reefs. In chapter 3, it is shown that monthly K_d(490), chlorophyll-*a* concentrations and suspended solids likely play a significant role in the growth rate of giant clams from high turbid reefs, while SST, cloud cover, and rainfall may influence growth dynamics in low turbid reefs. These findings reveal that environmental factors unique to high turbid reefs may be important in driving seasonal growth, indicating changes controlled by run off may be responsible for deviations in growth between high turbid and low turbid reefs during the wet season.

In addition to environmentally driven changes, physiology of the organism is known to play a significant role in the biomineralization pathways of bivalves and thence the architecture and geochemistry of shells (e.g. Schöne et al. 2013). During biomineralization, the organism tightly controls conditions in a chemically complex solution to favour nucleation of $CaCO_3$ (e.g. Gilbert et al. 2022). Consequently, any skeleton-recorded signature will suffer a degree of biological overprint deviating from thermodynamic equilibrium (Urey et al. 1951). In chapter 5, I show that the crystallography and El/Ca of shell biominerals are strongly modified between high turbid and low turbid reefs. I hypothesize that plasticity in biomineralization pathways is driven by physiological changes related to the dynamic trophic flexibility of *T. squamosa*. I ground this hypothesis on previous research that shows *T. squamosa* has strong reliance on heterotrophic feeding and its autotrophic range is extended by heterotrophy, in contrast to other tridacnid species who are functional autotrophs (Tedengren et al. 2000; Jantzen et al. 2008). I suggest that changes to available food source, light and thus symbiont activity between high turbid and low turbid reefs may play a key role on the influence of metabolic processes that lead to changes in concentrations of El/Ca and biomineral design.

3. **How does diagenetic alteration impact the structure of fossil giant clam shells?**

Chapter 6 provides insight into the impact of diagenetic alteration on fossil giant clam shells and the limitations of conventional methods in detecting mineral phase transformations. I utilized a multi-method screening method with techniques including XRD, Raman spectroscopy, LOI, SEM and EBSD to identify transformation of pristine- to secondary aragonite and shell crystallographic texture. Results highlighted that most fossil carbonate remains within the aragonite phase, although there was extensive evidence of textural alteration. Hence, methods solely detecting phase transformation from aragonite to calcite, such as XRD, do not adequately identify alteration in giant clam shells. This study advocates for the routine implementation of EBSD for fossil shells because it can quantitatively map and distinguish biogenic from abiogenic aragonite for each grain. Using EBSD herein, I was able to demonstrate highly heterogenous textural alteration in fossil samples and classify diagenesis on a gradient. Overall, it is imperative to be able to detect alteration from pristine to

secondary aragonite at an appropriate sampling resolution for successive techniques, such as high-resolution geochemical analysis, because early alteration may be highly localized and subtle.

Chapter 4: Methodological Advancements in EBSD

Chapter 4 demonstrates a methodological advancement in enhancing EBSD data quality for analysing crystallographic orientation in giant clam shells. The optimization of data acquisition steps, which can also be achieved by saving EBSD patterns and using post-acquisition refinement, enabled more accurate and detailed investigation into the structural characteristics of shells, contributing to a deeper understanding of biomineralization processes. In chapter 4, I showed an increase in indexing of the aragonite fraction by approximately 8% compared to default selection of parameters. I have addressed the challenges associated with poor data quality in aragonite bivalve shells, allowing less vigorous data clean up that may be unreliable due to extrapolation of data points, leading to oversimplification. The optimized method and enhanced quality of the EBSD maps extends its application to many aragonite skeletons with small grain sizes down to approximately 1 μm, including corals.

7.4 Limitations and future work

7.4.1 Age of specimens

In this thesis, investigation focuses on giant clam specimens that are relatively young in comparison to their natural life span (extending over decades), typically under 7 years old. While our sample size is sufficient for understanding growth patterns and biomineralization pathways in giant clams (e.g. Zhao et al. 2021; Zhao et al. 2023), longer-lived specimens would provide a more comprehensive understanding of growth dynamics over extended periods. Particularly, in relation to confirming patterns observed in intra-annual growth related to seasonality, such as occurrence of peaks in growth rate during the wet season. Yet, it is important to note that research on growth banding and crystallographic texture in giant clams, in addition to bivalves in general,

is still in its infancy. Studies on shorter-lived specimens remain valuable and informative despite these limitations.

7.4.2 Mixotrophy

The hypothesis discussed throughout this thesis regarding the observed differences in growth, microstructure, crystallography, and geochemistry is largely grounded in physiological responses to environmental variability, particularly related to feeding and symbiont activity. However, it's crucial to acknowledge that I did not directly test feeding behaviours in this study and my hypothesis is grounded in previous work. Experimentation of feeding is outside the scope of this research, which instead concentrates on the inorganic portion of shell material. Giant clams have been cultured for decades (e.g. Heslinga et al. 1984), providing baseline information on the effects of light level and feeding on trace element variability (e.g. Warter et al. 2018). However, there is a gap in our knowledge related to how differences in feeding relate to the physical features of shells. In addition, laboratory experiments cannot reproduce the complex multitude of contributing environmental stressors that take place within the natural environment. Hence, the *in situ* study presented in this thesis is valuable to understand natural behaviours, especially in regards to the wealth of environmental information gathered for each study site. Nevertheless, it is important to recognise there may be other contributing factors beyond those considered in my hypothesis that warrant further investigation for a more comprehensive understanding of the observed differences in biomineralization. Moreover, preliminary tests of bulk nitrogen isotope values ($\delta^{15}N$), an approach to measure the balance between trophic levels, were trialed on high- and low turbid shell samples herein at an early stage in this thesis. However, the $\delta^{15}N$ values did not yield significant differences and experimentation was not taken further.

7.4.3 EPMA sample size

In the geochemical analysis carried out in chapter 5, three small areas (100 µm x 100 µm) of two shells were chosen based on season of deposition and/or shell layer. One area of the inner layer was chosen that corresponded to growth in the wet season and another from the same layer in the dry season. In addition, an area of the outer layer

adjacent to the pallial line was investigated. While these data provided ultra-high-resolution insights at a sub-micron scale, which revealed sub-daily variability in elemental ratios, I acknowledge the limitation of interpreting these data as representations of seasonality. Although I hypothesize that differences in El/Ca may be linked to physiological function related to seasonal fluctuations in the environment, it's important to recognize that this EPMA data alone cannot robustly represent an entire season. This necessitates further research on larger shell areas for more complete insight into how elemental incorporation changes on longer timescales.

7.4.4 Biomechanical properties

A focal point of this thesis was the measurement of physical signatures of giant clam shells, including microstructure and crystallographic orientation. While the size, shape, and orientation of biominerals can significantly influence biomechanical properties such as hardness and elastic stiffness (e.g. Meng et al. 2018a, b), I did not directly measure these properties herein. In future research, direct measurements of the mechanical behaviour of giant clam shells, such as microhardness testing and nanoindentation, should complement crystallographic studies. These measurements will be essential for establishing a direct link between shell protective responses and resilience in relation to different environmental conditions, validating the hypothesis discussed in this thesis.

7.4.5 Geochemical alterations in diagenesis

While this thesis has demonstrated the value of a multimethod approach for assessing diagenetic alteration using the physical features of giant clam shells, further investigation is warranted to understand how observed structural changes relate to shell geochemistry. Future work should target shells with the presence of altered aragonite to access the fidelity of the material for geochemical studies. Recent studies on the shells of other bivalve species such as *Arctica islandica* (Pederson et al. 2020) have indicated a lead and lag pattern of structural and geochemical alteration respectively, warranting similar investigations in giant clams. This approach would

elucidate to what degree the textural alteration documented herein has the potential to affect geochemical proxy data.

7.4 Concluding remarks

As the degradation of tropical coral reefs continue, we must better understand the capabilities of potential reef refugia. Although nearshore turbid coral reefs are extremely widespread and have already been demonstrated to protect reef building corals from widespread disturbance, we understand very little about the dynamics of these environments and organismal responses to turbidity among different taxa. Before the research in this thesis, responses of key reef calcifiers aside from corals to environmental parameters on turbid reefs were not known or understood, restricting understanding of the validity of turbid reefs as refuges.

Owing to their close proximity to the coastline and human settlements, turbid reefs are known to be highly susceptible to local stressors and are hypothesised to lose resilience in the coming years if conservation action is not taken. It is therefore crucial their potential is asserted, allowing for the implementation of appropriate maintenance. This work provides a starting point for integrated management strategies and provides scientists with an understanding of resilience in giant clams and how turbidity impacts their calcification. For the first time, our findings have elucidated the substantial influence turbid reefs have on biomineralization pathways, unveiling distinct growth patterns, crystallographic features, and El/Ca ratios of biominerals. These observed differences hold significant implications for material properties and defence responses, suggesting that giant clam shells from high turbid reefs may possess biomechanical advantages over those from low turbid environments. This work underscores the critical role of turbid reefs as conservation hotspots, potentially offering refuge to giant clams amidst widespread disturbances induced by anthropogenic activities. If appropriate strategies are developed and enforced for the conservation of turbid reefs, reef builders may endure future events, such as bleaching, in these potential refugia. Overall, the findings herein suggest that habitats with elevated turbidity levels serve as important conservation hotspots for diverse reef building taxa, emphasizing the significance of understanding how organisms respond to environmental gradients for

effective conservation strategies. Such insights are crucial for the conservation of reef calcifying organisms amid anthropogenic change.

8. References

Addadi, L., & Weiner, S. (1992). Control and design principles in biological mineralization. *Angewandte Chemie International Edition in English*, ***31***(2), 153–169. https://doi.org/10.1002/anie.199201531

Agbaje, O. B. A., Thomas, D. E., Dominguez, J. G., Mclnerney, B. V., Kosnik, M. A., & Jacob, D. E. (2019). Biomacromolecules in bivalve shells with crossed lamellar architecture. *Journal of Materials Science*, ***54***(6), 4952–4969. https://doi.org/10.1007/s10853-018-3165-8

Agbaje, O. B. A., Wirth, R., Morales, L. F. G., Shirai, K., Kosnik, M., Watanabe, T., & Jacob, D. E. (2017). Architecture of crossed-lamellar bivalve shells: The southern giant clam (*Tridacna derasa*, Röding, 1798). *Royal Society Open Science*, ***4***(9), 170622. https://doi.org/10.1098/rsos.170622

Allemand, D., Tambutté, É., Zoccola, D., & Tambutté, S. (2011). Coral Calcification, Cells to Reefs. In Z. Dubinsky & N. Stambler (Eds.), *Coral Reefs: An Ecosystem in Transition* (pp. 119–150). Springer Netherlands. https://doi.org/10.1007/978-94-0070114-4_9

Almagro, I., Drzymała, P., Berent, K., Sainz-Díaz, C. I., Willinger, M. G., Bonarski, J., & Checa, A. G. (2016). New Crystallographic Relationships in Biogenic Aragonite: The Crossed-Lamellar Microstructures of Mollusks. *Crystal Growth & Design*, ***16***(4), 2083–2093. https://doi.org/10.1021/acs.cgd.5b01775

Anthony, K. R. N. (2000). Enhanced particle-feeding capacity of corals on turbid reefs (Great Barrier Reef, Australia). *Coral Reefs*, ***19***(1), 59–67. https://doi.org/10.1007/s003380050227

Anthony, K. R. N., Connolly, S. R., & Hoegh-Guldberg, O. (2007). Bleaching, energetics, and coral mortality risk: Effects of temperature, light, and sediment regime.

Limnology and Oceanography, ***52***(2), 716–726. https://doi.org/10.4319/lo.2007.52.2.0716

Apte, D., Narayana, S., & Dutta, S. (2019). Impact of sea surface temperature anomalies on giant clam population dynamics in Lakshadweep reefs: Inferences from a fourteen years study. *Ecological Indicators*, ***107***(1), 105604. https://doi.org/10.1016/j.ecolind.2019.105604

Arias-Ruiz, C., Elliot, M., Bézos, A., Pedoja, K., Husson, L., Cahyarini, S. Y., Cariou, E., Michel, E., La, C., & Manssouri, F. (2017). Geochemical fingerprints of climate variation and the extreme La Niña 2010–11 as recorded in a *Tridacna squamosa* shell from Sulawesi, Indonesia. *Palaeogeography, Palaeoclimatology, Palaeoecology*, ***487***(1), 216–228. https://doi.org/10.1016/j.palaeo.2017.08.037

Armstrong, E. J., Watson, S.-A., Stillman, J. H., & Calosi, P. (2022). Elevated temperature and carbon dioxide levels alter growth rates and shell composition in the fluted giant clam, *Tridacna squamosa*. *Scientific Reports*, ***12***(1), 1034. https://doi.org/10.1038/s41598-022-14503-4

Arndt, I., Coenen, D., Evans, D., Renema, W., & Müller, W. (2023). Quantifying SubSeasonal Growth Rate Changes in Fossil Giant Clams Using Wavelet Transformation of Daily Mg/Ca Cycles. *Geochemistry, Geophysics, Geosystems*, ***24***(10), e2023GC010992. https://doi.org/10.1029/2023GC010992

Asami, R., Konishi, M., Tanaka, K., Uemura, R., Furukawa, M., & Shinjo, R. (2015). Late Holocene coral reef environment recorded in Tridacnidae shells from archaeological sites in Okinawa-jima, subtropical southwestern Japan: Giant clams records from Okinawa-jima. *Island Arc*, ***24***(1), 61–72. https://doi.org/10.1111/iar.12076

Asis, J., Isnain, Z., Pungut, H., Tahir, S., Musta, B., & Saleh, H. (2017). GEOTOURISM POTENTIAL AT SILAM COAST CONSERVATION AREA (SCCA) SILAM, SABAH. *Borneo Science*, ***38***(1), 47–62. https://doi.org/10.51200/bsj.v38i1.4410

Aubert, A., Lazareth, C. E., Cabioch, G., Boucher, H., Yamada, T., Iryu, Y., & Farman, R. (2009). The tropical giant clam *Hippopus hippopus* shell, a new archive of environmental conditions as revealed by sclerochronological and $\delta^{18}O$ profiles. *Coral Reefs*, ***28***(4), 989–998. https://doi.org/10.1007/s00338-009-0538-0

Ayling, B. F., Chappell, J., Gagan, M. K., & McCulloch, M. T. (2015). ENSO variability during MIS 11 (424–374 ka) from *Tridacna gigas* at Huon Peninsula, Papua New Guinea. *Earth and Planetary Science Letters*, ***431***(1), 236–246. https://doi.org/10.1016/j.epsl.2015.09.037

Aztec EBSD User Guide. *Acquisition*. Oxford Instruments.

Bainbridge, Z., Lewis, S., Bartley, R., Fabricius, K., Collier, C., Waterhouse, J., Garzon-Garcia, A., Robson, B., Burton, J., Wenger, A., & Brodie, J. (2018). Fine sediment and particulate organic matter: A review and case study on ridge-to-reef transport, transformations, fates, and impacts on marine ecosystems. *Marine Pollution Bulletin*, ***135***, 1205–1220. https://doi.org/10.1016/j.marpolbul.2018.08.002

Ban, S. S., Graham, N. A. J., & Connolly, S. R. (2014). Evidence for multiple stressor interactions and effects on coral reefs. *Global Change Biology*, ***20***(3), 681–697. https://doi.org/10.1111/gcb.12453

Batenburg, S. J., Reichart, G. J., Jilbert, T., Janse, M., Wesselingh, F. P., & Renema, W. (2011). Interannual climate variability in the Miocene: High resolution trace element and stable isotope ratios in giant clams. *Palaeogeography, Palaeoclimatology, Palaeoecology*, ***306***(1–2), 75–81. https://doi.org/10.1016/j.palaeo.2011.03.031

Bayne, B. L. (2017). Evolution. In *Developments in Aquaculture and Fisheries Science* (Vol. 41, pp. 47–87). Elsevier. https://doi.org/10.1016/B978-0-12-803472-9.00002-9

Belda, C. A., Cuff, C., & Yellowlees, D. (1993a). Modification of shell formation in the giant clam *Tridacna gigas* at elevated nutrient levels in sea water. *Marine Biology*, ***117***(2), 251–257. https://doi.org/10.1007/BF00345670

Belda, C. A., Lucas, J. S., & Yellowlees, D. (1993b). Nutrient limitation in the giant clam-zooxanthellae symbiosis: Effects of nutrient supplements on growth of the symbiotic partners. *Marine Biology*, ***117***(4), 655–664. https://doi.org/10.1007/BF00349778

Belda-Baillie, C. A., Leggat, W., & Yellowlees, D. (1998). Growth and metabolic responses of the giant clam-zooxanthellae symbiosis in a reef-fertilisation experiment. *Marine Ecology Progress Series*, ***170***(1), 131–141. https://doi.org/10.3354/meps170131

Beniash, E., Ivanina, A., Lieb, N. S., Kurochkin, I., & Sokolova, I. M. (2010). Elevated level of carbon dioxide affects metabolism and shell formation in oysters *Crassostrea virginica*. *Marine Ecology Progress Series*, ***419***(1), 95–108. https://doi.org/10.3354/meps08841

Bieler, R., & Mikkelsen, P. M. (2006). Bivalvia—A look at the Branches. *Zoological Journal of the Linnean Society*, ***148***(3), 223–235. https://doi.org/10.1111/j.10963642.2006.00255.x

Bianconi, G.G. (1856). [Specimina zoologica Mosambicana]. Rendiconto dell'adunanza del 24 Gennaio 1856. *Rendiconto delle Sessioni dell'Accademia delle Scienze dell'Istituto di Bologna anno Accademico*, ***1855–56***(1), 41–48.

bin Othman, A. S., Goh, G. H., & Todd, P. A. (2010). The distribution and status of giant clams (family Tridacnidae)-a short review. *Raffles Bull Zool*, ***58***(1), 103-111.

Bjørlykke, K. (1998). Clay mineral diagenesis in sedimentary basins—A key to the prediction of rock properties. Examples from the North Sea Basin. *Clay Minerals*, ***33***(1), 15–34.

Bongaerts, P., Ridgway, T., Sampayo, E. M., & Hoegh-Guldberg, O. (2010). Assessing the 'deep reef refugia' hypothesis: Focus on Caribbean reefs. *Coral Reefs*, ***29***(2), 309–327. https://doi.org/10.1007/s00338-009-0581-x

Bonham, K. (1965). Growth Rate of Giant Clam *Tridacna gigas* at Bikini Atoll as Revealed by Radioautography. *Science*, ***149***(3681), 300–302. https://doi.org/10.1126/science.149.3681.300

Borsa, P., Fauvelot, C., Tiavouane, J., Grulois, D., Wabnitz, C., Abdon Naguit, M. R., & Andréfouët, S. (2015). Distribution of Noah's giant clam, *Tridacna noae*. *Marine Biodiversity*, ***45***(2), 339–344. https://doi.org/10.1007/s12526-014-0265-9

Bragg, W. L. (1924). The structure of aragonite. *Proceedings of the Royal Society of London. Series A, Containing Papers of a Mathematical and Physical Character*, ***105***(729), 16–39. https://doi.org/10.1098/rspa.1924.0002

Brahmi, C., Chapron, L., Le Moullac, G., Soyez, C., Beliaeff, B., Lazareth, C. E., Gaertner-Mazouni, N., & Vidal-Dupiol, J. (2019). Effects of temperature and pCO_2 on the respiration, biomineralization and photophysiology of the giant clam *Tridacna maxima*. *Conservation Physiology*, ***9***(1), coab041. https://doi.org/10.1101/672907

Brand, U. (1989). Aragonite-calcite transformation based on Pennsylvanian molluscs. *GSA Bulletin*, ***101***(3), 377–390. https://doi.org/10.1130/00167606(1989)101<0377:ACTBOP>2.3.CO;2

Brewer, L. N., & Michael, J. R. (2010). Risks of "Cleaning" Electron Backscatter Diffraction Data. *Microscopy Today*, ***18***(2), 10–15. https://doi.org/10.1017/S1551929510000040

Brosset, C., Höche, N., Shirai, K., Nishida, K., Mertz-Kraus, R., & Schöne, B. R. (2022). Strong Coupling between Biomineral Morphology and Sr/Ca of *Arctica islandica* (Bivalvia)—Implications for Shell Sr/Ca-Based Temperature Estimates. *Minerals*, ***12***(5), 500. https://doi.org/10.3390/min12050500

Browne, N., Braoun, C., McIlwain, J., Nagarajan, R., & Zinke, J. (2019). Borneo coral reefs subject to high sediment loads show evidence of resilience to various environmental stressors. *PeerJ*, ***7***(1), e7382. https://doi.org/10.7717/peerj.7382

Bruguière J.G. (1791-1797). *Tableau encyclopédique et méthodique des trois règnes de la nature. Vers, coquilles, mollusques et polypiers*. Part 7 [Livraison 46, 30 July 1791]: Tome 1, pp. [i]-viii, 1-83, pl. 1-95, Paris: Panckoucke. Part 10 [Livraison 49, May 1792]: Tome 1, pp. 85-132; Tome 2, pl. 96-189, Paris: Panckoucke. Part 19 [Livraison 62, 8 July 1797], pl. 190-286, Paris: H. Agasse. [dates and publishers after Evenhuis & Petit 2003].

Burke, L., Reytar, K., Spalding, M., & Perry, A. (2011). Reefs at Risk Revisited. *World Resources Institute*. https://www.wri.org/research/reefs-risk-revisited

Butler, P. G., Scourse, J. D., Richardson, C. A., Jr, A. D. W., Bryant, C. L., & Bennell, J. D. (2009). Continuous marine radiocarbon reservoir calibration and the 13C Suess effect in the Irish Sea: Results from the first multi-centennial shell-based marine master chronology. *Earth and Planetary Science Letters*, ***279***(3–4), 230–241. https://doi.org/10.1016/j.epsl.2008.12.043

Butler, P. G., Wanamaker, A. D., Scourse, J. D., Richardson, C. A., & Reynolds, D. J. (2013). Variability of marine climate on the North Icelandic Shelf in a 1357-year proxy archive based on growth increments in the bivalve *Arctica islandica*. *Palaeogeography, Palaeoclimatology, Palaeoecology*, ***373***, 141–151. https://doi.org/10.1016/j.palaeo.2012.01.016

Cabaitan, P. C., & Conaco, C. (2017). Bringing back the giants: Juvenile *Tridacna gigas* from natural spawning of restocked giant clams. *Coral Reefs*, ***36***(2), 519–519. https://doi.org/10.1007/s00338-017-1558-9

Cabaitan, P. C., Gomez, E. D., & Aliño, P. M. (2008). Effects of coral transplantation and giant clam restocking on the structure of fish communities on degraded patch reefs. *Journal of Experimental Marine Biology and Ecology*, ***357***(1), 85–98. https://doi.org/10.1016/j.jembe.2008.01.001

Cacciapaglia, C., & van Woesik, R. (2016). Climate-change refugia: Shading reef corals by turbidity. *Global Change Biology*, ***22***(3), 1145–1154. https://doi.org/10.1111/gcb.13166

Canadell, J. G., Monteiro, P. M., Costa, M. H., Da Cunha, L. C., Cox, P. M., Eliseev, A. V., ... & Lebehot, A. D. (2021). Global carbon and other biogeochemical cycles and feedbacks. In *Climate Change 2021: The Physical Science Basis. Contribution of Working Group I to the Sixth Assessment Report of the Intergovernmental Panel on Climate Change*, ed. V Masson-Delmotte, P Zhai, A Pirani, SL Connors, C Péan, et al., pp. 673–816. Cambridge, UK: Cambridge Univ. Press.

Carilli, J. E., Norris, R. D., Black, B. A., Walsh, S. M., & McField, M. (2009). Local Stressors Reduce Coral Resilience to Bleaching. *PLOS ONE*, ***4***(7), e6324. https://doi.org/10.1371/journal.pone.0006324

Carlos, A. A., Baillie, B. K., & Maruyama, T. (2000). Diversity of dinoflagellate symbionts (zooxanthellae) in a host individual. *Marine Ecology Progress Series*, ***195***(1), 93–100. https://doi.org/0.3354/meps195093

Casella, L. A., Griesshaber, E., Simonet Roda, M., Ziegler, A., Mavromatis, V., Henkel, D., Laudien, J., Häussermann, V., Neuser, R. D., Angiolini, L., Dietzel, M., Eisenhauer, A., Immenhauser, A., Brand, U., & Schmahl, W. W. (2018a). Micro- and nanostructures reflect the degree of diagenetic alteration in modern and fossil brachiopod shell calcite: A multi-analytical screening approach (CL, FE-SEM, AFM, EBSD). *Palaeogeography, Palaeoclimatology, Palaeoecology*, ***502***, 13–30. https://doi.org/10.1016/j.palaeo.2018.03.011

Casella, L. A., Griesshaber, E., Yin, X., Ziegler, A., Mavromatis, V., Müller, D., Ritter, A.-C., Hippler, D., Harper, E. M., Dietzel, M., Immenhauser, A., Schöne, B. R., Angiolini, L., & Schmahl, W. W. (2017). Experimental diagenesis: Insights into aragonite to calcite transformation of *Arctica islandica* shells by hydrothermal treatment. *Biogeosciences*, ***14***(6), 1461–1492. https://doi.org/10.5194/bg-14-14612017

Casella, L. A., He, S., Griesshaber, E., Fernández-Díaz, L., Greiner, M., Harper, E. M., Jackson, D. J., Ziegler, A., Mavromatis, V., Dietzel, M., Eisenhauer, A.,

Veintemillas-Verdaguer, S., Brand, U., & Schmahl, W. W. (2018b). Hydrothermal alteration of aragonitic biocarbonates: Assessment of micro- and nanostructural dissolution–reprecipitation and constraints of diagenetic overprint from quantitative statistical grain-area analysis. *Biogeosciences*, ***15***(24), 7451–7484. https://doi.org/10.5194/bg-15-7451-2018

Chambers, C. N. (2007). Pasua (*Tridacna maxima*) size and abundance in Tongareva Lagoon, Cook Islands. *SPC Trochus Information Bulletin*, ***13***(1), 7–12.

Chang, C. P., Liu, C. H., & Kuo, H. C. (2003). Typhoon Vamei: An equatorial tropical cyclone formation. *Geophysical Research Letters*, ***30***(3), 1150. https://doi.org/10.1029/2002GL016365

Checa, A. G. (2018). Physical and Biological Determinants of the Fabrication of Molluscan Shell Microstructures. *Frontiers in Marine Science*, ***5***(1), 353. https://doi.org/10.3389/fmars.2018.00353

Checa, A. G., Okamoto, T., & Ramírez, J. (2006). Organization pattern of nacre in Pteriidae (Bivalvia: Mollusca) explained by crystal competition. *Proceedings of the Royal Society B: Biological Sciences*, ***273***(1592), 1329–1337. https://doi.org/10.1098/rspb.2005.3460

Checa, A. G., & Rodrıgueź -Navarro, A. B. (2005). Self-organisation of nacre in the shells of Pterioida (Bivalvia: Mollusca). *Biomaterials*, ***26***(9), 1071–1079. https://doi.org/10.1016/j.biomaterials.2004.04.007

Checa, A. G., Yáñez-Ávila, M. E., González-Segura, A., Varela-Feria, F., Griesshaber, E., & Schmahl, W. W. (2019). Bending and branching of calcite laths in the foliated microstructure of pectinoidean bivalves occurs at coherent crystal lattice orientation. *Journal of Structural Biology*, ***205***(3), 7–17. https://doi.org/10.1016/j.jsb.2018.12.003

Chen, Z., Muller-Karger, F. E., & Hu, C. (2007). Remote sensing of water clarity in

Tampa Bay. *Remote Sensing of Environment*, ***109***(2), 249–259. https://doi.org/10.1016/j.rse.2007.01.002

Cinner, J. E., Huchery, C., MacNeil, M. A., Graham, N. A. J., McClanahan, T. R., Maina, J., Maire, E., Kittinger, J. N., Hicks, C. C., Mora, C., Allison, E. H., D'Agata, S., Hoey, A., Feary, D. A., Crowder, L., Williams, I. D., Kulbicki, M., Vigliola, L., Wantiez, L., … Mouillot, D. (2016). Bright spots among the world's coral reefs. *Nature*, ***535***(7612), 416–419. https://doi.org/10.1038/nature18607

Clark, M. S., Peck, L. S., Arivalagan, J., Backeljau, T., Berland, S., Cardoso, J. C. R., Caurcel, C., Chapelle, G., De Noia, M., Dupont, S., Gharbi, K., Hoffman, J. I., Last, K. S., Marie, A., Melzner, F., Michalek, K., Morris, J., Power, D. M., Ramesh, K., … Harper, E. M. (2020). Deciphering mollusc shell production: The roles of genetic mechanisms through to ecology, aquaculture and biomimetics. *Biological Reviews*, ***95***(6), 1812–1837. https://doi.org/10.1111/brv.12640

Collins, M., An, S.-I., Cai, W., Ganachaud, A., Guilyardi, E., Jin, F.-F., Jochum, M., Lengaigne, M., Power, S., Timmermann, A., Vecchi, G., & Wittenberg, A. (2010). The impact of global warming on the tropical Pacific Ocean and El Niño. *Nature Geoscience*, ***3***(6), 391–397. https://doi.org/10.1038/ngeo868

Coronado, I., Fine, M., Bosellini, F. R., & Stolarski, J. (2019). Impact of ocean acidification on crystallographic vital effect of the coral skeleton. *Nature Communications*, ***10***(1), 2896. https://doi.org/10.1038/s41467-019-10833-6

Crippa, G., Griesshaber, E., Checa, A. G., Harper, E. M., Roda, M. S., & Schmahl, W. W. (2020). Orientation patterns of aragonitic crossed-lamellar, fibrous prismatic and myostracal microstructures of modern *Glycymeris* shells. *Journal of Structural Biology,* ***212***(3), 107653. https://doi.org/10.1016/j.jsb.2020.107653

Cusack, M., England, J., Dalbeck, P., Tudhope, A. W., Fallick, A. E., & Allison, N. (2008). Electron backscatter diffraction (EBSD) as a tool for detection of coral diagenesis. *Coral Reefs*, ***27***(4), 905–911. https://doi.org/10.1007/s00338-008-0414-3

Currey, J. D. (1977). Mechanical Properties of Mother of Pearl in Tension. *Proceedings of the Royal Society of London. Series B*, ***196***, 443–463. https://cir.nii.ac.jp/crid/1571135650187160576

Dalbeck, P., & Cusack, M. (2006). Crystallography (electron backscatter diffraction) and chemistry (electron probe microanalysis) of the avian eggshell. *Crystal Growth & Design*, ***6***(11), 2558-2562. https://doi.org/10.1021/cg068008t

Dallmeyer, D. G., Porter, J. W., & Smith, G. J. (1982). Effects of particulate peat on the behavior and physiology of the Jamaican reef-building coral *Montastrea annularis*. *Marine Biology*, ***68***(3), 229–233. https://doi.org/10.1007/BF00409589

de Boer, R. B. (1977). Stability of Mg-Ca carbonates. *Geochimica et Cosmochimica Acta*, ***41***(2), 265–270. https://doi.org/10.1016/0016-7037(77)90234-4

de Winter, N. J., Killam, D., Fröhlich, L., de Nooijer, L., Boer, W., Schöne, B. R., Thébault, J., & Reichart, G. J. (2023). Ultradian rhythms in shell composition of photosymbiotic and non-photosymbiotic mollusks. *Biogeosciences*, ***20***(14), 3027–3052. https://doi.org/10.5194/bg-20-3027-2023

De'ath, G., Fabricius, K. E., Sweatman, H., & Puotinen, M. (2012). The 27–year decline of coral cover on the Great Barrier Reef and its causes. *Proceedings of the National Academy of Sciences*, ***109***(44), 17995–17999. https://doi.org/10.1073/pnas.1208909109

DeCarlo, T. M. (2018). Characterizing coral skeleton mineralogy with Raman spectroscopy. *Nature Communications*, ***9***(1), 5325. https://doi.org/10.1038/s41467018-07601-3

Department of Statistics Malaysia. (2022). Ministry of Economy and Department of Statistics Malaysia Official Portal. Retrieved 15 February 2024, from https://www.dosm.gov.my/

Ditlev, H., De Silva, M. W. R. N., Ridzwan, A. R., Toerring, D., & Widt, S. (1999). Hard corals of Darvel Bay. *Ekspedisi Galaxea*, ***98***(1), 51–71.

Ditlev, H. (2003). New scleractinian corals (Cnidaria: Anthozoa) from Sabah, North Borneo. Description of one new genus and eight new species, with notes on their taxonomy and ecology. *Zoologische Mededelingen,* ***77***(1), 193–219.

Doebelin, N., & Kleeberg, R. (2015). Profex: A graphical user interface for the Rietveld refinement program BGMN. *Journal of Applied Crystallography*, ***48***(5), 1573–1580. https://doi.org/10.1107/S1600576715014685

Dong, W., Huang, J., Liu, C., Wang, H., Zhang, G., Xie, L., & Zhang, R. (2022). Characterization of the Myostracum Layers in Molluscs Reveals a Conservative Shell Structure. *Frontiers in Marine Science*, ***9***(1), 862929. https://doi.org/10.3389/fmars.2022.862929

Douglas, A. E. (2003). Coral bleaching—How and why? *Marine Pollution Bulletin*, ***46***(4), 385–392. https://doi.org/10.1016/S0025-326X(03)00037-7

Draper, N. R., & Smith, H. (1966). *Applied regression analysis* (Vol. 326). John Wiley & Sons.

Driscoll, R., Elliot, M., Russon, T., Welsh, K., Yokoyama, Y., & Tudhope, A. (2014). ENSO reconstructions over the past 60 ka using giant clams (*Tridacna* sp.) from Papua New Guinea: PALEOENSO RECONSTRUCTIONS IN GIANT CLAMS. *Geophysical Research Letters*, ***41***(19), 6819–6825. https://doi.org/10.1002/2014GL061446

Duckworth, A., Giofre, N., & Jones, R. (2017). Coral morphology and sedimentation. *Marine Pollution Bulletin*, ***125***(1), 289–300. https://doi.org/10.1016/j.marpolbul.2017.08.036

Duprey, N., Lazareth, C. E., Dupouy, C., Butscher, J., Farman, R., Maes, C., & Cabioch, G. (2015). Calibration of seawater temperature and $\delta^{18}O$ seawater signals in *Tridacna maxima*'s $\delta^{18}O$ shell record based on in situ data. *Coral Reefs*, ***34***(2), 437–450. https://doi.org/10.1007/s00338-014-1245-z

Edinger, E. N., Limmon, G. V., Jompa, J., Widjatmoko, W., Heikoop, J. M., & Risk, M. J. (2000). Normal Coral Growth Rates on Dying Reefs: Are Coral Growth Rates Good Indicators of Reef Health? *Marine Pollution Bulletin*, ***40***(5), 404–425. https://doi.org/10.1016/S0025-326X(99)00237-4

Elfwing, T., Plantman, P., Tedengren, M., & Wijnbladh, E. (2001). Responses to temperature, heavy metal and sediment stress by the giant clam *Tridacna squamosa*. *Marine and Freshwater Behaviour and Physiology*, ***34***(4), 239–248. https://doi.org/10.1080/10236240109379077

Elliot, M., Welsh, K., Chilcott, C., McCulloch, M., Chappell, J., & Ayling, B. (2009). Profiles of trace elements and stable isotopes derived from giant long-lived *Tridacna gigas* bivalves: Potential applications in paleoclimate studies. *Palaeogeography, Palaeoclimatology, Palaeoecology*, ***280***(1), 132–142. https://doi.org/10.1016/j.palaeo.2009.06.007

Evans, J. W. (1972). Tidal growth increments in the cockle *Clinocardium nuttalli*. *Science*, ***176***(4033), 416–417. https://doi.org/10.1126/science.176.4033.416

Farfan, G. A., Apprill, A., Cohen, A., DeCarlo, T. M., Post, J. E., Waller, R. G., & Hansel, C. M. (2022). Crystallographic and chemical signatures in coral skeletal aragonite. *Coral Reefs, **41***(1)*, 19–34.* https://link.springer.com/article/10.1007/s00338-021-02198-4

Faylona, M. G. P. G., Lazareth, C. E., Sémah, A.-M., Caquineau, S., Boucher, H., & Ronquillo, W. P. (2011). Preliminary study on the preservation of giant clam (Tridacnidae) shells from the Balobok Rockshelter archaeological site, south Philippines. *Geoarchaeology*, ***26***(6), 888–901. https://doi.org/10.1002/gea.20377

Feely, R. A., Doney, S. C., & Cooley, S. R. (2009). Ocean Acidification: Present Conditions and Future Changes in a High-CO_2 World. *Oceanography*, ***22***(4), 36–47. https://www.jstor.org/stable/24861022

Field, R. D., Van Der Werf, G. R., Fanin, T., Fetzer, E. J., Fuller, R., Jethva, H., ... & Worden, H. M. (2016). Indonesian fire activity and smoke pollution in 2015 show persistent nonlinear sensitivity to El Niño-induced drought. *Proceedings of the National Academy of Sciences*, ***113***(33), 9204–9209. https://doi.org/10.1073/pnas.1524888113

Finch, A. A., & Allison, N. (2007). Coordination of Sr and Mg in calcite and aragonite. *Mineralogical Magazine*, ***71***(5), 539–552. https://doi.org/10.1180/minmag.2007.071.5.539

Fisher, C. R., Fitt, W. K., & Trench, R. K. (1985). PHOTOSYNTHESIS AND RESPIRATION IN *TRIDACNA GIGAS* AS A FUNCTION OF IRRADIANCE AND SIZE. *The Biological Bulletin*, ***169***(1), 230–245. https://doi.org/10.2307/1541400

Fitzer, S. C., Chung, P., Maccherozzi, F., Dhesi, S. S., Kamenos, N. A., Phoenix, V. R., & Cusack, M. (2016). Biomineral shell formation under ocean acidification: A shift from order to chaos. *Scientific Reports*, ***6***(1), 21076. https://doi.org/10.1038/srep21076

Fitzer, S. C., Cusack, M., Phoenix, V. R., & Kamenos, N. A. (2014). Ocean acidification reduces the crystallographic control in juvenile mussel shells. *Journal of Structural Biology*, ***188***(1), 39–45. https://doi.org/10.1016/j.jsb.2014.08.007

Forjanes, P., Simonet Roda, M., Greiner, M., Griesshaber, E., Lagos, N. A., Veintemillas-Verdaguer, S., Astilleros, J. M., Fernández-Díaz, L., & Schmahl, W. W. (2022). Experimental burial diagenesis of aragonitic biocarbonates: From organic matter loss to abiogenic calcite formation. *Biogeosciences*, ***19***(16), 3791–3823. https://doi.org/10.5194/bg-19-3791-2022

Fox, M. D., Williams, G. J., Johnson, M. D., Radice, V. Z., Zgliczynski, B. J., Kelly, E. L. A., Rohwer, F. L., Sandin, S. A., & Smith, J. E. (2018). Gradients in Primary Production Predict Trophic Strategies of Mixotrophic Corals across Spatial Scales. *Current Biology*, ***28***(21), 3355-3363.e4. https://doi.org/10.1016/j.cub.2018.08.057

Fox-Kemper, B., H.T. Hewitt, C. Xiao, G. Aðalgeirsdóttir, S.S. Drijfhout, T.L. Edwards, N.R. Golledge, M. Hemer, R.E. Kopp, G. Krinner, A. Mix, D. Notz, S. Nowicki, I.S. Nurhati, L. Ruiz, J.-B. Sallée, A.B.A. Slangen, & Y. Yu. (2021): Ocean, Cryosphere and Sea Level Change. In Climate Change 2021: The Physical Science Basis. Contribution of Working Group I to the Sixth Assessment Report of the Intergovernmental Panel on Climate Change [Masson-Delmotte, V., P. Zhai, A. Pirani, S.L. Connors, C. Péan, S. Berger, N. Caud, Y. Chen, L. Goldfarb, M.I. Gomis, M. Huang, K. Leitzell, E. Lonnoy, J.B.R. Matthews, T.K. Maycock, T. Waterfield, O. Yelekçi, R. Yu, and B. Zhou (eds.)]. Cambridge University Press, Cambridge, United Kingdom and New York, NY, USA. https://doi.org/10.1017/9781009157896

Frýda, J., Klicnarová, M., Frýdová, B., & Mergl, M. (2010). Variability in the crystallographic texture of bivalve nacre. *Bulletin of Geosciences*, ***85***(1), 645–662. https://doi.org/10.3140/bull.geosci.1217

Füllenbach, C. S., Schöne, B. R., Shirai, K., Takahata, N., Ishida, A., & Sano, Y. (2017). Minute co-variations of Sr/Ca ratios and microstructures in the aragonitic shell of *Cerastoderma edule* (Bivalvia) – Are geochemical variations at the ultra-scale masking potential environmental signals? *Geochimica et Cosmochimica Acta*, ***205***(1), 256–271. https://doi.org/10.1016/j.gca.2017.02.019

Gaetani, G. A., & Cohen, A. L. (2006). Element partitioning during precipitation of aragonite from seawater: A framework for understanding paleoproxies. *Geochimica et Cosmochimica Acta*, ***70***(18), 4617–4634. https://doi.org/10.1016/j.gca.2006.07.008

Gaffey, S. J., Kolak, J. J., & E. Bronnimann, C. (1991). Effects of drying, heating, annealing, and roasting on carbonate skeletal material, with geochemical and diagenetic implications. *Geochimica et Cosmochimica Acta*, ***55***(6), 1627–1640.

https://doi.org/10.1016/0016-7037(91)90134-Q

Gannon, M. E., Pérez-Huerta, A., Aharon, P., & Street, S. C. (2017). A biomineralization study of the Indo-Pacific giant clam *Tridacna gigas*. *Coral Reefs*, ***36***(2), 503–517. https://doi.org/10.1007/s00338-016-1538-5

Gaveau, D. L. A., Sheil, D., Husnayaen, Salim, M. A., Arjasakusuma, S., Ancrenaz, M., Pacheco, P., & Meijaard, E. (2016). Rapid conversions and avoided deforestation: Examining four decades of industrial plantation expansion in Borneo. *Scientific Reports*, ***6***(1), 32017. https://doi.org/10.1038/srep32017

Gaveau, D. L. A., Sloan, S., Molidena, E., Yaen, H., Sheil, D., Abram, N. K., Ancrenaz, M., Nasi, R., Quinones, M., Wielaard, N., & Meijaard, E. (2014). Four Decades of Forest Persistence, Clearance and Logging on Borneo. *PLoS ONE*, ***9***(7), e101654. https://doi.org/10.1371/journal.pone.0101654

Gilbert, P., Bergmann, K. D., Boekelheide, N., Tambutté, S., Mass, T., Marin, F., Adkins, J. F., Erez, J., Gilbert, B., Knutson, V., Cantine, M., Hernández, J. O., & Knoll, A. H. (2022). Biomineralization: Integrating mechanism and evolutionary history. *Science Advances*, ***8***(10), eabl9653. https://doi.org/10.1126/sciadv.abl9653

Gilbert, P., Porter, S. M., Sun, C.-Y., Xiao, S., Gibson, B. M., Shenkar, N., & Knoll, A. H. (2019). Biomineralization by particle attachment in early animals. *Proceedings of the National Academy of Sciences*, ***116***(36), 17659–17665. https://doi.org/10.1073/pnas.1902273116

Gilmour, J. P., Smith, L. D., Heyward, A. J., Baird, A. H., & Pratchett, M. S. (2013). Recovery of an Isolated Coral Reef System Following Severe Disturbance. *Science*, ***340***(6128), 69–71. https://doi.org/10.1126/science.1232310

Gomez, E. D., & Mingoa-Licuanan, S. S. (2006). Achievements and lessons learned in restocking giant clams in the Philippines. *Fisheries Research*, ***80***(1), 46–52. https://doi.org/10.1016/j.fishres.2006.03.017

Goodwin, D. H., Flessa, K. W., Schone, B. R., & Dettman, D. L. (2001). CrossCalibration of Daily Growth Increments, Stable Isotope Variation, and Temperature in the Gulf of California Bivalve Mollusk *Chione cortezi*: Implications for Paleoenvironmental Analysis. *Palaios,* ***16***(4), 387–398. https://doi.org/10.1669/0883-1351(2001)016<0387:CCODGI>2.0.CO;2

Grenier, C., Griesshaber, E., Schmahl, W. W., & Checa, A. G. (2023). Microstructure and Crystallographic Characteristics of Stenolaemate Bryozoans (Phylum Bryozoa and Class Stenolaemata). *Crystal Growth & Design*, ***23***(2), 965–9979. https://doi.org/10.1021/acs.cgd.2c01149

Guest, J. R., Todd, P. A., Goh, E., Sivalonganathan, B. S., & Reddy, K. P. (2008). Can giant clam (*Tridacna squamosa*) populations be restored on Singapore's heavily impacted coral reefs? *Aquatic Conservation: Marine and Freshwater Ecosystems*, ***18***(5), 570–579. https://doi.org/10.1002/aqc.888

Hamada, J. I., Yamanaka, M. D., Matsumoto, J., Fukao, S., Winarso, P. A., & Sribimawati, T. (2002). Spatial and Temporal Variations of the Rainy Season over Indonesia and their Link to ENSO. *Journal of the Meteorological Society of Japan*, ***80***(2), 285–310. https://doi.org/10.2151/jmsj.80.285

Hamner, W. M., & Jones, M. S. (1976). Distribution, burrowing, and growth rates of the clam *Tridacna crocea* on interior reef flats: Formation of structures resembling micro atolls. *Oecologia*, ***24***(3), 207–227. https://doi.org/10.1007/BF00345474

Hendon, H. H. (2003). Indonesian rainfall variability: Impacts of ENSO and local air–sea interaction. *Journal of Climate*, ***16***(11), 1775-1790. https://doi.org/10.1175/15200442(2003)016<1775:IRVIOE>2.0.CO;2

Hendry, J. P., Ditchfield, P. W., & Marshall, J. D. (1995). Two-stage neomorphism of Jurassic aragonitic bivalves; implications for early diagenesis. *Journal of Sedimentary Research*, ***65***(1a), 214–224. https://doi.org/10.1306/D4268077-2B26-11D7-8648000102C1865D

Hennige, S. J., Smith, D. J., Perkins, R., Consalvey, M., Paterson, D. M., & Suggett, D. J. (2008). Photoacclimation, growth and distribution of massive coral species in clear and turbid waters. *Marine Ecology Progress Series*, ***369***(1), 77–88. https://doi.org/10.3354/meps07612

Hennige, S. J., Wicks, L. C., Kamenos, N. A., Perna, G., Findlay, H. S., & Roberts, J. M. (2015). Hidden impacts of ocean acidification to live and dead coral framework. *Proceedings of the Royal Society B: Biological Sciences*, ***282***(1813), 20150990. https://doi.org/10.1098/rspb.2015.0990

Heslinga, G. A., Perron, F. E., & Orak, O. (1984). Mass culture of giant clams (F. Tridacnidae) in Palau. *Aquaculture*, ***39***(1), 197–215. https://doi.org/10.1016/00448486(84)90266-7

Highsmith, R. C. (1979). Coral growth rates and environmental control of density banding. *Journal of Experimental Marine Biology and Ecology*, ***37***(2), 105–125. https://doi.org/10.1016/0022-0981(79)90089-3

Höche, N., Peharda, M., Walliser, E. O., & Schöne, B. R. (2020). Morphological variations of crossed-lamellar ultrastructures of *Glycymeris bimaculata* (Bivalvia) serve as a marine temperature proxy. *Estuarine, Coastal and Shelf Science*, ***237***(1), 106658. https://doi.org/10.1016/j.ecss.2020.106658

Hoegh-Guldberg, O. (1999). Climate change, coral bleaching and the future of the world's coral reefs. *Marine and Freshwater Research,* ***50***(8), 839–866. https://doi.org/10.1071/MF99078

Hoegh-Guldberg, O., Mumby, P. J., Hooten, A. J., Steneck, R. S., Greenfield, P., Gomez, E., Harvell, C. D., Sale, P. F., Edwards, A. J., Caldeira, K., Knowlton, N., Eakin, C. M., Iglesias-Prieto, R., Muthiga, N., Bradbury, R. H., Dubi, A., & Hatziolos, M. E. (2007). Coral Reefs Under Rapid Climate Change and Ocean Acidification. *Science*, ***318***(5857), 1737–1742. https://doi.org/10.1126/science.1152509

Hori, M., Sano, Y., Ishida, A., Takahata, N., Shirai, K., & Watanabe, T. (2015). Middle Holocene daily light cycle reconstructed from the strontium/calcium ratios of a fossil giant clam shell. *Scientific Reports*, ***5***(1), 8734. https://doi.org/10.1038/srep08734

Hou, X., Yu, H., Hou, Z., Li, J., Chen, Y., Luo, L., Chen, X., Li, W., Yang, H., & Zeng, W. (2020). Structural and mechanical evolution of *Tridacna gigas* during permineralization. *Journal of the Mechanical Behavior of Biomedical Materials*, ***103***, 103609. https://doi.org/10.1016/j.jmbbm.2019.103609

Hu, Y., Sun, X., Cheng, H., & Yan, H. (2020). Evidence from giant-clam $\delta^{18}O$ of intense El Ninõ–Southern Oscillation-related variability but reduced frequency 3700 years ago. *Climate of the Past*, ***16***(2), 597–610. https://doi.org/10.5194/cp-16-597-2020

Hughes, T. P., Baird, A. H., Bellwood, D. R., Card, M., Connolly, S. R., Folke, C., ... & Roughgarden, J. (2003). Climate Change, Human Impacts, and the Resilience of Coral Reefs. *Science*, ***301***(5635), 929–933. https://doi.org/10.1126/science.1085046

Hughes, T. P., Barnes, M. L., Bellwood, D. R., Cinner, J. E., Cumming, G. S., Jackson, J. B., ... & Scheffer, M. (2017). Coral reefs in the Anthropocene. *Nature*, ***546***(7656), 82–90. https://doi.org/10.1038/nature22901

Ichikawa, H., & Yasunari, T. (2006). Time–Space Characteristics of Diurnal Rainfall over Borneo and Surrounding Oceans as Observed by TRMM-PR. *Journal of Climate*, ***19***(7), 1238–1260. https://doi.org/10.1175/JCLI3714.1

Ip, Y. K., & Chew, S. F. (2021). Light-dependent phenomena and related molecular mechanisms in giant clam-dinoflagellate associations: A review. *Frontiers in Marine Science*, ***8***(1), 627722. https://www.frontiersin.org/articles/10.3389/fmars.2021.627722/full

Ip, Y. K., Hiong, K. C., Goh, E. J. K., Boo, M. V., Choo, C. Y. L., Ching, B., Wong, W. P., & Chew, S. F. (2017). The Whitish Inner Mantle of the Giant Clam, *Tridacna squamosa*, Expresses an Apical Plasma Membrane Ca^{2+}-ATPase (PMCA) Which

Displays Light-Dependent Gene and Protein Expressions. *Frontiers in Physiology*, ***8***(1), 781. https://doi.org/10.3389/fphys.2017.00781

Iwase, K., & Mori, K. (2020). Crystal Structure, Microhardness, and Toughness of Biomineral $CaCO_3$. *Crystal Growth & Design*, ***20***(3), 2091–2098. https://doi.org/10.1021/acs.cgd.9b01720

Jakobsen, F., Hartstein, N., Frachisse, J., & Golingi, T. (2007). Sabah shoreline management plan (Borneo, Malaysia): Ecosystems and pollution. *Ocean & Coastal Management*, ***50***(1–2), 84–102. https://doi.org/10.1016/j.ocecoaman.2006.03.013

Jantzen, C., Wild, C., El-Zibdah, M., Roa-Quiaoit, H. A., Haacke, C., & Richter, C. (2008). Photosynthetic performance of giant clams, *Tridacna maxima* and *T. squamosa*, Red Sea. *Marine Biology*, ***155***(2), 211–221. https://doi.org/10.1007/s00227-008-1019-7

John, E. H., Staudigel, P. T., Buse, B., Lear, C. H., Pearson, P. N., & Slater, S. M. (2023). Revealing Their True Stripes: Mg/Ca Banding in the Paleogene Planktonic Foraminifera Genus Morozovella and Implications for Paleothermometry. *Paleoceanography and Paleoclimatology*, ***38***(9), e2023PA004652. https://doi.org/10.1029/2023PA004652

Jones, D. S., Williams, D. F., & Romanek, C. S. (1986). Life History of SymbiontBearing Giant Clams from Stable Isotope Profiles. *Science*, ***231***(4733), 46–48. https://doi.org/10.1126/science.231.4733.46

Jones, R., Fisher, R., & Bessell-Browne, P. (2019). Sediment deposition and coral smothering. *PLOS ONE*, ***14***(6), e0216248. https://doi.org/10.1371/journal.pone.0216248

Jonkers, L., Buse, B., Brummer, G.-J. A., & Hall, I. R. (2016). Chamber formation leads to Mg/Ca banding in the planktonic foraminifer *Neogloboquadrina pachyderma*. *Earth and Planetary Science Letters*, ***451***(1), 177–184. https://doi.org/10.1016/j.epsl.2016.07.030

Junchompoo, C., Sinrapasan, N., Penpain, C., & Patsorn, P. (2013). Changing seawater temperature effects on giant clams bleaching, Mannai Island, Rayong province, Thailand. In *PROCEEDINGS of the Design Symposium on Conservation of Ecosystem (2013) (The 12th SEASTAR2000 workshop)* (pp. 71-76). Kyoto University Design School.

Kahng, S. E., Garcia-Sais, J. R., Spalding, H. L., Brokovich, E., Wagner, D., Weil, E., Hinderstein, L., & Toonen, R. J. (2010). Community ecology of mesophotic coral reef ecosystems. *Coral Reefs*, ***29***(2), 255–275. https://doi.org/10.1007/s00338-010-05936

Kamaya, M. (2009). A procedure for estimating Young's modulus of textured polycrystalline materials. International Journal of Solids and Structures, ***46***(13), 2642–2649. https://doi.org/10.1016/j.ijsolstr.2009.02.013

Kayal, M., Vercelloni, J., Loma, T. L. de, Bosserelle, P., Chancerelle, Y., Geoffroy, S., Stievenart, C., Michonneau, F., Penin, L., Planes, S., & Adjeroud, M. (2012). Predator Crown-of-Thorns Starfish (*Acanthaster planci*) Outbreak, Mass Mortality of Corals, and Cascading Effects on Reef Fish and Benthic Communities. *PLOS ONE*, ***7***(10), e47363. https://doi.org/10.1371/journal.pone.0047363

Killam, D., Al-Najjar, T., & Clapham, M. (2021). Giant clam growth in the Gulf of Aqaba is accelerated compared to fossil populations. *Proceedings of the Royal Society B: Biological Sciences*, ***288***(1957), 20210991. https://doi.org/10.1098/rspb.2021.0991

Killam, D., Das, S., Martindale, R. C., Gray, K. E., Paytan, A., & Junium, C. K. (2023). Photosymbiosis and nutrient utilization in giant clams revealed by nitrogen isotope sclerochronology. *Geochimica et Cosmochimica Acta*, ***359***(1), 165–175. https://doi.org/10.1016/j.gca.2023.08.018

Killam, D., Thomas, R., Al-Najjar, T., & Clapham, M. (2020). Interspecific and Intrashell Stable Isotope Variation Among the Red Sea Giant Clams. *Geochemistry, Geophysics, Geosystems*, ***21***(7), e2019GC008669. https://doi.org/10.1029/2019GC008669

Klein, R. T., Lohmann, K. C., & Thayer, C. W. (1996). Bivalve skeletons record seasurface temperature and δ18O via Mg/Ca and 18O/16O ratios. *Geology*, ***24***(5), 415–418. https://doi.org/10.1130/0091-7613(1996)024<0415:BSRSST>2.3.CO;2

Kleypas, J. A., Mcmanus, J. W., & Meñez, L. A. B. (1999). Environmental Limits to Coral Reef Development: Where Do We Draw the Line? *American Zoologist*, ***39***(1), 146–159. https://doi.org/10.1093/icb/39.1.146

Klumpp, D., & Griffiths, C. (1994). Contributions of phototrophic and heterotrophic nutrition to the metabolic and growth requirements of four species of giant clam (Tridacnidae). *Marine Ecology Progress Series*, ***115***(1), 103–115. https://doi.org/10.3354/meps115103

Klumpp, D., & Lucas, J. (1994). Nutritional ecology of the giant clams *Tridacna tevoroa* and *T. derasa* from Tonga: Influence of light on filter-feeding and photosynthesis. *Marine Ecology Progress Series*, ***107***(1), 147–156. https://doi.org/10.3354/meps107147

Klumpp, D. W., Bayne, B. L., & Hawkins, A. J. S. (1992). Nutrition of the giant clam *Tridacna gigas* (L.) I. Contribution of filter feeding and photosynthates to respiration and growth. *Journal of Experimental Marine Biology and Ecology*, ***155***(1), 105–122. https://doi.org/10.1016/0022-0981(92)90030-E

Knights, A. M., Norton, M. J., Lemasson, A. J., & Stephen, N. (2020). Ocean Acidification Mitigates the Negative Effects of Increased Sea Temperatures on the Biomineralization and Crystalline Ultrastructure of *Mytilus*. *Frontiers in Marine Science*, ***7***(1), 567228. https://doi.org/10.3389/fmars.2020.567228

Komagoe, T., Watanabe, T., Shirai, K., Yamazaki, A., & Uematu, M. (2018). Geochemical and Microstructural Signals in Giant Clam *Tridacna maxima* Recorded Typhoon Events at Okinotori Island, Japan. *Journal of Geophysical Research: Biogeosciences*, ***123***(5), 1460–1474. https://doi.org/10.1029/2017JG004082

Kripalani, R. H., & Kulkarni, A. (1997). Climatic impact of El Niño/La Niña on the Indian monsoon: A new perspective. *Weather*, ***52***(2), 39–46. https://doi.org/10.1002/j.1477-8696.1997.tb06267.x

Ladd, H. S. (1934). Geology of Viti Levu, Fiji. *Bulletin of the Bernice P. Bishop Museum*, ***119***(1), 1–263.

Lamarck, J. B. M. (1779) Prodrome d'une nouvelle classification des coquilles, comprenant une rédaction appropriée des caractères géneriques, et l'établissement d'un grand nombre de genres nouveaux. *Mémoires de la Société d'Histoire Naturelle de Paris*, ***1***, 63–91.

Lamarck, J. B. M. (1819) *Histoire naturelle des animaux sans vertèbres*. Published by the author, Paris, pp. 106.

Lane, D. J. W., & Lim, G. P. C. (2013). Reef corals in a high sedimentation environment on the 'Mainland' coast of Brunei, Northwest Borneo. *Galaxea, Journal of Coral Reef Studies*, ***15***(Supplement), 166–171. https://doi.org/10.3755/galaxea.15.166

Latip, N. A., Marzuki, A., Umar, M. U., & Rais, N. S. (2015). Land use and Forestry Management in Sabah: Review of Literature. *Australian Journal of Basic and Applied Sciences*, ***9***(7), 317–322.

Lazareth, C. E., Putten, E. V., André, L., & Dehairs, F. (2003). High-resolution trace element profiles in shells of the mangrove bivalve *Isognomon ephippium*: A record of environmental spatio-temporal variations? *Estuarine, Coastal and Shelf Science*, ***57***(5–6), 1103–1114. https://doi.org/10.1016/S0272-7714(03)00013-1

Leggat, W., Buck, B. H., Grice, A., & Yellowlees, D. (2003). The impact of bleaching on the metabolic contribution of dinoflagellate symbionts to their giant clam host: Loss of dinoflagellates changes host metabolism. *Plant, Cell & Environment*, ***26***(12), 1951–1961. https://doi.org/10.1046/j.0016-8025.2003.01111.x

Lenthe, W., Singh, S., & De Graef, M. (2019). Prediction of potential pseudo-symmetry issues in the indexing of electron backscatter diffraction patterns. *Journal of Applied Crystallography*, ***52***(5), 1157–1168. https://doi.org/10.1107/S1600576719011233

Li, W., Cheng, H., Miao, X., Wu, T., Xie, Z., Wu, G., & Wei, J. (2023). Element variation in a clam shell and its implications for cold seep irregular eruptions: *Calyptogena* sp. in the Haima cold seep. *Science of The Total Environment*, ***858***(1), 160159. https://doi.org/10.1016/j.scitotenv.2022.160159

Li, X. W., Ji, H. M., Yang, W., Zhang, G. P., & Chen, D. L. (2017). Mechanical properties of crossed-lamellar structures in biological shells: A review. *Journal of the Mechanical Behavior of Biomedical Materials*, ***74***, 54–71. https://doi.org/10.1016/j.jmbbm.2017.05.022

Linnaeus, C. (1758). *Systema Naturae per regna tria naturae, secundum classes, ordines, genera, species, cum characteribus, differentiis, synonymis, locis.* 10th ed. Stockholm, Lawrence Salviua.

Lippmann, F. (1973). *Sedimentary Carbonate Minerals*. Springer. https://doi.org/10.1007/978-3-642-65474-9

Liu, C., Zhao, L., Zhao, N., Yang, W., Hao, J., Qu, X., Liu, S., Dodson, J., & Yan, H. (2022). Novel methods of resolving daily growth patterns in giant clam (*Tridacna* spp.) shells. *Ecological Indicators*, ***134***(1), 108480. https://doi.org/10.1016/j.ecolind.2021.108480

Loiola, M., Cruz, I. C. S., Lisboa, D. S., Mariano-Neto, E., Leão, Z. M. A. N., Oliveira, M. D. M., & Kikuchi, R. K. P. (2019). Structure of marginal coral reef assemblages under different turbidity regime. *Marine Environmental Research*, ***147***(1), 138–148. https://doi.org/10.1016/j.marenvres.2019.03.013

Lucas, J. (1994). The biology, exploitation, and mariculture of giant clams (Tridacnidae). *Reviews in Fisheries Science*, ***2***(1), 181–223. http://doi.org/10.1080/10641269409388557

Lucas, J. S., Nash, W. J., Crawford, C. M., & Braley, R. D. (1989). Environmental influences on growth and survival during the ocean-nursery rearing of giant clams, *Tridacna gigas* (L.). *Aquaculture*, ***80***(1–2), 45–61. https://doi.org/10.1016/00448486(89)90272-X

Ma, X., Yan, H., Fei, H., Liu, C., Shi, G., Huang, E., Wang, Y., Qu, X., Lian, E., & Dang, H. (2020). A high-resolution $\delta^{18}O$ record of modern *Tridacna gigas* bivalve and its paleoenvironmental implications. *Palaeogeography, Palaeoclimatology, Palaeoecology*, ***554***(1), 109800. https://doi.org/10.1016/j.palaeo.2020.109800

Mainprice, D., Hielscher, R., & Schaeben, H. (2011). Calculating anisotropic physical properties from texture data using the MTEX open-source package. *Geological Society, London, Special Publications*, ***360***(1), 175–192. https://doi.org/10.1144/SP360.10

Marali, S., Schöne, B. R., Mertz-Kraus, R., Griffin, S. M., Wanamaker, A. D., Butler, P. G., Holland, H. A., & Jochum, K. P. (2017). Reproducibility of trace element time-series (Na/Ca, Mg/Ca, Mn/Ca, Sr/Ca, and Ba/Ca) within and between specimens of the bivalve *Arctica islandica* – A LA-ICP-MS line scan study. *Palaeogeography, Palaeoclimatology, Palaeoecology*, ***484***(1), 109–128. https://doi.org/10.1016/j.palaeo.2016.11.024

Marcano, M. C., Frank, T. D., Mukasa, S. B., Lohmann, K. C., & Taviani, M. (2015). Diagenetic incorporation of Sr into aragonitic bivalve shells: Implications for chronostratigraphic and palaeoenvironmental interpretations. *The Depositional Record*, ***1***(1), 38–52. https://doi.org/10.1002/dep2.3

Marin, F., Le Roy, N., & Marie, B. (2012). The formation and mineralization of mollusk shell. *Frontiers in Bioscience*, ***S4***(3), 1099–1125. https://doi.org/10.2741/s321

Marin, F., & Luquet, G. (2004). Molluscan shell proteins. *Comptes Rendus Palevol*, ***3***(6), 469–492. https://doi.org/10.1016/j.crpv.2004.07.009

Mastropietro, F., Godard, P., Burghammer, M., Chevallard, C., Daillant, J., Duboisset, J., Allain, M., Guenoun, P., Nouet, J., & Chamard, V. (2017). Revealing crystalline domains in a mollusc shell single-crystalline prism. *Nature Materials*, ***16***(9), 946–952. https://doi.org/10.1038/nmat4937

Maxwell, R. S., & Larsson, L. A. (2021). Measuring tree-ring widths using the CooRecorder software application. *Dendrochronologia*, ***67***(1), 125841. https://doi.org/10.1016/j.dendro.2021.125841

McClanahan, T. R. (2022). Fisheries yields and species declines in coral reefs. *Environmental Research Letters*, ***17***(4), 044023. https://doi.org/10.1088/17489326/ac5bb4

McMurray, S. E., Blum, J. E., Leichter, J. J., & Pawlik, J. R. (2011). Bleaching of the giant barrel sponge *Xestospongia muta* in the Florida Keys. *Limnology and Oceanography*, ***56***(6), 2243–2250. https://doi.org/10.4319/lo.2011.56.6.2243

McPhaden, M. J., Zhang, X., Hendon, H. H., Wheeler, M. C. (2006) Large scale dynamics and MJO forcing of ENSO variability. *Geophysical Research Letters*, ***33***(1), L16702. https://doi.org/10.1029/2006GL026786

Meng, Y., Fitzer, S. C., Chung, P., Li, C., Thiyagarajan, V., & Cusack, M. (2018a). Crystallographic Interdigitation in Oyster Shell Folia Enhances Material Strength. *Crystal Growth & Design*, ***18***(7), 3753–3761. https://doi.org/10.1021/acs.cgd.7b01481

Meng, Y., Guo, Z., Fitzer, S. C., Upadhyay, A., Chan, V. B. S., Li, C., Cusack, M., Yao, H., Yeung, K. W. K., & Thiyagarajan, V. (2018b). Ocean acidification reduces hardness and stiffness of the Portuguese oyster shell with impaired microstructure: A hierarchical analysis. *Biogeosciences*, ***15***(22), 6833–6846. https://doi.org/10.5194/bg15-6833-2018

Milano, S., Nehrke, G., Wanamaker Jr., A. D., Ballesta-Artero, I., Brey, T., & Schöne, B. R. (2017). The effects of environment on *Arctica islandica* shell formation and architecture. *Biogeosciences*, ***14***(6), 1577–1591. https://doi.org/10.5194/bg-14-15772017

Miller, J., Muller, E., Rogers, C., Waara, R., Atkinson, A., Whelan, K. R. T., Patterson, M., & Witcher, B. (2009). Coral disease following massive bleaching in 2005 causes 60% decline in coral cover on reefs in the US Virgin Islands. *Coral Reefs*, ***28***(4), 925–937. https://doi.org/10.1007/s00338-009-0531-7

Mills, K. (2022). Understanding shell growth in giant clams with EBSD. *Nature Reviews Earth & Environment*, ***3***(7), 424. https://doi.org/10.1038/s43017-022-00311-x

Mills, K., John, E. H., Muir, D. D., Santodomingo, N., Johnson, K. G., Hussein, M. A. S., & Sosdian, S. (2023). Growth responses of mixotrophic giant clams on nearshore turbid coral reefs. *Coral Reefs*, **42**(1), 593–608. https://doi.org/10.1007/s00338-02302366-8

Mills, K., Muir, D. D., Oldroyd, A., John, E. H., Santodomingo, N., Johnson, K. G., Hussein, M. A. S., & Sosdian, S. (2024). Microstructure and crystallographic texture data in modern giant clam shells (*Tridacna squamosa* and *Hippopus hippopus*). *Data in Brief*, ***52***(1), 109947. https://doi.org/10.1016/j.dib.2023.109947

Montagne, A., Naim, O., Tourrand, C., Pierson, B., & Menier, D. (2013). Status of Coral Reef Communities on Two Carbonate Platforms (Tun Sakaran Marine Park, East Sabah, Malaysia). *Journal of Ecosystems*, ***2013***(1), 1–15. https://doi.org/10.1155/2013/358183

Moore, C. H. (1989). *Carbonate Diagenesis and Porosity*. Elsevier.

Morais, J., & Santos, B. A. (2018). Limited potential of deep reefs to serve as refuges for tropical Southwestern Atlantic corals. *Ecosphere*, ***9***(7), e02281. https://doi.org/10.1002/ecs2.2281

Moreno-Azanza, M., Mariani, E., Bauluz, B., & Canudo, J. I. (2013). Growth Mechanisms in Dinosaur Eggshells: An Insight from Electron Backscatter Diffraction. *Journal of Vertebrate Paleontology*, ***33***(1), 121–130. https://www.jstor.org/stable/23361076

Morgan, K. M., Perry, C. T., Johnson, J. A., & Smithers, S. G. (2017). Nearshore Turbid-Zone Corals Exhibit High Bleaching Tolerance on the Great Barrier Reef Following the 2016 Ocean Warming Event. *Frontiers in Marine Science*, ***4***(1), 224. https://doi.org/10.3389/fmars.2017.00224

Moriarty, T., Leggat, W., Huggett, M. J., & Ainsworth, T. D. (2020). Coral Disease Causes, Consequences, and Risk within Coral Restoration. *Trends in Microbiology*, ***28***(10), 793–807. https://doi.org/10.1016/j.tim.2020.06.002

Moynihan, M. A., Amini, S., Goodkin, N. F., Tanzil, J. T. I., Chua, J. Q. I., Fabbro, G. N., Fan, T. Y., Schmidt, D. N., & Miserez, A. (2021). Environmental impact on the mechanical properties of *Porites* spp. Corals. *Coral Reefs*, ***40***(1), 701–717. https://doi.org/10.1007/s00338-021-02064-3

Moynihan, M. A., Amini, S., Oalmann, J., Chua, J. Q. I., Tanzil, J. T. I., Fan, T. Y., Miserez, A., & Goodkin, N. F. (2022). Crystal orientation mapping and microindentation reveal anisotropy in *Porites* skeletons. *Acta Biomaterialia*, ***151***(1), 446–456. https://doi.org/10.1016/j.actbio.2022.08.012

Muscatine, L., Goiran, C., Land, L., Jaubert, J., Cuif, J.-P., & Allemand, D. (2005). Stable isotopes ($\delta^{13}C$ and $\delta^{15}N$) of organic matrix from coral skeleton. *Proceedings of the National Academy of Sciences*, ***102***(5), 1525–1530. https://doi.org/10.1073/pnas.0408921102

Negrini, M., Batson, P. B., Smith, A. M., Smith, S. a. F., Prior, D. J., Henry, H., Li, K. C., & Tamberg, Y. (2022). Understanding the crystallographic and nanomechanical properties of bryozoans. *Journal of Structural Biology*, ***214***(3), 107882.

https://doi.org/10.1016/j.jsb.2022.107882

Neo, M. L. (2020). Conservation of Giant Clams (Bivalvia: Cardiidae). In *Encyclopedia of the World's Biomes* (pp. 527–538). Elsevier. https://doi.org/10.1016/B978-0-12409548-9.11780-4

Neo, M. L., Eckman, W., Vicentuan, K., Teo, S. L.-M., & Todd, P. A. (2015). The ecological significance of giant clams in coral reef ecosystems. *Biological Conservation*, ***181***, 111–123. https://doi.org/10.1016/j.biocon.2014.11.004

Neo, M. L., Wabnitz, C. C. C., Braley, R. D., Heslinga, G. A., Fauvelot, C., Wynsberge, S. V., Andréfouët, Ser. G. E., Waters, C., Tan, A. S.-H., Gomez, E. D., Costello, M. J., & Todd, P. A. (2017). Giant Clams (Bivalvia: Cardiidae: Tridacninae): A Comprehensive Update of Species and their Distribution, Current Threats and Conservation Status. In S. J. Hawkins, A. J. Evans, A. C. Dale, L. B. Firth, D. J. Hughes, & I. P. Smith (Eds.), *Oceanography and Marine Biology* (1st ed., pp. 87–387). CRC Press. https://doi.org/10.1201/b21944-5

Neves, N. M., & Mano, J. F. (2005). Structure/mechanical behavior relationships in crossed-lamellar sea shells. *Materials Science and Engineering: C*, ***25***(2), 113–118. https://doi.org/10.1016/j.msec.2005.01.004

Norton, J. H., & Jones, G. W. (1992). The giant clam: An anatomical and histological atlas. *The Giant Clam: An Anatomical and Histological Atlas.* https://www.cabdirect.org/cabdirect/abstract/19932285551

Norton, J. H., Shepherd, M. A., Long, H. M., & Fitt, W. K. (1992). The Zooxanthellal Tubular System in the Giant Clam. *The Biological Bulletin*, ***183***(3), 503–506. https://doi.org/10.2307/1542028

Nudelman, F. (2015). Nacre biomineralisation: A review on the mechanisms of crystal nucleation. *Seminars in Cell & Developmental Biology*, ***46***(1), 2–10. https://doi.org/10.1016/j.semcdb.2015.07.004

Osuna-Mascaró, A. J., Cruz-Bustos, T., Marin, F., & Checa, A. G. (2015). Ultrastructure of the Interlamellar Membranes of the Nacre of the Bivalve Pteria hirundo, Determined by Immunolabelling. *PLOS ONE*, ***10***(4), e0122934. https://doi.org/10.1371/journal.pone.0122934

Otter, L. M., Agbaje, O. B. A., Kilburn, M. R., Lenz, C., Henry, H., Trimby, P., Hoppe, P., & Jacob, D. E. (2019). Insights into architecture, growth dynamics, and biomineralization from pulsed Sr-labelled *Katelysia rhytiphora* shells (Mollusca, Bivalvia). *Biogeosciences*, ***16***(17), 3439–3455. https://doi.org/10.5194/bg-16-34392019

Pabich, S., Vollmer, C., & Gussone, N. (2020). Investigating crystal orientation patterns of foraminiferal tests by electron backscatter diffraction analysis. *European Journal of Mineralogy*, ***32***(6), 613–622. https://doi.org/10.5194/ejm-32-613-2020

Pandolfi, J. M., Connolly, S. R., Marshall, D. J., & Cohen, A. L. (2011). Projecting Coral Reef Futures Under Global Warming and Ocean Acidification. *Science*, ***333***(6041), 418–422. https://doi.org/10.1126/science.1204794

Paquette, J., & Reeder, R. J. (1995). Relationship between surface structure, growth mechanism, and trace element incorporation in calcite. *Geochimica et Cosmochimica Acta*, ***59***(4), 735–749. https://doi.org/10.1016/0016-7037(95)00004-J

Parker, J. E., Thompson, S. P., Lennie, A. R., Potter, J., & Tang, C. C. (2010). A study of the aragonite-calcite transformation using Raman spectroscopy, synchrotron powder diffraction and scanning electron microscopy. *CrystEngComm*, ***12***(5), 1590. https://doi.org/10.1039/b921487a

Pastorok, R., & Bilyard, G. (1985). Effects of sewage pollution on coral-reef communities. *Marine Ecology Progress Series*, ***21***(1), 175–189. https://doi.org/10.3354/meps021175

Pätzold, J., Heinrichs, J. P., Wolschendorf, K., & Wefer, G. (1991). Correlation of stable oxygen isotope temperature record with light attenuation profiles in reefdwelling *Tridacna* shells. *Coral Reefs*, ***10***(1), 65–69. https://doi.org/10.1007/BF00571825

Payus, C., Ann Huey, L., Adnan, F., Besse Rimba, A., Mohan, G., Kumar Chapagain, S., Roder, G., Gasparatos, A., & Fukushi, K. (2020). Impact of Extreme Drought Climate on Water Security in North Borneo: Case Study of Sabah. *Water*, ***12***(4), 1135. https://doi.org/10.3390/w12041135

Pederson, C. L., Mavromatis, V., Dietzel, M., Rollion-Bard, C., Breitenbach, S. F. M., Yu, D., Nehrke, G., & Immenhauser, A. (2020). Variation in the diagenetic response of aragonite archives to hydrothermal alteration. *Sedimentary Geology*, ***406***(1), 105716. https://doi.org/10.1016/j.sedgeo.2020.105716

Peharda, M., Schöne, B. R., Black, B. A., & Corrège, T. (2021). Advances of sclerochronology research in the last decade. *Palaeogeography, Palaeoclimatology, Palaeoecology*, ***570***(1), 110371. https://doi.org/10.1016/j.palaeo.2021.110371

Pérez-Huerta, A., & Cusack, M. (2009). Optimizing electron backscatter diffraction of carbonate biominerals—resin type and carbon coating. *Microscopy and Microanalysis*, ***15***(3), 197–203. https://doi.org/10.1017/S1431927609090370

Perry, C. T., & Larcombe, P. (2003). Marginal and non-reef-building coral environments. *Coral Reefs*, ***22***(4), 427–432. https://doi.org/10.1007/s00338-0030330-5

Poulain, C., Gillikin, D. P., Thébault, J., Munaron, J. M., Bohn, M., Robert, R., Paulet, Y. M., & Lorrain, A. (2015). An evaluation of Mg/Ca, Sr/Ca, and Ba/Ca ratios as environmental proxies in aragonite bivalve shells. *Chemical Geology*, ***396***(1), 42–50. https://doi.org/10.1016/j.chemgeo.2014.12.019

Reaka, M. L., Rodgers, P. J., & Kudla, A. U. (2008). Patterns of biodiversity and endemism on Indo-West Pacific coral reefs. *Proceedings of the National Academy of*

Sciences, ***105***(supplement_1), 11474–11481. https://doi.org/10.1073/pnas.0802594105

Reid, P. C., Fischer, A. C., Lewis-Brown, E., Meredith, M. P., Sparrow, M., Andersson, A. J., Antia, A., Bates, N. R., Bathmann, U., Beaugrand, G., Brix, H., Dye, S., Edwards, M., Furevik, T., Gangstø, R., Hátún, H., Hopcroft, R. R., Kendall, M., Kasten, S., … Washington, R. (2009). Chapter 1 Impacts of the Oceans on Climate Change. In *Advances in Marine Biology* (Vol. 56, pp. 1–150). Academic Press. https://doi.org/10.1016/S0065-2881(09)56001-4

Renema, W., Warter, V., Novak, V., Young, J. R., Marshall, N., & Hasibuan, F. (2015). Ages of Miocene fossil localities in the northern Kutai basin (East Kalimantan, Indonesia). *Palaios*, ***30***(1), 26-39. https://doi.org/10.2110/palo.2013.127

Rhein, M., S.R. Rintoul, S. Aoki, E. Campos, D. Chambers, R.A. Feely, S. Gulev, G.C. Johnson, S.A. Josey, A. Kostianoy, C. Mauritzen, D. Roemmich, L.D. Talley & F. Wang. (2013): Observations: Ocean. In: *Climate Change 2013: The Physical Science Basis. Contribution of Working Group I to the Fifth Assessment Report of the Intergovernmental Panel on Climate Change* [Stocker, T.F., D. Qin, G.-K. Plattner, M. Tignor, S.K. Allen, J. Boschung, A. Nauels, Y. Xia, V. Bex and P.M. Midgley (eds.)]. Cambridge University Press, Cambridge, United Kingdom and New York, NY, USA. https://doi.org/10.1017/CBO9781107415324.010

Richter, C., Roa-Quiaoit, H., Jantzen, C., Al-Zibdah, M., & Kochzius, M. (2008). Collapse of a New Living Species of Giant Clam in the Red Sea. *Current Biology*, ***18***(17), 1349–1354. https://doi.org/10.1016/j.cub.2008.07.060

Rietveld, H. M. (1969). A profile refinement method for nuclear and magnetic structures. *Journal of Applied Crystallography*, ***2***(2), 65–71. https://doi.org/10.1107/S0021889869006558

Risk, M. J., & Sammarco, P. W. (1991). Cross-shelf trends in skeletal density of the massive coral *Porites lobata* from the Great Barrier Reef. *Marine Ecology Progress Series*, ***69***(1/2), 195–200. https://www.jstor.org/stable/44634779

Risk, M. J., Sayer, B. G., Tevesz, M. J. s., & Karr, C. D. (1996). Comparison of the organic matrix of fossil and recent bivalve shells. *Lethaia*, ***29***(2), 197–202. https://doi.org/10.1111/j.1502-3931.1996.tb01876.x

Ritter, A. C., Mavromatis, V., Dietzel, M., Kwiecien, O., Wiethoff, F., Griesshaber, E., Casella, L. A., Schmahl, W. W., Koelen, J., Neuser, R. D., Leis, A., Buhl, D., Niedermayr, A., Breitenbach, S. F. M., Bernasconi, S. M., & Immenhauser, A. (2017). Exploring the impact of diagenesis on (isotope) geochemical and microstructural alteration features in biogenic aragonite. *Sedimentology*, ***64***(5), 1354–1380. https://doi.org/10.1111/sed.12356

Roa-Quiaoit, H. A. F. (2005). *Ecology and culture of giant clams (Tridacnidae) in the Jordanian sector of the Gulf of Aqaba, Red Sea* (Doctoral dissertation, Universität Bremen). https://media.suub.uni-bremen.de/handle/elib/2141

Roberts, C. M. (1995). Effects of Fishing on the Ecosystem Structure of Coral Reefs. *Conservation Biology*, ***9***(5), 988–995. https://doi.org/10.1046/j.15231739.1995.9051332.x-i1

Röding, P. F. (1798) *Museum Boltenianum* sive Catalogus cimeliorum e tribus regnis naturæ quæ olim collegerat Joa. Fried Bolten, M. D. p. d. per XL. annos proto physicus Hamburgensis. Pars secunda continens Conchylia sive Testacea univalvia, bivalvia & multivalvia. Trapp, Hamburg.

Rodland, D. L., Schöne, B. R., Helama, S., Nielsen, J. K., & Baier, S. (2006). A clockwork mollusc: Ultradian rhythms in bivalve activity revealed by digital photography. *Journal of Experimental Marine Biology and Ecology*, ***334***(2), 316-323. https://doi.org/10.1016/j.jembe.2006.02.012

Rogers, C. (1990). Responses of coral reefs and reef organisms to sedimentation. *Marine Ecology Progress Series*, ***62***(1), 185–202. https://doi.org/10.3354/meps062185

Romanek, C. S., & Grossman, E. L. (1989). Stable Isotope Profiles of *Tridacna maxima* as Environmental Indicators. *Palaios*, ***4***(5), 402. https://doi.org/10.2307/3514585

Romanek, C. S., Jones, D. S., Williams, D. F., Krantz, D. E., & Radtke, R. (1987). Stable isotopic investigation of physiological and environmental changes recorded in shell carbonate from the giant clam *Tridacna maxima*. *Marine Biology*, ***94***(3), 385–393. https://doi.org/10.1007/BF00428244

Rondahl, S. H., Pointurier, F., Ahlinder, L., Ramebäck, H., Marie, O., Ravat, B., Delaunay, F., Young, E., Blagojevic, N., Hester, J. R., Thorogood, G., Nelwamondo, A. N., Ntsoane, T. P., Roberts, S. K., & Holliday, K. S. (2018). Comparing results of Xray diffraction, μ-Raman spectroscopy and neutron diffraction when identifying chemical phases in seized nuclear material, during a comparative nuclear forensics exercise. *Journal of Radioanalytical and Nuclear Chemistry*, ***315***(2), 395–408. https://doi.org/10.1007/s10967-017-5666-3

Rosedy, A., Ives, I., Waheed, Z., Hussein, M. A. S., Sosdian, S., Johnson, K., & Santodomingo, N. (2023). Turbid reefs experience lower coral bleaching effects in NE Borneo (Sabah, Malaysia). *Regional Studies in Marine Science*, ***68***(1), 103268. https://doi.org/10.1016/j.rsma.2023.103268

Rosewater, J. (1965). The family Tridacnidae in the indo-pacific. *Indo-Pacific Mollusca*, ***1***(1), 347.

Rosewater, J. (1982) A new species of *Hippopus* (Bivalvia: Tridacnidae). *The Nautilus.* ***96***(1), 3–6.

Sa'adi, Z., Shiru, M. S., Shahid, S., Ismail, T. (2020) Selection of general circulation models for the projections of spatio-temporal changes in temperature of Borneo Island based on CMIP5. *Theoretical and Applied Climatology*, ***139***(1), 351–371. https://doi.org/10.1007/s00704-019-02948-z

Saenz-Agudelo, P., Jones, G. P., Thorrold, S. R., & Planes, S. (2011). Detrimental effects of host anemone bleaching on anemonefish populations. *Coral Reefs*, ***30***(2), 497–506. https://doi.org/10.1007/s00338-010-0716-0

Saleh, E., Hoque, A., Rahman, R.A. (2007) Water circulation in Darvel Bay, Sabah, Malaysia. *In Oceans 2007-Europe (pp. 1-6). IEEE.* https://doi.org/10.1109/OCEANSE.2007.4302366

Sandberg, P. A., & Hudson, J. D. (1990). Aragonite Relic Preservation in Jurassic Calcite replaced Bivalves. In *Carbonate Diagenesis* (pp. 273–286). John Wiley & Sons, Ltd. https://doi.org/10.1002/9781444304510.ch23

Sano, Y., Kobayashi, S., Shirai, K., Takahata, N., Matsumoto, K., Watanabe, T., Sowa, K., & Iwai, K. (2012). Past daily light cycle recorded in the strontium/calcium ratios of giant clam shells. *Nature Communications*, ***3***(1), 761. https://doi.org/10.1038/ncomms1763

Santisteban, J., Mediavilla, R., Pamo, E., Dabrio, C., Zapata, M., Gil-García, M., Castaño Castaño, S., & Alfaro, P. (2004). Loss on Ignition: A Qualitative or Quantitative Method for Organic Matter and Carbonate Mineral Content in Sediments? *Journal of Paleolimnology*, ***32***(1), 287–299. https://doi.org/10.1023/B:JOPL.0000042999.30131.5b

Santodomingo, N., Perry, C., Waheed, Z., Syed Hussein, M. A. bin, Rosedy, A., & Johnson, K. G. (2021). Marine litter pollution on coral reefs of Darvel Bay (East Sabah, Malaysia). *Marine Pollution Bulletin*, ***173***(1), 112998. https://doi.org/10.1016/j.marpolbul.2021.112998

Santodomingo, N., Renema, W., & Johnson, K. G. (2016). Understanding the murky history of the Coral Triangle: Miocene corals and reef habitats in East Kalimantan (Indonesia). *Coral Reefs*, ***35***, 765–781. https://doi.org/10.1007/s00338-016-1427-y

Saruwatari, K., Matsui, T., Mukai, H., Nagasawa, H., & Kogure, T. (2009). Nucleation and growth of aragonite crystals at the growth front of nacres in pearl oyster, *Pinctada fucata*. *Biomaterials*, ***30***(16), 3028–3034. https://doi.org/10.1016/j.biomaterials.2009.03.011

Saw, J. V. M., Hunter, A. W., Johnson, K. G., & Abdul Rahman, A. H. B. (2019). Pliocene corals from the Togopi Formation of the Dent Peninsula, Sabah, northeastern Borneo, Malaysia. *Alcheringa: An Australasian Journal of Palaeontology*, ***43***(2), 291–319. https://doi.org/10.1080/03115518.2018.1510978

Sayco, S. L. G., Alabort Pomares, A., Cabaitan, P. C., & Kurihara, H. (2024). Reproductive consequences of thermal stress-induced bleaching in the giant clam *Tridacna crocea*. *Marine Environmental Research*, ***193***(1), 106280. https://doi.org/10.1016/j.marenvres.2023.106280

Sayco, S. L. G., Cabaitan, P. C., & Kurihara, H. (2023). Bleaching reduces reproduction in the giant clam *Tridacna gigas*. *Marine Ecology Progress Series*, ***706***(1), 47–56. https://doi.org/10.3354/meps14251

Schneider, C. A., Rasband, W. S., & Eliceiri, K. W. (2012). NIH Image to ImageJ: 25 years of image analysis. *Nature Methods*, ***9***(7), 671–675. https://doi.org/10.1038/nmeth.2089

Schöne, B. R. (2003). A 'clam-ring' master-chronology constructed from a short-lived bivalve mollusc from the northern Gulf of California, USA. *The Holocene*, ***13***(1), 39–49. https://doi.org/10.1191/0959683603hl593rp

Schöne, B. R., Fiebig, J., Pfeiffer, M., Gleβ, R., Hickson, J., Johnson, A. L. A., Dreyer, W., & Oschmann, W. (2005). Climate records from a bivalved Methuselah (*Arctica*

islandica, Mollusca; Iceland). *Palaeogeography, Palaeoclimatology, Palaeoecology*, ***228***(1–2), 130–148. https://doi.org/10.1016/j.palaeo.2005.03.049

Schöne, B. R., Radermacher, P., Zhang, Z., & Jacob, D. E. (2013). Crystal fabrics and element impurities (Sr/Ca, Mg/Ca, and Ba/Ca) in shells of *Arctica islandica*—Implications for paleoclimate reconstructions. *Palaeogeography, Palaeoclimatology, Palaeoecology*, ***373***(1), 50–59. https://doi.org/10.1016/j.palaeo.2011.05.013

Schöne, B. R., & Surge, D. M. (2012). Part N, Revised, Volume 1, Chapter 14: Bivalve sclerochronology and geochemistry. *Treatise online*, ***46***(1), 1–24.

Schöne, B. R., Zhang, Z., Jacob, D., Gillikin, D. P., Tütken, T., Garbe-Schönberg, D., Mcconnaughey, T., & Soldati, A. (2010). Effect of organic matrices on the determination of the trace element chemistry (Mg, Sr, Mg/Ca, Sr/Ca) of aragonitic bivalve shells (*Arctica islandica*)—Comparison of ICP-OES and LA-ICP-MS data. *Geochemical Journal*, ***44***(1), 23–37. https://doi.org/10.2343/geochemj.1.0045

Schwartzmann, C., Durrieu, G., Sow, M., Ciret, P., Lazareth, C. E., & Massabuau, J.C. (2011). *In situ* giant clam growth rate behavior in relation to temperature: A oneyear coupled study of high-frequency noninvasive valvometry and sclerochronology. *Limnology and Oceanography*, ***56***(5), 1940–1951. https://doi.org/10.4319/lo.2011.56.5.1940

Senior, N. (2020). *The response of shallow-turbid reefs to sedimentation in the Coral Triangle* (Master of Research, Natural History Museum London).

Shaver, E. C., Burkepile, D. E., & Silliman, B. R. (2018). Local management actions can increase coral resilience to thermally-induced bleaching. *Nature Ecology & Evolution*, ***2***(7), 1075–1079. https://doi.org/10.1038/s41559-018-0589-0

Shi, W., Wang, M. (2010). Characterization of global ocean turbidity from Moderate Resolution Imaging Spectroradiometer ocean color observations. *Journal of Geophysical Research: Oceans*, *115*(C11). https://doi.org/10.1029/2010JC006160

Silbiger, N., Guadayol, Ò., Thomas, F., & Donahue, M. (2014). Reefs shift from net accretion to net erosion along a natural environmental gradient. *Marine Ecology Progress Series*, ***515***(1), 33–44. https://doi.org/10.3354/meps10999

Sirenko, B. I., Scarlato, O. A. (1991). *Tridacna rosewateri* sp. n. Una nuova specie di *Tridacna* dall'Oceano Indiano. A new species of giant clam from Indian Ocean. *La Conchiglia.* **22**(1), 4–9.

Smith, S. D. A. (2011). Growth and population dynamics of the giant clam *Tridacna maxima* (Röding) at its southern limit of distribution in coastal, subtropical eastern Australia. *Molluscan Research*, ***31***(1), 5.

Soares, M. O. (2020). Marginal reef paradox: A possible refuge from environmental changes? *Ocean & Coastal Management*, ***185***(1), 105063. https://doi.org/10.1016/j.ocecoaman.2019.105063

Soo, P., & Todd, P. A. (2014). The behaviour of giant clams (Bivalvia: Cardiidae: Tridacninae). *Marine Biology*, ***161***(12), 2699–2717. https://doi.org/10.1007/s00227-014-2545-0

Steffen, W., Persson, Å., Deutsch, L., Zalasiewicz, J., Williams, M., Richardson, K., Crumley, C., Crutzen, P., Folke, C., Gordon, L., Molina, M., Ramanathan, V., Rockström, J., Scheffer, M., Schellnhuber, H. J., & Svedin, U. (2011). The Anthropocene: From Global Change to Planetary Stewardship. *AMBIO*, ***40***(7), 739–761. https://doi.org/10.1007/s13280-011-0185-x

Stephenson, A. E., DeYoreo, J. J., Wu, L., Wu, K. J., Hoyer, J., & Dove, P. M. (2008). Peptides enhance magnesium signature in calcite: Insights into origins of vital effects. *Science*, ***322***(5902), 724-727. https://doi.org/10.1126/science.115941

Sturany, R. (1901). Expedition S.M. Schiff “Pola” in das Rothe Meer, nördliche und südliche Hälfte. 1895/96 – 1897/98. Zoologische Ergebnisse XIV. Lamellibranchiaten des Rothen Meeres. *Denkschriften der Kaiserlichen Akademie der Wissenschaften, Mathematisch-Naturwissenschaftliche Classe*, ***69***(1), 255–295.

Sully, S., & van Woesik, R. (2020). Turbid reefs moderate coral bleaching under climate-related temperature stress. *Global Change Biology*, ***26***(3), 1367–1373. https://doi.org/10.1111/gcb.14948

Takahashi, S., & Murata, N. (2008). How do environmental stresses accelerate photoinhibition? *Trends in Plant Science*, ***13***(4), 178–182. https://doi.org/10.1016/j.tplants.2008.01.005

Tambutté, S., Holcomb, M., Ferrier-Pagès, C., Reynaud, S., Tambutté, É., Zoccola, D., & Allemand, D. (2011). Coral biomineralization: From the gene to the environment. *Journal of Experimental Marine Biology and Ecology*, ***408***(1), 58–78. https://doi.org/10.1016/j.jembe.2011.07.026

Tan, F., Lim, H.S., Abdullah, K. (2013) Effects of Orography on the Tail-End Effects of Typhoon Ketsana. *TOASCJ,* ***7***(1), 14–28. https://doi.org/10.2174/1874282301307010014

Tan, E. Y. W., Quek, Z. B. R., Neo, M. L., Fauvelot, C., & Huang, D. (2021). Genome skimming resolves the giant clam (Bivalvia: Cardiidae: Tridacninae) tree of life. *Coral Reefs,* ***41***(1), 497–510. https://doi.org/10.1007/s00338-020-02039-w

Taylor, J. D., Kennedy, W. J., & Hall, A. (1969) The shell structure and mineralogy of the Bivalvia: introduction Nuculacea-Trigonacea. *Bulletin of the British Museum (Natural History)*, ***3***(1), 1–125.

Tedengren, M., Blidberg, E., Elfwing, T. (2000) The effects of different light intensities on photosynthesis and filter-feeding of the giant clam, Tridacna squamosa. *In:* Mollusk research in Asia, Proceedings of the fifth Asian fishery forum 1998. Chiang Mai, Thailand, pp. 165–171.

The MathWorks Inc. (2022). MATLAB version: 9.13.0 (R2022b), Natick, Massachusetts: The MathWorks Inc. https://www.mathworks.com

Thomsen, K., Schmidt, N. H., Bewick, A., Larsen, K., & Goulden, J. (2013). Improving the accuracy of orientation measurements using EBSD. *Microscopy and Microanalysis*, ***19***(S2), 724–725. https://doi.org/10.1017/S1431927613005618

Thomson, D. J. (1982). Spectrum estimation and harmonic analysis. *Proceedings of the IEEE*, ***70***(9), 1055–1096.

Tran, D., Perrigault, M., Ciret, P., & Payton, L. (2020). Bivalve mollusc circadian clock genes can run at tidal frequency. *Proceedings of the Royal Society B: Biological Sciences*, ***287***(1918), 20192440. https://doi.org/10.1098/rspb.2019.2440

Travaglione, N., Evans, R., Moustaka, M., Cuttler, M., Thomson, D. P., Tweedley, J., & Wilson, S. (2023). Scleractinian corals rely on heterotrophy in highly turbid environments. *Coral Reefs*, ***47***(1), 997–1010. https://doi.org/10.1007/s00338-02302407-2

Urey, H. C., Lowenstam, H. A., Epstein, S., & McKinney, C. R. (1951). Measurement of paleotemperatures and temperatures of the Upper Cretaceous of England, Denmark, and the southeastern United States. *Geological Society of America Bulletin*, ***62***(4), 399–416. https://doi.org/10.1130/0016-7606(1951)62[399:MOPATO]2.0.CO;2

Urmos, J., Sharma, S. K., & Mackenzie, F. T. (1991). Characterization of some biogenic carbonates with Raman spectroscopy. *American Mineralogist*, ***76***(3–4), 641– 646.

Valentine, J. W., Jablonski, D., Kidwell, S., & Roy, K. (2006). Assessing the fidelity of the fossil record by using marine bivalves. *Proceedings of the National Academy of Sciences*, ***103***(17), 6599–6604. https://doi.org/10.1073/pnas.0601264103

van de Moortèle, B., Bezacier, L., Trullenque, G., & Reynard, B. (2010). Electron backscattering diffraction (EBSD) measurements of antigorite lattice-preferred orientations (LPO). *Journal of Microscopy*, ***239***(3), 245–248. https://doi.org/10.1111/j.13652818.2010.03398.x

van Hooidonk, R., Maynard, J. A., Manzello, D., & Planes, S. (2014). Opposite latitudinal gradients in projected ocean acidification and bleaching impacts on coral reefs. *Global Change Biology*, ***20***(1), 103–112. https://doi.org/10.1111/gcb.12394

van Wynsberge, S., Andréfouët, S., Gaertner-Mazouni, N., Wabnitz, C. C. C., Menoud, M., Le Moullac, G., Levy, P., Gilbert, A., & Remoissenet, G. (2017). Growth, Survival and Reproduction of the Giant Clam *Tridacna maxima* (Röding 1798, Bivalvia) in Two Contrasting Lagoons in French Polynesia. *PLoS One*, ***12***(1), e0170565. https://doi.org/10.1371/journal.pone.0170565

Vargas, C. A., Lagos, N. A., Lardies, M. A., Duarte, C., Manríquez, P. H., Aguilera, V. M., Broitman, B., Widdicombe, S., & Dupont, S. (2017). Species-specific responses to ocean acidification should account for local adaptation and adaptive plasticity. *Nature Ecology & Evolution*, ***1***(4), 0084. https://doi.org/10.1038/s41559-017-0084

Veizer, J., & Prokoph, A. (2015). Temperatures and oxygen isotopic composition of Phanerozoic oceans. *Earth-Science Reviews*, ***146***(1), 92–104. https://doi.org/10.1016/j.earscirev.2015.03.008

Veron, J. E. N., Devantier, L. M., Turak, E., Green, A. L., Kininmonth, S., StaffordSmith, M., & Peterson, N. (2009). Delineating the Coral Triangle. *Galaxea, Journal of Coral Reef Studies*, ***11***(2), 91–100. https://doi.org/10.3755/galaxea.11.91

Vijith, H., & Dodge-Wan, D. (2020). Spatial and temporal characteristics of rainfall over a forested river basin in NW Borneo. *Meteorology and Atmospheric Physics*, ***132***(5), 683–702. https://doi.org/10.1007/s00703-019-00714-4

Vogel, K., Gektidis, M., Golubic, S., Kiene, W. E., & Radtke, G. (2000). Experimental studies on microbial bioerosion at Lee Stocking Island, Bahamas and One Tree Island, Great Barrier Reef, Australia: Implications for paleoecological reconstructions. *Lethaia*, ***33***(3), 190–204. https://doi.org/10.1080/00241160025100053

Wacey, D., Saunders, M., Roberts, M., Menon, S., Green, L., Kong, C., ... & Brasier, M. D. (2014). Enhanced cellular preservation by clay minerals in 1 billion-year-old lakes. *Scientific reports*, ***4***(1), 5841. https://doi.org/10.1038/srep05841

Waheed, Z., van Mil, H. G., Syed Hussein, M. A., Jumin, R., Golam Ahad, B., & Hoeksema, B. W. (2015). Coral Reefs at the Northernmost Tip of Borneo: An Assessment of Scleractinian Species Richness Patterns and Benthic Reef Assemblages. *PLoS One, **10**(12), e0146006.*

Waheed, Z., & Hoeksema, B. W. (2013). A tale of two winds: Species richness patterns of reef corals around the Semporna peninsula, Malaysia. *Marine Biodiversity*, ***43***(1), 37–51. https://doi.org/10.1007/s12526-012-0130-7

Walls, R. A., Ragland, P. C., & Crisp, E. L. (1977). Experimental and natural early diagenetic mobility of Sr and Mg in biogenic carbonates. *Geochimica et Cosmochimica Acta*, ***41***(12), 1731–1737.

Warter, V., Erez, J., & Müller, W. (2018). Environmental and physiological controls on daily trace element incorporation in *Tridacna crocea* from combined laboratory culturing and ultra-high resolution LA-ICP-MS analysis. *Palaeogeography, Palaeoclimatology, Palaeoecology*, ***496***(1), 32–47. https://doi.org/10.1016/j.palaeo.2017.12.038

Warter, V., & Müller, W. (2017). Daily growth and tidal rhythms in Miocene and modern giant clams revealed via ultra-high resolution LA-ICPMS analysis—A novel methodological approach towards improved sclerochemistry. *Palaeogeography, Palaeoclimatology, Palaeoecology*, ***465***(1), 362–375. https://doi.org/10.1016/j.palaeo.2016.03.019

Warter, V., Muller, W., Wesselingh, F. P., Todd, J. A., & Renema, W. (2015). Late Miocene seasonal to subdecadal climate variability in the Indo-West Pacific (East Kalimantan, Indonesia) preserved in giant clams. *Palaios*, ***30***(1), 66–82. https://doi.org/10.2110/palo.2013.061

Watanabe, T., & Oba, T. (1999). Daily reconstruction of water temperature from oxygen isotopic ratios of a modern *Tridacna* shell using a freezing microtome sampling technique. *Journal of Geophysical Research: Oceans*, ***104***(C9), 20667–20674. https://doi.org/10.1029/1999JC900097

Watanabe, T., Suzuki, A., Kawahata, H., Kan, H., & Ogawa, S. (2004). A 60-year isotopic record from a mid-Holocene fossil giant clam (*Tridacna gigas*) in the Ryukyu Islands: Physiological and paleoclimatic implications. *Palaeogeography, Palaeoclimatology, Palaeoecology*, ***212***(3–4), 343–354. https://doi.org/10.1016/S0031-0182(04)00358-X

Watson, S. A., & Neo, M. L. (2021). Conserving threatened species during rapid environmental change: Using biological responses to inform management strategies of giant clams. *Conservation Physiology*, ***9***(1), coab082. https://doi.org/10.1093/conphys/coab082

Wear, S. L., & Thurber, R. V. (2015). Sewage pollution: Mitigation is key for coral reef stewardship. *Annals of the New York Academy of Sciences*, ***1355***(1), 15–30. https://doi.org/10.1111/nyas.12785

Weiner, S., & Dove, P. M. (2003). An Overview of Biomineralization Processes and the Problem of the Vital Effect. *Reviews in Mineralogy and Geochemistry*, ***54***(1), 1– 29. https://doi.org/10.2113/0540001

Weiner, S., & Traub, W. (1984) Macromolecules in mollusc shells and their functions in biomineralization. *Transactions of the Royal Society of London. B, Biological Sciences,* ***304***(1121), 425–434.

Welsh, K., Elliot, M., Tudhope, A., Ayling, B., & Chappell, J. (2011). Giant bivalves (*Tridacna gigas*) as recorders of ENSO variability. *Earth and Planetary Science Letters*, ***307***(3), 266–270. https://doi.org/10.1016/j.epsl.2011.05.032

Wichern, N. M. A., de Winter, N. J., Johnson, A. L. A., Goolaerts, S., Wesselingh, F., Hamers, M. F., Kaskes, P., Claeys, P., & Ziegler, M. (2023). The fossil bivalve *Angulus benedeni benedeni*: A potential seasonally resolved stable-isotope-based climate archive to investigate Pliocene temperatures in the southern North Sea basin. *Biogeosciences*, ***20***(12), 2317–2345. https://doi.org/10.5194/bg-20-2317-2023

Winkelmann, A., Jablon, B. M., Tong, V. S., Trager-Cowan, C., & Mingard, K. P. (2020). Improving EBSD precision by orientation refinement with full pattern matching. *Journal of Microscopy*, ***277***(2), 79–92. https://doi.org/10.1111/jmi.12870

Wolfe, K., Smith, A. M., Trimby, P., & Byrne, M. (2013). Microstructure of the paper nautilus (*Argonauta nodosa*) shell and the novel application of electron backscatter diffraction (EBSD) to address effects of ocean acidification. *Marine Biology*, ***160***(8), 2271–2278. https://doi.org/10.1007/s00227-012-2032-4

Yan, H., Liu, C., An, Z., Yang, W., Yang, Y., Huang, P., Qiu, S., Zhou, P., Zhao, N., Fei, H., Ma, X., Shi, G., Dodson, J., Hao, J., Yu, K., Wei, G., Yang, Y., Jin, Z., & Zhou, W. (2020). Extreme weather events recorded by daily to hourly resolution biogeochemical proxies of marine giant clam shells. *Proceedings of the National Academy of Sciences*, ***117***(13), 7038–7043. https://doi.org/10.1073/pnas.1916784117

Yan, H., Zhao, N., Zhou, P., Liu, C., Fei, H., Li, M., Liu, F., Yang, Y., Yang, W., & Dodson, J. (2021). The first detection of the Madden-Julian Oscillation signal in daily to hourly resolution proxy records derived from a natural archive of Giant Clam Shell (*Tridacna* spp.). *Earth and Planetary Science Letters*, ***555***(1), 116703. https://doi.org/10.1016/j.epsl.2020.116703

Yao, Q., Wang, Y., Zhang, Y., Li, H., & Zhou, G. (2019). A biomimetic experimental study of magnesium ion mineralization in Mg-enriched aragonite. *Science China Earth Sciences*, ***62***(10), 1619–1629. https://doi.org/10.1007/s11430-018-9336-6

Yau, A. J. Y., & Fan, T. Y. (2012). Size-dependent photosynthetic performance in the giant clam *Tridacna maxima*, a mixotrophic marine bivalve. *Marine Biology*, ***159***(1), 65–75. https://doi.org/10.1007/s00227-011-1790-8

Ye, F., Crippa, G., Garbelli, C., & Griesshaber, E. (2018). Microstructural data of six recent brachiopod species: SEM, EBSD, morphometric and statistical analyses. *Data in Brief*, ***18***(1), 300–318. https://doi.org/10.1016/j.dib.2018.02.071

Yee, S. H., & Barron, M. G. (2010). Predicting coral bleaching in response to environmental stressors using 8 years of global-scale data. *Environmental Monitoring and Assessment*, ***161***(1–4), 423–438. https://doi.org/10.1007/s10661-009-0758-3

Yong, W. L., Todd, P. A., Ang, A. C. F., Ying, L. S. M., Teo, A., Lee, S. H. R., Low, J., & Neo, M. L. (2022). Fluted giant clam (*Tridacna squamosa*) restocking experiment in an urban turbid reef environment. *Aquatic Conservation: Marine and Freshwater Ecosystems*, ***32***(4), 633–644. https://doi.org/10.1002/aqc.3789

Yoshimura, T., Tamenori, Y., Takahashi, O., Nguyen, L. T., Hasegawa, H., Iwasaki, N., Kuroyanagi, A., Suzuki, A., & Kawahata, H. (2015). Mg coordination in biogenic carbonates constrained by theoretical and experimental XANES. *Earth and Planetary Science Letters*, ***421***(1), 68–74. https://doi.org/10.1016/j.epsl.2015.03.048

Yu, X., Salama, Mhd. S., Shen, F., & Verhoef, W. (2016). Retrieval of the diffuse attenuation coefficient from GOCI images using the 2SeaColor model: A case study in the Yangtze Estuary. *Remote Sensing of Environment*, ***175***(1), 109–119. https://doi.org/10.1016/j.rse.2015.12.053

Zhang, T., & Fell, F. (2007). An empirical algorithm for determining the diffuse attenuation coefficient Kd in clear and turbid waters from spectral remote sensing reflectance. *Limnology and Oceanography: Methods*, ***5***(12), 457–462. https://doi.org/10.4319/lom.2007.5.457

Zhao, N., Yan, H., Luo, F., Yang, Y., Liu, S., Zhou, P., Liu, C., & Dodson, J. (2023). Daily growth rate variation in *Tridacna* shells as a record of tropical cyclones in the

South China Sea: Palaeoecological implications. *Palaeogeography, Palaeoclimatology, Palaeoecology*, ***615***(1), 111444. https://doi.org/10.1016/j.palaeo.2023.111444

Zhao, N., Yan, H., Yang, Y., Liu, C., Ma, X., Wang, G., Zhou, P., Wen, H., Qu, X., & Dodson, J. (2021). A 23.7-year long daily growth rate record of a modern giant clam shell from South China Sea and its potential in high-resolution paleoclimate reconstruction. *Palaeogeography, Palaeoclimatology, Palaeoecology*, ***583***(1), 110682. https://doi.org/10.1016/j.palaeo.2021.110682

Zhou, G. T., Yao, Q. Z., Ni, J., & Jin, G. (2009). Formation of aragonite mesocrystals and implication for biomineralization. *American Mineralogist*, ***94***(2–3), 293–302. https://doi.org/10.2138/am.2009.2957

Ziuganov, V., Miguel, E. S., Neves, R. J., Longa, A., Fernández, C., Amaro, R., Beletsky, V., Popkovitch, E., Kaliuzhin, S., & Johnson, T. (2000). Life Span Variation of the Freshwater Pearl Shell: A Model Species for Testing Longevity Mechanisms in Animals. *AMBIO: A Journal of the Human Environment*, ***29***(2), 102–105. https://doi.org/10.1579/0044-7447-29.2.102

Zweifler, A., O'Leary, M., Morgan, K., & Browne, N. K. (2021). Turbid Coral Reefs: Past, Present and Future—A Review. *Diversity*, ***13***(6), 251. https://doi.org/10.3390/d13060251

Appendix A

The R code for assembling growth chronologies and data analysis in chapter 3 is available from the Mendeley Data Repository at Mills, Kimberley (2023), “Growth responses of mixotrophic giant clams on nearshore turbid coral reefs”, https://doi.org/10.17632/mbjzc2nbsn.1

Appendix B

The raw EBSD data files and MATLAB code used in chapter 4 is available from the Mendeley Data Repository at Mills, Kimberley (2023), “Microstructure and crystallographic texture data from modern giant clam shells (*Tridacna squamosa* and *Hippopus hippopus*)”, https://doi.org/10.17632/2zfgjy27wg.5

Appendix C

The element-to-calcium ratios used in chapter 5 are available from the Mendeley Data Repository at Mills, Kimberley (2023), “Giant clams modify crystallographic and geochemical pathways of shell formation in response to turbidity”, https://doi.org/10.17632/w93czv65vg.2

Appendix D

Raw Raman spectroscopy data and EBSD quantitative grain area data associated with chapter 6 are available from the Mendeley Data Repository at Mills, Kimberley (2023), “Diagenetic alteration in fossil giant clam shells: crystallographic texture detects alteration from pristine to secondary aragonite ”, https://doi.org/10.17632/vkmsk6gc3m.1